

**BROADBAND GRAPHITIC CARBON NITRIDE-BASED
PHOTOCATALYSTS FOR ENVIRONMENTAL AND ENERGY
APPLICATIONS**

Par

Qingzhe Zhang

Thèse présentée pour l'obtention
du grade de Philosophiae Doctor (Ph.D.)
en sciences de l'énergie et des matériaux

Jury d'évaluationPrésident du jury et
examineur interneProfesseur Francois Vidal
INRS-ÉMT

Examineur externe

Professeur Adam Duong
Université du Québec à Trois-Rivières

Examineur externe

Professeur Patanjali Kambhampati
Université McGill

Directeur de recherche

Professeur Dongling Ma
INRS-ÉMT

Codirecteur de recherche

Professeur Mohamed Chaker
INRS-ÉMT

*Dedicated to all my teachers,
my friends,
and my family members;
to all the people
who are fighting against the Covid-19 pandemic.*

ACKNOWLEDGEMENTS

First and foremost, I would like to express my deepest gratitude to my supervisor, Prof. Dongling Ma, for her constant encouragement, invaluable guidance, and immense patience during the past four years. I am extremely grateful for her continuing, unconditional support and for providing me with great opportunities to develop myself, such as attending international conferences, serving as conference assistant, and competing for various awards. Her ability to transform my raw and immature ideas into insightful storylines has always been fascinating me. She helped me to cope with the challenges of academic research and the difficulties in life. I have learned so much from her, including the way of thinking, giving credit to people, valuing collaboration and reputation, and communicating ideas effectively. I feel extremely lucky to be her student to work with her.

My special thanks go to my co-supervisor, Prof. Mohamed Chaker, for his substantial support and guidance throughout my Ph.D. journey. He has always been giving me inspiring motivation and encouragement when I was stuck in a problem or could not see the value of my work. He taught me how to know or judge a problem from a macroscopic perspective. He always looks energetic even though he just had a 4-hour sleep one night. It is my great privilege to have had him as my co-supervisor.

Being able to learn from my two supervisors has been my great fortune.

I am indebted to my previous supervisors and teachers, Prof. Yanjun Xin, Prof. Nan Bao, and Prof. Dong Ma who brought me to this research field. Their mentorship made me start along the path to where I am today.

I would like to thank Prof. Francois Vidal, Prof. Adam Duong, and Prof. Patanjali Kambhampati for being the members of my thesis committee and offering their precious comments and valuable time.

I have been fortunate to collaborate with many excellent individuals, including Shuai Zhou, Prof. Nan Bao, Gang Wang, Prof. Yanjun Xin, Dr. Xin Jin, Prof. Luca Razzari, Prof. Alexander O. Govorov, Prof. Giacomo Giorgi, and Prof. Maurizia Palummo, who gave me enormous help both in experimental and theoretical aspects. Their contributions made this thesis possible.

I felt incredibly lucky and a great honor to meet Prof. Ma's wonderful friends and collaborators, including but not limited to Prof. Nianqiang Wu, Prof. Jin Zhong Zhang, Prof. Baoquan Sun, Prof. Xuhui Sun, Prof. Dunwei Wang, Prof. Hong Liu, Prof. Bruce Koel, and Prof. Ricardo Izquierdo.

Talking with them always benefit me a lot. I especially thank Prof. Nianqiang Wu who enlightened me with his profound knowledge and unique views and encouraged me to aim high.

Prof. Dongling Ma's group is an amazing community, where I shared joys with and gained assistance from current and former group members and friends, Prof. Zhenhe Xu, Prof. Jiujun Deng, Prof. Jianming Zhang, Prof. Guozhu Chen, Prof. Hongyan Liang, Prof. Haiguang Zhao, Prof. Kun Zhang, Dr. Fan Yang, Dr. Fuqiang Ren, Dr. Long Tan, Dr. Yannan Liu, Dr. Xiaolei Liu, Dr. Amir Mirzaei, Yanlong Liu, Deepak T. Gangadharan, Shengyun Huang, Pandeng Li, Yong Wang, Chen Wang, Ting Yu, Wanting He, and Guolong Song. I especially thank Prof. Zhenhe Xu for training me to start my research work in INRS.

I really enjoy my stay in the INRS-EMT center. I would like to thank Prof. Marc A. Gauthier, Prof. Ana Tavares, Prof. Fiorenzo Vetrone, Prof. Andreas Ruediger, Prof. Shuhui Sun, and Prof. Jinyang Liang, for the inspiring conversations with them. I benefited tremendously from them. I would also like to thank the nice and helpful technicians and administrative staffs in INRS-EMT, especially Christophe Chabanier, Catalin Harnagea, Etienne Charette, Georges Lamoureux, Claude Sirois, Julie Gaudet, Sylvain Gingras, Louise Hudon, H  l  ne Sabourin, H  l  ne Tanguay, Michelle Marcotte, Priscille Ernotte, and Jean-Yves Lavoie. I feel lucky to know a lot of friends (in addition to our group members) to share joys with them during the past years, particularly Mengyang Fan, Xin Chai, Li Shi, Yuting Lei, Minghui Hao, Xin Liu, Xianglei Liu, Cheng Jiang, Jiyun Chen, Faying Li, Min Zhang, Na Xu, Daling Cui, Xin Tong, Chao Wang, Hui Zhang, Jiabin Liu, Nathanael Komba, Artiom Skripka, Jes  s Angel Valdez, Lucas Vazquez Besteiro, Zineb Matouk, and many others. Thank Xin Chai for helping me in French translation.

I am also very grateful to Jean-Philippe Masse, Gwena  l Chamoulaud, Alexandre Arnold, and Galyna Shul, who provided massive help and support in the characterizations of my samples.

Last, but not least, I am profoundly indebted to my grandpa, parents and sister for their continual love, understanding, support, and patience, which keep me grounded and energetic regardless of all the ups and downs in life. They also shared my pains and joys of this journey.

It could not be possible to complete this thesis without the contributions from so many people along the journey in the past four years. The names listed herein are just some representatives I am grateful to, and I apologize in advance if I failed to mention you. But rest assured that I really appreciate those who are reading these lines.

ABSTRACT

As a semiconductor photocatalyst, graphitic carbon nitride ($g\text{-C}_3\text{N}_4$) has attracted tremendous interest of material scientists by virtue of its fascinating merits, such as nontoxicity, facile preparation, moderate bandgap, strong redox capability, “earth-abundant” nature, and good physicochemical stability. However, $g\text{-C}_3\text{N}_4$ still suffers from poor photocatalytic activity and low quantum efficiency due to the high recombination rate of photogenerated charge carriers. Moreover, the optical bandgap (2.7 eV) of $g\text{-C}_3\text{N}_4$ largely restrains the range of its visible light absorption to wavelengths shorter than 460 nm. Thus, the development of efficient and broadband responsive (from ultraviolet (UV), visible to near-infrared (NIR) regions) $g\text{-C}_3\text{N}_4$ based photocatalysts is a task of great significance and urgency, though challenging. In this thesis, three kinds of $g\text{-C}_3\text{N}_4$ based broadband photocatalysts were developed and used in photocatalytic degradation of organic pollutants and green fuel production.

Firstly, a plasmon and upconversion enhanced broadband photocatalyst based on Au nanoparticle (NP) and $\text{NaYF}_4:\text{Yb}^{3+}, \text{Er}^{3+}, \text{Tm}^{3+}$ (NYF) microsphere loaded $g\text{-C}_3\text{N}_4$ nanosheets (Au-NYF/ $g\text{-C}_3\text{N}_4$) was subtly designed and synthesized. The simple one-step synthesis of NYF in the presence of $g\text{-C}_3\text{N}_4$, which has not been reported in the literature either, leads to both high NYF yield and high coupling efficiency between NYF and $g\text{-C}_3\text{N}_4$. The Au-NYF/ $g\text{-C}_3\text{N}_4$ structure exhibits high stability, wide photoresponse from the UV, to visible and NIR regions, and prominently enhanced photocatalytic activities compared with the plain $g\text{-C}_3\text{N}_4$ sample in the degradation of a common pollutant, methyl orange. The high performance of the Au-NYF/ $g\text{-C}_3\text{N}_4$ nanocomposite under different light irradiations was ascribed to the distinctively promoted charge separation and suppressed recombination, and the efficient transfer of charge carriers and energy among these components. The promoted charge separation and transfer were further confirmed by photoelectrochemical measurements. Different mechanisms of the photodegradation under separate UV, visible, and NIR illuminations are unveiled and discussed in detail. Under simulated solar light illumination, the involved reactive species were identified by performing trapping experiments.

Secondly, a heterojunction made of 0-dimensional (0D) NIR-responsive $\text{PbS}@\text{CdS}@\text{ZnS}$ core@shell@shell quantum dots (PCZ QDs) and 2-dimensional (2D) $g\text{-C}_3\text{N}_4$ nanosheets, named 0D/2D heterojunction, was rationally constructed. In addition to some typical advantages of 0D/2D composites, such as short required-charge-diffusion-distance and high charge mobility, our designed PCZ QDs/ $g\text{-C}_3\text{N}_4$ photocatalysts offer additional beneficial features. The broadband

optical absorption of high-quality PCZ QDs highly dispersed on the surface of the g-C₃N₄ nanosheets and their strong interaction yield efficient charge transfer between them and endow PCZ QDs/g-C₃N₄ with high photocatalytic activity from UV to NIR regions. Actually, with the optimization of PCZ QDs loading levels, the achieved, normalized rate constant is higher than the best-reported value for NIR-driven photocatalysis. The charge transfer was investigated and supported by steady-state and time-resolved photoluminescence spectroscopy and solid-state electron spinning spectroscopy (ESR) as well as photoelectrochemical measurements. Superoxide radicals were identified as the most important active species in photocatalysis by scavenger experiments and ESR spectra. PCZ QDs/g-C₃N₄ possesses good recycling performance and no metal release was detected in the solution after photocatalysis.

Thirdly, a 2D/2D heterojunction of black phosphorus (BP)/g-C₃N₄ was designed and synthesized for photocatalytic H₂ evolution. The ice-assisted exfoliation method developed herein for preparing BP nanosheets from bulk BP, leads to high yield of few-layer BP nanosheets (≈ 6 layers on average) with large lateral size at reduced duration and power for liquid exfoliation. The combination of BP with g-C₃N₄ protects BP from oxidation and contributes to enhanced activity both under $\lambda > 420$ nm and $\lambda > 475$ nm light irradiation and to long-term stability. The H₂ production rate of BP/g-C₃N₄ (384.17 $\mu\text{mol g}^{-1} \text{h}^{-1}$) is comparable to, and even surpasses that of the previously reported, precious metal-loaded photocatalyst under $\lambda > 420$ nm light. The efficient charge transfer between BP and g-C₃N₄ (likely due to formed N-P bonds) and broadened photon absorption (supported both experimentally and theoretically) contributed to the excellent photocatalytic performance. The possible mechanisms of H₂ evolution under various forms of light irradiation is unveiled.

Keywords: broadband photocatalyst, carbon nitride, plasmonic, upconversion, near-infrared quantum dots, metal-free, black phosphorus, photocatalytic degradation, hydrogen evolution

RÉSUMÉ

En tant que photocatalyseur à semi-conducteur, le nitrure de carbone graphitique ($g\text{-C}_3\text{N}_4$) présente un grand intérêt pour le domaine des matériaux, pour ses mérites tels que la non-toxicité, la facilité de préparation, la bande interdite modérée, la forte capacité rédox, l'abondance sur terre et la bonne stabilité physico-chimique. Cependant, le $g\text{-C}_3\text{N}_4$ souffre toujours d'une activité photocatalytique médiocre et d'un rendement quantique faible en raison du taux de recombinaison élevé des porteurs de charge photogénérés. En plus, la bande interdite optique (2,7 eV) du $g\text{-C}_3\text{N}_4$ limite grandement la plage d'absorption de la lumière visible aux longueurs d'onde inférieures à 460 nm. Ainsi, le développement de photocatalyseurs basés sur du $g\text{-C}_3\text{N}_4$ répondant efficacement dans une large bande d'absorption couvrant l'ultraviolet (UV), le visible, et l'infrarouge (NIR), demeure une tâche de grande importance et de grande urgence, bien que difficile. Dans cette thèse, trois types de photocatalyseurs à large bande basés sur le $g\text{-C}_3\text{N}_4$ ont été développés et utilisés pour la dégradation photocatalytique de polluants organiques et la production de carburant écologique.

Tout d'abord, nous avons synthétisé un photocatalyseur à large bande amélioré par plasmon et conversion ascendante (upconversion, UP), basé sur des nano-feuilles de $g\text{-C}_3\text{N}_4$ chargées de nanoparticules (NP) d'or et de microsphères de $\text{NaYF}_4:\text{Yb}^{3+}, \text{Er}^{3+}, \text{Tm}^{3+}$ (NYF) ($\text{Au-NYF}/g\text{-C}_3\text{N}_4$). La synthèse en une simple étape de NYF en présence de $g\text{-C}_3\text{N}_4$, qui n'a pas été rapportée dans la littérature, conduit à la fois à un rendement élevé en NYF et à une efficacité de couplage élevée entre NYF et $g\text{-C}_3\text{N}_4$. La structure $\text{Au-NYF}/g\text{-C}_3\text{N}_4$ présente une stabilité élevée, une large bande de photoréponse allant de l'UV aux régions visibles et NIR, ainsi qu'une activité photocatalytique nettement accrue au $g\text{-C}_3\text{N}_4$ lors de la dégradation du méthyl orange. Les hautes performances du nano-composite $\text{Au-NYF}/g\text{-C}_3\text{N}_4$ sous différentes irradiations lumineuses sont attribuées au fait que la séparation des charges est nettement favorisée et à la suppression de la recombinaison ainsi qu'au transfert efficace des porteurs de charge et de l'énergie entre ces composants. Le fait que la séparation et le transfert de charge soient favorisés a ensuite été confirmé par des mesures photoélectrochimiques. Différents mécanismes de photo-dégradation réalisés séparément sous des éclairages UV, visible et NIR sont mis en évidence et discutés en détail. En simulant une illumination solaire, les espèces réactives impliquées ont été identifiées en effectuant des expériences de piégeage.

Deuxièmement, une hétérojonction, constituée de points quantiques $\text{PbS}@ \text{CdS}@ \text{ZnS}$ core@shell@shell (PCZ QDs) et de $g\text{-C}_3\text{N}_4$ à deux dimensions (2D), et dénommée hétérojonction

0D/2D, a été synthétisée. En plus des avantages typiques des composites 0D/2D, tels qu'une courte distance de diffusion par charge et une mobilité élevée des charges, nos photocatalyseurs PCZ QDs/g-C₃N₄ offrent des fonctionnalités supplémentaires. L'absorption optique à large bande de PCZ QD de haute qualité dispersés sur toute la surface des nano-feuilles de g-C₃N₄ et leur forte interaction permettent un transfert de charge efficace entre eux. Ceci confère aux hétérojonctions PCZ QDs/g-C₃N₄ une activité photocatalytique élevée de l'UV à la région NIR. En fait, avec l'optimisation des niveaux de charge des PCZ QD, l'efficacité photocatalytique normalisée est supérieure à la meilleure valeur rapportée dans la littérature pour la photocatalyse dans le NIR. Le transfert de charge a été étudié et analysé grâce à la spectroscopie à photoluminescence en régime continu et résolu dans le temps, par spectroscopie à spin électronique (ESR) ainsi que par des mesures photoélectrochimiques. Les radicaux superoxydes ont été identifiés comme l'espèce active la plus importante dans la photocatalyse par des expériences «scavenger» et des spectres d'ESR. Les PCZ QDs/g-C₃N₄ possèdent de bonnes performances de recyclage et aucun relâchement de métal n'a été détecté dans la solution après photocatalyse.

Troisièmement, une hétérojonction 2D/2D de phosphore noir (BP)/g-C₃N₄ a été conçue et synthétisée pour le dégagement photocatalytique de H₂. La méthode d'exfoliation assistée par de la glace développée ici pour la préparation de nano-feuilles de BP à partir de BP massif conduit à un rendement élevé en nano-feuilles de BP à plusieurs couches (6 couches en moyenne) avec une grande taille latérale et une exfoliation liquide de courte durée et de faible puissance. La combinaison de BP avec le g-C₃N₄ protège le BP de l'oxydation et contribue à une activité accrue sous irradiation lumineuse $\lambda > 420$ nm et $\lambda > 475$ nm et à une grande stabilité à long terme. Le taux de production de H₂ à partir de BP/g-C₃N₄ (384,17 $\mu\text{mol g}^{-1} \text{h}^{-1}$) est comparable voire supérieur à ce qui a été rapporté dans la littérature, à savoir celui d'un photocatalyseur chargé de métaux précieux sous irradiation $\lambda > 420$ nm. Le transfert de charge efficace entre BP et g-C₃N₄ (probablement dû à la formation de liens N-P) et la large bande d'absorption (démontrés à la fois expérimentalement et théoriquement) contribuent à l'excellente performance photocatalytique. Les mécanismes possibles d'évolution de H₂ sous différentes types d'irradiation lumineuse sont mis en évidence.

Mots-clés: photocatalyseur à large bande, nitrure de carbone, plasmonique, conversion ascendante, points quantiques dans le proche infrarouge, sans métal, phosphore noir, dégradation photocatalytique, dégagement d'hydrogène

TABLE OF CONTENTS

ACKNOWLEDGEMENTS	III
ABSTRACT	V
RÉSUMÉ	VII
TABLE OF CONTENTS	IX
LIST OF FIGURES	XIII
LIST OF TABLES	XIX
LIST OF ABBREVIATIONS AND ACRONYMS	XXI
LIST OF PUBLICATIONS, CONFERENCE PRESENTATIONS, AND AWARDS	XXIII
1 INTRODUCTION	1
1.1 General Background	1
1.2 Fundamentals of Photocatalysis.....	2
1.3 Requirements and Current Challenges for Photocatalysis.....	5
1.3.1 <i>Photo-response range</i>	5
1.3.2 <i>Redox capability</i>	5
1.3.3 <i>Charge separation and transportation</i>	6
1.3.4 <i>Adsorptivity and stability</i>	6
1.4 Graphitic Carbon Nitride Photocatalyst.....	7
1.4.1 <i>Microstructure</i>	7
1.4.2 <i>Electronic structure</i>	8
1.4.3 <i>Synthesis methods</i>	8
1.4.4 <i>Inherent drawbacks</i>	9
1.5 Strategies to Construct Broadband g-C ₃ N ₄ Based Photocatalysts	10
1.5.1 <i>Employing upconversion materials</i>	11
1.5.2 <i>Introducing surface plasmon resonance effect</i>	14
1.5.3 <i>Coupling with narrow-bandgap semiconductor</i>	20

1.6	Thesis Objectives and Organizations	27
1.6.1	<i>Thesis objectives</i>	27
1.6.2	<i>Thesis organizations</i>	28
2	EXPERIMENTAL	31
2.1	Materials	31
2.2	Synthesis of g-C ₃ N ₄ Nanosheets	31
2.3	Synthesis of Au-NYF/g-C ₃ N ₄	31
2.3.1	<i>Preparation of Au NP colloids</i>	31
2.3.2	<i>In-situ synthesis of NYF/g-C₃N₄ composites</i>	32
2.3.3	<i>Preparation of Au NP loaded NYF/g-C₃N₄ photocatalysts</i>	32
2.4	Synthesis of PCZ QDs/g-C ₃ N ₄ Nanosheets.....	32
2.4.1	<i>Synthesis of PbS QDs</i>	32
2.4.2	<i>Synthesis of PbS@CdS core@shell QDs</i>	33
2.4.3	<i>Synthesis of PCZ core@shell@shell QDs</i>	33
2.4.4	<i>Preparation of PCZ QDs/g-C₃N₄ nanosheets</i>	34
2.5	Synthesis of BP/g-C ₃ N ₄ Nanosheets	34
2.5.1	<i>NMP-ice-assisted preparation of BP nanosheets</i>	34
2.5.2	<i>Preparation of BP/g-C₃N₄ photocatalysts</i>	34
2.6	Characterizations	35
2.7	Photoelectrochemical Measurements.....	36
2.8	Photocatalytic Activity Evaluation and Trapping Experiments.....	37
2.8.1	<i>Photocatalytic degradation of MO by Au-NYF/g-C₃N₄</i>	37
2.8.2	<i>Photocatalytic degradation of MO by PCZ QDs/g-C₃N₄</i>	37
2.8.3	<i>Trapping experiments</i>	38
2.8.4	<i>Photocatalytic H₂ evolution by BP/g-C₃N₄</i>	38
2.9	Theoretical Calculations	38
3	PLASMON AND UPCONVERSION ENHANCED CARBON NITRIDE	41
3.1	Introduction	43

3.2	Experimental Section	45
3.2.1	<i>Materials</i>	45
3.2.2	<i>Preparation of Au NP colloids</i>	45
3.2.3	<i>Preparation of g-C₃N₄</i>	46
3.2.4	<i>In-situ synthesis of NYF/g-C₃N₄ composites</i>	46
3.2.5	<i>Preparation of Au NP loaded NYF/g-C₃N₄ photocatalysts</i>	46
3.2.6	<i>Photocatalytic experiment and the detection of active species</i>	46
3.2.7	<i>Characterization</i>	47
3.3	Results and Discussions	48
3.3.1	<i>Structural and morphological characterization</i>	48
3.3.2	<i>Optical properties</i>	50
3.3.3	<i>Photocatalytic activities</i>	52
3.3.4	<i>Detection of active species and relevant mechanisms</i>	55
3.4	Conclusions	59
	Acknowledgements	60
3.5	Supporting Information.....	60
4	NIR-RESPONSIVE QUANTUM DOTS/CARBON NITRIDE	63
4.1	Introduction	65
4.2	Experimental Details	67
4.2.1	<i>Materials</i>	67
4.2.2	<i>Synthesis of PbS QDs</i>	67
4.2.3	<i>Synthesis of PbS@CdS core@shell QDs</i>	68
4.2.4	<i>Synthesis of PCZ core@shell@shell QDs</i>	68
4.2.5	<i>Preparation of PCZ QDs/g-C₃N₄ nanosheets</i>	69
4.2.6	<i>Characterization</i>	69
4.2.7	<i>Photocatalytic activity measurements and trapping experiments</i>	70
4.3	Results and Discussion	71
4.3.1	<i>Microstructures and optical properties</i>	71

4.3.2	<i>Photocatalytic activity and stability</i>	75
4.3.3	<i>Charge transfer dynamics and PEC measurements</i>	78
4.3.4	<i>Detection of active species</i>	79
4.3.5	<i>Proposed possible mechanism</i>	80
4.4	Conclusions	82
	Acknowledgements	82
4.5	Supporting Information	83
5	METAL-FREE BLACK PHOSPHORUS/CARBON NITRIDE	93
5.1	Introduction	95
5.2	Results and Discussions	97
5.2.1	<i>Preparation of BP nanosheets and BP/g-C₃N₄ photocatalysts</i>	97
5.2.2	<i>Morphological and structural characterization</i>	98
5.2.3	<i>Optical properties</i>	102
5.2.4	<i>Photocatalytic H₂ evolution</i>	103
5.2.5	<i>PEC measurements and charge transfer dynamics</i>	105
5.2.6	<i>UPS measurement</i>	106
5.2.7	<i>Mechanism of photocatalytic H₂ evolution under different light irradiations</i>	107
5.3	Conclusions	108
	Acknowledgements	108
5.4	Supporting Information	109
5.4.1	<i>Experimental section</i>	109
5.4.2	<i>Theoretical calculations</i>	112
6	CONCLUSIONS AND PERSPECTIVES	121
6.1	Conclusions	121
6.2	Perspectives	122
	BIBLIOGRAPHY	125
	SOMMAIRE RÉCAPITULATIF	157

LIST OF FIGURES

- Figure 1.1** Schematic illustration of the principle of semiconductor photocatalysis. (I) the formation of charge carriers by a photon; (II) the charge carrier recombination to liberate heat; (III) the initiation of a reductive pathway by a CB electron; (IV) the initiation of an oxidative pathway by a CB hole; (V) the further thermal (e.g., hydrolysis or reaction with active oxygen species) and photocatalytic reactions to yield mineralization products; (VI) the trapping of a conduction band electron in a dangling surficial bond; (VII) the trapping of a VB hole at the surface of the semiconductor. Reprinted with permission.³⁹ Copyright 2014, The Royal Society of Chemistry..... 3
- Figure 1.2** (a-b) Electronic structure of semiconductor photocatalysts and Gibbs energy change in photocatalytic reactions. (c-d) Two distinct classifications of photocatalytic reactions, namely downhill (c) and uphill (d) reactions. Reprinted with permission.²⁹ Copyright 2018, WILEY-VCH. 4
- Figure 1.3** Spectral distribution of the solar photon irradiation based on the AM1.5 global data. Reprinted with permission.⁴⁰ Copyright 2012, The Royal Society of Chemistry. . 5
- Figure 1.4** The hypothetical ideal structure of g-C₃N₄ based on (a) s-triazine and (b) tri-s-triazine (heptazine) tectonic units. Reprinted with permission.⁹² Copyright 2012, American Chemical Society. 8
- Figure 1.5** Schematic illustration of the synthesis process of g-C₃N₄ by thermal polymerization of different precursors such as melamine,^{103,104} cyanamide,^{101,105} dicyandiamide,^{106,107} urea,^{108,109} thiourea.^{110,111} The black, blue, white, red, and yellow balls denote C, N, H, O, and S atoms, respectively. Reprinted with permission.⁹³ Copyright 2016, American Chemical Society. 9
- Figure 1.6** Lanthanide-doped UC particles and photon UC. (a) Schematic energy level diagram showing that UC luminescence primarily originates from electron transitions between energy levels of localized dopant ions. (b) Schematic illustration of UC particles composed of a crystalline host and lanthanide dopant ions embedded in the host lattice. Reprinted with permission.¹⁵³ Copyright 2010, The Royal Society of Chemistry. (c) Typical lanthanide-based UC emission bands covering a broad range of wavelengths from UV (~290 nm) to NIR (~880 nm) and their corresponding main optical transitions. Reprinted with permission.¹⁴⁹

Copyright 2015, Springer Nature. (d) Typical emission spectra showing multiple narrow and well-separated emissions produced by cubic NaYF₄:Yb/Tm (20/0.2 mol%) and NaYF₄:Yb/Er (18/2 mol%) particles. (e) UC multicolor fine-tuning through the use of lanthanide-doped NaYF₄ particles with varied dopant ratios. Note that the emission spectra and colors are associated with the host composition, particle size, and particle surface properties. Reprinted with permission.¹⁵⁴ Copyright 2008, American Chemical Society..... 12

Figure 1.7 Illustration of the UC enhanced photocatalysis. Reprinted with permission.¹⁵² Copyright 2019, Royal Society of Chemistry. 13

Figure 1.8 Schematic illustration of plasmon oscillation on a plasmonic metal sphere. An oscillation of conduction electron charge cloud relative to the nuclei is established by the external oscillating electric field. Reproduced with permission.²⁰⁰ Copyright 2003, American Chemical Society. 14

Figure 1.9 (a) Normalized extinction spectra of spherical Ag (38 ± 12 nm diameter), Au (25 ± 5 nm) and Cu (133 ± 23 nm) particles. The intensity of solar radiation (data for air mass 1.5 solar spectrum from the National Renewable Energy Laboratory) is also shown, in black. The metal extinction is a consequence of the excitation of SPR. Dashed portions of the metal extinction curves indicate interband transitions. (b) Normalized extinction spectra for Ag wire (90 ± 12 nm diameter and > 30 aspect ratio), cube (79 ± 12 nm edge length) and sphere (38 ± 12 nm diameter) NPs. (c) Normalized extinction spectra for Ag nanocubes as a function of size (56 ± 8 nm, 79 ± 13 nm and 129 ± 7 nm edge lengths correspond to orange, red and blue spectra, respectively). The inset shows a photograph of the three nanocube samples suspended in ethanol. Reproduced with permission.¹⁹⁹ Copyright 2011, Springer Nature. 15

Figure 1.10 Mechanism of SPR-induced charge transfer with approximate energy levels on the NHE scale. Dashed red lines refer to the water-splitting redox potentials. (i) Electrons near the metal Fermi level, E_f are excited to surface plasmon (SP) states; (ii) the electrons transfer to a nearby semiconductor particle; (iii) this activates electron-driven processes such as the H₂-evolution. Reproduced with permission.¹⁹⁹ Copyright 2011, Springer Nature..... 16

Figure 1.11 Optical simulations showing SPR-enhanced electric fields owing to photo-excited Au particles, permeating into a neighboring TiO₂ structure. The color bar shows electric field intensity normalized by the light source intensity ($|E|^2/|E_0|^2$). The

electric field intensity (and therefore charge-carrier generation) is the highest at the metal/semiconductor/liquid three-phase boundary. Reproduced with permission.²²³ Copyright 2011, American Chemical Society..... 17

Figure 1.12 (a) Illustration of the phenomenon where electron-hole pairs generated deep under the surface of the semiconductor recombine easily. (b) Illustration of the situation when plasmonic metals are loaded at the surface of the semiconductor. The light-absorption layer becomes thinner where electron-hole pairs are generated at a high rate as a result of near-field electromagnetic resonant energy transfer. The generated electron-hole pairs take part in the reactions easily owing to their shorter migration length. Reproduced with permission.⁴³ Copyright 2015, WILEY-VCH..... 18

Figure 1.13 (a) Schematic illustration of the energy flux (Poynting vectors) and the electric-field intensity for an incident electromagnetic wave with an electric field in the plane of the image. Red/blue represent high/low electric-field intensity. The scattering effect is neglected. Reproduced with permission.²⁰¹ Copyright 2011, Royal Society of Chemistry. (b) Schematic illustrating the scattering mechanism. The addition of optically excited plasmonic nanoparticles increases the average path length of photons in the composite structure. Reproduced with permission.¹⁹⁹ Copyright 2011, Springer Nature..... 19

Figure 1.14 (a) Schematic representation of the quantum confinement effect on the energy level structure of a semiconductor material. The lower panel shows colloidal suspensions of CdSe nanocrystals of different sizes under UV excitation. Courtesy of R. Koole (Philips Research Laboratories, Netherlands). Reproduced with permission.³⁰³ Copyright 2011, Royal Society of Chemistry. (b) Absorbance spectra of PbS QDs with diameter being tuned from 3 to 10 nm, leading to excitonic maxima ranging from 900 to 2100 nm. Reproduced with permission.³⁰⁶ Copyright 2011, American Chemical Society. 24

Figure 1.15 (a) UV-visible-NIR absorption spectra of CN, CN-Zn, BiS, and CN-Zn/BiS. (b) Linear volt-ampere curve of CN, CN-Zn, BiS, and CN-Zn/BiS with and without 808 nm NIR irradiation. (c) ROS detection of CN-Zn/BiS through ESR with DMPO probe. Blue arrows indicated $\bullet\text{O}_2^-$ and purple arrows indicated $\bullet\text{OH}$. (d) The mechanism of ROS enhancement based on the DFT calculation compared with individual CN-Zn and BiS. Red arrows mean generated ROS species. (e) MRSA and (f) E. coli strain counts calculated from spread-plate assays after treatment

with CN, CN-Zn, BiS, or CN-Zn/BiS ($200 \mu\text{g mL}^{-1}$) under 808 nm light irradiation. Reproduced with permission.²⁴⁵ Copyright 2019, WILEY-VCH.....26

- Figure 3.1** TEM images of (a) Au NPs, (b) g-C₃N₄ nanosheets, (c) 1 wt% Au-NYF/g-C₃N₄ photocatalysts, (d) the enlarged view and (e) the EDX spectrum of the rectangle area in (c). The inset in (a) is the high magnification TEM image of Au NPs. (f) XRD patterns of g-C₃N₄, NYF, NYF/g-C₃N₄ and 1 wt% Au-NYF/g-C₃N₄ samples. The corresponding standard data for the β -NaYF₄ phase (JCPDS 28-1192) is also given at the bottom.49
- Figure 3.2** (a) UV-vis-NIR absorption spectra and (b) upconversion photoluminescence spectra of the obtained samples. The inset in (a) is the absorption spectrum of Au NPs in water.51
- Figure 3.3** Time-dependent UV-vis absorption spectra for the photocatalytic degradation of MO over 1 wt% Au-NYF/g-C₃N₄ (a) and the plot of (c/c_0) vs reaction time (b) under UV light irradiation. The plot of $\ln(c_0/c)$ vs reaction time (c, d, e, f) for the photocatalytic degradation of MO over x wt% Au-NYF/g-C₃N₄ (x=0, 1, 2, 3, 4 and 5) photocatalysts, under UV light (c), $\lambda > 420$ nm (d), $\lambda > 475$ nm (e), and the NIR light (f) irradiation. The insets in (c, d, e, f) are the apparent rate constants (k value) vs Au loading.54
- Figure 3.4** (a) Photocatalytic degradation of MO and (b) the kinetics study over different photocatalysts under simulated solar light illumination. The inset in (b) shows the rate constants vs Au loading. (c) Photocatalytic stability of 1 wt% Au-NYF/g-C₃N₄ photocatalyst in five successive cycling reactions. The duration of simulated solar light exposure in each cycle is 7 h. (d) Photocatalytic degradation of MO in the presence of three types of scavengers and 1 wt% Au-NYF/g-C₃N₄ photocatalyst under simulated solar light irradiation.....56
- Figure 3.5** (a) EIS Nyquist plots of NYF/g-C₃N₄ and 1 wt% Au-NYF/g-C₃N₄ in the dark and under illumination; (b) transient photocurrent density response of NYF/g-C₃N₄ and 1 wt% Au-NYF/g-C₃N₄ during on/off cycles under a 0.2 V bias versus Ag/AgCl..57
- Figure 3.6** Proposed photocatalytic mechanism of Au-NYF/g-C₃N₄ photocatalyst under (a) UV and (b) visible light ($\lambda > 475$ nm) irradiation, respectively. (c) Schematic energy level diagrams, upconversion excitation and UV- visible light emissions for the NYF microspheres under the NIR light (980 nm laser) illumination.58

- Figure 4.1** TEM images of (a) g-C₃N₄ nanosheets, (b-c) PCZ QDs, (d-f) 2 wt% QDs/g-C₃N₄ photocatalysts with different magnifications. Insets in (c) and (f) are the HRTEM images of PCZ QDs and PCZ QDs/g-C₃N₄, respectively. Scale bars in (a-b) and (d-f) are 50 nm. (g) EDX spectrum of (f). (h) XRD patterns of g-C₃N₄, PCZ QDs, and PCZ QDs/g-C₃N₄ samples.....73
- Figure 4.2** (a) FTIR spectra, (b) survey XPS spectra, high-resolution (c) C 1s and (d) N 1s XPS spectra of g-C₃N₄ and PCZ QDs/g-C₃N₄ samples, (e) high-resolution S 2p XPS spectra of PCZ QDs and PCZ QDs/g-C₃N₄, and (f) absorption spectra of g-C₃N₄ and PCZ QDs/g-C₃N₄. Insets in (f) are the photographs of the prepared powder samples and the NIR absorption spectrum of PCZ QDs.75
- Figure 4.3** Photocatalytic degradation of MO over bare PCZ QDs and 0-11 wt% QDs/g-C₃N₄ samples under (a) UV, (b) $\lambda > 420$ nm, (c) $\lambda > 495$ nm, and (d) NIR light irradiation (980 nm). (e) The plot of $\ln(c_0/c)$ vs reaction time of (d). (f) Photocatalytic stability of 2 wt % QDs/g-C₃N₄ photocatalyst in six successive cycling reactions under simulated solar light irradiation.....77
- Figure 4.4** (a) PL spectra with the excitation at 375 nm, (b) TRPL decay curves with emission at 460 nm, and (c) solid-state ESR spectra in the dark and after visible light irradiation of g-C₃N₄ and 2 wt% QDs/g-C₃N₄. (d) PL spectra with the excitation at 780 nm of PCZ QDs and 7 wt% QDs/g-C₃N₄. (e) Photocurrent response and (f) EIS Nyquist plots in the dark and under simulated solar light irradiation of g-C₃N₄ and PCZ QDs/g-C₃N₄ samples. (g) Photocatalytic degradation of MO over 2 wt% QDs/g-C₃N₄ in the presence of three different scavengers under simulated solar light irradiation. DMPO spin-trapping ESR spectra of (h) $\bullet\text{O}_2^-$ and (i) $\bullet\text{OH}$ radicals for g-C₃N₄ and PCZ QDs/g-C₃N₄ in the dark and under visible light ($\lambda > 420$ nm) irradiation.....80
- Figure 4.5** Proposed possible mechanism for the photocatalysis over PCZ QDs/g-C₃N₄ samples under a) UV or $\lambda > 420$ nm and b) $\lambda > 495$ nm or NIR light irradiation. Band energies (in eV referenced to the vacuum level) are taken from literatures.81
- Figure 5.1** (a) Schematic illustration of the preparation of BP nanosheets with NMP-ice-assisted exfoliation method. (b) TEM image of BP nanosheets and (c) EDX spectrum of (b). (d) Tapping mode AFM topographical image of few-layer BP nanosheets. Scale bars in b) and d) are 500 nm. (e) The height profiles of BP nanosheets along the blue Line 1 and green Line 2 in (d). (f) Distribution of BP

layers calculated from the height profiles of 150 BP nanosheets in AFM images.98

Figure 5.2 Typical TEM images of (a) g-C₃N₄ and (b-d) BP/g-C₃N₄ with different magnifications. (e) HAADF STEM image of (d), (f-i) STEM-EDX mapping of C, N, P, and the overlay of all the elements of the selected area in (e). (j) HRTEM image of BP/g-C₃N₄, and (k) EDX spectrum of (j). Scale bars: (a) and (c-i), 250 nm; (b), 1 μm; (j), 5 nm. The TEM grids used in (a), (j) and (k) are carbon film coated copper grids, and those used in the other figures are lacey carbon film coated nickel grids. 100

Figure 5.3 High-resolution (a) C1s and (b) N1s XPS spectra of g-C₃N₄ and BP/g-C₃N₄, and (c) P2p XPS spectra of BP and BP/g-C₃N₄ samples. (d) XRD patterns of bulk BP, BP nanosheets, g-C₃N₄ and BP/g-C₃N₄ samples. The inset is the amplification of XRD patterns of bulk BP and BP nanosheets in the lower-angle range, which is marked by the dashed rectangle in (d). (e) UV-vis-NIR absorption spectra of g-C₃N₄ and BP/g-C₃N₄ powder samples. Insets in (e) are the absorption spectrum of BP nanosheets in dispersion (top), photos of BP/g-C₃N₄ (middle) and g-C₃N₄ (bottom) powders. (f) Theoretical Tauc-plot curves of BP with different layer numbers (1-4 and 6 layers). (g, i) Photocatalytic H₂ evolution and (h) H₂ evolution rate achieved in the presence of BP (orange), g-C₃N₄ (blue), 3 wt% BP/g-C₃N₄ (red), 10 wt% BP/g-C₃N₄ (green) and 15 wt% BP/g-C₃N₄ (purple) photocatalysts under (g-h) λ > 420 nm and (i) λ > 475 nm light irradiations. 101

Figure 5.4 (a) EIS Nyquist plots of g-C₃N₄ and BP/g-C₃N₄ with and without illumination. (b) Transient photocurrent density response of g-C₃N₄ and BP/g-C₃N₄ during light on/off cycles under a 0.2 V bias versus Ag/AgCl electrode. (c) Steady-state PL spectra with the excitation at 380 nm, and (d) TRPL decay curves measured at 457 nm of g-C₃N₄ and BP/g-C₃N₄ samples. Valence band UPS cut-off spectra of (e) BP and (f) g-C₃N₄ samples. 106

Figure 5.5 Schematic energy diagram of BP/g-C₃N₄ photocatalyst and proposed possible mechanism for the photocatalytic H₂ evolution under (a) λ > 420 nm and (b) λ > 475 nm light irradiation. 108

LIST OF TABLES

Table 1.1	Representative narrow-bandgap materials and their bandgap values.	21
Table 1.2	Some examples of the broadband photocatalysts based on narrow-bandgap semiconductor/g-C ₃ N ₄ heterostructure for NIR photocatalytic applications.	25
Table S4.1	Reaction rates for photocatalytic degradation of organics under NIR light irradiation in recent published literatures.	90
Table S4.2	ICP-OES detection of metals released into the reaction solution after 24 h of photocatalysis under simulated solar light irradiation in the presence of PCZ QDs/g-C ₃ N ₄	90
Table S4.3	ICP-OES detection of metals released into the reaction solution for PbS@CdS QDs under simulated solar light irradiation.	91
Table S4.4	PL Lifetime of g-C ₃ N ₄ and PCZ QDs/g-C ₃ N ₄ samples obtained from TRPL measurements with excitation and emission at 408 nm and 460 nm, respectively.	91
Table S5.1	Comparison of the yield of few-layer BP nanosheets from different exfoliation methods.	114
Table S5.2	Atomic composition of g-C ₃ N ₄ and BP/g-C ₃ N ₄ photocatalysts.	114
Table S5.3	Photocatalytic H ₂ production rate under visible light ($\lambda > 420$ nm) irradiation.	116
Table S5.4	The atomic percentage of P1, P2, and P3 in BP and BP/g-C ₃ N ₄ photocatalysts estimated from Figure S5.3.	117

LIST OF ABBREVIATIONS AND ACRONYMS

0D	Zero-dimensional
1D	One-dimensional
2D	Two-dimensional
3D	Three-dimensional
AFM	Atomic force microscopy
BP	Black phosphorus
BQ	Benzoquinone
CB	Conduction band
CdO	Cadmium oxide
DMF	N,N-dimethylformamide
DMPO	5,5-dimethyl-1-pyrroline N-oxide
EDX	Energy dispersive X-ray spectroscopy
ESR	Electron spin resonance
FTIR	Fourier transform infrared spectroscopy
GC	Gas chromatography
g-C ₃ N ₄	Graphitic carbon nitride
HCl	Hydrochloric acid
HNO ₃	Nitric acid
ICP-OES	Inductively coupled plasma-optical emission spectrometry
IPA	Isopropanol
MB	Methylene blue
MO	Methyl orange
MPA	Mercaptopropionic acid
NAA	Neutron activation analysis

Na ₂ EDTA	Disodium ethylenediaminetetraacetate
NaF	Sodium fluoride
NaOH	Sodium hydroxyl
NHE	Normal hydrogen electrode
NIR	Near-infrared
NMP	N-methyl-2-pyrrolidinone
NPs	Nanoparticles
OA	Oleic acid
ODE	Octadecene
OLA	Oleylamine
PbCl ₂	Lead chloride
PEC	Photoelectrochemical
PL	Photoluminescence
QDs	Quantum dots
ROS	Reactive oxygen species
RhB	Rhodamine B
SPR	Surface plasmon resonance
SEM	Scanning electron microscope
t-BuOH	tert-butyl alcohol
TEM	Transmission electron microscopy
UC	Upconversion
UPS	Ultraviolet photoelectron spectroscopy
UV	Ultraviolet
VB	Valance band
XPS	X-ray photoelectron spectroscopy
XRD	X-ray diffraction

LIST OF PUBLICATIONS, CONFERENCE PRESENTATIONS, AND AWARDS

Book Chapter

1. **Zhang Q**, Liu Y, Xu Z, Zhao Y, Chaker M, Ma D (2018) Visible-Light-Driven Photocatalysts. *Nanomaterials for Energy Conversion and Storage*, Wang D & Cao G (Eds.) World Scientific, New Jersey. p. 109-173.

Patent

2. **Zhang Q**, Ma D, Chaker M (2019) *Facile Method for Large-scale Producing Few-layer Black Phosphorous Nanosheets*. International Patent, PCT/CA2019/050813.

Peer-Reviewed Articles

3. Deng J ¹, **Zhang Q** ¹, Lv X, Zhang D, Xu H, Ma D, Zhong J (2020) Understanding Hematite Photoelectrochemical Water Splitting with X-ray Absorption Spectroscopy. *ACS Energy Lett.* 5: 975-993. (Co-first author)
4. Wang G ¹, **Zhang Q** ¹, Chen Q, Ma X, Xin Y, Zhu X, Dong M, Cui C, Zhang J, Xiao Z (2019) Photocatalytic degradation performance and mechanism of dibutyl phthalate by graphene/TiO₂ nanotube array photoelectrodes. *Chem. Eng. J.* 358:1083-1090. (Co-first author)
5. Gao Y, Lin J, **Zhang Q** *, Yu H, Ding F, Xu B, Sun Y, Xu Z (2018) Facile Synthesis of Heterostructured YVO₄/g-C₃N₄/Ag Photocatalysts with Enhanced Visible-Light Photocatalytic Performance. *Appl. Catal., B* 224:586-593. (Corresponding author)
6. **Zhang Q**, Yang F, Zhou S, Bao N, Xu Z, Chaker M, Ma D (2020) Broadband Photocatalysts Enabled by 0D/2D Heterojunctions of Near-Infrared Quantum Dots/Graphitic Carbon Nitride Nanosheets. *Appl. Catal., B.* 270:118879.
7. **Zhang Q**, Deng J, Xu Z, Chaker M, Ma D (2017) High-Efficiency Broadband C₃N₄ Photocatalysts: Synergistic Effects from Upconversion and Plasmons. *ACS Catal.* 7(9):6225-6234.
8. **Zhang Q**, Jin X, Xu Z, Zhang J, Rendon UF, Razzari L, Chaker M, Ma D (2018) Plasmonic Au Loaded Hierarchical Hollow Porous TiO₂ Spheres: Synergistic Catalysts for Nitroaromatic Reduction. *J. Phys. Chem. Lett.* 9(18):5317-5326.

9. **Zhang Q**, Huang S, Deng J, Gangadharan DT, Yang F, Xu Z, Giorgi G, Palumbo M, Chaker M, Ma D (2019) Ice-Assisted Synthesis of Black Phosphorus Nanosheets as a Metal-Free Photocatalyst: 2D/2D Heterostructure for Broadband H₂ Evolution. *Adv. Funct. Mater.* 29(28):1902486.
10. **Zhang Q**, Yang F, Xu Z, Chaker M, Ma D (2019) Are lanthanide-doped upconversion materials good candidates for photocatalysis? *Nanoscale Horiz.* 4(3):579-591.
11. **Zhang Q**, Thrithamarassery Gangadharan D, Liu Y, Xu Z, Chaker M, Ma D (2017) Recent Advancements in Plasmon-Enhanced Visible Light-Driven Water Splitting. *J. Materiomics* 3(1):33-50.
12. **Zhang Q**, Liu Y, Xu Z, Zhao Y, Chaker M, Ma D (2019) Optimized design and mechanistic understanding of plasmon and upconversion enhanced broadband photocatalysts. *Catal. Today* DOI: 10.1016/j.cattod.2019.05.017.
13. **Zhang Q**, Bao N, Wang X, Hu X, Miao X, Chaker M, Ma D (2016) Advanced Fabrication of Chemically Bonded Graphene/TiO₂ Continuous Fibers with Enhanced Broadband Photocatalytic Properties and Involved Mechanisms Exploration. *Sci. Rep.* 6:38066.
14. Huang S, **Zhang Q**, Li P, Ren F, Yurtsever A, Ma D (2018) High-Performance Suspended Particle Devices Based on Copper-Reduced Graphene Oxide Core-Shell Nanowire Electrodes. *Adv. Energy Mater.* 8(18):1703658.
15. Deng J, **Zhang Q**, Feng K, Lan H, Zhong J, Chaker M, Ma D (2018) Efficient Photoelectrochemical Water Oxidation on Hematite with Dual Cocatalysts of Fluorine-doped FeOOH and FeNiOOH. *ChemSusChem* 11:3783-3789.
16. Huang S, **Zhang Q**, Yang F, Gangadharan DT, Li P, Ren F, Sun B, Ma D (2020) An Effective Way for Scalable Fabrication of High Performance Silver Nanowire Network Transparent Conductive Electrodes for Flexible Smart Windows. *J. Mater. Chem. A. Revision.*
17. Tan L, Li P, **Zhang Q**, Izquierdo R, Chaker M, Ma D (2018) Toward Enhancing Solar Cell Performance: An Effective and "Green" Additive. *ACS Appl. Mater. Interfaces* 10(7):6498-6504.
18. Gangadharan DT, Li P, **Zhang Q**, Yang F, Izquierdo R, Sun B, Giorgi G, Palumbo M, Ma D (2019) Reducing trap-assisted recombination in Pb-less perovskite solar cells by combined compositional and 2D/3D engineering. *ACS Appl. Energy Mater. Revision.*

19. Xu Z, Kibria MG, AlOtaibi B, Duchesne PN, Besteiro LV, Gao Y, **Zhang Q**, Mi Z, Zhang P, Govorov AO, Mai L, Chaker M, Ma D (2018) Towards Enhancing Photocatalytic Hydrogen Generation: Which is More Important, Alloy Synergistic Effect or Plasmonic Effect? *Appl. Catal., B* 221:77-85.

Conference Presentations

1. **Zhang Q**, Chaker M, Ma D (2019) Broadband solar harvesting via plasmonic nanostructures for catalysis. International Conference on Energy, Materials and Photonics 2019, EMP19, Shanghai, China, 14-16 July, *invited oral presentation*.
2. **Zhang Q**, Chaker M, Ma D (2019) Constructing broadband photocatalysts for environmental and energy applications. 102nd Canadian Chemistry Conference and Exhibition, CCCE2019, Quebec City, Canada, 3-7 June, *oral presentation*.
3. **Zhang Q**, Chaker M, Ma D (2018) Broadband solar harvesting via plasmonic photocatalysts for environmental applications. 256th ACS National Meeting & Exposition, Boston, USA, 19-23 August, *oral presentation*.
4. **Zhang Q**, Chaker M, Ma D (2018) Enhanced solar harvesting via plasmonic and upconversion nanostructures for catalysis. Annual Symposium of Inorganic Chemistry of Quebec 2018, SACIQ 2018, 3 August, *oral presentation*.
5. **Zhang Q**, Chaker M, Ma D (2018) Enhanced solar harvesting via plasmonic nanostructures for broadband photocatalysis. International Conference on Energy, Materials and photonics 2018, EMP 18, 8-11 July, Montreal, Canada, *invited oral presentation*.
6. **Zhang Q**, Chaker M, Ma D (2018) Plasmonic photocatalysts toward broadband solar harvesting for efficient photocatalysis. 2nd Annual Conference of the Quebec Centre for Advanced Materials, QCAM 2018, 3-4 May, Montreal, Canada, *oral presentation*.
7. **Zhang Q**, Chaker M, Ma D (2017) Upconversion and plasmon-enhanced photocatalysis for broadband solar harvesting. 2017 MRS Fall Meeting, 26 November-1 December, Boston, USA, *oral presentation*.
8. **Zhang Q**, Chaker M, Ma D (2017) Plasmon-enhanced Photocatalysis for Broadband Solar Harvesting. 1st Annual Conference of the Quebec Centre for Advanced Materials, QCAM 2017, 23-24 October, Sherbrook, Canada, *oral presentation*.

9. **Zhang Q**, Xu Z, Chaker M, Ma D (2017) Broadband solar harvesting for photocatalysis via plasmonic Au nanoparticles. Colloque Plasma-Québec 2017, 17-18 May, Montreal, Canada, *oral presentation*.
10. **Zhang Q**, Xu Z, Chaker M, Ma D (2017) Enhancing photon harvesting via plasmonic nanostructures. 41st International Conference and Expo on Advanced Ceramics and Composites, ICACC 2017, 22-27 Jan, Daytona Beach, USA, *oral presentation*.
11. **Zhang Q**, Xu Z, Chaker M, Ma D (2016) Synthesis and applications of Au, Pt and Pt-Au alloy nanoparticles. Colloque Plasma-Québec 2016, 1-2 June, Montreal, Canada, *poster presentation*.

Awards and Honors

1. Fonds de recherche du Québec-Nature et technologies (**FRQNT**) - **Doctoral Research Award**, 2019-2020 (**Rank 2/32** in Quebec province)
2. **Scholarship from the China Scholarship Council (CSC)** for Pursuing Ph.D. Overseas under State Scholarship Fund, 2015-2019
3. **New research star award** (Relève étoile Louis-Berlinguet) of FRQNT, January 2020
4. **Outstanding Reviewer**, *Applied Catalysis B: Environmental, Elsevier*
5. **Outstanding Reviewer**, *Journal of Environmental Chemical Engineering, Elsevier*
6. **Best Talk**, SACIQ 2018, 3 August 2018, Trois-Rivières, Canada
7. **Best Talk**, EMP 18, 8-11 July 2018, Montreal, Canada
8. **Speaker Travel Stipend**, the American Ceramic Society
9. Visit of a Chinese delegation-**INRS Excellence Scholarship**, 20 November 2017
10. **INRS Excellence Scholarship for 2017**
11. **Scholarship from INRS**, 2015-2019

1 INTRODUCTION

1.1 General Background

Since the industrial revolution, our thirst for energy provided by fossil fuels, including oil, coal, and natural gas, has been becoming stronger and stronger. During the past hundreds of years, fossil fuels have boosted the progress of human society and economic development, and it is not too much to claim that they are the cornerstone of our modern civilization. It is further predicted that in 2050 the worldwide energy consumption will be 25-27 Terawatts (TW), over 80% of which will still rely on fossil fuels, which are neither renewable nor sustainable, and will undoubtedly be exhausted sooner or later.¹⁻⁴ Moreover, the combustion of these fossil fuels causes the emission of hazardous substances, which has led to severe air and water contamination. With the rampant unregulated industrial growth and the unceasing world population increase, the energy crisis and environmental pollution caused by the intensive consumption of fossil fuels have been the two main issues facing human beings. To maintain the sustainability of our human society, the seeking of green and renewable energy sources is imperative and urgent.

Of the various renewable and clean energy sources, solar energy that powers all the lives on our planet is considered to be an inexhaustible and secure natural resource. The solar energy striking Earth per hour (4.3×10^{20} J) is more than the annual global energy demand (4.1×10^{20} J in 2001), which dwarfs all other fossil-based and renewable energy resources combined together.⁵⁻
⁸ Solar power has thus emerged as a promising alternative to finite fossil fuels and its efficient utilization is also attracting extensive and heightened attention though challenging.

Semiconductor photocatalysis, which can directly harvest and convert solar energy for green, solar fuel production and environmental remediation at room temperature and standard atmospheric pressure (atm), has been recognized as one of the green sustainable and ideal avenues to address the global energy and environmental concerns.⁹⁻¹¹ In 1972, Fujishima and Honda first discovered that the TiO_2 electrodes can be used for photocatalytic water splitting to produce H_2 under ultraviolet (UV) light irradiation.¹² In 1977, Frank and Bard, for the first time, realized the remediation of environmental pollution by photocatalysis via reducing CN^- ion in aqueous TiO_2 suspensions under light illumination.¹³ Since these pioneering work, photocatalysis has by far spurred immense and incessant research interests in many different fields, such as photocatalytic degradation of various harmful and toxic organic contaminants, solar water splitting, CO_2 reduction, heavy-metal removal, and N_2 fixation.¹⁴⁻²⁴

From the economic and environmental point of view, H₂ produced from solar-driven water splitting is an ideal substitute for fossil fuels, due to the abundance of solar energy and water, the extraordinarily high specific energy density of H₂ (33.3 kWh kg⁻¹), as well as the emissions free of CO₂ and other toxic gases.²⁵⁻²⁷ Photocatalytic oxidation of organic substances constitutes another field of significant importance, as it can fully degrade some hazardous organic contaminants. The increasing amounts of wastewater containing organic pollutants with high toxicity and the encountered difficulties for the traditional treatment technologies, such as energy-consuming, low efficiency, the co-existence of inorganics and organics, have prompted extensive research in photocatalytic oxidation.^{14,21,28-31} As a fundamental and applied science, photocatalysis will continue to be an integral component of modern chemistry and a promising approach to pursue a sustainable future by utilizing sunlight to drive energy conversion in the 21st century.

1.2 Fundamentals of Photocatalysis

The term “photocatalysis” is made from the combination of photochemistry and catalysis, signifying that light and catalysts are required to trigger or/and to accelerate a redox reaction.³² For semiconductor photocatalysis, the energy band theory has been used to demonstrate the underlying complex physicochemical processes.³³ Differing from conductors, the electron-filled valence band (VB), and the vacant conduction band (CB) of semiconductor are clearly separated by a bandgap, which is the energy difference between the lowest unoccupied state in the CB and the highest occupied state in the VB.^{26,34,35}

As displayed in Figure 1.1, multiple processes occur in an illuminated semiconductor. When the semiconductor photocatalyst is irradiated by photons ($h\nu$, where h and ν represents the Planck constant and photon frequency, and $h\nu$ refers to one photon energy) with energy equal to or greater than its bandgap energy (E_g), the electrons (e^-) in the VB can be promoted to the CB, simultaneously leaving positively charged holes (h^+) in the VB (Figure 1.1 I).

There are several pathways that the photogenerated charge carriers can take after photoexcitation. The photo-induced e^- and h^+ separate and migrate rapidly within photocatalysts to their surface. In the absence of a suitable acceptor, the photo-induced charge carriers tend to recombine in the bulk phase or on the surface on a nanosecond time scale and dissipate the additional energy in the form of light emissions or phonon vibrations (Figure 1.1 II), which is unfavorable for photocatalysis and decreases the overall efficiency.³⁶⁻³⁹

The photo-generated electrons and holes possess strongly reductive and oxidative capabilities, respectively, and they migrate to the surface to drive redox reactions. Specifically, the excited electrons in the CB have a reduction potential of +0.5 to -1.5 V vs the normal hydrogen electrode (NHE) and the holes in the VB possess an oxidation potential of +1.0 to +3.5 V, which can reduce (Figure 1.1 III) the adsorbed electron acceptors (A) and oxidize (Figure 1.1 IV) or even mineralize (Figure 1.1 V) the electron donors (D) into CO₂ and H₂O.³⁹ In the photocatalytic degradation system, electrons react with the adsorbed O₂ to produce superoxide ($\bullet\text{O}_2^-$) radicals, while holes react with H₂O or OH⁻ to generate hydroxyl ($\bullet\text{OH}$) radicals. The produced $\bullet\text{O}_2^-$ radicals, $\bullet\text{OH}$ radicals, and holes are strongly oxidative and active and can effectively degrade the present organic substances. For water splitting, the electrons and holes are used to reduce and oxidize water to produce H₂ and O₂. In addition, the charge carriers can migrate to the surface of the semiconductor and get trapped in metastable surface states (Figure 1.1 VI and Figure 1.1 VII), such as crystalline defects and dangling surficial bonds. Therefore, the semiconductor with a better crystallinity can lead to lower recombination rate of charge carriers and generally show higher photocatalytic efficiency.⁴⁰

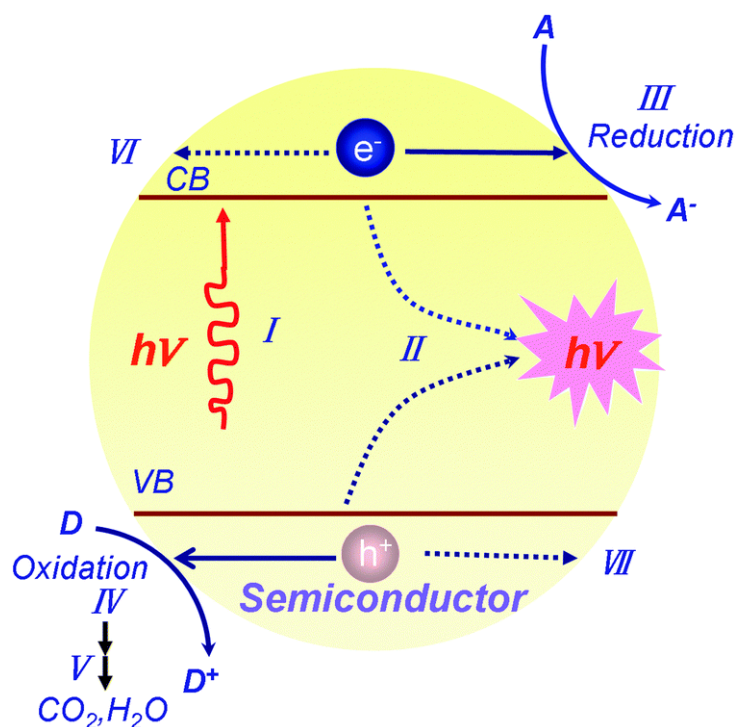


Figure 1.1 Schematic illustration of the principle of semiconductor photocatalysis. (I) the formation of charge carriers by a photon; (II) the charge carrier recombination to liberate heat; (III) the initiation of a reductive pathway by a CB electron; (IV) the initiation of an oxidative pathway by a CB hole; (V) the further thermal (e.g., hydrolysis or reaction with active oxygen species) and photocatalytic reactions to yield mineralization products; (VI) the trapping of a conduction band electron in a dangling surficial bond; (VII) the trapping of a valence band hole at the surface of the semiconductor. Reprinted with permission.³⁹ Copyright 2014, The Royal Society of Chemistry.

For a photocatalytic reaction to occur, the redox potentials of the charge carriers, which are determined by the band position, should meet some requirements. The VB maximum should be more positive than the oxidation potential of the reactant to be oxidized (P_{ox}), while the CB minimum is supposed to be more negative than the reduction potential of the reactant to be reduced (P_{red}).²⁹ The energy difference between P_{red} and P_{ox} represents the overall change of Gibbs free energy (ΔG) (Figure 1.2a-b).⁴¹ In terms of energy, when P_{red} is lower than P_{ox} , ΔG is negative, otherwise, ΔG is positive. It is thereby concluded that photocatalysis can drive both negative- ΔG and positive- ΔG reactions. For example, photocatalytic degradation of organics in the presence of O_2 is generally a downhill reaction with a negative ΔG change (Figure 1.2c), while CO_2 reduction and water splitting are thermodynamically uphill reactions, *i.e.*, positive- ΔG reactions (Figure 1.2d).⁴² It is worth noting that only if both the partial ΔG in oxidation by h^+ (ΔG_h) and reduction by e^- (ΔG_e) are negative, the redox reactions can be triggered.⁴¹ Meeting thermodynamic requirements is a sufficient condition for the occurrence of a photocatalytic reaction.

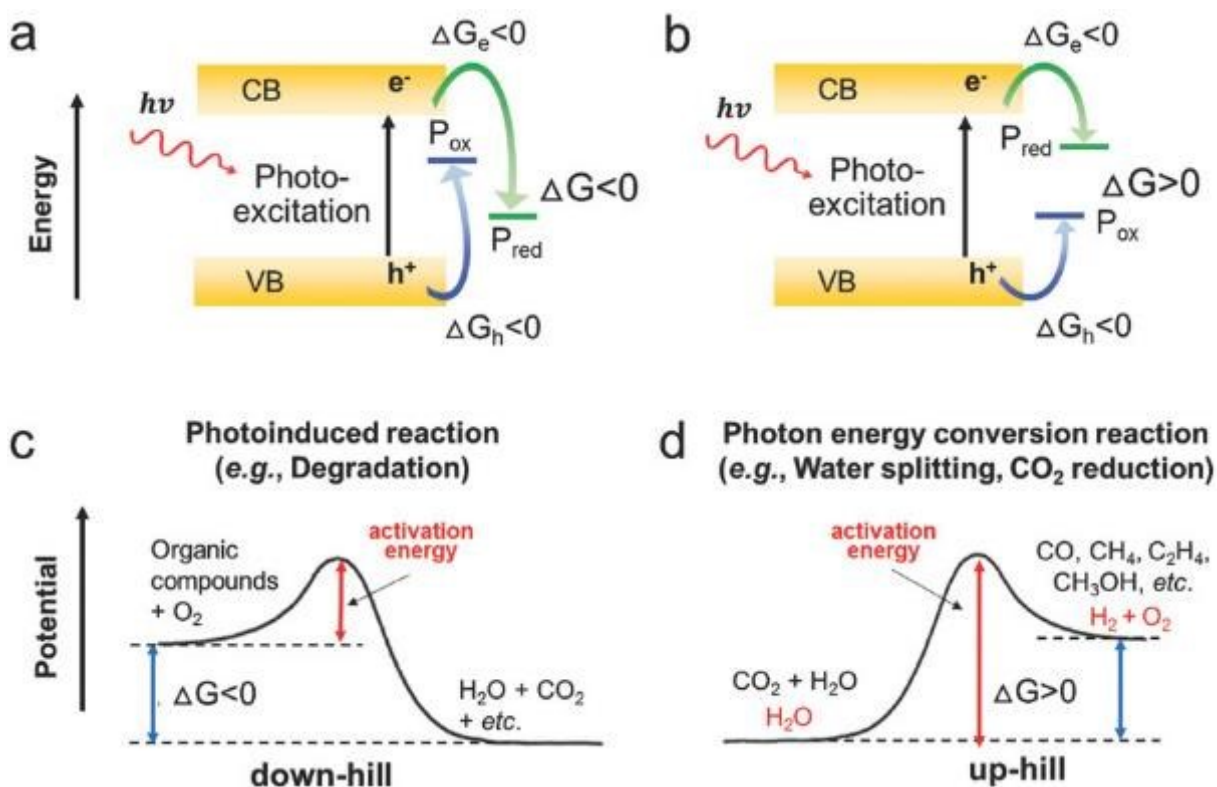


Figure 1.2 (a-b) Electronic structure of semiconductor photocatalysts and Gibbs energy change in photocatalytic reactions. (c-d) Two distinct classifications of photocatalytic reactions, namely downhill (c) and uphill (d) reactions. Reprinted with permission.²⁹ Copyright 2018, WILEY-VCH.

1.3 Requirements and Current Challenges for Photocatalysis

To render the practical application of the photocatalysis possible, it is crucial to develop an efficient and broadband photocatalyst which can achieve the high solar energy utilization efficiency. Based on the aforementioned photocatalytic processes, there are several requirements to construct a superior photocatalyst.

1.3.1 Photo-response range

A narrow bandgap is desired to enable strong and broadband absorption of solar photons. For photoexcitation, only if the incident photons have higher energy than the bandgap of the photocatalyst they can be absorbed. Therefore, a match between the solar spectrum and bandgap is generally required to maximize the harvesting of solar light. However, the most widely studied semiconductors have wide bandgaps (>3.0 eV) and can only respond to the UV light,^{15,33,43} which accounts for merely $\sim 3\text{-}5\%$ of the incident solar spectrum (Figure 1.3), leaving the visible ($\sim 44\%$) and near-infrared (NIR) light ($\sim 53\%$) underutilized.^{40,44} Such a situation makes the target photocatalytic efficiency of greater than 10% challenging.³⁷

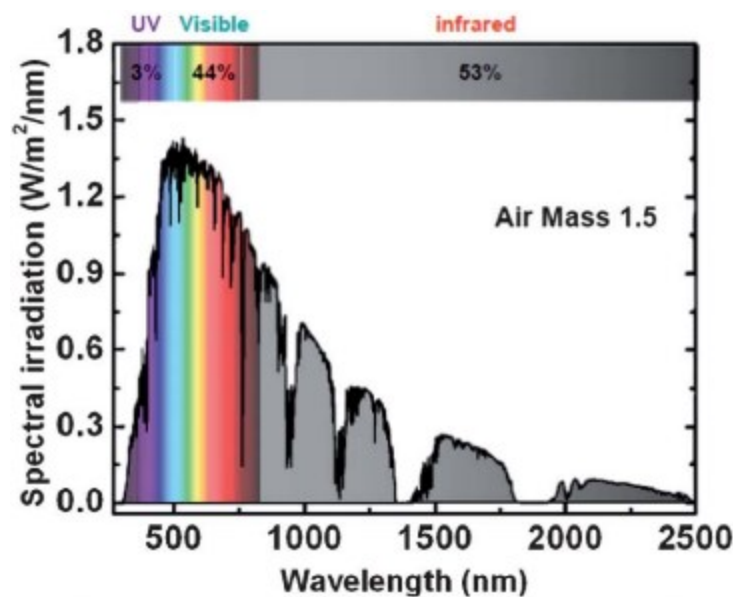


Figure 1.3 Spectral distribution of the solar photon irradiation based on the AM1.5 global data. Reprinted with permission.⁴⁰ Copyright 2012, The Royal Society of Chemistry.

1.3.2 Redox capability

The excitons are expected to possess strong redox capabilities which are determined by the positions of the VB and CB. Take solar water splitting as an example. As mentioned in Section

1.2, solar water splitting is a thermodynamically uphill reaction. A ΔG of $237.2 \text{ kJ mol}^{-1}$ is required to make one water molecule split into $1/2 \text{ O}_2$ and H_2 at room temperature and 1 atm.⁴⁵ Photocatalytic water splitting is thus endothermic and an oxidation-reduction reaction, and according to the Nernst equation, theoretically, the ΔG corresponds to the increased energy (ΔE) of 1.23 V per transferred electron.^{46,47} In fact, to initiate the solar water splitting reaction, the photocatalyst should have a much larger bandgap than 1.23 eV (corresponding to the absorption edge of much shorter than 1008 nm) to overcome the over potentials of both water reduction ($\sim 0.05 \text{ V}$) and oxidation (0.25 V).^{48,49} Thus, the narrow bandgap and the strong redox potentials of excitons are contradictory and a balance between them should be established.

1.3.3 Charge separation and transportation

The charge carriers should be efficiently generated, separated and transported, and be of minimal or largely suppressed recombination. Charge recombination and separation/migration take place simultaneously while compete with each other during photocatalytic processes. It was reported that most of the photo-induced electrons and holes recombine very fast (within 10 ns),^{37,50} which makes achieving high photocatalytic efficiency very difficult as water splitting and other photocatalytic reactions occur on a time scale slower than this. Therefore, to gain high photocatalytic efficiency, the efficient generation, separation and transportation of charge carriers to the active redox sites or surface of photocatalysts are desired. Generally, a semiconductor with high crystallinity can decrease the trapping and recombination sites and facilitate the separation/transportation of charge carriers. In addition, photocatalysts with smaller size in some dimension, such as zero-dimensional (0D) nanodots,⁵¹⁻⁵³ one-dimensional (1D) nanowires or fibers,⁵⁴⁻⁵⁶ two-dimensional (2D) nanosheets,^{9,57-60} can minimize the required diffusion distance of the excited electrons and holes to the surface and can consequently lower their recombination rate.

1.3.4 Adsorptivity and stability

Adsorption of water and reactants is the prerequisite for the occurrence of photocatalytic water splitting or decomposition of organic contaminants. To make the desired photocatalytic reaction happen, the charge carriers prior to their recombination are supposed to be transferred to the adsorbed molecules. The physical adsorptivity for photocatalysts is normally determined by the surface area. To increase the surface area, photocatalysts with different morphologies, such as porous and hollow structures,⁶¹⁻⁶⁵ and the above mentioned 0D, 1D, as well as 2D nanostructures,

were rationally designed and synthesized. As the photo-generated charge carriers are highly reactive, if they cannot be timely consumed for desired photochemical reactions, they can often react with the photocatalyst itself, resulting in the deactivation and disintegration of the photocatalyst. Thus, the stability of the semiconductor photocatalyst is supposed to be excellent to resist both chemical corrosion and photocorrosion. In addition, the cost should also be taken into consideration in designing photocatalyst.

During the past decades, various semiconductor photocatalysts have been extensively explored and reported, such as TiO_2 ,^{11,66-69} ZnO ,⁷⁰⁻⁷² ZrO_2 ,⁷³⁻⁷⁵ Fe_2O_3 ,⁷⁶⁻⁷⁸ WO_3 ,⁷⁹⁻⁸¹ BiVO_4 ,⁸²⁻⁸⁴ Bi_2WO_6 ,⁸⁵⁻⁸⁷ and CdS .⁸⁸⁻⁹¹ Despite tremendous efforts have been paid to date, a practically viable photocatalyst which is efficient, stable, cost-effective and able to harvest photons with a broad wavelength range has not yet been developed. Most of the semiconductor photocatalysts are still suffering from fundamental efficiency bottlenecks, including the confined photon absorption, inefficient charge separation and transfer, a limited number of active sites and insufficient surface area and poor stability. To achieve the goal of sustainable development with the aid of photocatalysis, the exploration of a high-quality photocatalyst which can address the aforementioned challenges has been a hot research area and a “holy grail” for researchers.

1.4 Graphitic Carbon Nitride Photocatalyst

Among the various categories of semiconductor photocatalysts, graphitic carbon nitride ($\text{g-C}_3\text{N}_4$) has recently attracted tremendous interest of material scientists by virtue of its fascinating merits, such as nontoxicity, facile preparation, moderate bandgap (~ 2.7 eV), strong redox capability, “earth-abundant” nature, and good physicochemical stability.⁹²⁻⁹⁵

1.4.1 Microstructure

With a graphite-like layered structure, $\text{g-C}_3\text{N}_4$ is in a form of 2D sheets, based on s-triazine (Figure 1.4a) or tri-s-triazine (Figure 1.4b) tectonic unit interconnected via tertiary amines.⁹⁶ In these cases, as the nitride pore size and the electronic environment of the N atom are different, the energetic stability of the allotropes is thus different. Among all the allotropes of C_3N_4 , tri-s-triazine based $\text{g-C}_3\text{N}_4$ is energetically favored and is the most stable one under ambient conditions.^{93,97,98} Benefiting from the aromatic C-N heterocycles and the high condensation, $\text{g-C}_3\text{N}_4$ with tri-s-triazine ring structure is thermally stable with temperature up to 600 °C in air, which is confirmed by the thermogravimetric analysis (TGA) results.⁹² Furthermore, the strong interlayer van der Waals interactions render $\text{g-C}_3\text{N}_4$ chemically stable, which can resist most of the organic solvents,

acid and alkali solutions.^{92,99} The 2D g-C₃N₄ nanosheets provides large specific surface area due to its graphite-like layered structure, and the theoretical value of g-C₃N₄ with monolayers is up to 2500 m²g⁻¹,¹⁰⁰ which is favorable for the adsorption of reactants and thus facilitates photocatalysis.

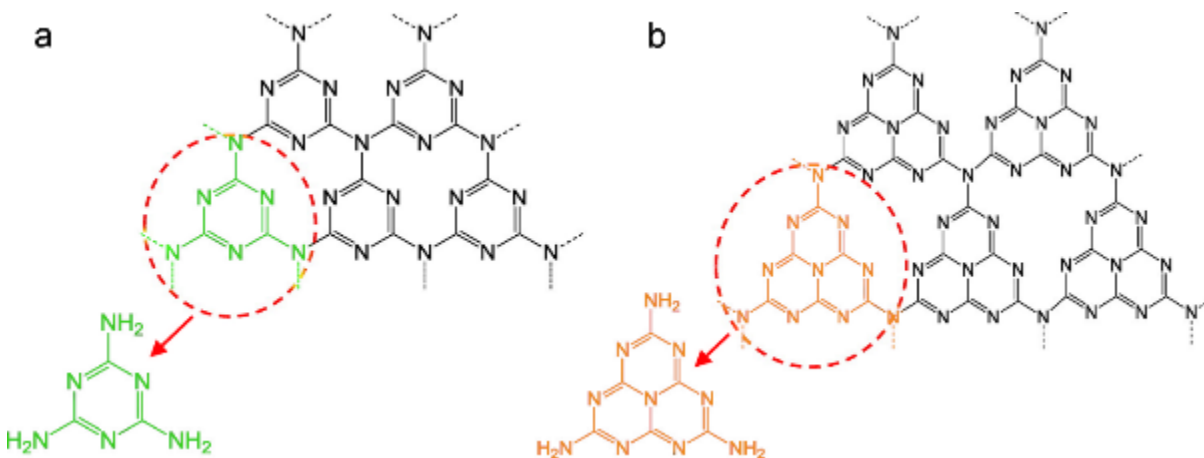


Figure 1.4 The hypothetical ideal structure of g-C₃N₄ based on (a) s-triazine and (b) tri-s-triazine (heptazine) tectonic units. Reprinted with permission.⁹² Copyright 2012, American Chemical Society.

1.4.2 Electronic structure

The presence of sp²-hybridized C and N results in the unique established π -conjugated electronic structures of g-C₃N₄ with a direct bandgap of ~2.7 eV. The appropriate VB and CB band positions at +1.6 eV and -1.1 eV vs NHE are anodically and cathodically sufficient for water oxidation and reduction to produce O₂ and H₂, respectively.^{101,102} In comparison to TiO₂, which has a bandgap of 3.0-3.2 eV and can only respond to the UV light,^{11,35} g-C₃N₄ shows photocatalytic activity in the visible light region. As a metal-free photocatalyst, Wang et al. in 2009 used g-C₃N₄ for water splitting to generate H₂ under visible light irradiation for the first time.¹⁰² Since this pioneering work and due to the aforementioned intriguing properties, g-C₃N₄ has elicited ripples of excitement in the scientific community and has drawn worldwide attention in recent years.

1.4.3 Synthesis methods

As g-C₃N₄ consists of earth-abundant C and N elements, it is supposed to be prepared with accessible raw materials at low cost. Several cheap N-rich precursors with C-N core structure, such as melamine,^{103,104} cyanamide,^{101,105} dicyandiamide,^{106,107} urea,^{108,109} thiourea,^{110,111} or mixtures thereof,¹¹² have been widely used to prepare g-C₃N₄ via thermal polycondensation method (Figure 1.5).⁹³ The N-rich molecules are polymerized into g-C₃N₄ during a facile annealing process at the temperature of 450-650 °C. The electronic band structure and textual properties of obtained g-C₃N₄ can be affected by the selected precursor. For example, the g-C₃N₄ synthesized

from urea normally has a higher specific surface area than that synthesized from melamine.¹¹³ While the g-C₃N₄ obtained from urea shows a larger bandgap than that prepared from thiourea.¹¹⁴

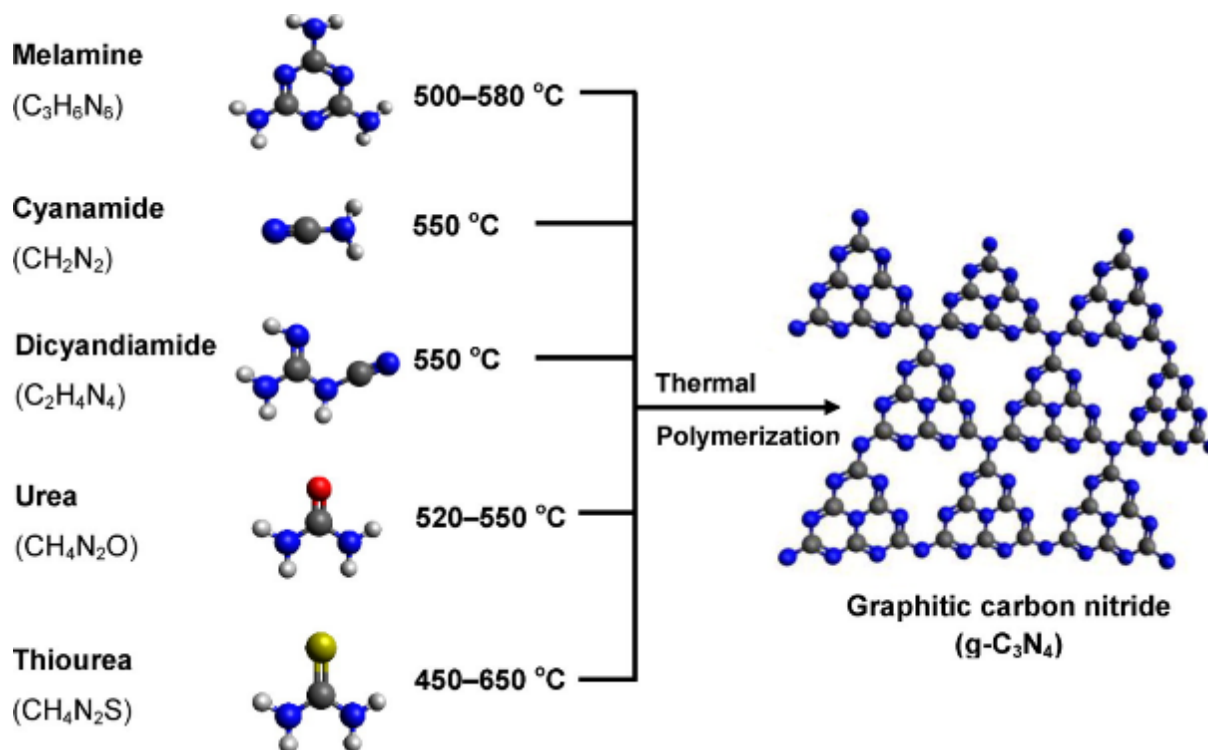


Figure 1.5 Schematic illustration of the synthesis process of g-C₃N₄ by thermal polymerization of different precursors such as melamine,^{103,104} cyanamide,^{101,105} dicyandiamide,^{106,107} urea,^{108,109} thiourea.^{110,111} The black, blue, white, red, and yellow balls denote C, N, H, O, and S atoms, respectively. Reprinted with permission.⁹³ Copyright 2016, American Chemical Society.

1.4.4 Inherent drawbacks

Although g-C₃N₄ has been regarded as the most promising visible light-driven metal-free photocatalyst, several inherent shortcomings are still hindering its practical applications in solar water splitting and photocatalytic decomposition of organic contaminants.^{104,115} For example, the high recombination rate of the photoexcited electrons and holes along their migration from the bulk to the surface leads to relatively low photocatalytic activity of pristine g-C₃N₄.¹¹⁶ In addition, the not-so-narrow bandgap of g-C₃N₄ (~2.7 eV) confines its light response range only into the UV range and a small portion of visible light with wavelength shorter than 460 nm.^{117,118} As discussed in Section 1.3.1, sunlight covers a broad range of photon wavelengths (250-2500 nm). Therein, the UV (< 400 nm), visible (400-800 nm) and NIR (800-1400 nm) photons account for ~5%, ~45% and ~44%, respectively, of the total incident solar flux reaching the Earth surface.^{87,119-121} As the high percentage (~90%) of visible and NIR light is needed to essentially increase the overall solar energy utilization efficiency, the narrow light response range of g-C₃N₄ is far from “ideal”

expectations and industrial applications. Therefore, the development of an efficient and broadband responsive (from UV, visible to NIR regions) g-C₃N₄ based photocatalyst is highly desired and of paramount importance.

1.5 Strategies to Construct Broadband g-C₃N₄ Based Photocatalysts

As g-C₃N₄ solely comprises earth-abundant C and N, it not only indicates that g-C₃N₄ can be prepared cost-effectively, but also suggests that its surface activity can be altered without significantly changing the theoretical composition and structure.^{93,98} Furthermore, the polymeric nature endows g-C₃N₄ with sufficient flexibility of the structure, which can serve as a host matrix for easy anchoring of various organic and inorganic compounds. Thus, this feature is beneficial to improve the activity of g-C₃N₄ through introducing other materials to form hybrid nanocomposites. During the past decades, numerous strategies have been adopted to increase the photocatalytic activity of g-C₃N₄ and render it broadened response to photons with wavelength above 460 nm. They include, for example, electronic structure modulation via heteroatom doping¹²²⁻¹²⁶ or defect engineering,^{117,127,128} nanostructure design,¹²⁹⁻¹³³ and dye sensitization.¹³⁴⁻¹³⁷ As a matter of fact, ion doping or defect engineering are effective in modifying the energy band configuration and electronic structure by introducing impurities into the g-C₃N₄ matrix.^{117,122-128,138} Reducing the dimension of g-C₃N₄ from bulk crystals to nanosheets can increase the specific surface area, make more active sites exposed to reactants, and thus allowing the reactants and charges more accessible to each other.^{104,139-142} Dye organic molecules, such as dibromofluorescein,¹³⁶ Eosin Y,¹³⁵ Erythrosin B,¹⁴³ fluorescein,¹³⁶ magnesium phthalocyanine,¹³⁷ magnesium phthalocyanine,¹³⁷ Zinc phthalocyanine,¹³⁴ and Rose Bengal,¹³⁵ have been widely used as a sensitizer to absorb light at longer wavelengths for photocatalysis. However, with some of these methods, the modified materials are still suffering from thermal instability, photocorrosion, poor photocatalytic activity; in some cases, they can even result in un-desired secondary pollution.^{11,144,145}

The past several years have witnessed a surge of interest in introducing surface plasmon resonance (SPR) via loading plasmonic metallic nanostructures, and constructing heterojunction via coupling with narrower-bandgap semiconductor, which have effectively circumvent the inherent defects of g-C₃N₄ to uncommonly improve the photocatalytic efficiency of g-C₃N₄.^{29,93,94,121,146,147} We also noticed that there are some explorations on employing upconversion (UC) materials to make g-C₃N₄ a broadband-responsive photocatalyst in recent years. This section will be focused on the state-of-the-art advancements in the abovementioned three

strategies toward achieving broadband solar harvesting by g-C₃N₄ for efficient photocatalysis, including environmental remediation and H₂ evolution from water splitting.

1.5.1 Employing upconversion materials

1.5.1.1 Introduction of upconversion

Photon UC is essentially a nonlinear, anti-Stokes emission process, whereby sequential absorption of two or more lower-energy excitation photons to generate emissions with higher-energy (Figure 1.6a).¹⁴⁸⁻¹⁵² UC particles generally consist of an inorganic crystalline host matrix and lanthanide ions doped in the host lattice (Figure 1.6b). For trivalent lanthanide ions, the $4f^7$ electronic configuration splits into many energy sublevels due to the strong Coulombic repulsion and spin-orbit coupling, resulting in a rich energy level pattern, which renders lanthanides promising in realizing efficient UC. The symbol $^{2S+1}L_J$, where S , L , J are the total spin, orbital and angular momentum quantum number of the electron, respectively, is normally used to represent the energy levels. Most of the lanthanide ions are theoretically able to generate UC emissions, while only UC particles doped with Er³⁺, Ho³⁺, and Tm³⁺ as activators can emit visible photons under the excitation of low power density (~ 10 W/cm²).¹⁵³ For efficient UC to proceed, Yb³⁺ ion is frequently doped as a sensitizer due to its large absorption cross-section in the NIR region. Through tuning the combinations and ratios of different dopants in UC materials, UC emission can be precisely modulated to a particular wavelength spanning from the UV to the NIR region and the emission intensities can also be controlled relatively (Figure 1.6c-1.6e).^{149,154}

1.5.1.2 Synthesis of lanthanide-doped upconversion materials

The luminescence properties of the UC materials, such as emission and excitation wavelengths, lifetimes and UC quantum yields, are determined not only by their composition, but also by their size, shape, crystallinity, and the defect concentration in the host crystals.^{155,156} Through delicately controlling the experimental conditions, such as solvents, raw materials, reaction time and temperature, the UC luminescence properties can be substantially tuned. Therefore, by selecting a suitable synthetic method, it is possible to design UC particles with specific required properties for targeted applications. To date, various routes have been developed for the synthesis of lanthanide-doped UC materials, such as thermal decomposition,¹⁵⁷⁻¹⁶⁴ co-precipitation methods,¹⁶⁵⁻¹⁷⁰ and hydro/solvothermal,¹⁷¹⁻¹⁷⁵ as well as other emerging strategies, including micro-emulsion method,¹⁷⁶ sol-gel approach,¹⁷⁷ and microwave-assisted process,^{178,179} etc.

Therein, thermal decomposition is the most effective method to prepare monodisperse and phase-pure lanthanide-doped UC nanocrystals with high crystallinity, while the synthesis procedure is complicated and the obtained UC nanoparticles (UCNPs) are generally hydrophobic. The hydro/solvothermal approach is facile and user-friendly, and the synthesized materials can be hydrophobic or hydrophilic. Nevertheless, the invisible reaction process and the difficult sampling render the formation mechanism rarely understood.

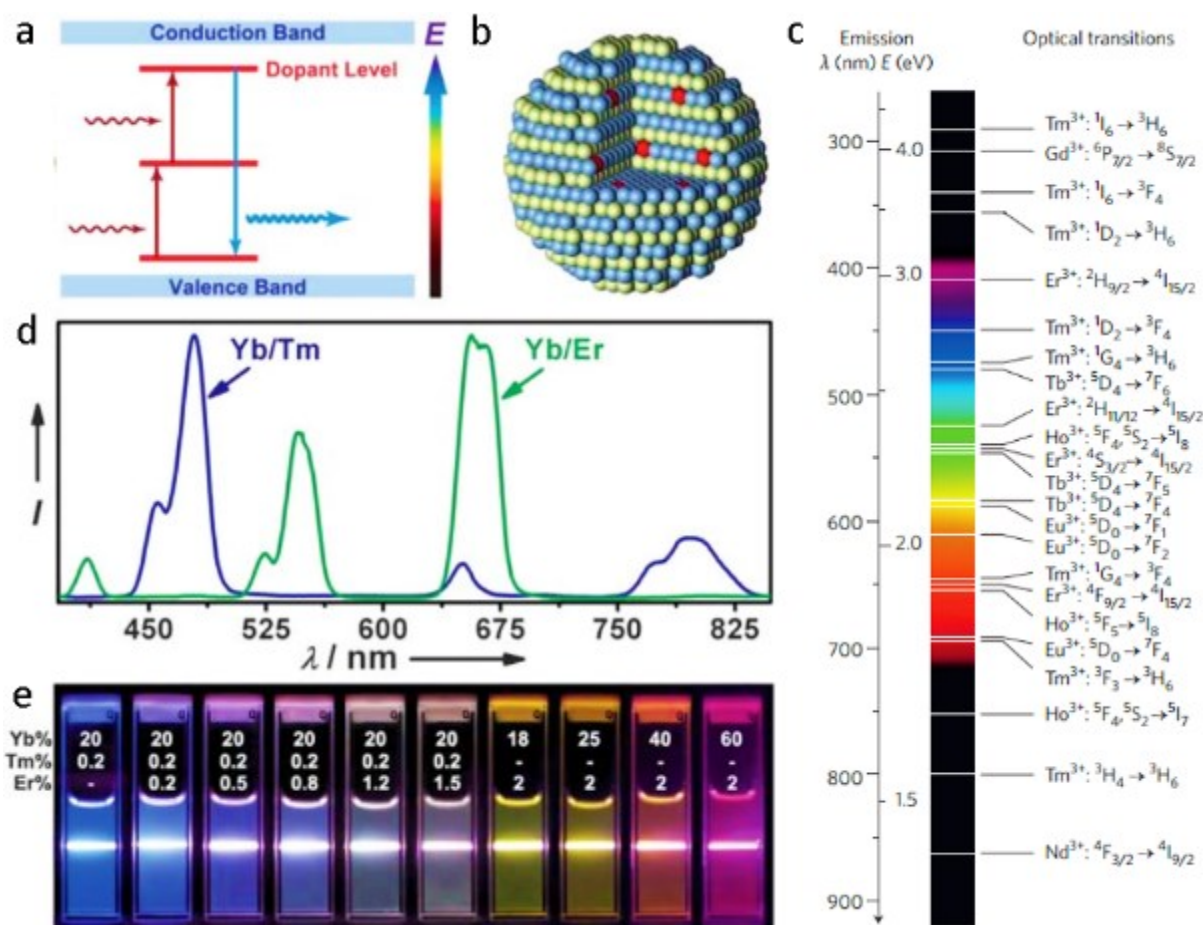


Figure 1.6 Lanthanide-doped UC particles and photon UC. (a) Schematic energy level diagram showing that UC luminescence primarily originates from electron transitions between energy levels of localized dopant ions. (b) Schematic illustration of UC particles composed of a crystalline host and lanthanide dopant ions embedded in the host lattice. Reprinted with permission.¹⁵³ Copyright 2010, The Royal Society of Chemistry. (c) Typical lanthanide-based UC emission bands covering a broad range of wavelengths from UV (~290 nm) to NIR (~880 nm) and their corresponding main optical transitions. Reprinted with permission.¹⁴⁹ Copyright 2015, Springer Nature. (d) Typical emission spectra showing multiple narrow and well-separated emissions produced by cubic $\text{NaYF}_4:\text{Yb}/\text{Tm}$ (20/0.2 mol%) and $\text{NaYF}_4:\text{Yb}/\text{Er}$ (18/2 mol%) particles. (e) UC multicolor fine-tuning through the use of lanthanide-doped NaYF_4 particles with varied dopant ratios. Note that the emission spectra and colors are associated with the host composition, particle size, and particle surface properties. Reprinted with permission.¹⁵⁴ Copyright 2008, American Chemical Society.

1.5.1.3 Upconversion enhanced photocatalysis

Current studies regarding NIR photocatalysts are still quite rare as compared to UV and visible ones. As discussed above, NIR light accounts for ~44% of solar spectrum, while g-C₃N₄ can only capture photons with wavelength shorter than 460 nm. Recently, UC materials are gradually coming into the visions of researchers as a potential candidate to combine with semiconductor photocatalysts, including TiO₂,^{145,180-186} g-C₃N₄,¹⁸⁷⁻¹⁹⁰ CdS,^{191,192} BiVO₄,^{193,194} and ZnO,^{195,196} etc., and the composites thereof,^{195,197,198} for NIR photocatalysis. The UC enabled NIR photocatalysis requires that the UC emissions by the lanthanide-doped UC materials should be capable of exciting the proximal semiconductor or plasmonic photocatalyst to produce charge carriers for targeted photocatalytic reactions (Figure 1.7).

The most commonly used lanthanide ions in NIR photocatalysis are Yb³⁺, Tm³⁺ and Er³⁺. Yb³⁺ can strongly absorb at 980 nm, and usually serves as a sensitizer. It only possesses one excited state and once excited, its energy can be transferred to Tm³⁺ and Er³⁺ ions, which act as activators to generate UV, blue and visible emissions *via* the successive energy transfer processes.¹⁵²

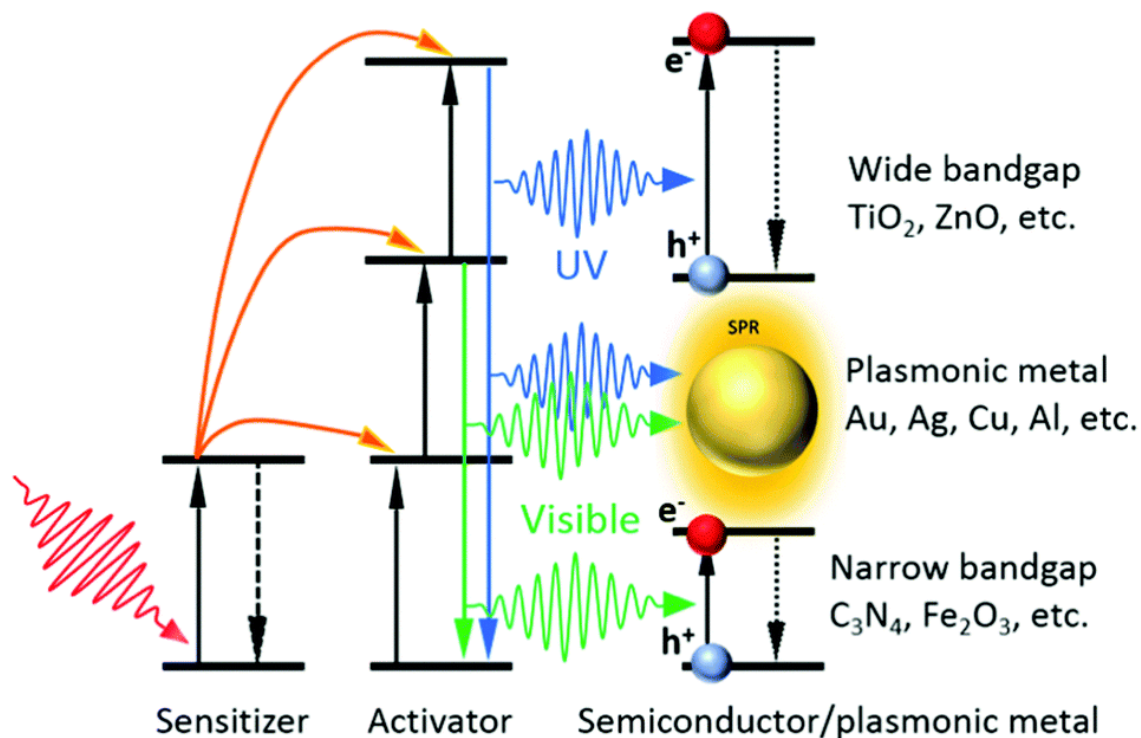


Figure 1.7 Illustration of the UC enhanced photocatalysis. Reprinted with permission.¹⁵² Copyright 2019, Royal Society of Chemistry.

1.5.2 Introducing surface plasmon resonance effect

1.5.2.1 Introduction of surface plasmon resonance

SPR can be described as the photo-induced coherent collective oscillation of free electrons in plasmonic metallic nanostructures, such as Au, Ag and Cu NPs. It takes place when the frequency of incident photons matches the natural frequency of surface electrons oscillating against the Coulombic restoring force of positive nuclei (Figure 1.8).^{43,199,200} As a result, an electric field in the opposite direction to the electric field of the light, is created due to the redistribution of the charge density.²⁰⁰ These coherent oscillations of charge density and electric field are known as localized surface plasmons and can last for ~ 10 fs.²⁰¹ The wavelength (frequency) at which the oscillation of conduction electrons in metallic NPs occurs with minimal power dissipation is called the plasmon resonance photon wavelength (frequency).

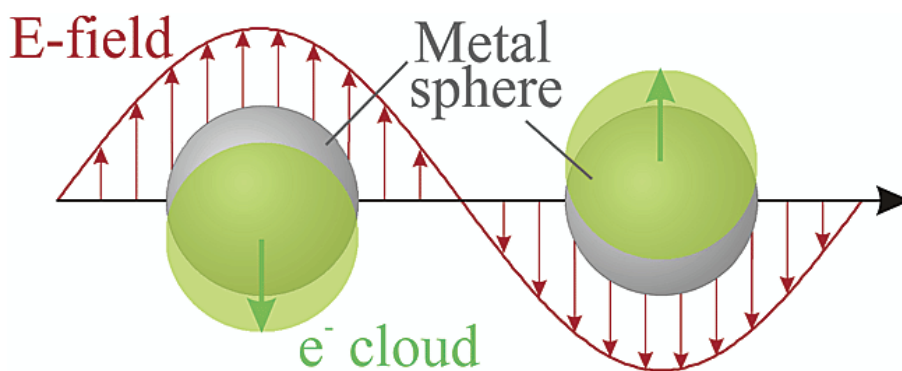


Figure 1.8 Schematic illustration of plasmon oscillation on a plasmonic metal sphere. An oscillation of conduction electron charge cloud relative to the nuclei is established by the external oscillating electric field. Reproduced with permission.²⁰⁰ Copyright 2003, American Chemical Society.

For different plasmonic metals, the plasmon resonance photon wavelength is different. For example, Au, Ag and Cu NPs show the SPR behavior when interacting with UV and visible photons (Figure 1.9a). In addition, the resonant photon wavelength and the SPR intensity are determined not only by the nature of the metal, but also by the size and shape of metallic nanostructures as well as the surrounding dielectric environment.^{200,202,203} Through tuning the composition (Figure 1.9a), shape (Figure 1.9b), and size (Figure 1.9c) of plasmonic metal NPs, it is possible to engineer nanostructures that can harvest the photons of the entire solar spectrum and beyond.^{43,204-207}

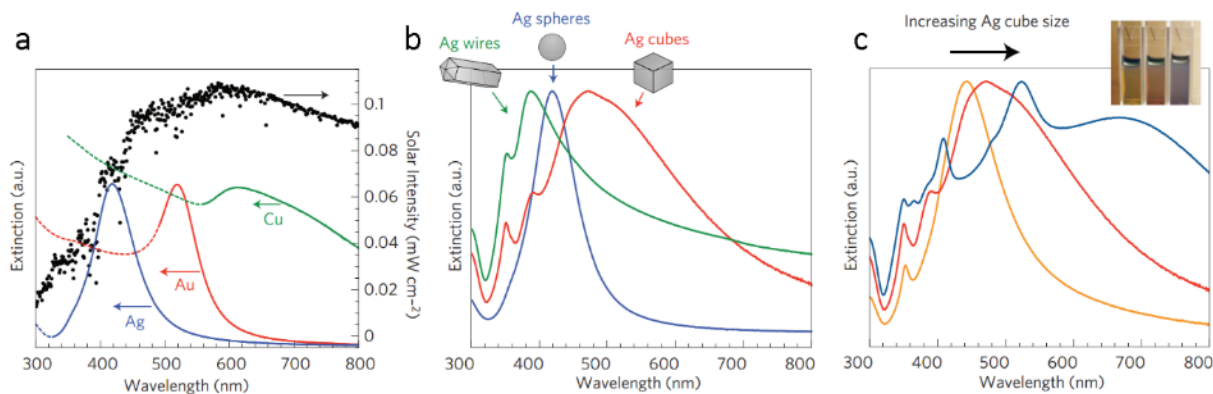


Figure 1.9 (a) Normalized extinction spectra of spherical Ag (38 ± 12 nm diameter), Au (25 ± 5 nm) and Cu (133 ± 23 nm) particles. The intensity of solar radiation (data for air mass 1.5 solar spectrum from the National Renewable Energy Laboratory) is also shown, in black. The metal extinction is a consequence of the excitation of SPR. Dashed portions of the metal extinction curves indicate interband transitions. (b) Normalized extinction spectra for Ag wire (90 ± 12 nm diameter and > 30 aspect ratio), cube (79 ± 12 nm edge length) and sphere (38 ± 12 nm diameter) NPs. (c) Normalized extinction spectra for Ag nanocubes as a function of size (56 ± 8 nm, 79 ± 13 nm and 129 ± 7 nm edge lengths correspond to orange, red and blue spectra, respectively). The inset shows a photograph of the three nanocube samples suspended in ethanol. Reproduced with permission.¹⁹⁹ Copyright 2011, Springer Nature.

1.5.2.2 Mechanisms of plasmon-enhanced photocatalysis

The absorption cross section of plasmonic NPs was reported to be several orders of magnitude larger than that of dye-sensitizer molecules.²⁰⁸ Together with the tunable optical properties, plasmonic metallic NPs have been integrated to semiconductor photocatalysts to enhance their photocatalytic activities.²⁰⁹ During photocatalytic transformations, both the plasmonic metals and the semiconductors in the composite photocatalysts can interact with light and reaction solution, resulting in complicated charge-transfer and energy-transfer processes. Thus, to date, the enhancement mechanisms of SPR effect to photocatalysis have not been fully understood and clarified. There are three non-mutually exclusive major mechanisms by which SPR can enhance the photocatalytic activities of a proximate semiconductor, namely hot electron injection, near-field and light scattering enhancement.

SPR-induced hot electron injection. The hot electron injection mechanism is analogous to dye sensitization. The plasmonic NPs essentially act as a dye sensitizer, which absorb resonant photons and generate hot electrons with upshifted energy states via SPR excitation.^{210,211} These SPR-induced energetic electrons are injected to the CB of neighboring semiconductor to participate in photocatalysis (Figure 1.10). Thus, the combination of plasmonic NPs with wide bandgap semiconductor photocatalysts can extend the light absorption range towards longer wavelengths. As plasmonic metallic NPs are characterized by high absorption cross-sections and

high mobility of charge carriers, the tuning of the resonance wavelength suggests that the entire solar spectrum can be potentially efficiently utilized with the use of plasmonic-metal sensitizers.

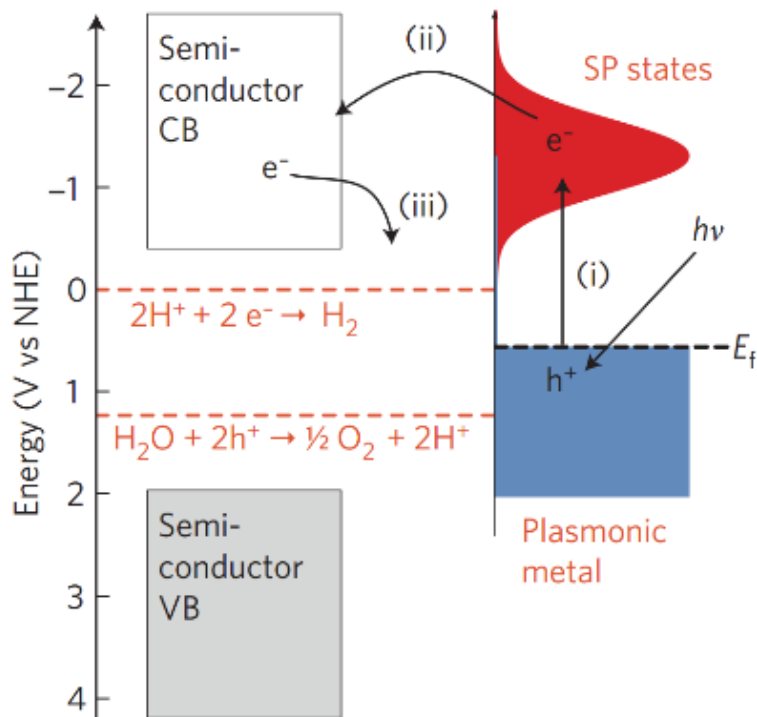


Figure 1.10 Mechanism of SPR-induced charge transfer with approximate energy levels on the NHE scale. Dashed red lines refer to the water-splitting redox potentials. (i) Electrons near the metal Fermi level, E_f are excited to surface plasmon (SP) states; (ii) the electrons transfer to a nearby semiconductor particle; (iii) this activates electron-driven processes such as the H_2 -evolution. Reproduced with permission.¹⁹⁹ Copyright 2011, Springer Nature.

The hot electron injection mechanism was found to be possible only when the SPR-induced electrons have sufficient energy to surmount the Schottky barrier formed between the plasmonic NPs and the semiconductor photocatalyst in direct contact.²¹²⁻²¹⁴ Thus, the hot-electron-injection efficiency is determined by the fraction of hot electrons with energy higher than the Schottky barrier. It can be affected by the size, shape, and composition of the plasmonic NPs, the physicochemical properties of the adjacent semiconductor, as well as the interfacial conditions between them.²¹⁵ For example, it was reported by Govorov et al. that 10-20 nm is the optimal size range of spherical Au NPs for efficient generation of hot charge carriers with energy over the Schottky barrier.²¹⁶ For small non-spherical NPs, such as cubes, nanowires, platelets, slabs, and stars, the direction of light polarization is important. The polarization direction along the small dimension of the plasmonic NPs is beneficial for generating high fraction of hot electrons. Under non-polarization light excitation, NPs with sharp tips or corners are normally more efficient in generating energetic charge carriers and thereby preferred for hot electron injection.²¹⁷

Plasmon-enhanced photocatalytic activity was also observed in the system where the plasmonic NPs were separated from the semiconductor by a thin, non-conductive spacers (e.g. SiO₂) which make the charge transfer between these two building blocks impossible.²¹⁸⁻²²⁰ In these cases, energy transfer from the plasmonic NPs to the semiconductor can occur through the near-field electromagnetic mechanism and resonant photon-scattering mechanism.

Near-field electromagnetic enhancement. Near-field electromagnetic mechanism is often known as plasmon resonance energy transfer (PRET) mechanism.⁴³ SPR-excited plasmonic NPs are characterized by strong electromagnetic fields, which are spatially non-homogenous and the highest intensity shown at the surface of NPs is orders of magnitude higher than the incident field.¹⁹⁹ These fields decrease exponentially as $1/s^4$ with distance from the surface (s) within ~20-30 nm, and decrease linearly further away.^{43,199} These intense fields can thus greatly affect the semiconductor which is in the proximity of a SPR-excited plasmonic NP. The photon absorption rate (generation rate of electron-hole pairs) in a semiconductor is proportional to $|E|^2$, where E is the electric field.^{221,222} Thus, for example, the charge carrier formation rate in some regions of the N-TiO₂, in the proximity of SPR-excited Au NPs, increases by a few orders of magnitude (Figure 1.11).

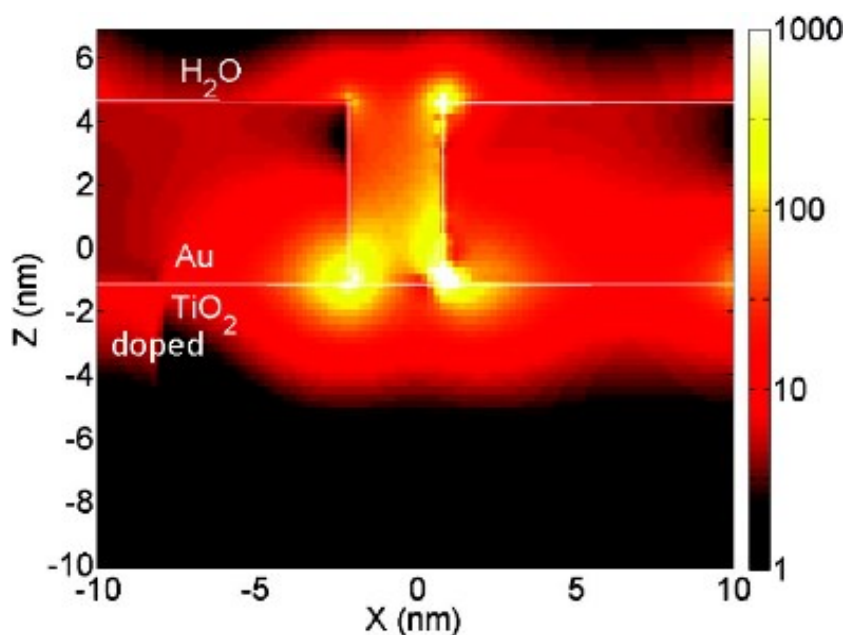


Figure 1.11 Optical simulations showing SPR-enhanced electric fields owing to photo-excited Au particles, permeating into a neighboring TiO₂ structure. The color bar shows electric field intensity normalized by the light source intensity ($|E|^2/|E_0|^2$). The electric field intensity (and therefore charge-carrier generation) is the highest at the metal/semiconductor/liquid three-phase boundary. Reproduced with permission.²²³ Copyright 2011, American Chemical Society.

A strong near-field electromagnetic resonance would also be beneficial to reduce the charge carrier recombination in a semiconductor by allowing the use of a thinner layer of the semiconductor with metal NPs situated at the semiconductor/liquid interface (Figure 1.12). Such energy transfer can occur even in the presence of a thin non-conductive spacer between the plasmonic metal and semiconductor.²²⁴

Most of the experimental results suggest that energy of the near-field should be above the bandgap of the semiconductor for the enhanced generation of electron-hole pairs through PRET. However, Wu et al. observed unprecedented plasmonic enhancement with an energy below the bandgap.²²⁴ They well explained their observation by proposing that plasmon-induced resonance energy transfer is indeed a non-radiative process and relies on the dipole-dipole interaction between the semiconductor and plasmonic metallic NPs.²²⁵ For utilizing this mechanism in plasmon-enhanced photocatalysis, it should meet two requirements: 1) the distance between plasmonic metal and semiconductor needs to be short, 2) the SPR band of a plasmonic material needs to overlap the intrinsic absorption region of the semiconductor.

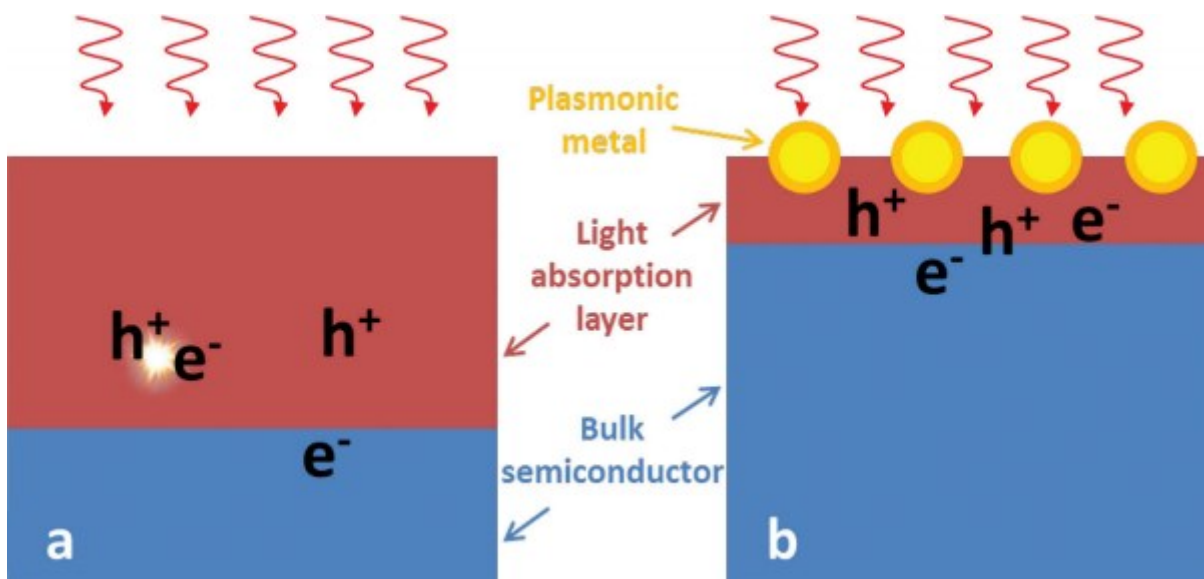


Figure 1.12 (a) Illustration of the phenomenon where electron-hole pairs generated deep under the surface of the semiconductor recombine easily. (b) Illustration of the situation when plasmonic metals are loaded at the surface of the semiconductor. The light-absorption layer becomes thinner where electron-hole pairs are generated at a high rate as a result of near-field electromagnetic resonant energy transfer. The generated electron-hole pairs take part in the reactions easily owing to their shorter migration length. Reproduced with permission.⁴³ Copyright 2015, WILEY-VCH.

Light-scattering enhancement. Plasmonic metal NPs have much larger absorption and scattering cross-sections than their actual sizes. For a SPR-excited plasmonic metal NP, the energy flux within a much enlarged area compared with the geometric cross section will be captured and absorbed (Figure 1.13a). On the other hand, enhanced light scattering due to the

presence of plasmonic NPs can be associated with a radiative energy transfer process from the plasmonic NPs to the semiconductor, which can be used to enhance the efficiency of photocatalysis. Basically, the enhanced light scattering increases the average photon path length in plasmonic-metal/semiconductor composites and thereby enhancing the formation of charge carriers in the semiconductor that can take part in photocatalytic reaction (Figure 1.13b).

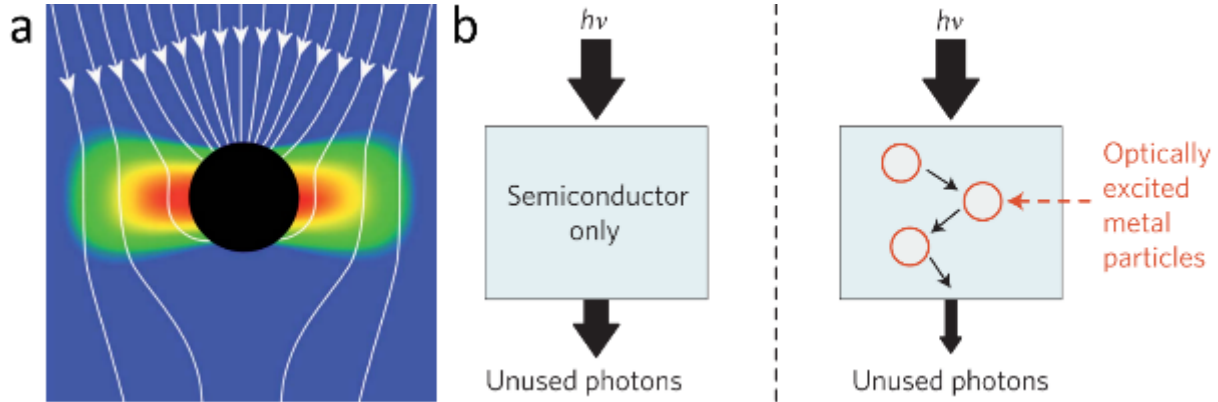


Figure 1.13 (a) Schematic illustration of the energy flux (Poynting vectors) and the electric-field intensity for an incident electromagnetic wave with an electric field in the plane of the image. Red/blue represent high/low electric-field intensity. The scattering effect is neglected. Reproduced with permission.²⁰¹ Copyright 2011, Royal Society of Chemistry. (b) Schematic illustrating the scattering mechanism. The addition of optically excited plasmonic nanoparticles increases the average path length of photons in the composite structure. Reproduced with permission.¹⁹⁹ Copyright 2011, Springer Nature.

Contribution from this aspect highly depends on the light scattering efficiency of plasmonic nanostructures, which can be estimated by calculated light scattering-to-absorption ratios. A high scattering-to-absorption ratio is a very important condition to be satisfied for utilizing photons effectively to enhance the efficiency of plasmon-enhanced photocatalysis. The scattering cross section (C_{sca}) and absorption cross section (C_{abs}) are expressed following Equations (1) and (2):^{226,227}

$$C_{sca} = \frac{8\pi}{3} k^4 a^6 \left| \frac{\varepsilon - \varepsilon_m}{\varepsilon + 2\varepsilon_m} \right|^2 \quad (1)$$

$$C_{abs} = 4\pi k a^3 \text{Im} \left(\frac{\varepsilon - \varepsilon_m}{\varepsilon + 2\varepsilon_m} \right) \quad (2)$$

Where k is the wavenumber ($k = \frac{2\pi}{\lambda}$), λ represents wavelength

a is the diameter of a plasmonic NP

ε is the dielectric function of a plasmonic NP

ε_m is the dielectric function of surrounding medium

Im is the imaginary component of the dielectric function.

From the above equations, it can be seen that both C_{sca} and C_{abs} largely and directly depend on the diameter of a metallic sphere, which scales with a^6 and a^3 , respectively. Therefore, a larger NP (~60 nm) predominately scatters incident electromagnetic field whereas a smaller NP (~20 nm) absorbs light and localizes the field.^{208,228}

In addition to the size of metallic NPs, shape and loading level also determine the enhancement of photocatalytic efficiency by scattering. For instance, it has been observed that photoreaction rate was highest for Ag nanocubes compared to Ag nanospheres and nanowires mainly due to the difference in their scattering efficiency.²²⁹ Finite-difference time-domain (FDTD) simulations further confirmed that the Ag nanocubes showed the highest scattering efficiency.

1.5.2.3 Plasmonic metal loaded g-C₃N₄ photocatalysts

Plasmonic metallic NPs, such as Au NPs,²³⁰⁻²³² Ag NPs,²³³⁻²³⁵ have been loaded onto g-C₃N₄ photocatalyst to enhance the light absorption and charge separation due to their strong SPR effect. Ag generally suffers from easy oxidation and thereby can lose its SPR effect. In addition, as shown in Figure 1.9a, the SPR peak of Au NPs locates in longer wavelength range compared with that of Ag NPs with the similar size, which is favorable for capturing broader band solar spectrum for photocatalysis. Thus, as a more stable metal, Au has recently been used for preparing plasmonic photocatalyst.²³⁶ For Ag or Au NPs loaded g-C₃N₄, the visible light absorption was largely enhanced due to the SPR effect of Ag or Au NPs that are mainly covering the visible light region. However, the visible light at longer wavelengths and the NIR light are still not utilized. The longitudinal SPR peaks of the Au nanorods (NRs) can be tuned from the visible to NIR ranges.^{237,238} Thus, to further extend the light response range, it is promising to design Au NRs/g-C₃N₄ photocatalysts. In addition, to make the utmost of photons in both NIR and visible regions, the combination of UC and SPR effect has also been tried,^{145,192,239,240} which is another prospect idea to prepare broadband and efficient g-C₃N₄ based composite photocatalysts.

1.5.3 Coupling with narrow-bandgap semiconductor

In plasmon-enhanced photocatalysis, noble metallic NPs are always involved. The practical application of introducing SPR effect to extend the light response range is limited by the high cost and the low abundance of precious metals. To circumvent this limitation to reach the same goal, i.e., making g-C₃N₄ efficiently harvest broadband solar spectrum, the coupling of g-C₃N₄ with cost-effective narrow-bandgap semiconductor can be a promising alternative strategy.

1.5.3.1 Representative narrow-bandgap semiconductors

The exploration of narrow-bandgap materials greatly stimulates the evolution of photocatalysts and the past few years have witnessed the fast growth of this research area. Table 1.1 summarizes some of the frequently-used narrow-bandgap semiconductors and their bandgap values.

Table 1.1 Representative narrow-bandgap materials and their bandgap values.

Materials	Bandgap (eV)	References
Ag ₂ O	1.2	241,242
Ag ₂ S	0.9-1.2	243,244
Bi ₂ S ₃	1.3	245,246
Co _{2.67} S ₄	0.92	247
CuInS ₂	1.0-1.42	248-250
MoS ₂	1.2 (bulk)-1.9 (monolayer)	251-255
PbS	0.4 (bulk)-1.5 (quantum dots)	256-259
Sb ₂ S ₃	1.5	260
Sn ₂ S ₃	0.68-1.1	261,262
VS ₄	0.8-1.2	263,264
WS ₂	1.35 (bulk)-2.14 (monolayer)	265-269
CuSe	1.5	270,271
InSe	1.0 (bulk)-2.1 (monolayer)	272-274
Sb ₂ Se ₃	1.0-1.2	275,276
In ₂ Te ₃	1.0	277
Cu ₂ (OH)PO ₄	0.62	120,278
Black phosphorus	0.3 (bulk)-2.0 (monolayer)	279-282
CaFe ₂ O ₄	1.9	283
ZnFe ₂ O ₄	1.9	284-286

It is worth noting that the chalcogenides (materials containing at least one chalcogen elements, e.g. S, Se or Te, as a substantial constituent, and at least one electropositive element), such as Ag₂S,^{243,244} Bi₂S₃,^{245,246} MoS₂,²⁵¹⁻²⁵⁴ WS₂,²⁶⁵⁻²⁶⁹ Sb₂Se₃,^{275,276} In₂Te₃,²⁷⁷ account for a large proportion of narrow-bandgap semiconductors. They have also been directly utilized in photocatalysis to gain broadband photocatalytic activity. For example, Liu et al. reported a WS₂ nanosheet semiconductor with a narrow bandgap of 1.35 eV.²⁶⁸ It strongly absorbs photons ranging from UV, visible to NIR regions and thus exhibiting broadband photocatalytic

performance. $\text{Co}_{2.67}\text{S}_4$ NPs were synthesized by Yuan and Wang et al. which were measured to possess a bandgap of ~ 0.92 eV and showed obvious light absorption in the range of 240-2200 nm, especially for the NIR region of 760-2200 nm.²⁴⁷ As a result, the as-prepared $\text{Co}_{2.67}\text{S}_4$ NPs exhibited photocatalytic activity in the removal of MB under the light from UV to NIR regions.

In search of photoactive narrow-bandgap semiconductors, Huang et al. developed a transition-metal hydroxide phosphate photocatalyst, $\text{Cu}_2(\text{OH})\text{PO}_4$, with an absorption edge up to ~ 2000 nm.^{120,278} The developed $\text{Cu}_2(\text{OH})\text{PO}_4$ showed effective activity in the photocatalytic oxidation of 2,4-dichlorophenol in aqueous solution under $\lambda > 800$ nm light irradiation.

Most recently, as a new 2D material, black phosphorus (BP) has grabbed a great research attention with its enticing electrical and optical properties, such as sufficiently high carrier mobility, high photoelectronic response, and tunable bandgap from 0.3 eV (bulk) to 2.0 eV (monolayer).²⁸⁷⁻²⁹¹ These favorable properties make BP, particularly few-layer BP nanosheets (≤ 10 nm in thickness), a promising candidate for broadband photocatalysis.

However, for narrow-bandgap semiconductors, the fast recombination of charge carriers has been seriously hindering their direct application in photocatalysis. For example, BP itself shows very poor photocatalytic activity no matter in photocatalytic degradation or H_2 evolution due to the fast recombination of photo-induced electrons and holes in it. That is the reason why Majima et al. synthesized a Pt NP and reduced graphene oxide (rGO) loaded few-layer BP nanoflakes (Pt-rGO-BP).²⁹² The photons from UV to NIR regions can be harnessed by BP to generate electron-hole pairs. The loaded Pt NP and rGO facilitated the separation of charge carriers to enhance the photocatalytic activity in H_2 evolution of the Pt-rGO-BP hybrid. In addition, the band positions of these narrow-bandgap semiconductors are normally not possessing enough oxidation/reduction potentials to initiate some redox reactions. Therefore, the fast recombination of charge carriers and the weak redox capability render these narrow-bandgap semiconductors difficult to be efficient broadband photocatalysts by themselves. Furthermore, BP is suffering from instability as it is very reactive to moisture and ambient oxygen, and can be easily oxidized due to the exposed lone pairs at its surface. For the preparation of few-layer BP nanosheets, as BP possesses stronger interlayer interactions compared with graphene and other 2D materials, the exfoliation by ultrasonication would be difficult and would require long processing time or a sonicator with high power.²⁹³⁻²⁹⁵ Howbeit the yield of few-layer BP nanosheets is still very low. These features are greatly restricting the practical applications of BP.

1.5.3.2 Narrow-bandgap semiconductor quantum dots

Basics of semiconductor quantum dots (QDs). Semiconductor QDs are nanocrystals with physical sizes smaller than the exciton Bohr radius in three dimensions and show properties in between bulk semiconductors and molecules or discrete atoms.^{203,296} Exciton Bohr radius is a dimension describing the spatial extension of electron-hole pairs in solids, ranging from 2 to 50 nm depending on the type of materials,²⁹⁷⁻²⁹⁹ such as ~5 nm for CdSe and ~20 nm for PbS.^{300 258,301,302} When the nanocrystal size is small compared to the exciton Bohr radius, the exciton wave functions undergo confinement, which induces the quantization of the electronic bands. Thus, the discrete energy levels appear near the band edges of QDs and the bandgap increases with decreasing size (Figure 1.14a).^{297,298,303} Due to the quantum confinement effect, semiconductor QDs have demonstrated unique size-dependent optoelectronic properties in exciton generation and light harvesting, which perhaps is the most attractive feature of QDs in many photon-related applications. For example, the redox capabilities of excitons in QDs can be readily tuned through size alteration.^{304,305} Similarly, it is possible to realize the better energy level matching between donors and acceptors as well as tune the absorption of QDs to cover the full solar spectrum by varying the size of the QDs (Figure 1.14b).³⁰⁶ In addition, the abundant surface sites lead to the strong interaction between QDs and other materials, favoring their interfacial charge transfer.³⁰⁷ Unlike bulk counterparts, the surface atoms of semiconductor QDs account for the significant content of the total atoms, which makes the utmost of the material without much wasting the inner part. As a result of the unique electronic and optical properties, QDs have become promising candidates for applications in photocatalysis (by acting as sensitizers, for example), photovoltaics, and optoelectronics.

Synthetic methods. For most QDs-based applications, it is generally desired to synthesize highly monodisperse QDs with a narrow size distribution and high crystallinity, which can be achieved by the thermal decomposition method.^{296,300,308,309} The formation of monodisperse QDs typically consists of two steps: rapid nucleation followed by slow growth. Thus, the separation of these two steps during thermal decomposition is essential to obtain monodisperse samples. To this end, hot-injection and heat-up methods were developed. The hot-injection method involves the rapid injection of suitable reactive precursors into a vigorously stirred, hot solvent with high-boiling point. Upon injection, the induced supersaturation initiates the nucleation. The injection of the precursor solution with room temperature can lower the overall reaction temperature, and thus the nucleation step is terminated and the growth step begins. For the heat-up method without injection, the separation of nucleation and growth is achieved through the steady heating of a

mixture of precursors and surfactants dissolved in high-boiling-point solvents as these two steps occur at different temperatures.

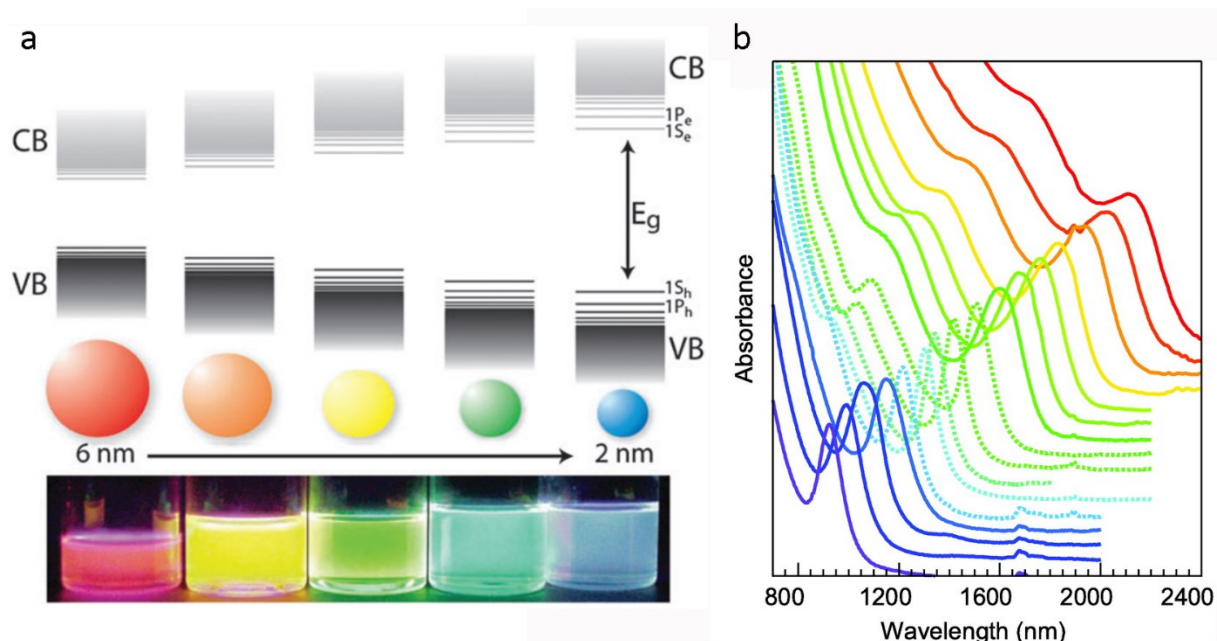


Figure 1.14 (a) Schematic representation of the quantum confinement effect on the energy level structure of a semiconductor material. The lower panel shows colloidal suspensions of CdSe nanocrystals of different sizes under UV excitation. Courtesy of R. Koole (Philips Research Laboratories, Netherlands). Reproduced with permission.³⁰³ Copyright 2011, Royal Society of Chemistry. (b) Absorbance spectra of PbS QDs with diameter being tuned from 3 to 10 nm, leading to excitonic maxima ranging from 900 to 2100 nm. Reproduced with permission.³⁰⁶ Copyright 2011, American Chemical Society.

Ligand exchange. Long-chain surfactants usually involved in the above mentioned thermal decomposition synthesis make QDs stable in colloidal suspension; however, they also act as an insulating layer covering the QDs.³⁰⁹ The hydrophobic surfactant layer enables QDs readily dispersible in non-polar solvents. Nevertheless, in some applications, such as photocatalysis and biomedical imaging, water-soluble QDs are generally desired. Both the above two problems can be addressed by partially or fully exchanging the native ligands (e.g., oleylamine) with relatively short-chain and hydrophilic ones (e.g., hexanethiol, mercaptopropionic acid).³¹⁰⁻³¹²

In virtue of the rapid development of synthetic technologies, semiconductor QDs have recently shown great potentials and appealing performance in solar energy conversion, particularly for solar cells.³¹³⁻³¹⁶

1.5.3.3 Narrow-bandgap semiconductor/g-C₃N₄ heterostructure

In recent years, the coupling of narrow-bandgap semiconductors with g-C₃N₄ to prepare efficient and broadband photocatalysts have piqued great interest of researchers. For example, Zhang and co-workers constructed a Z-scheme heterojunction based on CuInS₂/g-C₃N₄ for photocatalytic water splitting.³¹⁷ The as-prepared sample demonstrated efficient charge separation and an enhanced photocatalytic H₂ evolution rate under visible light irradiation. Most recently, Majima et al. synthesized two kinds of nanostructured MoS₂ (nanodots and monolayer) coupled g-C₃N₄ samples.¹¹⁶ They systematically investigated charge transfer kinetics between g-C₃N₄ and MoS₂ by using single-particle photoluminescence (PL) spectroscopy and femtosecond time-resolved transient absorption spectroscopy. The results indicated faster and more efficient electron transfer from g-C₃N₄ to MoS₂ nanodots than that to MoS₂ monolayer, which is attributed to the stronger interaction between g-C₃N₄ and MoS₂ nanodots. Also, the photodeposition of MoS₂ enhanced the light absorption in the range of 450-800 nm. Thus, the g-C₃N₄/MoS₂ nanodots exhibited higher photocatalytic activity for H₂ evolution than both pure g-C₃N₄ and g-C₃N₄/MoS₂ monolayer under visible light irradiation ($\lambda > 400$ nm).

Although the coupling of narrow-bandgap semiconductors with g-C₃N₄ has been studied for several years, the reported g-C₃N₄ based broadband photocatalysts that indeed show NIR photocatalytic activity are still quite limited. Table 1.2 summarizes some examples of the g-C₃N₄ based NIR photocatalysts and their applications in solar-driven environmental purification and fuel production.

Table 1.2 Some examples of the broadband photocatalysts based on narrow-bandgap semiconductor/g-C₃N₄ heterostructure for NIR photocatalytic applications.

Photocatalysts	Light source	Wavelength	Application ^a	Ref.
g-C ₃ N ₄ @Bi ₂ S ₃ NRs	diode laser	808 nm	PEC and antibacterial	245
g-C ₃ N ₄ QDs-Sb ₂ S ₃ /g-C ₃ N ₄ ^b	300 W xenon lamp	> 760 nm	MO Degradation	260
Ag ₂ O/g-C ₃ N ₄	250 W NIR lamp	> 760 nm	Phenol, imidacloprid, MB, MO Degradation	318
BP/g-C ₃ N ₄	320 W xenon lamp	> 780 nm	H ₂ Production	319
NiS@g-C ₃ N ₄	diode laser	980 nm	H ₂ Production	320
Cu ₂ (OH)PO ₄ /g-C ₃ N ₄	200 W NIR light	> 800 nm	H ₂ O ₂ production	321

a, Photocatalytic applications; b, g-C₃N₄ quantum dots loaded Sb₂S₃ rods/g-C₃N₄ nanosheets.

For instance, a multifunctional Zn-doped g-C₃N₄@Bi₂S₃ nanorod heterojunction (CN-Zn/BiS) was developed by Wu and coworkers.²⁴⁵ The absorption spectrum of Zn-doped g-C₃N₄ (CN-Zn)

showed enhanced light absorption and the red-shift was observed for its absorption edge because the doping introduced more lattice defects (Figure 1.15a). CN-Zn/BiS exhibited further enhanced light absorption from UV, visible to NIR regions due to the introduction of Bi_2S_3 . A higher photocurrent density was achieved by CN-Zn/BiS photocathode than that by BiS, while almost no photocurrent density was observed for the CN and CN-Zn samples with or without 808 nm laser irradiation (Figure 1.15b). To detect the involved reactive oxygen species (ROS) in this system, the electron spin resonance (ESR) spectroscopy was employed. $\cdot\text{O}_2^-$ and $\cdot\text{OH}$ radicals were detected for CN-Zn/BiS sample after NIR light irradiation (Figure 1.15c). The band structures of CN, CN-Zn, BiS, and CN-Zn/BiS were determined by performing density functional theory (DFT) calculations and then the ROS generation mechanism was proposed (Figure 1.15d). Under 808 nm NIR light illumination, BiS can be excited to produce photo-induced electrons and holes, and thereby to generate ROS. These ROS can be used for disinfection. As shown in Figure 1.16e-f, for CN-Zn/BiS ($200 \mu\text{g mL}^{-1}$), 99.2% of *Staphylococcus aureus* (MRSA) and 99.6% of *Escherichia coli* (*E. coli*) were killed when exposed to 808 nm laser for 10 min, largely surpassing the other control samples.

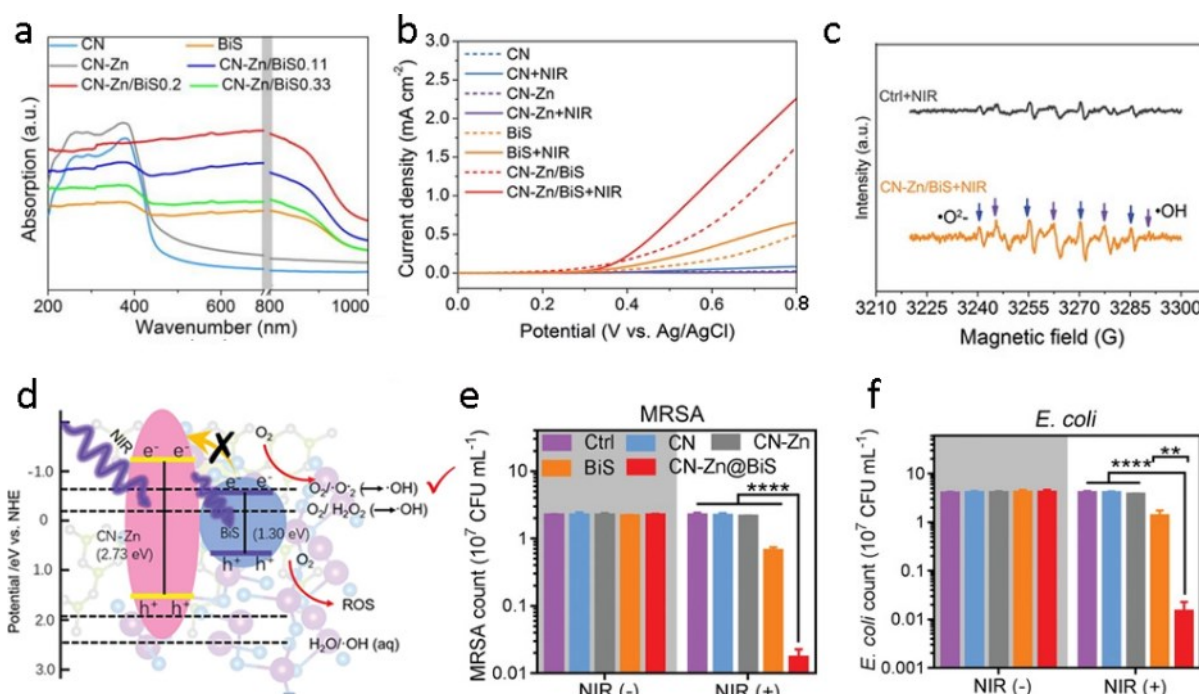


Figure 1.15 (a) UV-visible-NIR absorption spectra of CN, CN-Zn, BiS, and CN-Zn/BiS. (b) Linear volt-ampere curve of CN, CN-Zn, BiS, and CN-Zn/BiS with and without 808 nm NIR irradiation. (c) ROS detection of CN-Zn/BiS through ESR with DMPO probe. Blue arrows indicated $\cdot\text{O}_2^-$ and purple arrows indicated $\cdot\text{OH}$. (d) The mechanism of ROS enhancement based on the DFT calculation compared with individual CN-Zn and BiS. Red arrows mean generated ROS species. (e) MRSA and (f) *E. coli* strain counts calculated from spread-plate assays after treatment with CN, CN-Zn, BiS, or CN-Zn/BiS ($200 \mu\text{g mL}^{-1}$) under 808 nm light irradiation. Reproduced with permission.²⁴⁵ Copyright 2019, WILEY-VCH.

1.6 Thesis Objectives and Organizations

1.6.1 Thesis objectives

As discussed above, energy crisis and environmental pollution caused by the intensive consumption of fossil fuels have been the two main issues facing human beings. To maintain the sustainability of human society, the seeking of green and renewable energy sources is imperative and urgent. Solar energy that powers all the lives on our planet is considered to be an inexhaustible, secure and clean natural resource. Semiconductor photocatalysis, which can directly harvest and convert solar energy for green fuel production and environmental remediation at room temperature and standard atmospheric pressure, has been recognized as one of the green, sustainable and ideal avenues to address the global energy and environmental concerns. Among the various categories of semiconductor photocatalysts, g-C₃N₄ has attracted tremendous interest of material scientists by virtue of its fascinating merits, such as nontoxicity, facile preparation, moderate bandgap, strong redox capability, “earth-abundant” nature, and good physicochemical stability. However, g-C₃N₄ still suffers from poor photocatalytic activity and low quantum efficiency due to the high recombination rate of photogenerated charge carriers. Moreover, the optical bandgap (2.7 eV) of g-C₃N₄ largely restrains the range of its visible light absorption to wavelengths shorter than 460 nm. Accordingly, the large portion of visible light, which accounts for ~43% of incoming solar energy, remains underutilized. Thus, the development of efficient and broadband responsive (from UV, visible to NIR regions) g-C₃N₄ based photocatalysts is a task of great significance and urgency, though challenging. To date, the reported g-C₃N₄ based broadband photocatalysts that indeed show from UV to NIR photocatalytic activity are still quite limited. Therefore, the objectives of this thesis are as follows:

- (1) Introducing both UC and plasmonic effects into photocatalysis to construct efficient and broadband photocatalysts for photocatalytic degradation of organic dye in aqueous solution.
- (2) Loading NIR-responsive, narrower-bandgap semiconductor QDs onto g-C₃N₄ nanosheets to more economically harvest solar photons ranging from UV, visible to NIR regions for photocatalytic degradation of organic dye in aqueous solution.
- (3) Coupling a narrower-bandgap 2D semiconductor with 2D g-C₃N₄ nanosheets to construct a metal-free 2D/2D heterojunction to more efficiently, economically, environmental-friendly utilize solar energy for the broadband production of a green, zero-emission fuel, H₂.

1.6.2 Thesis organizations

This thesis is composed of 6 chapters and the structures are as follows:

Chapter 1 introduces the background of this thesis and outlines the motivation of my research work. Afterwards, a literature review is presented focusing on the development of efficient and broadband g-C₃N₄ based photocatalysts and their applications in solar-driven environmental purification and fuel production. The publications related to this chapter are:

Zhang Q, Liu Y, Xu Z, Zhao Y, Chaker M, Ma D (2018) Visible-Light-Driven Photocatalysts. *Nanomaterials for Energy Conversion and Storage*, Wang D & Cao G (Eds.) World Scientific, New Jersey. p. 109-173.

Zhang Q, Yang F, Xu Z, Chaker M, Ma D (2019) Are lanthanide-doped upconversion materials good candidates for photocatalysis? *Nanoscale Horizons*, 4(3):579-591.

Zhang Q, Thrithamarassery Gangadharan D, Liu Y, Xu Z, Chaker M, Ma D (2017) Recent Advancements in Plasmon-Enhanced Visible Light-Driven Water Splitting. *Journal of Materiomics*, 3(1):33-50.

Chapter 2 provides the experimental and computational details. Synthesis methods of all the samples, characterization information, photocatalytic degradation of organic dye and H₂ production, and adopted models and parameters for theoretical calculations are all provided.

Chapter 3 corresponds to **the first objective**. A plasmon and UC enhanced broadband photocatalyst based on plasmonic Au NP and upconverting NaYF₄:Yb³⁺, Er³⁺, Tm³⁺ (NYF) microsphere loaded g-C₃N₄ nanosheets was subtly designed and synthesized, and used for broadband (from UV to NIR) photocatalytic degradation of MO. The publication related to this chapter is:

Zhang Q, Deng J, Xu Z, Chaker M, Ma D (2017) High-Efficiency Broadband C₃N₄ Photocatalysts: Synergistic Effects from Upconversion and Plasmons. *ACS Catalysis*, 7(9):6225-6234.

Chapter 4 corresponds to **the second objective**. NIR-responsive PbS@CdS@ZnS QDs (PCZ QDs) were loaded onto g-C₃N₄ nanosheets to construct a 0D/2D heterostructure, which was used for harvesting solar photons from UV, visible to NIR regions for efficient photocatalytic degradation of MO. The publication related to this chapter is:

Zhang Q, Yang F, Zhou S, Bao N, Xu Z, Chaker M, Ma D (2020) Broadband Photocatalysts Enabled by 0D/2D Heterojunctions of Near-Infrared Quantum Dots/Graphitic Carbon Nitride Nanosheets. *Applied Catalysis B: Environmental*, 270:118879.

Chapter 5 corresponds to *the third objective*. A 2D/2D heterojunction of BP/g-C₃N₄ was designed and synthesized for broadband photocatalytic H₂ evolution. The publication and applied patent related to this chapter is:

Zhang Q, Huang S, Deng J, Gangadharan DT, Yang F, Xu Z, Giorgi G, Palumbo M, Chaker M, Ma D (2019) Ice-Assisted Synthesis of Black Phosphorus Nanosheets as a Metal-Free Photocatalyst: 2D/2D Heterostructure for Broadband H₂ Evolution. *Advanced Functional Materials*, 29(28):1902486.

Zhang Q, Ma D, Chaker M (2019) *Facile Method for Large-scale Producing Few-layer Black Phosphorus Nanosheets. International Patent*, PCT/CA2019/050813.

Chapter 6 briefly summarizes the main conclusions of this work and provides the current challenges and perspectives toward this dynamic field.

Following the main body of this thesis is a synopsis of this thesis in French as per the INRS requirements.

2 EXPERIMENTAL

2.1 Materials

Au target (99.99%, diameter × thickness: 8 mm × 1.5 mm), 1,4-benzoquinone (BQ), butylamine (99.5%), cadmium oxide (CdO, 99%), 5,5-dimethyl-1-pyrroline N-oxide (DMPO), disodium ethylenediaminetetraacetate (Na₂EDTA), ethanol (99%), hexane (99.9%), isopropanol (IPA, 99.5%, anhydrous), lead chloride (PbCl₂, 98%), methanol (anhydrous, 99.8%), 3-Mercaptopropionic acid (MPA, ≥99.0%), methyl orange (MO), N-methyl-2-pyrrolidinone (NMP, ≥99%), NMP (99.5%, anhydrous), nitric acid (HNO₃), N,N-dimethylformamide (DMF, 99.8%), octadecene (ODE), oleic acid (OA), oleylamine (OLA, technical grade, 70%), phosphorus pentasulfide (P₂S₅, 99%), rare-earth nitrate hydrate (Y(NO₃)₃·6H₂O, Yb(NO₃)₃·5H₂O, Er(NO₃)₃·5H₂O, Tm(NO₃)₃·5H₂O; 99.9 wt%), sodium fluoride (NaF), sodium hydroxyl (NaOH), sulfur powder (S, 100%), tert-butyl alcohol (t-BuOH), toluene (99.9%), urea (NH₂CONH₂), and zinc chloride (ZnCl₂, 99.999%) were purchased from Sigma-Aldrich and used without further purification. Black phosphorus (BP) crystals of high-purity (~99.998%) were purchased from Smart Elements. The absolute pure water, purified by a Millipore Ultrapure water system and having a resistivity of 18.2 MΩ cm at 25 °C, was used in the current investigation.

2.2 Synthesis of g-C₃N₄ Nanosheets

For the synthesis of g-C₃N₄, urea (30 g) was placed into a covered alumina crucible, and then heated in a quartz tube furnace with a heating rate of 2 °C min⁻¹ to 250 °C, 350 °C, and 550 °C, and maintained at these three target temperatures for 1 h, 2 h and 2 h, respectively. After being naturally cooled down to room temperature, the yellow powder was collected and washed for three times with HNO₃ (0.1 mol L⁻¹) and water to remove potential alkaline residue (e.g. ammonia). After centrifugation, the precipitate was dried in the vacuum at 80 °C overnight.

2.3 Synthesis of Au-NYF/g-C₃N₄

2.3.1 Preparation of Au NP colloids

The Au NP colloids were prepared by using the pulsed laser ablation in liquid (PLAL) technique. A KrF excimer laser (GSI Lumonics PM-846, λ: 248 nm; pulse width: 25 ns; repetition rate: 20 Hz) was employed for laser ablation. The Au target was fixed at the bottom of a glass vessel filled with 5 mL of NaOH solution (pH ≈ 9.5). The beam was focused onto the Au target by an objective

lens with 7.5 cm focal length. The depth of the NaOH solution layer above the target was about 10 mm. Laser fluence on the target was set to a constant value ($\sim 40.0 \text{ J cm}^{-2}$). The concentration of the as-prepared Au NP colloids was 50 ppm based on the neutron activation analysis (NAA) measurements.

2.3.2 In-situ synthesis of NYF/g-C₃N₄ composites

NYF microspheres were synthesized and anchored onto the g-C₃N₄ nanosheets in a single step via in-situ synthesis of NYF microspheres in the presence of g-C₃N₄. Typically, 0.60 g of the obtained g-C₃N₄ was dispersed into 60 mL of water by ultrasonication for 12 h. Then 3.133 mL of Y(NO₃)₃ (0.5 M), 0.801 mL of Yb(NO₃)₃ (0.5 M), 1.000 mL of Tm(NO₃)₃ (0.01 M), and 0.203 mL of Er(NO₃)₃ (0.01 M) solutions were added to the above g-C₃N₄ dispersion and the mixture was further magnetically stirred for 2 h. Subsequently, 0.30 g of NaF was introduced into the solution. After stirring for 1h, the reaction mixture was transferred into a 100 mL Teflon-lined stainless steel autoclave and subjected to heating for 12 h at 180 °C. After the autoclave was cooled down naturally to room temperature, the product was washed three times with pure water and ethanol in sequence. The purified precipitate was then dried at 80 °C in an oven for 12h to obtain the composite of NYF microsphere loaded g-C₃N₄ nanosheets.

2.3.3 Preparation of Au NP loaded NYF/g-C₃N₄ photocatalysts

A certain amount of the freshly prepared Au NP colloid was added to 10 mg of NYF/g-C₃N₄ and mixed by shaking. After being incubated for ~ 30 min at room temperature, the precipitate from the mixture solution was collected by centrifugation, followed by washing with pure water. By adding different volumes of Au NP solution, the Au-NYF/g-C₃N₄ photocatalysts with different loading levels of Au NPs were prepared. The mass fraction of Au NPs in the Au-NYF/g-C₃N₄ photocatalysts was denoted as $x \text{ wt}\%$ ($x=1, 2, 3, 4$ and 5).

2.4 Synthesis of PCZ QDs/g-C₃N₄ Nanosheets

2.4.1 Synthesis of PbS QDs

The PbS QDs were synthesized via a previous reported method.³²² Typically, 24 mL of OLA and 10 g of PbCl₂ were mixed in one three-neck flask and heated to 160 °C. After stirring for 1h at this temperature under N₂, the solution was cooled down to 120 °C and vacuumed for 40 min. At this time, a solution containing 115 mg of sulfur powder and 4 mL of OLA was immediately injected into the above flask under the protection of N₂, which was cooled down to 100 °C and kept for 1

min for the growth of PbS QDs to reach the desired size. Afterwards, the solution was quenched with cold water to terminate the reaction. The PbS QDs were separated from the colloidal solution and the supernatant was collected. 20 mL of hexane and 30 mL of ethanol were added to wash the obtained QDs for two times. The final product was re-dispersed in toluene to get the colloidal PbS QDs solution.

2.4.2 Synthesis of PbS@CdS core@shell QDs

A microwave-assisted cation exchange approach was used to synthesize PbS@CdS core@shell QDs³²³. Specifically, the colorless Cd precursor solution was prepared by heating a flask containing OA (15 mL), ODE (20 mL), and CdO (3 g) to 200-250 °C, and then cooled to 100 °C and degassed for 30 min to remove moisture and oxygen. When the solution was cooled down to 20 °C, 12 mL of the as-synthesized PbS QD dispersion was added to obtain a mixture. 20 mL of the mixture was transferred to a 35 mL vial and underwent heating in a Discover SP microwave reactor (CEM Corporation) to 100 °C for 3 min. Certain volume of ethanol was added to precipitate QDs, which were separated by centrifugation and re-dispersed in toluene. The precipitation and re-dispersion procedures were repeated three times to purify the obtained PbS@CdS QDs, which were finally re-dispersed in toluene.

2.4.3 Synthesis of PCZ core@shell@shell QDs

Through a microwave-assisted procedure, the coating of ZnS shell on the PbS@CdS QDs and replacing the OA with MPA ligand to make them water-dispersible were simultaneously achieved. Typically, P₂S₅ (0.02 g) was dissolved into MPA (0.5 g), butylamine (0.3 mL), and NMP (10 mL) by heating at 110 °C for 20 min in a sealed flask to prepare S precursor solution. Under the same condition, Zn precursor solution was synthesized by dissolving ZnCl₂ (0.07 g) into same amount of MPA, butylamine, and NMP in another sealed flask. After cooling down to room temperature, 0.007 g of as-synthesized PbS@CdS QDs were dissolved in the S precursor solution, and then Zn precursor solution was added into the mixture. The obtained solution was heated in a Discover SP microwave oven at 70 °C for 30 min to yield the MPA-capped PCZ core@shell@shell QDs. The synthesized QDs were purified by repeating four times the centrifugation and re-dispersion using toluene. The purified QDs were dried overnight in a vacuum oven and dispersed in 10 mL of water.

2.4.4 Preparation of PCZ QDs/g-C₃N₄ nanosheets

A certain amount of the prepared PCZ core@shell@shell QDs was added to 10 mg of g-C₃N₄ nanosheets and mixed by shaking for 5 min, and then the mixture was incubated at room temperature until the supernatant became transparent and colorless. The precipitate was collected and washed by water. By varying the added volumes of QD solution, PCZ QDs/g-C₃N₄ with different loading mass fractions of QDs were prepared, denoted as x wt% QDs/g-C₃N₄. The actual contents of PCZ QDs in the composites were measured by inductively coupled plasma-optical emission spectrometry (ICP-OES). The measured values, 0.95, 2.14, 2.97, 7.02 and 10.89 wt%, are quite close to the nominal loading mass fractions, 1, 2, 3, 7 and 11 wt%.

2.5 Synthesis of BP/g-C₃N₄ Nanosheets

2.5.1 NMP-ice-assisted preparation of BP nanosheets.

BP nanosheets were synthesized by developing a NMP-ice-assisted exfoliation method. Specifically, 25 mg of bulk BP was ground into ultrafine powder and dispersed into 25 mL of NMP solvent. The dispersion was completely frozen with a liquid nitrogen bath for 5-10 min, and then sonicated in a bath sonicator (BRANSONIC, 70 W, 40 kHz) for ~10 min to make the “NMP ice” melt. The procedure of freezing and melting was repeated 3 times. To protect the BP from oxygen and water, the dispersion was sealed in a vial, and all the experimental manipulations were performed in a glovebox or with nitrogen bubbling. Afterwards, the dispersion was centrifuged at 4000 rpm for 15 min to remove the residual un-exfoliated BP. The light yellow supernatant was decanted gently, which was the dispersion of BP nanosheets in NMP. The obtained BP nanosheets were washed with IPA by centrifugation at 12000 rpm for 2 times. The collected precipitate was re-dispersed into 25 mL of IPA. The concentration of BP in this dispersion was determined to be 0.75 mg mL⁻¹ by ICP-OES.

2.5.2 Preparation of BP/g-C₃N₄ photocatalysts.

BP/g-C₃N₄ nanosheets were prepared by dispersing 10 mg of g-C₃N₄ powder into 0.4 mL of BP nanosheet dispersion in IPA. The mixture was stirred for 2 h to couple BP nanosheets with g-C₃N₄ nanosheets under the protection of N₂. Subsequently, the sample was collected by centrifugation at 6000 rpm for 5 min, and then washed completely with IPA. The final product was obtained by drying the washed sample in an oven under vacuum at 60 °C overnight. The obtained BP/g-C₃N₄ nanosheets contain about 3 wt% of BP. The composites with 10 wt% and 15 wt% of BP were prepared with adding 1.3 mL and 2 mL of BP dispersion, respectively.

2.6 Characterizations

The microstructure and composition of the photocatalysts were studied by a transmission electron microscope (TEM, JEOL 2100F, operated at 200 kV), equipped with an energy-dispersive X-ray (EDX) spectrometer.

The crystal structures of all the samples were analyzed by the X-ray diffraction instrument (XRD, PANalytical X'Pert MRD) with a Cu K α radiation source ($\lambda = 0.15406$ nm) operated at 45 kV and 40 mA.

The UV-visible-NIR absorption spectra of samples and the absorbance of MO in aqueous solutions were measured using a Varian Cary 5000 scan spectrometer equipped with an integrating sphere (for solid samples) at room temperature. The bandgap energy (E_g) of the prepared samples were determined from Tauc plots, *i.e.* $(\alpha h\nu)^2$ as a function of $h\nu$.

A VG Escalab 220i-XL X-ray photoelectron spectroscopy (XPS) equipped with a twin anode Al K α radiation x-ray source was used to analyze the chemical composition of the samples. All the XPS spectra were calibrated using the C1s peak at 284.8 eV as reference.

Ultraviolet photoelectron spectroscopy (UPS) measurements were carried out with an unfiltered Helium gas discharge lamp emitting predominantly at 21.22 eV to determine the valence band (VB) position of as-prepared samples.

Fourier transform infrared (FTIR) spectra of the prepared samples were recorded on a Thermo Scientific 4700 FTIR spectrometer.

The UC luminescence spectra were obtained by using a Thorlabs fiber-coupled laser diode (maximum power: 330 mW) as the 980 nm excitation light source. The laser was focused on the powder to obtain a spot (0.4 mm in diameter) with a Gaussian distribution of intensity. The emission was collected at 90° from the incident beam, and then transferred and recorded on a spectrophotometer (Avaspec-2048L-USB2). All the measurements were performed under ambient conditions.

Steady-state photoluminescence (PL) and time-resolved PL (TRPL) spectra were obtained by a Horiba Jobin Yvon Fluorolog-3 fluorescence spectrometer.

The electron spin resonance (ESR) characterizations were performed by using a JEOL JES-X320 spectrometer with a microwave power of 10.00 mW and a frequency of 9.15 GHz at room temperature to study the electron mobility. The 5,5-dimethyl-1-pyrroline N-oxide (DMPO) was

used as the spin-trapping agent to detect the reactive species. The measurements were carried out in aqueous dispersion and methanol dispersion for DMPO-•OH and DMPO-•O₂⁻, respectively.

The topography image of the BP nanosheets on a pre-cleaned glass was observed by an atomic force microscopy (AFM, Bruker, MultiMode 8) in a tapping mode.

Zeta potential of the as-prepared samples was recorded with a Brookhaven ZetaPlus system in a standard 10 mm all-side-transparent polymethyl methacrylate cuvette.

Neutron activation analysis (NAA) measurements were performed using a SLOWPOKE nuclear reactor to determine the concentration of Au NPs in colloids, and the weight content of Au, Er, Tm and NYF in Au-NYF/g-C₃N₄ samples.

The concentration of actual contents of PCZ QDs in the PCZ QDs/g-C₃N₄ composites was measured by an Agilent 5100 ICP-OES.

The concentration of BP nanosheets in IPA dispersion and the content of BP in the composites were determined by an IRIS Intrepid II XSP ICP-OES (Thermal Scientific, USA).

2.7 Photoelectrochemical Measurements

Photoelectrochemical (PEC) properties were measured with a standard three electrode system in an electrochemical workstation (CHI 660E, CH Instruments). The working electrode was prepared by coating the as-synthesized sample on fluorine-doped tin oxide (FTO) glass with its boundaries being protected by Scotch tape. Specifically, 2 mg of powder sample was dispersed into 2 mL of DMF under sonication for 30 min to obtain evenly dispersed slurry, which was drop-casted onto the FTO glass. After drying under ambient condition, the epoxy resin glue was used to isolate the uncoated part of the FTO glass. A Pt wire and a Ag/AgCl electrode were used as the counter and reference electrode, respectively. The 0.2 M of Na₂SO₄ (pH = 6.8) aqueous solution pre-purged with nitrogen for 30 min was used as an electrolyte. A 300 W Xe lamp or a 150 W Newport solar simulator equipped with an AM1.5G filter (LCS-100, Newport) was utilized as the light source. Nyquist plots were recorded over the frequency range of 100 mHz to 100 kHz at a bias of 0.2 V.

2.8 Photocatalytic Activity Evaluation and Trapping Experiments

2.8.1 Photocatalytic degradation of MO by Au-NYF/g-C₃N₄

The evaluation of the photocatalytic activities of the x wt% Au-NYF/g-C₃N₄ was carried out in the photodegradation of MO. In a typical experiment, 10 mg of the x wt% Au-NYF/g-C₃N₄ photocatalyst was dispersed into 25 mL of MO solution (10 mg L⁻¹) in a 100 mL quartz reactor with circulating cooling water to keep the reaction temperature constant. Prior to illumination, the mixed suspension was magnetically stirred in the dark for 30 min to obtain the adsorption-desorption equilibrium. The UV photocatalysis experiment was performed using a commercial photoreactor (LUZ-4V, Luzchem), which was equipped with fourteen 8 W UV lamps (Luzchem LZC-UVA). Visible light with different wavelengths, $\lambda > 420$ nm and $\lambda > 475$ nm, was generated by applying appropriate long-pass optical filters onto a 300 W xenon lamp. A 980 nm diode laser was set at 2 W to work as the NIR light source. The simulated solar light photocatalysis reaction was carried out using a solar simulator (AM 1.5). After irradiation for various time intervals, 0.6 mL of MO solution was collected and centrifuged. The absorbance of MO in the supernatant was analyzed by UV-vis absorption spectrometry. Also, the precipitates after centrifugation were recovered, washed and dried, and re-used five times to test the photocatalytic stability of x wt% Au-NYF/g-C₃N₄.

2.8.2 Photocatalytic degradation of MO by PCZ QDs/g-C₃N₄

The photocatalytic activity of the PCZ QDs/g-C₃N₄ samples was evaluated for removal of MO in water. Photocatalysis was carried out in a 100 mL quartz reactor in the presence of 10 mg of the PCZ QDs/g-C₃N₄ and 25 mL of MO solution (10 mg L⁻¹). The reaction temperature was kept constant with circulating cooling water. Prior to irradiation, the suspension was stirred in the dark for 30 min to reach adsorption-desorption equilibrium between photocatalysts and MO. A commercial Luzchem LUZ-4V photoreactor equipped with fourteen 8 W LZC-UVA lamps was used for the UV photocatalytic experiment. A 300 W xenon lamp with long-pass optical filters was used for the photocatalysis under $\lambda > 420$ nm and $\lambda > 495$ nm irradiations. For the NIR photocatalysis, a 980 nm diode laser was set at 2 W to act as the NIR light source. For practical application, the photodegradation reaction was performed using a solar simulator (AM 1.5). The solution was irradiated with the above-mentioned light along with magnetic stirring. At different irradiation time points, 0.5 mL of aliquot was collected and centrifuged to separate the MO solution and photocatalysts. The MO residue in the supernatant was measured using a UV-vis spectrometry by following the absorbance at wavelength of 465 nm. After the simulated solar light

photocatalysis, QDs/g-C₃N₄ were recycled by centrifugation, and then washed and dried overnight. Five more runs of experiments were carried out in the presence of the recovered samples under identical conditions to test the stability.

2.8.3 Trapping experiments

To detect the involved active species in the photocatalytic removal of MO, trapping experiments were performed by using different scavengers. Specifically, t-BuOH (1 mM), BQ (1 mM), and Na₂EDTA (1 mM) served as scavengers to capture hydroxyl radical (\bullet OH), superoxide radical (\bullet O₂⁻), and hole, respectively, during the photocatalysis testing with all other conditions being identical.

2.8.4 Photocatalytic H₂ evolution by BP/g-C₃N₄

Photocatalytic H₂ evolution experiment was performed in a 500 mL Pyrex top-irradiation reactor with a quartz cover. A 300 W Xenon lamp equipped with cut-off filters (420 nm and 475 nm) was used to provide the irradiation source in the visible wavelength range. Typically, 10 mg of photocatalysts were dispersed in 100 mL of aqueous solution containing 10% of triethanolamine (TEOA) as sacrificial reagents. The mixture was deaerated by N₂ gas for 20 min and sonicated for 5 min. The system was sealed and vacuumed prior to photocatalysis. During the irradiation, the suspension was stirred continuously and kept at a constant temperature by circulating cooling water. The evolved H₂ was analyzed by a gas chromatography (GC, 7890B, Agilent Technologies) equipped with a thermal conductivity detector. For stability measurements, the photocatalysts were collected from the final reaction slurry by centrifugation, and then washed with ethanol and water thoroughly. Subsequently, the recycled sample underwent the photocatalytic H₂ evolution experiment under identical conditions and repeated for 5 cycles with a total irradiation time of 120 h.

2.9 Theoretical Calculations

Calculated absorption spectra (Figure 5.3f) were obtained by performing Many-Body Perturbation theory calculations (namely GW method and Bethe-Salpeter equation)³²⁴ on top of density functional theory (DFT) simulations.³²⁵ In the G₀W₀ simulations we used a cutoff of 40 Ry to expand the wavefunctions, 160 Ry to evaluate the difference between the exchange self-energy and exchange-correlation matrix elements $\langle \sum_x - V_{xc} \rangle$. For the screening term W and the correlation self-energy matrix elements $\langle \sum_c \rangle$ we performed careful convergence tests for the

monolayer finding that 12 Ry and 400 bands provide well converged gaps within 0.05 eV. We further checked that using lower convergence parameters, namely 6 Ry and 100 bands in G the gap correction reduces of about 0.1 eV. For the same system we verified that performing partial self-consistency in the Green Function as GW_0 scheme the gap increases of about 0.1 eV. In order to speed up the calculations we performed, for all the other systems, calculations using a cutoff of 6 Ry and $N_b = (N) \cdot 100$ (N number of layers) bands and avoiding self-consistency. We then added the estimated difference of 0.2 eV, after verifying that this value really occurs for the case of the bilayer. The convergence on k-points has been carefully checked both at GW and BSE level and a grid of $24 \times 21 \times 1$ is enough to converge both quantities within 0.1 eV. A box-like cutoff in the Coulomb potential, as implemented in the yambo code, has been used to avoid spurious interactions between the images and speed up the convergence with the vacuum size. The geometries of the layered structures have been obtained using norm conserving pseudopotentials³²⁶ and Perdew-Burke-Ernzerhof (PBE) exchange-correlation functional with Van der Waals correction,³²⁷ able to reproduce with very good accuracy the structural lattice parameters of bulk BP. The vacuum in the aperiodic direction has been selected to be larger than 15 Å for monolayer and bilayer and for all the other cases larger than the thickness of the few-layer phosphorene atomic structure.

3 PLASMON AND UPCONVERSION ENHANCED CARBON NITRIDE

High-Efficiency Broadband C₃N₄ Photocatalysts: Synergistic Effects from Upconversion and Plasmons

Photocatalyseur à large bande C₃N₄ à haute efficacité: effets synergiques de la conversion ascendante et des plasmons

Authors:

Qingzhe Zhang[†], Jiujun Deng[†], Zhenhe Xu^{*‡}, Mohamed Chaker[†], Dongling Ma^{*†}

[†] Institut National de la Recherche Scientifique (INRS), Centre Énergie Matériaux et Télécommunications, Université du Québec, 1650 Boulevard Lionel-Boulet, Varennes, Québec J3X 1S2, Canada

[‡] The Key Laboratory of Inorganic Molecule-Based Chemistry of Liaoning Province, College of Applied Chemistry, Shenyang University of Chemical Technology, Shenyang 110142, China

Publication:

ACS Catalysis

Publication Date: August 8, 2017

Volume 7, Issue 9, Pages 6225-6234

DOI: 10.1021/acscatal.7b02013

Contribution of authors:

Qingzhe Zhang, Dr. Zhenhe Xu (postdoctoral fellow, currently Prof. at Shenyang University of Chemical Technology, China) and Prof. Dongling Ma conceived and designed the research. Qingzhe Zhang prepared most of the samples with the training of Dr. Zhenhe Xu and conducted most of the characterizations, and all the photocatalysis reactions. Qingzhe Zhang carried out the photoelectrochemical measurements with the training of Dr. Jiujun Deng (postdoctoral fellow, currently Prof. at Jiangsu University, China). The TEM measurements were performed by Jean-Philippe Masse at Polytechnique Montréal. Prof. Mohamed Chaker and Prof. Dongling Ma supervised the experimental work. Qingzhe Zhang wrote the manuscript, which was carefully modified by Prof. Dongling Ma. Prof. Mohamed Chaker also gave good comments on revising the manuscript. All authors discussed the results and commented on the manuscript.

3.1 Introduction

Photocatalysis is considered to be one of the most promising technologies for tackling the energy crisis and environmental pollution by directly harvesting and utilizing the solar energy. Over the past decades, numerous semiconductor photocatalysts have been developed.^{98,328-332} However, there are still many challenges to address, such as a limited photoresponse range, the fast recombination of photo-induced charge carriers, high cost in materials, complicated or time-consuming preparation processes, and poor stability, *etc.*, which pose obstacles to the practical application of photocatalysts.^{328,333} The seeking of suitable photocatalysts to solve the above problems becomes one of the researchers' noble missions.

Recently, graphitic carbon nitride (g-C₃N₄) has gained extensive attention as a two dimensional (2D) π -conjugated photocatalyst with the merits of earth-abundance, visible-light response and high chemical inertness.^{102,142,334,335} Nevertheless, g-C₃N₄ still suffers from poor photocatalytic activity and low quantum efficiency due to the high recombination rate of photogenerated charge carriers.^{236,336,337} Moreover, the optical bandgap (2.7 eV) of g-C₃N₄ largely restrains the range of its visible light absorption to wavelengths shorter than 470 nm.^{236,338} Accordingly, the large portion of visible light, which accounts for ~43% of incoming solar energy, remains underutilized.³³⁹ To address the above-mentioned intrinsic drawbacks of g-C₃N₄, various strategies have been adopted for enhancing its photocatalytic performance and expanding its visible-light absorption towards longer wavelengths, including morphology modification,^{140,340,341} doping with metal^{232,236,342} or non-metal elements,³⁴³⁻³⁴⁵ and coupling with semiconductors to form heterojunctions.³⁴⁶⁻³⁴⁹

Plasmonic metallic nanostructures, for example Au and Ag nanoparticles (NPs), with unique size-tunable localized surface plasmon resonance (SPR) have been extensively investigated for combining with semiconductor photocatalysts towards achieving high-efficiency photocatalysis.^{44,199,232,236,350-354} In particular, Au nanostructures hold high promise, thanks to their strong visible-light absorption capability over a wide range and extremely high resistance to corrosion and oxidation under various conditions.²³⁶ In the case of Au/g-C₃N₄, the layered g-C₃N₄ can not only serve as the Au-supporting material, but also the acceptor of SPR excitation-generated hot electrons injected from Au NPs that initiate the photocatalytic reaction under visible light irradiation.³⁵⁵ Moreover, it has been demonstrated that Au NPs can act as sinks to capture electrons from the bandgap excitation of g-C₃N₄ under ultraviolet (UV) and visible light illumination.³⁵⁶ The electron transfer can extend the lifetime of photogenerated charge carriers

and effectively enhance the photocatalytic activity. Such plasmonic metal-semiconductor interactions strongly rely on the direct contact between Au NPs and g-C₃N₄. Nevertheless, in most of the cases, chemical synthesis yields Au NPs with organic ligands on the surface, which will suppress the transport of charge carriers that is detrimental to photocatalysis. In a previous study, we synthesized tiny Au NPs with “bare and clean” surfaces by using “Pulsed Laser Ablation in Liquid” (PLAL).^{145,357-359} These Au NPs free of any ligands exhibited much higher catalytic efficiency compared with those prepared chemically. Due to their “bare” surface, they are expected to form a physical barrier-free interface with g-C₃N₄, favoring the charge transfer process. The fascinating properties of PLAL generated Au NPs endow PLAL-Au/g-C₃N₄ huge potential for highly efficient photocatalysis,³⁶⁰ however, to the best of our knowledge, few efforts have been made in this field. Additionally, the exact mechanisms and processes in Au/g-C₃N₄ systems under separate UV and visible light illumination are still ambiguous. Therefore, it is of great significance to carry out systematic studies to understand the underlying pathways and explore critical parameters for the design of Au/g-C₃N₄ photocatalysts.

Nonetheless, in order to substantially utilize the solar energy, it is far from satisfactory to make photocatalysts only respond to UV and visible light, with the near-infrared (NIR) photons being wasted, which make up about 44% of the whole solar spectrum.³⁶¹ To date, only a few studies report on NIR photocatalysis. A promising type of luminescent materials, the lanthanide-ions-doped upconversion particles, can convert two or more NIR photons with lower energy to UV and visible emissions,^{145,362} which can subsequently be used to excite the Au NPs and g-C₃N₄, enabling the indirect utilization of the NIR photons for photocatalysis. Therefore, integrating plasmonic Au NPs, upconversion microspheres and g-C₃N₄ nanosheets into a single photocatalyst is of great potential in harvesting UV, visible and NIR light at the same time for efficient photocatalysis. To our knowledge, such a design strategy for the novel broadband photocatalyst has seldom been reported yet. Furthermore, in most of the published papers, upconversion particles were synthesized separately, and then combined with other semiconductors.^{145,161,180,363} This ex-situ synthesis method can be time-consuming, and usually requires extra surface modification steps for promoting coupling and thus is more complicated. It does not favor the close integration of the components in composite materials either.³⁶⁴

In the present study, we demonstrate for the first time a novel composite photocatalyst that includes three components: (1) the 2D g-C₃N₄ sheets with relatively narrow bandgap as the support and major photocatalyst, (2) the plasmonic Au NPs free of any organic ligands prepared by the PLAL method, (3) and the in-situ synthesized upconversion NaYF₄:Yb³⁺, Er³⁺, Tm³⁺ (NYF)

microspheres on the g-C₃N₄ nanosheets, which can convert the NIR photons to UV, blue and green emissions. The designed all-in-one photocatalysts, denoted herein as Au-NYF/g-C₃N₄, took full advantage of the plasmonic and upconversion effects for photocatalysis. In the photocatalytic degradation of methyl orange (MO), they exhibit not only significantly enhanced activity under the UV and visible light irradiation, but also possess superior NIR photocatalytic performance as compared to the reported performance in comparable systems. Furthermore, the charge transfer processes and mechanisms for enhanced photocatalytic activity were thoroughly investigated and discussed, and found to be different under UV, visible or NIR illuminations. The present work provides an innovative solution for designing broadband photocatalysts to make good use of solar photons, and contributes to the mechanistic understanding of the plasmon and upconversion enhanced photocatalysis as well.

3.2 Experimental Section

3.2.1 Materials

Au target (99.99%, diameter × thickness: 8 mm × 1.5 mm), sodium hydroxyl (NaOH), nitric acid (HNO₃), Urea (NH₂CONH₂), rare-earth nitrate hydrate (Y(NO₃)₃·6H₂O, Yb(NO₃)₃·5H₂O, Er(NO₃)₃·5H₂O, Tm(NO₃)₃·5H₂O; 99.9 wt%), sodium fluoride (NaF) and MO, 1,4-benzoquinone (BQ), disodium ethylenediaminetetraacetate (Na₂EDTA), and tert-butyl alcohol (t-BuOH) were purchased from Sigma-Aldrich and used without further purification. The absolute pure water, purified by a Millipore Ultrapure water system and having a resistivity of 18.2 MΩ cm at 25 °C, was used in the current investigation.

3.2.2 Preparation of Au NP colloids

The Au NP colloids were prepared by using the PLAL technique. A KrF excimer laser (GSI Lumonics PM-846, λ: 248 nm; pulse width: 25 ns; repetition rate: 20 Hz) was employed for laser ablation. The Au target was fixed at the bottom of a glass vessel filled with 5 mL of NaOH solution (pH ≈ 9.5). The beam was focused onto the Au target by an objective lens with 7.5 cm focal length. The depth of the NaOH solution layer above the target was about 10 mm. Laser fluence on the target was set to a constant value (~40.0 J cm⁻²). The concentration of the as-prepared Au NP colloids was 50 ppm based on the neutron activation analysis (NAA) measurements.

3.2.3 Preparation of g-C₃N₄

For the synthesis of g-C₃N₄, urea (30 g) was placed into a covered alumina crucible, and then heated in a quartz tube furnace with a heating rate of 2 °C min⁻¹ to 250 °C, 350 °C, and 550 °C, and maintained at these three target temperatures for 1h, 2h and 2 h, respectively. After being naturally cooled down to room temperature, the yellow powder was collected and washed for three times with HNO₃ (0.1 mol L⁻¹) and water to remove potential alkaline residue (e.g. ammonia). After centrifugation, the precipitate was dried in the vacuum at 80 °C overnight.

3.2.4 In-situ synthesis of NYF/g-C₃N₄ composites

NYF microspheres were synthesized and anchored onto the g-C₃N₄ nanosheets in a single step via in-situ synthesis of NYF microspheres in the presence of g-C₃N₄. Typically, 0.60 g of the obtained g-C₃N₄ was dispersed into 60 mL of water by ultrasonication for 12 h. Then 3.133 mL of Y(NO₃)₃ (0.5 M), 0.801 mL of Yb(NO₃)₃ (0.5 M), 1.000 mL of Tm(NO₃)₃ (0.01 M), and 0.203 mL of Er(NO₃)₃ (0.01 M) solutions were added to the above g-C₃N₄ dispersion and the mixture was further magnetically stirred for 2 h. Subsequently, 0.30 g of NaF was introduced into the solution. After stirring for 1h, the reaction mixture was transferred into a 100 mL Teflon-lined stainless steel autoclave and subjected to heating for 12 h at 180 °C. After the autoclave was cooled down naturally to room temperature, the product was washed three times with pure water and ethanol in sequence. The purified precipitate was then dried at 80 °C in an oven for 12h to obtain the composite of NYF microsphere loaded g-C₃N₄ nanosheets.

3.2.5 Preparation of Au NP loaded NYF/g-C₃N₄ photocatalysts

A certain amount of the freshly prepared Au NP colloid was added to 10 mg of NYF/g-C₃N₄ and mixed by shaking. After being incubated for ~30 min at room temperature, the precipitate from the mixture solution was collected by centrifugation, followed by washing with pure water. By adding different volumes of Au NP solution, the Au-NYF/g-C₃N₄ photocatalysts with different loading levels of Au NPs were prepared. The mass fraction of Au NPs in the Au-NYF/g-C₃N₄ photocatalysts was denoted as *x wt%* (*x*=1, 2, 3, 4 and 5).

3.2.6 Photocatalytic experiment and the detection of active species

The evaluation of the photocatalytic activities of the *x wt%* Au-NYF/g-C₃N₄ was carried out in the photodegradation of MO. In a typical experiment, 10 mg of the *x wt%* Au-NYF/g-C₃N₄ photocatalyst was dispersed into 25 mL of MO solution (10 mg L⁻¹) in a 100 mL quartz reactor

with circulating cooling water to keep the reaction temperature constant. Prior to illumination, the mixed suspension was magnetically stirred in the dark for 30 min to obtain the adsorption-desorption equilibrium. The UV photocatalysis experiment was performed using a commercial photoreactor (LUZ-4V, Luzchem), which was equipped with fourteen 8 W UV lamps (Luzchem LZC-UVA). Visible light with different wavelengths, $\lambda > 420$ nm and $\lambda > 475$ nm, was generated by applying appropriate long-pass optical filters onto a 300 W xenon lamp. A 980 nm diode laser was set at 2 W to work as the NIR light source. The simulated solar light photocatalysis reaction was carried out using a solar simulator (AM 1.5). After irradiation for various time intervals, 0.6 mL of MO solution was collected and centrifuged. The absorbance of MO in the supernatant was analyzed by UV-vis absorption spectrometry. Also, the precipitates after centrifugation were recovered, washed and dried, and re-used five times to test the photocatalytic stability of x wt% Au-NYF/g-C₃N₄. To study the MO degradation kinetics in the presence of x wt% Au-NYF/g-C₃N₄, the apparent reaction rate constant (k) was calculated by using the following first-order reaction model (Equation (3)). The normalized reaction rate constant was calculated by normalizing k with the total mass of catalysts.

$$\ln\left(\frac{c_0}{c}\right) = kt \quad (3)$$

Where c_0 is the initial concentration of MO solution

c is the concentration of MO solution at time t

The normalized reaction rate constant was calculated by normalizing k with the total mass of catalysts.

In addition, in order to detect the generated active species in the photocatalysis, BQ (1 mM), Na₂EDTA (1 mM) and t-BuOH (1 mM) were used as superoxide radical ($\bullet\text{O}_2^-$), hole and hydroxyl radical ($\bullet\text{OH}$) scavengers, respectively, during the photocatalysis testing with all other conditions being the same.

3.2.7 Characterization

The microstructure and composition of the photocatalysts were studied by a transmission electron microscope (TEM, JEOL 2100F, operated at 200 kV), equipped with an energy-dispersive X-ray (EDX) spectrometer. The crystal structures of all the samples were analyzed by the x-ray diffraction instrument (XRD, PANalytical X'Pert MRD) with a Cu K α radiation source ($\lambda = 0.15406$ nm) operated at 45 kV and 40 mA. The UV-vis-NIR absorption spectra of samples and the absorbance of MO in aqueous solutions were measured using a Varian Cary 5000 scan

spectrometer. NAA measurements were performed using a SLOWPOKE nuclear reactor to determine the concentration of Au NPs in colloids, and the weight content of Au, Er, Tm and NYF in Au-NYF/g-C₃N₄ samples. The upconversion luminescence spectra were obtained by using a Thorlabs fiber-coupled laser diode (maximum power: 330 mW) as the 980 nm excitation light source. The laser was focused on the powder to obtain a spot (0.4 mm in diameter) with a Gaussian distribution of intensity. The emission was collected at 90° from the incident beam, and then transferred and recorded on a spectrophotometer (Avaspec-2048L-USB2). All the measurements were performed under ambient conditions. The photoelectrochemical (PEC) measurements were performed with an electrochemical workstation (CHI 660E, CH Instruments) in a standard three electrodes cell, using a Pt wire and a Ag/AgCl electrode (3 M KCl) as the counter and reference electrode, respectively. The working electrode was prepared on fluorine-doped tin oxide (FTO) glass with its boundary being protected by Scotch tape. Five milligrams of as-synthesized powder was dispersed into 1 mL of dimethylformamide under sonication for 30 min to get a colloidal dispersion. The dispersion was drop-casted onto the FTO glass. After natural air drying, the uncoated part of the FTO glass was isolated with epoxy resin glue. The 0.2 M of Na₂SO₄ (pH = 6.8) aqueous solution pre-purged with nitrogen for 30 min was used as an electrolyte. A 300 W Xe lamp was utilized as a light source for the measurements. Nyquist plots were recorded over the frequency range of 100 mHz to 100 kHz at a bias of 0.2 V.

3.3 Results and Discussions

3.3.1 Structural and morphological characterization

The *x wt%* Au-NYF/g-C₃N₄ (*x*=0, 1, 2, 3, 4 and 5) photocatalysts were thoroughly characterized by various instruments. All of the samples show the similar structure and morphology. Herein the 1 *wt%* Au-NYF/g-C₃N₄ sample is used as an example to demonstrate the typical microstructure and morphology.

The morphology and structure of PLAL generated Au NPs, g-C₃N₄ nanosheets and Au-NYF/g-C₃N₄ photocatalysts were investigated by TEM (Figure 3.1). As shown in Figure 3.1a and its inset, the Au NPs prepared by the PLAL method are individually dispersed on the TEM grid without any obvious agglomeration and have a uniform size of about 5 nm in diameter. The as-synthesized g-C₃N₄ nanosheets reveal wrinkled laminar morphology like a silk veil (Figure 3.1b). The appearance of the thin nanosheets is quite similar to that of graphene or graphene oxide. For the Au-NYF/g-C₃N₄ sample, the g-C₃N₄ nanosheets serve as the support of NYF microspheres and Au NPs, and are capable of retaining their initial morphology when introducing these two

components (Figure 3.1c and 3.1d). The elements of C, N, F, Na, Yb, Y and Au were observed in the EDX spectrum (Figure 3.1e) of the Au-NYF/g-C₃N₄ sample, which supports the co-existence of the major elements of NYF and Au; the absence of Er and Tm signal is due to their low concentrations below the limit of detection of the EDX system. It can be easily seen that the NYF microspheres and the small Au NPs are dispersed on the surface of the nanosheets uniformly, which can facilitate the utilization of light by all the three components. In addition, as shown in the TEM image, the in-situ synthesized NYF microspheres are all anchored on the g-C₃N₄ nanosheets; no un-coupled NYF microspheres were observed. The size and morphology of NYF microspheres are similar to that of the microspheres synthesized in the absence of g-C₃N₄.¹⁴⁵ Furthermore, according to the NAA analysis, the weight content of NYF in the NYF/g-C₃N₄ sample is about 36.17 wt %, which is quite close to the nominal value of 37.88 wt %. These results underline the advantages of the in-situ synthesis of NYF on g-C₃N₄: high synthesis yield of NYF and remarkable coupling efficiency between NYF on g-C₃N₄. The measured values of Tm and Er are 0.16 wt% and 0.03 wt%, respectively, which are very close to the nominal concentration of 0.1726 wt% and 0.0347 wt%.

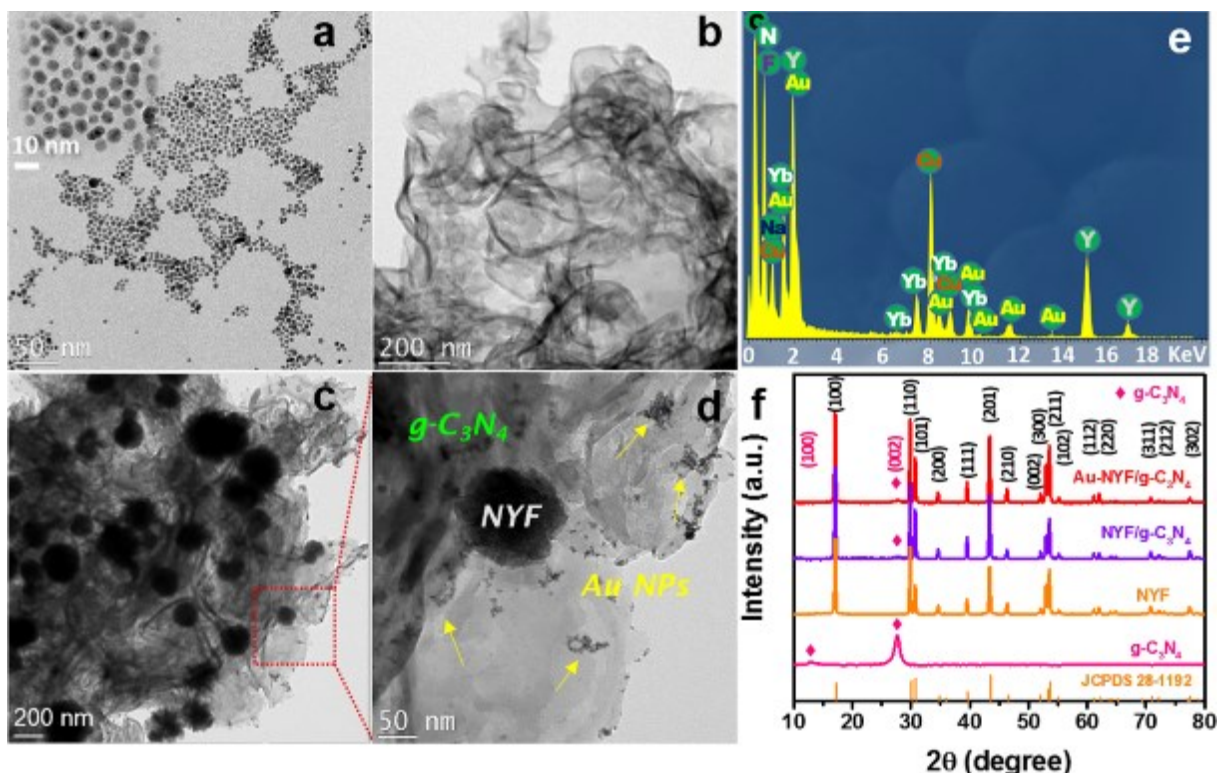


Figure 3.1 TEM images of (a) Au NPs, (b) g-C₃N₄ nanosheets, (c) 1 wt% Au-NYF/g-C₃N₄ photocatalysts, (d) the enlarged view and (e) the EDX spectrum of the rectangle area in (c). The inset in (a) is the high magnification TEM image of Au NPs. (f) XRD patterns of g-C₃N₄, NYF, NYF/g-C₃N₄ and 1 wt% Au-NYF/g-C₃N₄ samples. The corresponding standard data for the β -NaYF₄ phase (JCPDS 28-1192) is also given at the bottom.

The crystal structure of as-prepared g-C₃N₄, NYF, NYF/g-C₃N₄ and 1 wt% Au-NYF/g-C₃N₄ was analyzed by XRD (Figure 3.1f). The g-C₃N₄ shows two prominent peaks in its XRD pattern at 13.1° and 27.4°, suggesting the presence of phase pure g-C₃N₄ layered structure.^{102,365} The peak at 13.1° corresponds to the (100) plane and stems from the in-plane structural packing motif (tri-s-triazine units) with a repeating period of 0.675 nm.^{355,366} The dominant peak at 27.7°, assigned to the (002) plane in graphitic materials, is a diffraction feature of interplanar stacking of the conjugated aromatic system.^{111,140} In the XRD patterns of the NYF, NYF/g-C₃N₄ and 1 wt% Au-NYF/g-C₃N₄ samples, multiple distinctive peaks indexed to the hexagonal β-NaYF₄ (JCPDS 016-334) were observed. The involvement of C₃N₄ during the synthesis of NYF microspheres does not seem affecting the crystalline phase of NYF. On the other hand, the weak peak at 27.7° ascribed to the g-C₃N₄ structure also appears in NYF/g-C₃N₄ and 1 wt% Au-NYF/g-C₃N₄, confirming that the graphitic phase of C₃N₄ remains unchanged after the in-situ formation of NYF microspheres via the hydrothermal process and the subsequent loading of Au NPs. For the 1 wt% Au-NYF/g-C₃N₄ photocatalyst, it is difficult to identify metallic Au by XRD analysis because of the overlap of the Au and NYF diffraction peaks, and of the low content of Au NPs in the composite.

3.3.2 Optical properties

For the comparison of optical properties, the UV-vis-NIR absorption spectra of g-C₃N₄, NYF, NYF/g-C₃N₄ and 1 wt% Au-NYF/g-C₃N₄ photocatalysts were recorded as presented in Figure 3.2a. In the UV-vis region, the typical absorption feature of g-C₃N₄ with an absorption edge at 460 nm is observed in all the samples involving g-C₃N₄. It corresponds to the electron excitation from the valence band (VB) to the conduction band (CB) of g-C₃N₄ which represents a bandgap energy of ~2.7 eV.^{115,342} The NYF microspheres present no absorption in this region, but a distinctive absorption band is observed in the NIR region at about 980 nm, which is caused by the ²F_{7/2} → ²F_{5/2} transition of the dopant Yb³⁺ ions in the NaYF₄ host.³⁶⁷ Since NYF/g-C₃N₄ and 1 wt% Au-NYF/g-C₃N₄ share the same dopants with NYF, they both exhibit the similar absorption band in the range from 900 to 1000 nm. After the 1 wt% Au NP loading, an additional shoulder peak apparently appears around 550 nm in the absorption spectrum, which can be mainly attributed to the SPR excitation of Au NPs. Compared with the resonance peak (around 520 nm) of pure Au NPs dispersed in water, a redshift of about 30 nm is possibly due to the formation of Au NP agglomerates and/or to the higher refractive index of the neighbouring g-C₃N₄ (~1.8).^{368,369} In the latter case, this shift would indicate the close contact between the Au NPs and the g-C₃N₄ nanosheets in the 1 wt% Au-NYF/g-C₃N₄ photocatalyst.

As aforementioned, the NYF microspheres were employed to upconvert the NIR photons from the 980 nm laser into higher energy emissions in the UV and visible ranges, via successive energy transfer processes.^{180,370} In order to investigate whether these emissions are capable of exciting the g-C₃N₄ and Au NPs, the photoluminescence spectra of as-synthesized NYF, NYF/g-C₃N₄ and 1 wt% Au-NYF/g-C₃N₄ were measured under the excitation of the 980 nm laser (Figure 3.2b). The photoluminescence spectrum of NYF microspheres shows two green-emission peaks centered at 521 and 540 nm, two blue-emission peaks at 477 and 451 nm, and two peaks at 361 and 345 nm in the UV region, corresponding to the transitions of $^2H_{11/2} \rightarrow ^4I_{15/2}$, $^4S_{3/2} \rightarrow ^4I_{15/2}$, $^1G_4 \rightarrow ^3H_6$, $^1D_2 \rightarrow ^3F_4$, $^1D_2 \rightarrow ^3H_6$, and $^1I_6 \rightarrow ^3F_4$, respectively. According to the analysis of the absorption spectra (Figure 3.2a), the green and blue emission can be reabsorbed by the Au NPs due to SPR excitation and/or interband absorption; the blue and UV emissions will be mainly absorbed by g-C₃N₄. The calculated intensity ratio of the UV plus blue emissions (the four peaks centered at 477, 451, 361 and 345 nm) to green emissions decreases from 3.3 of NYF to 1.4 of NYF/g-C₃N₄, which indicates that the converted emissions are absorbed by the g-C₃N₄ in the NYF/g-C₃N₄ sample, verifying the energy transfer from the NYF microspheres to g-C₃N₄ nanosheets. After the loading of Au NPs, the intensity ratios of blue-to-green emissions are increased from 1.3 for the NYF/g-C₃N₄ to 2.7 for 1 wt% Au-NYF/g-C₃N₄ due to the SPR excitation of Au NPs. Therefore, the subtly designed Au-NYF/g-C₃N₄ photocatalyst achieved the indirect utilization of NIR photons by upconverting them into UV and visible light. The upconverted emissions efficiently reabsorbed by g-C₃N₄ and Au NPs are beneficial to photocatalysis to be discussed later in the text.

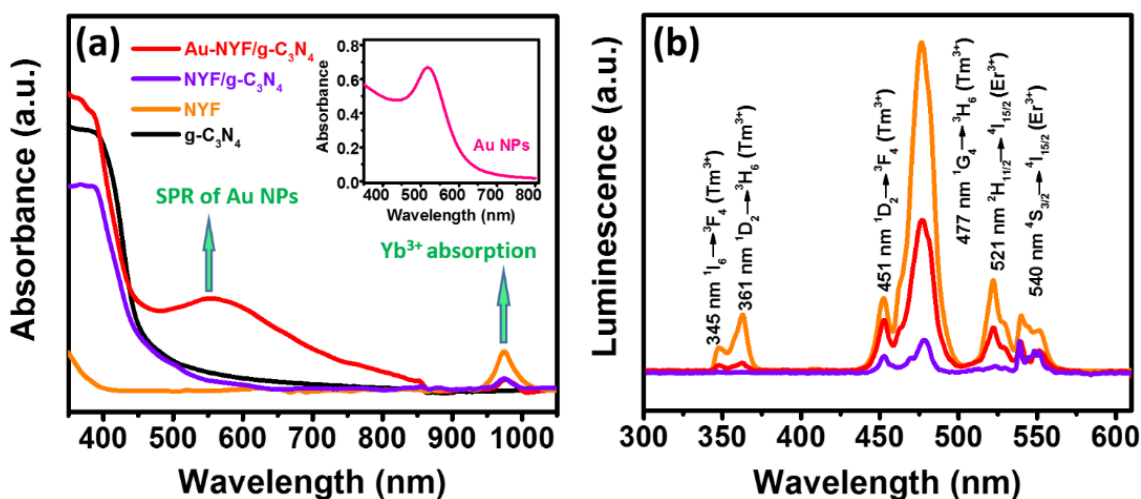


Figure 3.2 (a) UV-vis-NIR absorption spectra and (b) upconversion photoluminescence spectra of the obtained samples. The inset in (a) is the absorption spectrum of Au NPs in water.

3.3.3 Photocatalytic activities

The photocatalytic activities of x wt% Au-NYF/g-C₃N₄ were evaluated by monitoring the degradation of MO under UV, visible ($\lambda > 420$ nm and $\lambda > 475$ nm), NIR and simulated solar light irradiation (Figures 3.3-4, Figures S3.1-S3.3 in Supporting Information). As the Au NP loading is an important factor in achieving high photocatalytic activity, the dependence of the degradation of MO on photocatalysts loaded with varying Au NP amount (0-5 wt%) was studied systematically. As shown in the absorption spectra of MO over 1 wt% Au-NYF/g-C₃N₄ (Figure 3.3a, Figure S3.1a, S3.2a and S3.3a in Supporting Information), after reaching the absorption-desorption equilibrium, the intensities of characteristic peak of MO, positioning at ~ 465 nm, are still relatively high. With the increase of light irradiation time, the intensities steadily decrease, reflecting that MO in solution is degraded gradually. The control experiments which were performed only in the presence of light or photocatalysts showed almost no change in the absorption spectra of MO (Figure S3.4 and S3.5 in Supporting Information). In addition, no significant degradation of MO is observed in the sole presence of Au NPs or NYF under visible light and the 980 nm laser irradiation, respectively, suggesting that the SPR excitation in Au NPs and the upconversion in NYF cannot directly trigger the photocatalytic reaction. These observations confirmed the pivotal role of the g-C₃N₄ photocatalyst in the photocatalytic degradation of MO.

Under UV light illumination, all the Au NP loaded samples exhibit higher photocatalytic activity than the NYF/g-C₃N₄ photocatalyst (Figure 3.3b). Figure 3.3c shows the kinetic study of MO degradation over x wt% Au-NYF/g-C₃N₄. The rate constant calculated from the first-order reaction model follows the order: 1 wt% Au-NYF/g-C₃N₄ > 2 wt% Au-NYF/g-C₃N₄ > 3 wt% Au-NYF/g-C₃N₄ > 4 wt% Au-NYF/g-C₃N₄ > 5 wt% Au-NYF/g-C₃N₄ > NYF/g-C₃N₄ (inset in Figure 3.3c). The highest normalized reaction rate constant ($8.74 \times 10^{-4} \text{ min}^{-1} \text{ mg}^{-1}$) achieved by 1 wt% Au-NYF/g-C₃N₄ is 3.1 times higher than that ($2.78 \times 10^{-4} \text{ min}^{-1} \text{ mg}^{-1}$) by NYF/g-C₃N₄. As the UV light exposure cannot lead to the SPR excitation of Au NPs, the enhanced UV light activity was not induced by the plasmonic effect of Au NPs. It was reported that the UV light-excited electrons can be transferred from the CB of g-C₃N₄ to the Au NPs, leading to the decreased recombination rate of the charge carriers to improve the photocatalytic activity.²³⁰ However, further Au NP loading (> 1 wt%) causes the reduction in the photocatalytic activity, which is attributed to the introduced interface defects and to the competition between the g-C₃N₄ and the loaded Au NPs in utilizing incident light due to the interband absorption of Au NPs.^{369,371}

When the reaction system is exposed to visible light ($\lambda > 420$ nm), the photodegradation processes become more complicated. According to the UV-vis-NIR diffuse reflectance spectra,

the bandgap excitation of g-C₃N₄ and the SPR excitation of Au NPs take place under $\lambda > 420$ nm irradiation. The loading of Au NPs greatly improves the photocatalytic degradation rate of MO (Figure S3.1b in Supporting Information), with the normalized reaction rate being increased from 0.032 h⁻¹ mg⁻¹ of the NYF/g-C₃N₄ to 0.009 h⁻¹ mg⁻¹ of the 1 wt% Au-NYF/g-C₃N₄ (Figure 3.3d). The reaction rate decays with further Au loading to over 1 wt%, but all the Au loaded samples have higher *k* values than the NYF/g-C₃N₄ photocatalyst. The SPR excitation of Au NPs under visible light irradiation leads to the generation of energetic electrons that are capable of injecting to the g-C₃N₄ photocatalyst to participate in the photocatalysis. At the same time, the electrons in the VB of g-C₃N₄ are excited to the CB and then, in principle, can be transferred to the Au NPs. It is challenging to unravel the exact contribution from each individual process to the photocatalysis. In order to elucidate the important effect of SPR excitation of Au NPs on the photocatalytic degradation, the light with $\lambda < 475$ nm was cut off to completely rule out the bandgap excitation of g-C₃N₄. As shown in Figure S3.2b, the photocatalytic activity of NYF/g-C₃N₄ free of Au NPs in the degradation of MO is quite poor. After integrating with Au NPs, a significant enhancement of the photodegradation rate of MO is observed in *x* wt% Au-NYF/g-C₃N₄ photocatalysts. These results confirm the important role of the SPR effect of the Au NPs in improving the visible-light-driven photocatalytic performance. In principle, the reaction rate will be increased with increasing Au loading, however as a matter of fact the 1 wt% Au loaded sample was found to display the highest *k* value, which is about 6.2 times larger than that of NYF/g-C₃N₄ (Figure 3.3e). The defects introduced by excessive Au NPs at the interface between Au NPs and g-C₃N₄ can act as the recombination centers for charge carriers,^{369,371} which is accounted for the presence of the optimal Au loading amount.

Figure S3.3b shows the photocatalytic degradation of MO over Au-NYF/g-C₃N₄ photocatalysts under NIR light illumination. The concentration reduction of MO with time is clear over all the as-prepared samples. As the Au NPs and g-C₃N₄ cannot be directly excited by the NIR light, these observations reveal the significant role that upconversion materials play in the photodegradation of MO under NIR light irradiation. As demonstrated in the section of optical properties and Figure 3.2b, the NaYF₄ co-doped with Yb³⁺, Tm³⁺ and Er³⁺ ions create strong upconverted emissions in the UV and visible regions, which are expected to be reabsorbed by the g-C₃N₄ nanosheets and Au NPs owing to their bandgap and SPR excitations, respectively. The bandgap excitation of g-C₃N₄ for photocatalysis is straightforwardly evidenced by the degradation of MO over NYF/g-C₃N₄ under the NIR illumination. Furthermore, the excitation of Au SPR effect is induced by the upconverted emission in visible range. As shown in Figure S3.3b, the loading of Au NPs greatly enhances the NIR photocatalytic activity and the 2 wt% Au-NYF/g-C₃N₄ shows the highest

degradation rate of $0.1612 \text{ mg}^{-1} \text{ L}^{-1} \text{ h}^{-1}$, which is over 6 times higher than the largest value ($0.0267 \text{ mg}^{-1} \text{ L}^{-1} \text{ h}^{-1}$) ever reported for NIR-driven photocatalysis based on our extensive literature search.³⁷² Furthermore, the highest normalized reaction rate constant ($0.0035 \text{ h}^{-1} \text{ mg}^{-1}$), also obtained by the 2 wt% Au-NYF/g-C₃N₄ photocatalyst (Figure 3.3f), is about 6.4 times higher than that of the reported highest one ($0.00055 \text{ h}^{-1} \text{ mg}^{-1}$).³⁷³ It has to be pointed out that as the reports on NIR photocatalysis are limited, it is difficult to identify a significant number of proper systems in the literature for comparison, which is further complicated by different experimental conditions. It is observed that the degradation rate and the k value decrease with increasing Au NP loading from 2-5 wt%, and that the 5 wt% Au loaded sample even shows poorer activity than the Au NP-free sample. As aforementioned, the introduction of Au NPs is a double-edged sword. The competition between the positive plasmonic effect and the negative effect resulting from interface defect and reduced light penetration yields an optimal amount of Au loading of 2 wt%.

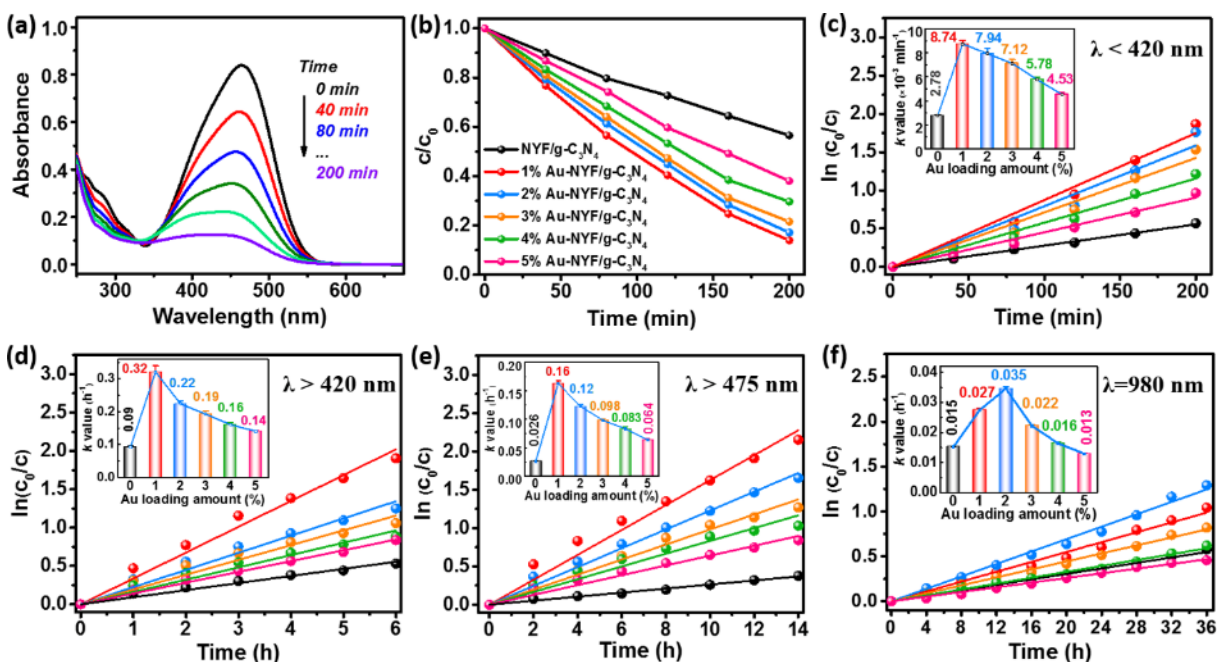


Figure 3.3 Time-dependent UV-vis absorption spectra for the photocatalytic degradation of MO over 1 wt% Au-NYF/g-C₃N₄ (a) and the plot of (c/c_0) vs reaction time (b) under UV light irradiation. The plot of $\ln(c_0/c)$ vs reaction time (c, d, e, f) for the photocatalytic degradation of MO over x wt% Au-NYF/g-C₃N₄ (x=0, 1, 2, 3, 4 and 5) photocatalysts, under UV light (c), $\lambda > 420 \text{ nm}$ (d), $\lambda > 475 \text{ nm}$ (e), and the NIR light (f) irradiation. The insets in (c, d, e, f) are the apparent rate constants (k value) vs Au loading.

The ultimate goal of our research is to use solar energy in photocatalysis to tackle environmental and energy issues. Hence, the photocatalytic performance of the as-prepared photocatalysts was investigated under simulated solar light (Figure 3.4a-3.4c). In this case, the bandgap excitation of g-C₃N₄, the SPR excitation of Au NPs and the upconversion of NYF microspheres coexist in the

same system. The combined effect of these three processes leads to significantly improved performance of Au-NYF/g-C₃N₄ with respect to plain g-C₃N₄ under the otherwise same conditions. The sample with 1 wt% Au loading gains a maximum degradation percentage of 83% (Figure 3.4a) and a normalized reaction rate constant of 0.0035 h⁻¹ mg⁻¹ (Figure 3.4b). The small loading amount (1 wt%) of the Au NPs required for achieving the optimal photocatalytic performance is of practical significance in terms of economic cost. In addition, the as-prepared photocatalysts were proven to possess excellent stability in the photocatalytic degradation of MO. After conducting five successive runs under simulated solar light illumination, almost no activity change is found for the Au-NYF/g-C₃N₄ photocatalyst, and the percentage of degradation of MO over 1 wt% Au-NYF/g-C₃N₄ still remains as high as 81% (Figure 3.4c). The high performance, low Au loading together with the high stability of the as synthesized photocatalysts under solar light are beneficial to the large-scale application of photocatalysis in the environmental pollution remediation by using abundant solar energy.

3.3.4 Detection of active species and relevant mechanisms

The dramatically increased photocatalytic properties of as-prepared Au-NYF/g-C₃N₄ photocatalysts with respect to the plain g-C₃N₄ photocatalyst motivated us to further elucidate the processes involved in the degradation of MO. It is expected that the active species, such as photogenerated holes, superoxide radicals ($\bullet\text{O}_2^-$) and hydroxyl radicals ($\bullet\text{OH}$), are likely to be actively involved in the photocatalytic degradation of organic molecules.^{348,374} Accordingly, the trapping experiments in the presence of three different types of scavengers, BQ, t-BuOH and Na₂EDTA, were designed to identify the active species involved in this reaction system (Figure 3.4d). The slight suppression in the degradation of MO is observed by the addition of the hole scavenger, Na₂EDTA (1 mM).^{235,375} While in the presence of the $\bullet\text{O}_2^-$ radical scavenger, BQ (1 mM), and $\bullet\text{OH}$ radical scavenger, t-BuOH (1 mM),^{361,362} the photocatalytic reaction was obviously retarded, with the photocatalytic degradation rate being reduced by 67.2% and 37.1%, respectively, after 7 h of simulated solar light exposure. Apparently, the $\bullet\text{O}_2^-$ and $\bullet\text{OH}$ radicals play more important roles than the holes in the photocatalytic degradation of MO.

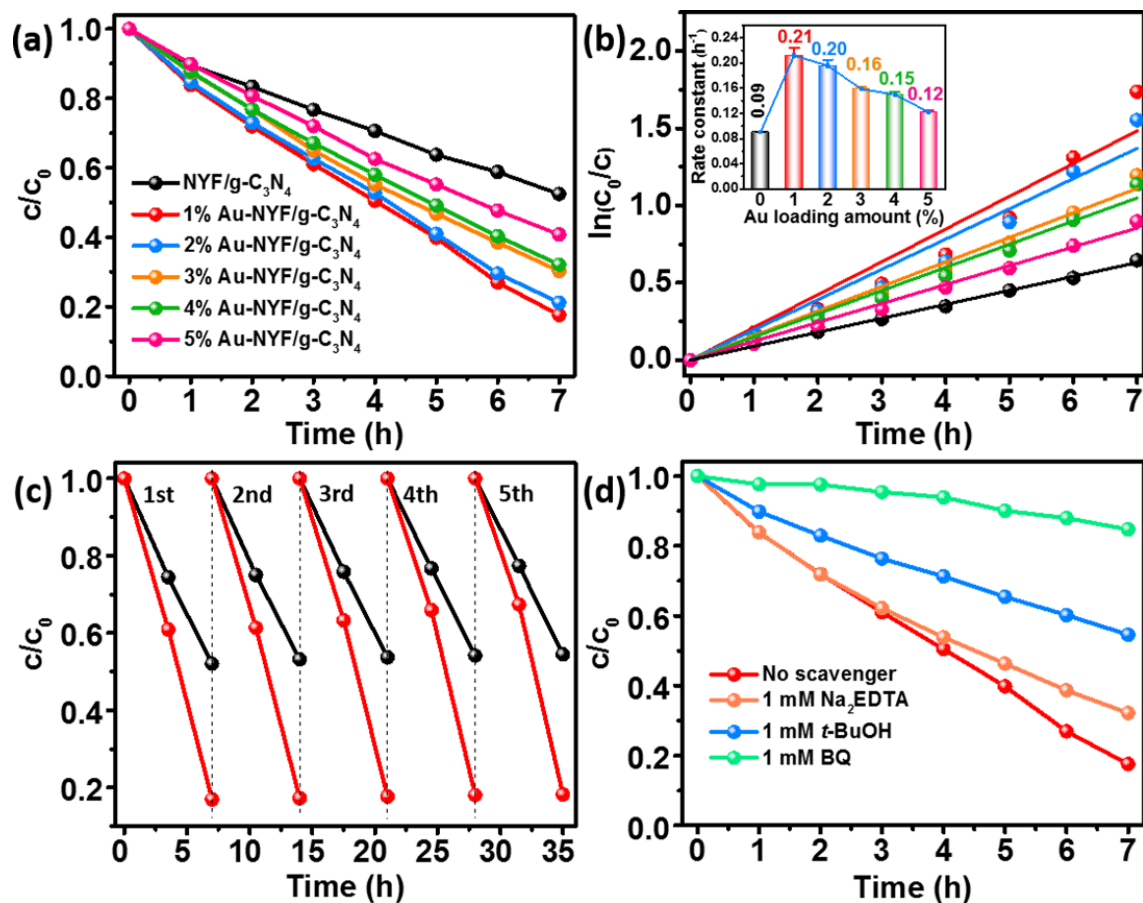


Figure 3.4 (a) Photocatalytic degradation of MO and (b) the kinetics study over different photocatalysts under simulated solar light illumination. The inset in (b) shows the rate constants vs Au loading. (c) Photocatalytic stability of 1 wt% Au-NYF/g-C₃N₄ photocatalyst in five successive cycling reactions. The duration of simulated solar light exposure in each cycle is 7 h. (d) Photocatalytic degradation of MO in the presence of three types of scavengers and 1 wt% Au-NYF/g-C₃N₄ photocatalyst under simulated solar light irradiation.

Photoelectrochemical (PEC) measurements, including electrochemical impedance spectroscopy (EIS) and transient photocurrent responses, of NYF/g-C₃N₄ and 1 wt% Au-NYF/g-C₃N₄ samples are shown in Figure 3.5. The high frequency region of Nyquist plots, which can provide useful information on charge transfer resistance, are displayed in Figure 3.5a. The arc radius on the EIS Nyquist plots of the 1 wt% Au-NYF/g-C₃N₄ is smaller than that of NYF/g-C₃N₄ both in the dark and under irradiation, indicating that the loading of Au NPs can reduce the charge transfer resistance and thus accelerate the interfacial charge transfer.^{341,347,376} This represents another beneficial effect of the Au NPs on the photocatalysis. Additionally, the transient photocurrent measurements were carried out during light on-off cycles (Figure 3.5b), to further assess the charge carrier generation and transfer performance in the reaction system. The saturation photocurrent densities remain constant with light on, and immediately drops to nearly zero once the light is switched off. The photocurrent density over 1 wt% Au-NYF/g-C₃N₄ (~6.36 $\mu\text{A cm}^{-2}$) is about 5.5 times higher

than that of the NYF/g-C₃N₄ sample (~1.15 μA cm⁻²). The increased photocurrent confirms that the incorporation of Au NPs could facilitate the separation and prolong the lifetime of the photoinduced charge carriers,³⁴¹ and improve the visible light absorption due to SPR, which are all responsible for the enhanced photocatalytic activity in MO degradation. Moreover, the almost unchanged photocurrent response during repeated light on-off cycles is another evidence of the excellent stability of the as-prepared NYF/g-C₃N₄ and Au-NYF/g-C₃N₄ photocatalysts.

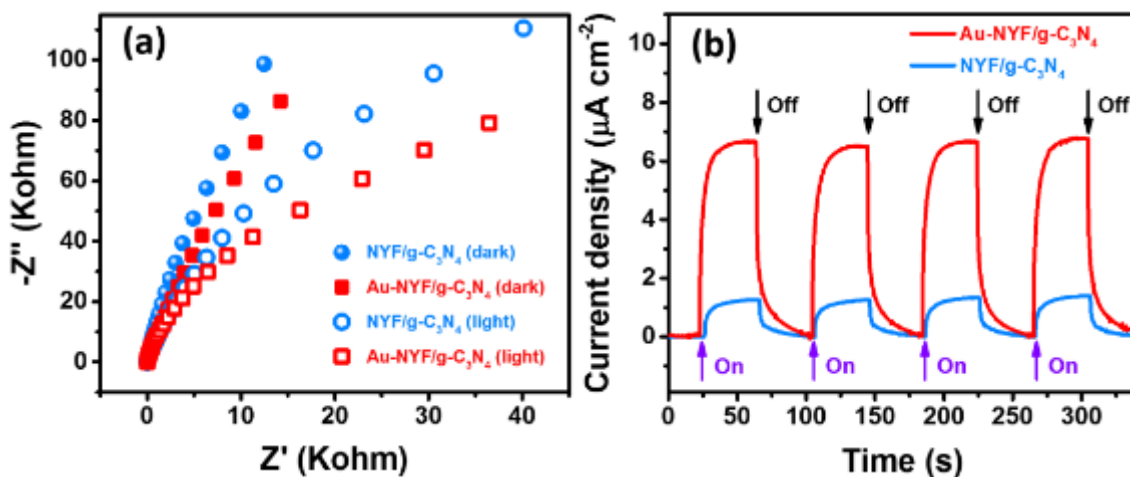


Figure 3.5 (a) EIS Nyquist plots of NYF/g-C₃N₄ and 1 wt% Au-NYF/g-C₃N₄ in the dark and under illumination; (b) transient photocurrent density response of NYF/g-C₃N₄ and 1 wt% Au-NYF/g-C₃N₄ during on/off cycles under a 0.2 V bias versus Ag/AgCl.

On the basis of the structural and optical characterizations, as well as the photocatalytic activities, different pathways could be involved in the photocatalytic degradation of MO over Au-NYF/g-C₃N₄ photocatalysts under different light irradiations. For better understanding the underlying mechanisms, a possible schematic for the charge transfer processes is depicted in Figure 3.6. Under UV light illumination (Figure 3.6a), the electrons in the VB of g-C₃N₄ can be excited to the CB, simultaneously leaving behind the positively charged holes in the VB. The Au NPs in close contact can act as an electron reservoir due to their more negative work function than the CB level of g-C₃N₄, and favor the electron transfer from the VB of g-C₃N₄ to the Au NP surface.^{231,356} The transferred electrons react with O₂ to produce •O₂⁻ radicals and the remaining holes in the VB of g-C₃N₄ can react with OH⁻/H₂O to generate •OH radicals. The MO in aqueous solution is oxidized by these active radicals. Although it may also be directly oxidized by the holes in the VB, the chance is much lower according to the scavenger experiment. Although the SPR of Au NPs is not excited, the boosted separation of photoinduced charge carriers results in the greatly enhanced photocatalytic activity under UV light exposure.

When the system is irradiated by visible light longer than 475 nm, as shown in Figure 3.6b, the bandgap excitation of g-C₃N₄ is almost excluded and the Au SPR becomes the major source of photo generated charge carriers. The hot electrons with higher energy from the SPR excitation can be injected to the CB of g-C₃N₄ by crossing the energy barrier, leaving the holes behind inside the Au NPs.^{355,377} The injected hot electrons can be rapidly transferred to the nearby O₂ to facilitate the generation of •O₂⁻ radicals. At the same time, the holes in the Au NPs can be used to produce •OH radicals, and hence also drive the decomposition of MO.

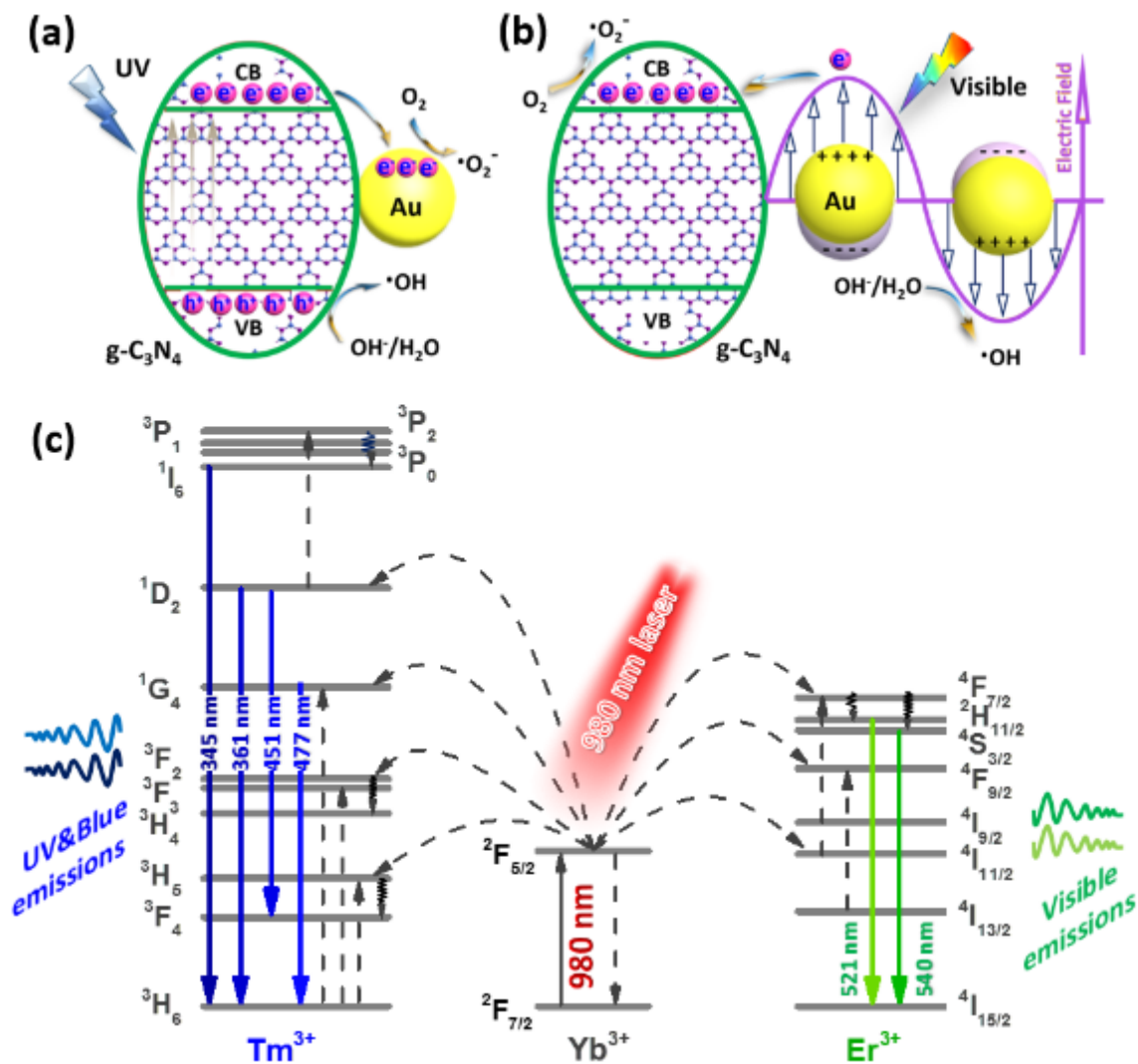


Figure 3.6 Proposed photocatalytic mechanism of Au-NYF/g-C₃N₄ photocatalyst under (a) UV and (b) visible light ($\lambda > 475$ nm) irradiation, respectively. (c) Schematic energy level diagrams, upconversion excitation and UV- visible light emissions for the NYF microspheres under the NIR light (980 nm laser) illumination.

As for the NIR-driven photocatalysis, the schematic illustration of the upconversion and energy transfer processes under 980 nm irradiation is depicted in Figure 3.6c. The doped Yb³⁺ ion

possesses only one excited state and acts as a sensitizer, and the Er^{3+} and Tm^{3+} ions function as activators. Only the Yb^{3+} ion can be excited by the 980 nm photons with its long-lived $^2\text{F}_{5/2}$ level being populated. Then the successive energy transfers from Yb^{3+} to Er^{3+} , and from Yb^{3+} to Tm^{3+} , occur to populate the corresponding $^4\text{I}_{11/2}$ and $^4\text{F}_{7/2}$ levels of Er^{3+} ions, and $^3\text{H}_5$, $^3\text{F}_2$, and $^1\text{G}_4$ levels of Tm^{3+} ions, respectively.^{378,379} The emissions of Tm^{3+} ion span from UV to blue regions, centered at 345, 361, 451 and 477 nm, and are assigned to the transitions of $^1\text{I}_6 \rightarrow ^3\text{F}_4$, $^1\text{D}_2 \rightarrow ^3\text{H}_6$, $^1\text{D}_2 \rightarrow ^3\text{F}_4$, and $^1\text{G}_4 \rightarrow ^3\text{H}_6$, respectively. According to the absorption and the upconversion luminescence spectra, the generated UV and blue emissions of Tm^{3+} ion can be reabsorbed by the vicinal g- C_3N_4 nanosheets. Similar to the photocatalysis under UV and visible light irradiation, these indirectly excited g- C_3N_4 nanosheets can drive the photocatalytic degradation of MO by producing the charge carriers. Simultaneously, the fast relaxation from the $^4\text{F}_{7/2}$ level to the $^2\text{H}_{11/2}$ and $^4\text{S}_{3/2}$ levels of Er^{3+} ions yields green emissions centered at 521 and 540 nm, associated with the transitions of $^2\text{H}_{11/2} \rightarrow ^4\text{I}_{15/2}$ and $^4\text{S}_{3/2} \rightarrow ^4\text{I}_{15/2}$, respectively. The green emissions match well with the SPR band of Au NPs. As demonstrated in the reaction under visible light ($\lambda > 475$ nm) irradiation, the injection of SPR-induced hot electrons from Au NPs to g- C_3N_4 and the remaining holes in Au NPs participate in the photocatalysis. In this way, the NIR light is indirectly utilized by Au NPs and g- C_3N_4 for photocatalytic reactions via the energy transfer process followed by the energetic electron transfer process.

3.4 Conclusions

In this work, both plasmonic and upconversion effects were introduced into photocatalysis to gain largely broadened light response range and enhanced photocatalytic activity. The Au-NYF/g- C_3N_4 composite photocatalysts with different Au contents were successfully designed and prepared for the first time by subtly integrating Au NPs, NYF microspheres and g- C_3N_4 nanosheets into a single nano-architecture. The as-synthesized Au-NYF/g- C_3N_4 photocatalysts successfully use solar light from UV-visible to NIR regions, and show exceptional activity in the photocatalytic degradation of MO compared with plain g- C_3N_4 , as well as excellent stability. Based on optical properties and photodegradation experiments under different light irradiations, the underlying mechanisms were elucidated. The photocatalysis pathways were also unveiled by performing trapping experiments of active species. The present study offers a feasible strategy to design and simultaneously prepare plasmon- and upconversion-enhanced high-performance photocatalysts for effectively harvesting solar energy over a wide spectral range.

Acknowledgements

Financial support from the Natural Sciences and Engineering Research Council of Canada, and le Fonds de recherche du Quebec-Nature et technologies (FRQNT) is greatly appreciated. Dr. M. Chaker is also grateful to the Canada Research Chairs Program. In addition, Q. Zhang acknowledges the support under State Scholarship Fund from the China Scholarship Council (CSC, No. 201506220152), Dr. Z. Xu acknowledges the National Natural Science Foundation of China (NSFC 51402198) and Natural Science Foundation of Liaoning Province (201602592) for financial support.

3.5 Supporting Information

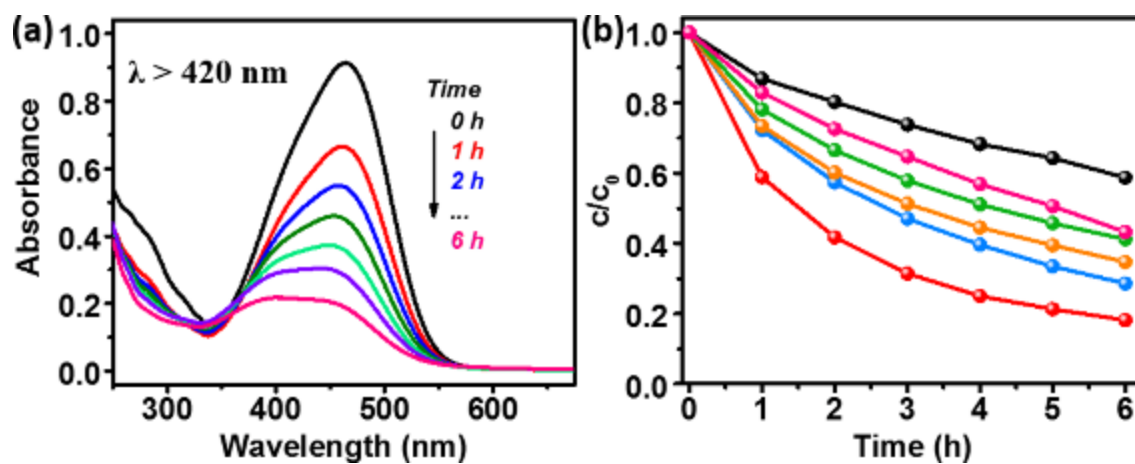


Figure S3.1 Time-dependent UV-vis absorption spectra (a) and the plot of (c/c_0) vs reaction time (b) for the photocatalytic degradation of methyl orange (MO) over 1 wt% Au-NiYF/g-C₃N₄ under $\lambda > 420$ nm light irradiation.

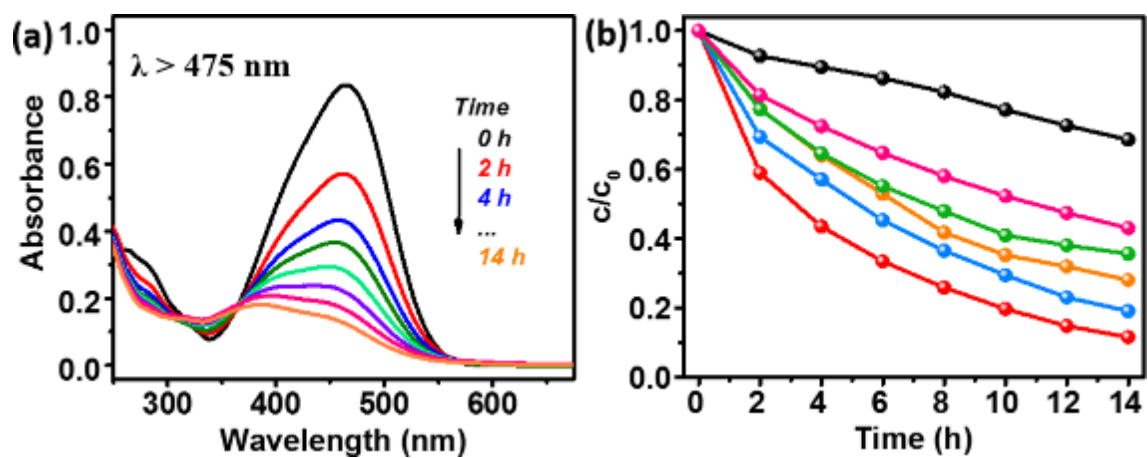


Figure S3.2 Time-dependent UV-vis absorption spectra (a) and the plot of (c/c_0) vs reaction time (b) for the photocatalytic degradation of MO over 1 wt% Au-NYF/g-C₃N₄ under $\lambda > 475$ nm light irradiation.

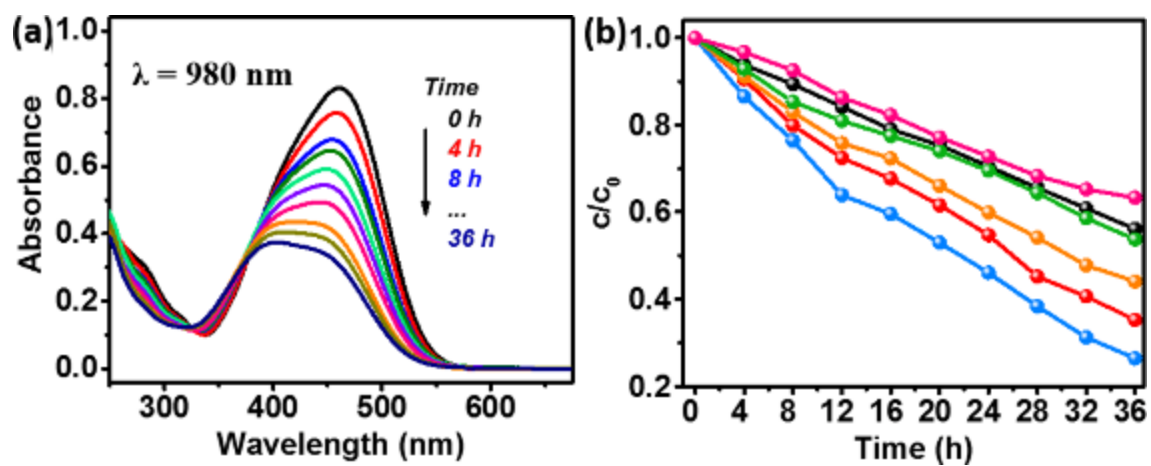


Figure S3.3 Time-dependent UV-vis absorption spectra (a) and the plot of (c/c_0) vs reaction time (b) for the photocatalytic degradation of MO over 1 wt% Au-NYF/g-C₃N₄ under near-infrared (NIR) light irradiation.

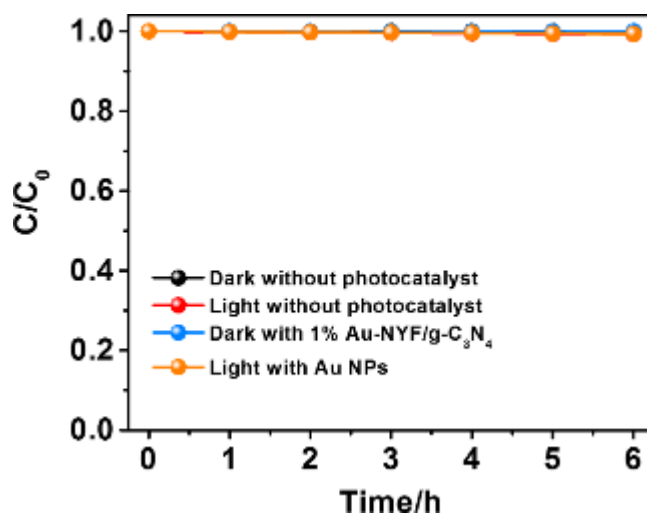


Figure S3.4 Photocatalytic degradation of MO with or without 1 wt% Au-NYF/g-C₃N₄ photocatalyst in the dark, and without photocatalysts or with Au NPs under visible light ($\lambda > 420$ nm) irradiation.

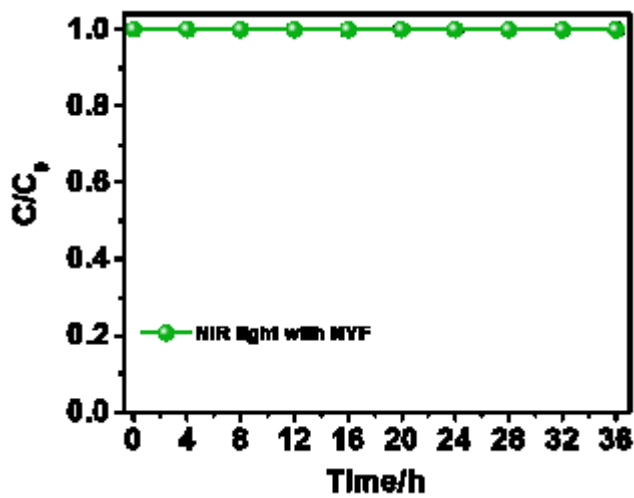


Figure S3.5 Photocatalytic degradation of MO in the presence of NYF only under NIR light ($\lambda = 980$ nm) illumination.

4 NIR-RESPONSIVE QUANTUM DOTS/CARBON NITRIDE

Broadband Photocatalysts Enabled by 0D/2D Heterojunctions of Near-Infrared Quantum Dots/Graphitic Carbon Nitride Nanosheets

Photocatalyseurs à large bande activés par des hétérojonctions 0D/2D de points quantiques proches de l'infrarouge/Nanosheets de nitrure de carbone graphitique

Authors:

Qingzhe Zhang[†], Fan Yang[†], Shuai Zhou[‡], Nan Bao^{*‡}, Zhenhe Xu^{*§}, Mohamed Chaker[†], Dongling Ma^{*†}

[†] Institut National de la Recherche Scientifique (INRS), Centre Énergie Matériaux et Télécommunications, Université du Québec, 1650 Boulevard Lionel-Boulet, Varennes, Québec J3X 1S2, Canada

[‡] Shandong Key Laboratory of Water Pollution Control and Resource Reuse, School of Environmental Science and Engineering, Shandong University, Qingdao 266237, China

[§] The Key Laboratory of Inorganic Molecule-Based Chemistry of Liaoning Province, College of Applied Chemistry, Shenyang University of Chemical Technology, Shenyang 110142, China

Publication:

Applied Catalysis B: Environmental

Publication Date: March 12, 2020

Volume 270, Pages 118879

DOI: 10.1016/j.apcatb.2020.118879.

Contribution of authors:

Qingzhe Zhang, Dr. Zhenhe Xu and Prof. Dongling Ma conceived and designed the research. Qingzhe Zhang prepared most of the samples and conducted most of the characterizations, such as XRD, XPS, ICP-OES, UV-Visible-NIR absorption spectra, and photoelectrochemical measurements and all the photocatalysis reactions. Quantum dots were prepared by Qingzhe

Zhang with the training of Fan Yang. Shuai Zhou and Prof. Nan Bao from Shandong University, China, carried out the ESR measurements. The TEM measurements were performed by Jean-Philippe Masse at Polytechnique Montréal. FTIR spectra were measured by Gwenaël Chamoulaud from Université du Québec à Montréal (UQAM). Prof. Mohamed Chaker and Prof. Dongling Ma supervised the experimental work. Qingzhe Zhang wrote the manuscript, which was carefully modified by Prof. Dongling Ma. Prof. Mohamed Chaker and Prof. Nan Bao also gave good comments on revising the manuscript. All authors discussed the results and commented on the manuscript.

Link between articles:

As aforementioned, both plasmonic and upconversion effects were introduced into photocatalysis to gain largely broadened light response range and enhanced photocatalytic activity. The Au-NYF/g-C₃N₄ composite photocatalysts were successfully designed and prepared by subtly integrating plasmonic Au NPs, upconverting NYF microspheres and g-C₃N₄ nanosheets into a single nano-architecture. The as-synthesized Au-NYF/g-C₃N₄ photocatalysts successfully use solar light from UV, visible to NIR regions, and show exceptional activity in the photocatalytic degradation of MO compared with plain g-C₃N₄, as well as excellent stability.

Due to the intermittency of solar energy together with the temporal and geographical divergence between production and demand mean that solar energy harvesting must be made more efficient and cost effective. However, the used Au and rare-earth metals in this work are still expensive. In addition, the upconversion efficiency of lanthanide-doped upconversion materials is quite low. To utilize solar energy more efficiently and more cost-effectively, a 0D/2D heterojunction based on NIR-responsive quantum dots loaded g-C₃N₄ nanosheets was constructed, which is expected to efficiently harvest solar photons from UV to NIR regions and used for photocatalytic degradation of organic dye in wastewater.

4.1 Introduction

Graphitic carbon nitride (g-C₃N₄) has attracted extensive attention in photocatalysis since Wang *et al.* discovered g-C₃N₄ as a promising visible-responsive photocatalyst for H₂ generation from solar water splitting in 2009.^{94,95,102,380-382} Compared to most commonly used, ultraviolet (UV)-active-only TiO₂ photocatalyst, the UV and visible light responsivity makes g-C₃N₄ highly attractive in more effectively utilizing solar energy. Furthermore, the 2-dimensional (2D) structure of g-C₃N₄ nanosheets provides large surface area for the adsorption of reactants and the easy loading of other nanomaterials. Nevertheless, g-C₃N₄'s bandgap (~2.7 eV) is still relatively wide.^{98,236,368,383} As a result, its light response is indeed mainly confined to UV photons, plus only a very limited range in the visible ($\lambda < 460$ nm), resulting in the underutilization of more than 90% of solar energy in the longer wavelength visible and near-infrared light (NIR) regions. Along with rapid charge carrier recombination, the photocatalytic activity of pristine g-C₃N₄ remains rather poor.

Our group has made efforts in developing effective broadband photocatalysts via upconversion (UC) and/or plasmonic nanostructures by rationally integrating them with semiconductor photocatalysts.^{44,65,145,188,384} Although some of these developed photocatalysts show broadband UV-, visible- and NIR-light activity, the NIR photocatalytic performance is still far from satisfactory due to the relatively low UC quantum efficiency of the UC materials.^{149,152} Therefore, seeking an alternative to endow g-C₃N₄ with enhanced photocatalytic activity in a broad range of the solar spectrum, in particular, in the NIR range is of great significance.

On the other hand, quantum dots (QDs) have charmed material researchers with their enticing optical and electronic characteristics, especially the large optical cross-sections, short required-charge-migration-distance and size-tunable bandgaps due to the quantum confinement effect^{300,385-388}. The bandgap of QDs can be readily tuned over a broad range, thereby their absorption at different wavelengths. This makes it possible to tune the size of certain types of QDs so as to make them responsive to nearly all the visible and even a significant portion of NIR light. PbS QDs are of such a kind. They have piqued the interest of researchers due to their small bandgap (0.41 eV for bulk) and large exciton Bohr radius (20 nm),^{258,301,302} resulting in the strong quantum size effect, and thus great promise in harvesting the full solar spectrum for photovoltaic and photocatalytic applications.^{259,389-391} It is anticipated that the photocatalytic performance can be largely enhanced by introducing PbS QDs, thanks to their light-harvesting capability, potential multiple-exciton-generation and efficient spatial separation of photoinduced charge carriers between the QDs and other materials.³⁰¹ Yet the abundant surface defects make PbS QDs

inherently unstable compared with their bulk counterparts, especially under various post-synthetic manipulations and environmental conditions, such as washing, dilution, and exposure to air or light.^{385,391} The coating of CdS shell was reported to passivate these surface defects, which may act as charge carrier trap sites, and protect the QDs from interactions with external environments, giving rise to greatly improved thermal and photo stability in comparison with the core-only QDs.³⁹²⁻³⁹⁵ In addition, our previous work has reported that the coating of CdS shell can effectively prevent PbS QDs from releasing Pb²⁺ ions.^{396,397} CdS was chosen as a shell material also because of the relatively good lattice match between CdS and PbS.³⁹⁸ However, the toxicity issue has heretofore been the primary concern for QDs containing heavy metals, such as PbS and CdS, which can be further exacerbated due to the enhanced metal ion release under the exposure to air or light irradiations.^{398,399} Bhatia et al. detected the release of Cd²⁺ ions in Cd-based QDs colloidal solution and also found that the concentration of the Cd²⁺ ions directly determined the level of cytotoxicity.³⁹⁹ They demonstrated that the release of Cd²⁺ ions can be prevented by coating appropriate shells, such as ZnS or an organic shell, to encapsulate the Cd-based QDs to make them non-toxic. Parak et al. encapsulated CdSe QDs with different layers, such as mercaptopropionic acid (MPA), SiO₂, ZnS, and polymer, and compared their cytotoxicity.⁴⁰⁰ They found that the coating of CdSe QDs with a ZnS shell increased critical concentration, below which no toxicity could be detected, by up to 10 times, with respect to the CdSe QDs capped only by MPA. Ye et al. performed a pilot study by injecting phospholipid micelle-modified CdSe/CdS/ZnS QDs into rhesus macaques and found no any evidence of toxicity.⁴⁰¹ After injection the blood and biochemical markers remained within normal ranges, and histology of major organs after 90 days showed no abnormalities. In our previous work, we also applied PCZ QDs for in vivo fluorescence imaging in living mice.³²² The PCZ QDs showed no noticeable toxicity for both cells and animals, which was concluded based on the cell culture assays, as well as the lack of adverse health effects (no significant weight changes or behavior abnormalities were found over 25 days) for mice injected with PCZ QDs. Thus, the encapsulation of QDs with a robust ZnS outer shell can greatly suppress the release of inner heavy metal ions and significantly reduce cytotoxic effects.^{322,385,400,401} Furthermore, for photocatalytic applications, such as water splitting and water treatment, QDs are generally required to be dispersible in aqueous solution. In this context, we developed an approach to synthesize a uniform CdS shell, and then grow a very thin ZnS outer shell as well as simultaneously replace the hydrophobic oleate ligands on the surface of PbS@CdS QDs with the hydrophilic MPA ligands through a rapid, low-cost microwave-assisted approach.^{322,323} Thanks to the uniform heating feature provided by microwave irradiation, homogeneous, water-dispersible, high-quality (with much fewer defects) PbS@CdS@ZnS (PCZ)

core@shell@shell QDs were synthesized in a very short time frame. Although the final QDs are water-dispersive, they may still aggregate, depending on external environments.^{309,402} To overcome these drawbacks, one of the most effective strategies is to load these 0D QDs onto 2D ultrathin nanosheets to construct the 0D/2D heterojunction.^{403,404}

Herein, we for the first time designed and synthesized a novel 0D/2D heterojunction of PCZ QDs/g-C₃N₄ nanosheets. The 2D g-C₃N₄ nanosheets provide large surface area for the adsorption of reactants and easy loading and uniform distribution of PCZ QDs. The N/C-coordinating framework of g-C₃N₄ formed by the unique tri-s-triazine structure renders it an ideal host for robustly supporting ultra-small PCZ QDs to make them more stable and dispersive. Under shorter-wavelength light irradiation ($\lambda < 460$ nm), QDs not only increase light absorption, but also act as the electron acceptor and suppress the recombination of charge carriers in excited g-C₃N₄. The introduction of NIR-responsive PCZ QDs can sensitize the composite photocatalysts to respond longer-wavelength light, and reciprocally the presence of 2D g-C₃N₄ nanosheets can promote the charge transfer from excited QDs. As a result, the obtained PCZ QDs/g-C₃N₄ photocatalysts exhibit greatly enhanced UV, visible and NIR light photocatalytic activities compared with pristine g-C₃N₄ and most of the reported broadband photocatalysts.

4.2 Experimental Details

4.2.1 Materials

Butylamine (99.5%), ethanol, hexane (99.9%), methanol (anhydrous, 99.8%), N,N-dimethylformamide (DMF, 99.8%), MPA ($\geq 99.0\%$), 1-methyl-2-pyrrolidinone (NMP, $\geq 99\%$), octadecene (ODE), oleic acid (OA), oleylamine (OLA, technical grade, 70%), toluene (99.9%), cadmium oxide (CdO, 99%), lead chloride (98%), phosphorus pentasulfide (P₂S₅, 99%), sulfur powder (100%), zinc chloride (ZnCl₂, 99.999%), disodium ethylenediaminetetraacetate (Na₂EDTA), 1,4-benzoquinone (BQ), and tert-butyl alcohol (t-BuOH) were purchased from Sigma-Aldrich Corporation. All chemicals were used as received without further treatment.

4.2.2 Synthesis of PbS QDs

The PbS QDs were synthesized via a previous reported method.³²² Typically, 24 mL of OLA and 10 g of PbCl₂ were mixed in one three-neck flask and heated to 160 °C. After stirring for 1h at this temperature under N₂, the solution was cooled down to 120 °C and vacuumed for 40 min. At this time, a solution containing 115 mg of sulfur powder and 4 mL of OLA was immediately injected

into the above flask under the protection of N_2 , which was cooled down to 100 °C and kept for 1 min for the growth of PbS QDs to reach the desired size. Afterwards, the solution was quenched with cold water to terminate the reaction. The PbS QDs were separated from the colloidal solution and the supernatant was collected. 20 mL of hexane and 30 mL of ethanol were added to wash the obtained QDs for two times. The final product was re-dispersed in toluene to get the colloidal PbS QDs solution.

4.2.3 Synthesis of PbS@CdS core@shell QDs

A microwave-assisted cation exchange approach was used to synthesize PbS@CdS core@shell QDs.³²³ Specifically, the colorless Cd precursor solution was prepared by heating a flask containing OA (15 mL), ODE (20 mL), and CdO (3 g) to 200-250 °C, and then cooled to 100 °C and degassed for 30 min to remove moisture and oxygen. When the solution was cooled down to 20 °C, 12 mL of the as-synthesized PbS QD dispersion was added to obtain a mixture. 20 mL of the mixture was transferred to a 35 mL vial and underwent heating in a Discover SP microwave reactor (CEM Corporation) to 100 °C for 3 min. Certain volume of ethanol was added to precipitate QDs, which were separated by centrifugation and re-dispersed in toluene. The precipitation and re-dispersion procedures were repeated three times to purify the obtained PbS@CdS QDs, which were finally re-dispersed in toluene.

4.2.4 Synthesis of PCZ core@shell@shell QDs

Through a microwave-assisted procedure, the coating of ZnS shell on the PbS@CdS QDs and replacing the OA with MPA ligand to make them water-dispersible were simultaneously achieved. Typically, P_2S_5 (0.02 g) was dissolved into MPA (0.5 g), butylamine (0.3 mL), and NMP (10 mL) by heating at 110 °C for 20 min in a sealed flask to prepare S precursor solution. Under the same condition, Zn precursor solution was synthesized by dissolving $ZnCl_2$ (0.07 g) into same amount of MPA, butylamine, and NMP in another sealed flask. After cooling down to room temperature, 0.007 g of as-synthesized PbS@CdS QDs were dissolved in the S precursor solution, and then Zn precursor solution was added into the mixture. The obtained solution was heated in a Discover SP microwave oven at 70 °C for 30 min to yield the MPA-capped PCZ core@shell@shell QDs. The synthesized QDs were purified by repeating four times the centrifugation and re-dispersion using toluene. The purified QDs were dried overnight in vacuum oven and dispersed in 10 mL of water.

4.2.5 Preparation of PCZ QDs/g-C₃N₄ nanosheets

g-C₃N₄ nanosheets were prepared following a thermolysis method in our previous report.^{188,384} Briefly, a covered alumina crucible containing 30 g of urea was heated in a furnace at 250, 350, and 550 °C, for 1, 2, and 2 h, respectively, with a temperature ramping rate of 2 °C min⁻¹. Afterwards, the cooled yellow powder was collected and washed with water and dilute HNO₃ to remove potential alkaline residue. The products were collected by centrifugation and dried at 80 °C overnight. A certain amount of the prepared PCZ core@shell@shell QD was added to 10 mg of g-C₃N₄ nanosheets and mixed by shaking for 5 min, and then the mixture was incubated at room temperature until the supernatant became transparent and colorless. The precipitate was collected and washed by water. By varying the added volumes of QD solution, PCZ QDs/g-C₃N₄ with different loading mass fractions of QDs were prepared, denoted as x wt% QDs/g-C₃N₄. The actual contents of PCZ QDs in the composites were measured by inductively coupled plasma-optical emission spectrometry (ICP-OES). The measured values, 0.95, 2.14, 2.97, 7.02 and 10.89 wt%, are quite close to the nominal loading mass fractions, 1, 2, 3, 7 and 11 wt%.

4.2.6 Characterization

Transmission electron microscopy (TEM), high-resolution TEM (HRTEM), and energy dispersive X-ray spectroscopy (EDX) were conducted on a JEOL 2100F TEM at an acceleration voltage of 200 kV for structural analysis. X-ray diffraction (XRD) patterns were recorded on a PANalytical X'Pert MRD X-ray diffractometer with a Cu K α radiation ($\lambda = 1.5406 \text{ \AA}$) and operated at 40 mA and 45 kV. Fourier transform infrared (FTIR) spectra of the prepared samples were recorded on a Thermo Scientific 4700 FTIR spectrometer. A VG Escalab 220i-XL X-ray photoelectron spectroscopy (XPS) equipped with a twin anode Al K α radiation x-ray source was used to analyze the chemical composition of the samples. Optical absorption spectra of photocatalysts and methyl orange (MO) in aqueous solution were taken using a Varian Cary 5000 scan UV-vis-NIR spectrometer at room temperature. Steady-state photoluminescence (PL) and time-resolved PL (TRPL) spectra were obtained by a Horiba Jobin Yvon Fluorolog-3 fluorescence spectrometer. The average PL lifetime (τ) was estimated by firstly fitting the TRPL decay curves with the bi-exponential fitting Equation (4), which led to the best fit, and then by using Equation (5):^{134,405}

$$\text{Fit} = A + B_1 \exp\left\{-\frac{t}{\tau_1}\right\} + B_2 \exp\left\{-\frac{t}{\tau_2}\right\} \quad (4)$$

$$\tau = \frac{B_1 \tau_1^2 + B_2 \tau_2^2}{B_1 \tau_1 + B_2 \tau_2} \quad (5)$$

Where A , B_1 , and B_2 are constants obtained from the fitting of decay curves

τ_1 and τ_2 are different decay components resolved also from the fitting

The weight content of PCZ QDs in PCZ QDs/g-C₃N₄ was determined by an Agilent 5100 ICP-OES. The electron spin resonance (ESR) characterizations were performed by using a JEOL JES-X320 spectrometer with a microwave power of 10.00 mW and a frequency of 9.15 GHz at room temperature to study the electron mobility. The 5,5-dimethyl-1-pyrroline N-oxide (DMPO) was used as the spin-trapping agent to detect the reactive species. The measurements were carried out in aqueous dispersion and methanol dispersion for DMPO-•OH and DMPO-•O₂⁻, respectively. Photoelectrochemical (PEC) measurements were performed in a standard three-electrode cell with a CHI 660E electrochemical workstation (CH Instruments). A Ag/AgCl electrode (3 M KCl) and a Pt wire acted as the reference and counter electrode, respectively. The photocatalysts (5 g) were dispersed into DMF (1 mL). The colloidal dispersion was drop-casted onto a F-doped tin oxide (FTO) glass, of which the boundary was protected by Scotch tape. After naturally drying, the epoxy resin glue was used to isolate the uncoated part of the FTO glass. Prior to the measurement, the electrolyte solution (0.2 M of Na₂SO₄) was purged with N₂ for 30 min to remove the dissolved O₂. The PEC measurements were performed under the irradiation of a 150 W Newport solar simulator (100 mW cm⁻²). Nyquist plots were obtained at a bias of 0.2 V with the frequency range of 100 mHz to 100 kHz.

4.2.7 Photocatalytic activity measurements and trapping experiments

The photocatalytic activity of the QDs/g-C₃N₄ samples was evaluated for removal of MO in water. Photocatalysis was carried out in a 100 mL quartz reactor in the presence of 10 mg of the QDs/g-C₃N₄ and 25 mL of MO solution (10 mg L⁻¹). The reaction temperature was kept constant with circulating cooling water. Prior to irradiation, the suspension was stirred in the dark for 30 min to reach adsorption-desorption equilibrium between photocatalysts and MO. A commercial Luzchem LUZ-4V photoreactor equipped with fourteen 8 W LZC-UVA lamps was used for the UV photocatalytic experiment. A 300 W xenon lamp with long-pass optical filters was used for the photocatalysis under $\lambda > 420$ nm and $\lambda > 495$ nm irradiations. For the NIR photocatalysis, a 980 nm diode laser was set at 2 W to act as the NIR light source. For practical application, the photodegradation reaction was performed using a solar simulator (AM 1.5). The solution was irradiated with the above-mentioned light along with magnetic stirring. At different irradiation time points, 0.5 mL of aliquot was collected and centrifuged to separate the MO solution and photocatalysts. The MO residue in the supernatant was measured using a UV-vis spectrometry by following the absorbance at wavelength of 465 nm. After the simulated solar light

photocatalysis, QDs/g-C₃N₄ were recycled by centrifugation, and then washed and dried overnight. Five more runs of experiments were carried out in the presence of the recovered samples under identical conditions to test the stability.

To detect the involved active species in the photocatalytic removal of MO, trapping experiments were performed by using different scavengers. Specifically, t-BuOH (1 mM), BQ (1 mM), and Na₂EDTA (1 mM) served as scavengers to capture hydroxyl radical (\bullet OH), superoxide radical (\bullet O₂⁻), and hole, respectively.

4.3 Results and Discussion

4.3.1 Microstructures and optical properties

A representative TEM image of g-C₃N₄ shows the 2D thin nanosheet and graphene-like structure (Figure 4.1a). Figure 4.1b and 4.1c reveals that the as-prepared water-dispersible PCZ QDs are well-defined, monodisperse and quite uniform in size with a mean diameter of 4.7 ± 0.3 nm. Clear lattice fringes are shown in the HRTEM image of PCZ QDs and an interplanar spacing of 0.30 nm was observed (inset of Figure 4.1c), which corresponds to the (200) lattice plane of the rock-salt cubic PbS nanocrystal.^{406,407} More TEM images, size distributions, the absorption and PL spectra of PbS QDs, PbS@CdS QDs and PCZ QDs are displayed in Figure S4.1-S4.4. No obvious size change was observed after the CdS shell formation on the surface of PbS QDs via ligand exchange between Pb²⁺ and Cd²⁺ (Figure S4.1-S4.2). In this reaction, as cation exchange proceeds from the surface inward, the size of the remaining PbS core QDs decreases, leading to an increase in the confinement energy and, therefore, the observed blue shift of the first excitonic absorption peak from 1265 nm of PbS QDs to 1134 nm of PbS@CdS QDs (Figure S4.4a). The peak PbS@CdS QDs of PL spectrum also blue shifted accordingly due to the same reason (Figure S4.4b). The size of PbS QDs can be estimated according to the following Equation (6) established by Zeger Hens et al.,⁴⁰⁸

$$E_0 = 0.41 + \frac{1}{0.025d^2 + 0.283d} = \frac{1240}{\lambda_0} \quad (6)$$

Where E_0 is the quantum confinement bandgap of PbS QDs
 λ_0 represents the first excitonic absorption peak position
 d is the diameter of PbS QDs in nm.

In our specific case, the diameter of PbS QDs and PbS core in PbS@CdS QDs were estimated to be 4.45 nm (in agreement with TEM image shown in Figure S4.1) and 3.85 nm. Thus, the

thickness of CdS shell was calculated to be ~ 0.3 nm. These are all strong evidence of the successful coating of CdS shell onto PbS QDs.^{322,398,401,409-414} Moreover, the growth of the ZnS layer led to an increase of diameter from ~ 4.5 nm for PbS@CdS QDs (Figure S4.2) to ~ 4.7 nm for PCZ QDs (Figure S4.3). The increased overall size of QDs after coating indicated the formation of ZnS shell once again and the thickness of the ZnS shell was thus estimated to be ~ 0.1 nm. Although it was difficult to clearly resolve the very thin ZnS shell by TEM, both Zn and S were observed in EDX spectrum (Fig. S4.5), in line with the shell formation. It is critical to construct the very thin yet compact and uniform ZnS shell that can permit the charge transfer from core QDs to g-C₃N₄ and meanwhile stabilizing PbS@CdS QDs to avoid any release of Pb²⁺ and Cd²⁺ ions into the aqueous solution. Figure 4.1d-4.1e shows the TEM images of 2 wt% QDs/g-C₃N₄ samples at different magnifications. The TEM images of 1 wt% QDs/g-C₃N₄ and 7 wt% QDs/g-C₃N₄ are also displayed in Figure S4.6. Ultra-small QDs are uniformly distributed on the surface of g-C₃N₄ nanosheets without any agglomeration. It is noteworthy that no free QDs were observed, suggesting the high coupling efficiency between PCZ QDs and g-C₃N₄ nanosheets. HRTEM image (inset of Figure 4.1f) clearly shows lattice fringes with a spacing of 0.34 nm, which can be readily indexed to the (111) plane of rock-salt cubic PbS.²⁵⁷ Furthermore, the presence of peaks assigned to C, N, Pb, S, Cd, and Zn in the EDX spectrum is another evidence for the formation of CdS shell and ZnS shell onto PbS QDs, and also confirms the successful integration of PCZ QDs and g-C₃N₄ (Figure 4.1g).

XRD analysis was performed to further study the crystal structure of g-C₃N₄, PCZ QDs, and 2 wt% QDs/g-C₃N₄ samples (Figure 4.1h). Two apparent peaks at 13.1° and 27.4° were observed in the XRD pattern of g-C₃N₄, corresponding to the (100) plane and (002) plane, which stem from the in-plane repeating unit (tri-s-triazine units), and the interplanar stacking of the conjugated aromatic rings, respectively.^{102,142,415} The peaks shown in the XRD pattern of PCZ QDs can be readily indexed to the rock-salt cubic PbS (JCPDS 78-1055), which is consistent with the HRTEM results. Due to the very thin thickness of the CdS and ZnS shells and the overlapping of diffraction peaks, it is not easy to identify the crystalline structure of CdS and ZnS by XRD. The coexistence of peaks of g-C₃N₄ and PbS core QDs in the pattern of PCZ QDs/g-C₃N₄ sample suggests the successful integration of these two components.

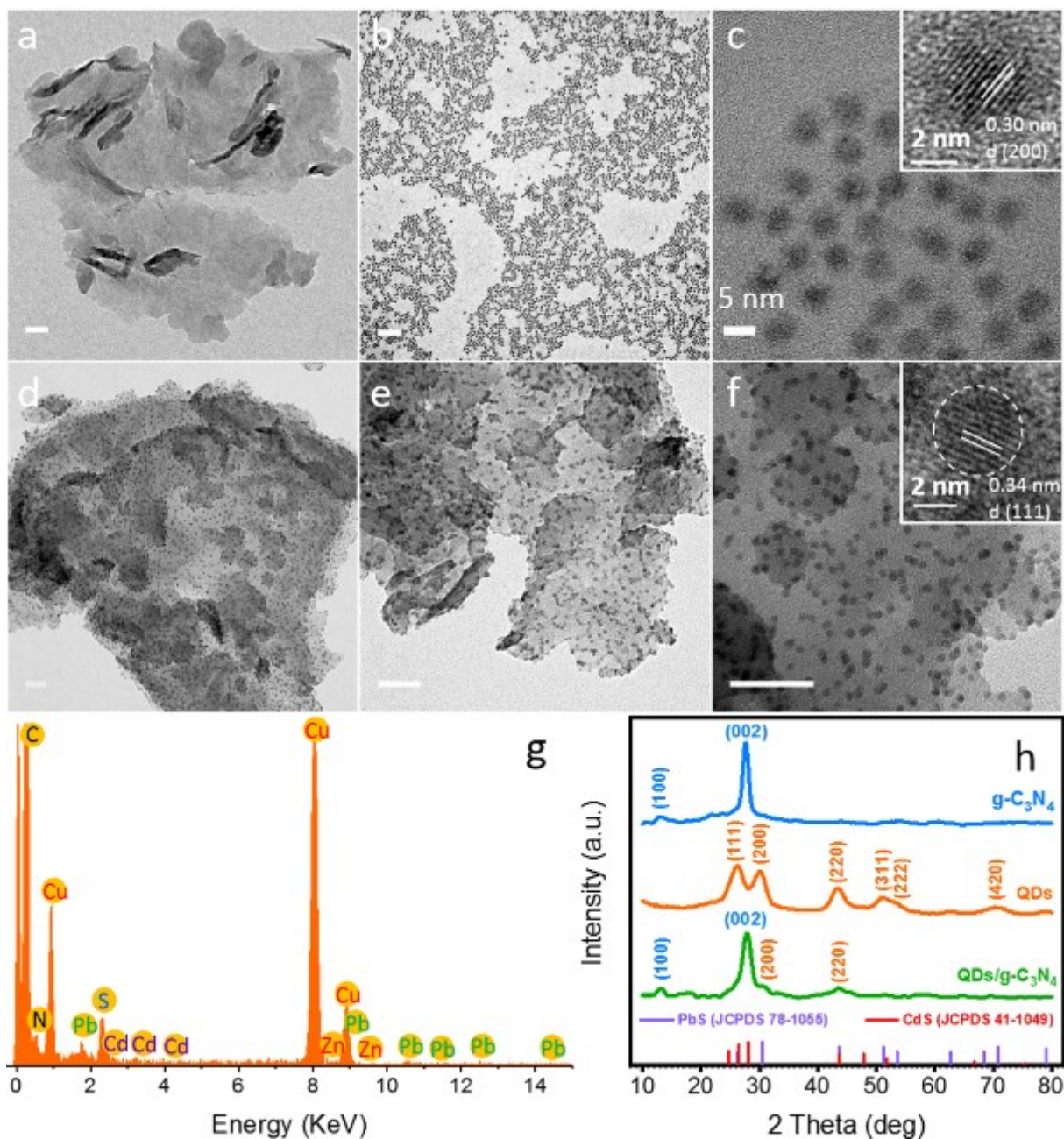


Figure 4.1 TEM images of (a) g-C₃N₄ nanosheets, (b-c) PCZ QDs, (d-f) 2 wt% QDs/g-C₃N₄ photocatalysts with different magnifications. Insets in (c) and (f) are the HRTEM images of PCZ QDs and PCZ QDs/g-C₃N₄, respectively. Scale bars in (a-b) and (d-f) are 50 nm. (g) EDX spectrum of (f). (h) XRD patterns of g-C₃N₄, PCZ QDs, and PCZ QDs/g-C₃N₄ samples.

FT-IR and XPS measurements of g-C₃N₄ and 2 wt% QDs/g-C₃N₄ were carried out to investigate the interactions between PCZ QDs and g-C₃N₄ nanosheets in the PCZ QDs/g-C₃N₄ sample (Figure 4.2a-e). Two samples show essentially similar FTIR spectra, but only from this observation, it is difficult to conclude that the chemical structure of g-C₃N₄ nanosheets was not affected by the introduction of PCZ QDs as the QD loading level is very low (Figure 4.2a). The

broad absorption band in 3600-2900 cm^{-1} can be ascribed to the N-H stretching vibration modes or the adsorbed water.^{111,404,416-418} Several bands are shown in the fingerprint region of 1650-1200 cm^{-1} , which are ascribed to the characteristic skeletal vibrations of aromatic CN heterocycles.^{404,416} The sharp band at $\sim 810 \text{ cm}^{-1}$ is attributed to the breathing vibration modes of the main motifs of g- C_3N_4 , the s-triazine ring units.^{404,417}

As for the XPS measurements, both the survey spectra of g- C_3N_4 and PCZ QDs/g- C_3N_4 show peaks for C, N and O elements (Figure 4.2b). Additional peaks for S, Pb, Cd and Zn elements were also observed in the survey spectrum of PCZ QDs/g- C_3N_4 (Figure 4.2b), and Figure S4.7-S4.9 show high-resolution Pb 4f, Cd 3d, and Zn 2p XPS spectra of both PCZ QDs and PCZ QDs/g- C_3N_4 , indicating the successful preparation of PCZ QDs and the successful integration of g- C_3N_4 and PCZ QDs. In the high-resolution C 1s XPS spectrum of g- C_3N_4 , two distinctive peaks are displayed at 284.8 and 288.2 eV (Figure 4.2c), corresponding to the adventitious hydrocarbons or the sp^2 graphitic C in C-C bonds, and sp^2 C in N-C=N bonds, respectively.^{98,418} Deconvolution of N 1s XPS spectrum of g- C_3N_4 led to three peaks centered at 398.6, 400.2 and 401.2 eV, which can be attributed to the sp^2 N in N=C-N, tertiary N groups (N- C_3), and amino functions carrying hydrogen (C-N-H or C-N- H_2), respectively (Figure 4.2d).^{404,419-421} The two peaks at 161.3 eV (S 2 $p_{3/2}$) and 162.5 eV (S 2 $p_{1/2}$) in the S 2p XPS spectrum of PCZ QDs (Figure 4.2e) correspond to the S element in the QDs.^{407,422,423} Remarkably, after the loading of PCZ QDs onto g- C_3N_4 , the obvious shifting of the peaks toward lower binding energy by 0.2 eV in the S 2p XPS spectrum occurs. This indicates that the electron density of S atoms in PCZ QDs increases, which is most likely due to the strong interfacial interactions and to the electron transfer from C atoms in g- C_3N_4 . Such a peak shifting has also been observed in $\text{SnS}_2/\text{g-}\text{C}_3\text{N}_4$ composite and S-doped g- C_3N_4 materials, in which it was reasonably ascribed to the introduction of C-S coordinate bonds.⁴²⁴⁻⁴²⁶ The experimental results and theoretical calculations in the literature excluded the possibility of forming N-S bonds and confirmed that S atom preferentially substitutes for the edge N site of the g- C_3N_4 lattice to form C-S bond.⁴²⁴⁻⁴²⁶ No obvious shifting was observed in the C 1s spectrum of g- C_3N_4 and that of PCZ QDs/g- C_3N_4 composite as the loading level of PCZ QDs is very low (2 wt%). In addition, no peak shifting was observed in the Zn 2p XPS spectra (Figure S4.9), which rules out the presence of N-Zn bond. Just as previously reported N-P bond, the formed C-S bond can also act as the shallow charge trapping sites to inhibit charge carrier recombination and thus enhance the photocatalytic activity.^{319,381,427}

Figure 4.2f shows the UV-visible-NIR absorption spectra of PCZ QDs and 2 wt% QDs/g- C_3N_4 samples. The color change from the light yellow of g- C_3N_4 to dark grey of PCZ QDs/g- C_3N_4 powder

indicates their different optical properties. Both samples exhibit typical $g\text{-C}_3\text{N}_4$ absorption with the absorption edge at ~ 466 nm, corresponding to the bandgap of ~ 2.66 eV. The additional absorption from 466 nm up to 1300 nm was achieved by the loading of PCZ QDs, which makes the broad-solar-spectrum photocatalysis possible.

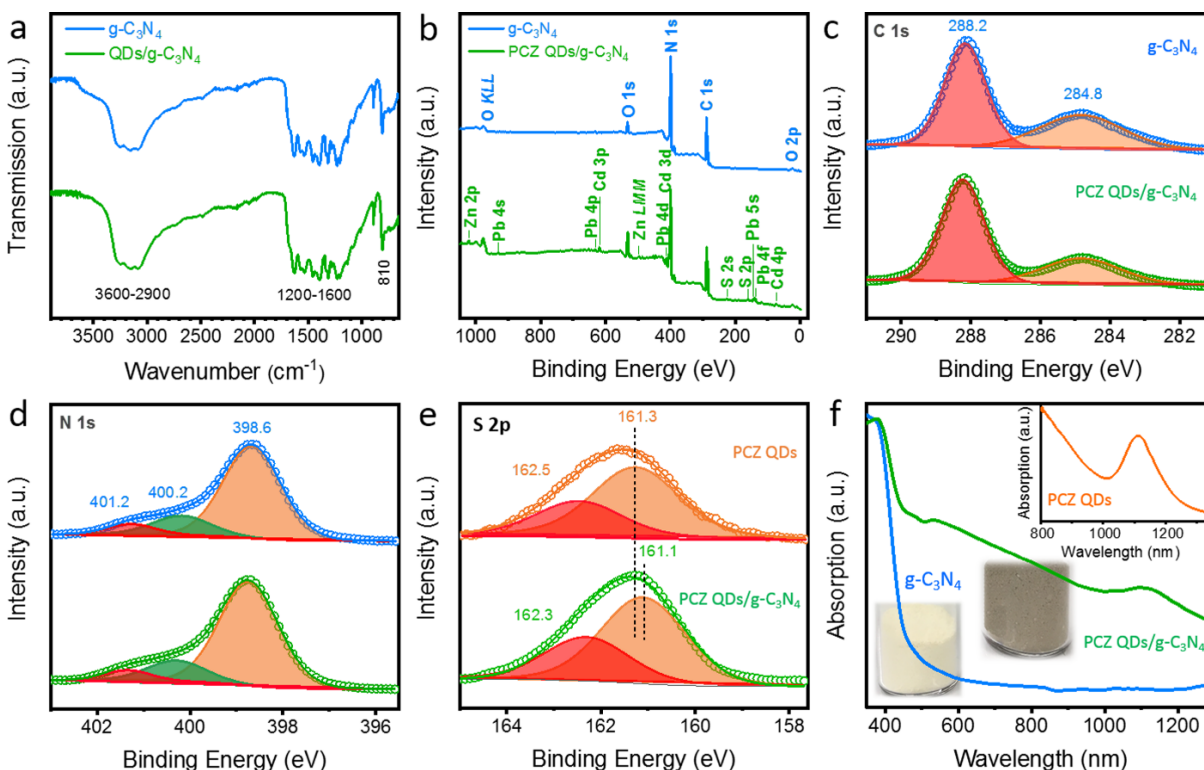


Figure 4.2 (a) FTIR spectra, (b) survey XPS spectra, high-resolution (c) C 1s and (d) N 1s XPS spectra of $g\text{-C}_3\text{N}_4$ and PCZ QDs/ $g\text{-C}_3\text{N}_4$ samples, (e) high-resolution S 2p XPS spectra of PCZ QDs and PCZ QDs/ $g\text{-C}_3\text{N}_4$, and (f) absorption spectra of $g\text{-C}_3\text{N}_4$ and PCZ QDs/ $g\text{-C}_3\text{N}_4$. Insets in (f) are the photographs of the prepared powder samples and the NIR absorption spectrum of PCZ QDs.

4.3.2 Photocatalytic activity and stability

The photocatalytic activities of the as-prepared samples were evaluated by photocatalytic degradation of MO under different light irradiations (Figure 4.3). As both the $g\text{-C}_3\text{N}_4$ and the loaded PCZ QDs can strongly absorb UV and short-wavelength visible photons to generate potentially useful electrons and holes for photocatalysis, the charge carrier dynamics, including possible charge transfer and back transfer between them under short wavelength irradiation, is expected to be complicated. The QD loading amount is required to be optimized in order to maximize the photocatalysis efficiency by balancing underlying optical and electronic processes of these two components. The photocatalytic degradation of MO over varying contents of PCZ QDs was thus investigated systematically.

Under UV light illumination (Figure 4.3a), the loading of PCZ QDs prominently increases the overall photocatalytic activity with respect to g-C₃N₄, while no obvious activity was detected over bare PCZ QDs. The kinetic study of MO degradation over 0-3 wt% QDs/g-C₃N₄ is shown in Figure S4.10. Through fitting the data with the first-order reaction model, the apparent reaction rate constant (k_{app}) was calculated, which was further normalized with the mass (10 mg) of the added catalyst in the reaction solution. The highest normalized k_{app} (k) value obtained by 2 wt% QDs/g-C₃N₄ ($3.4 \times 10^{-3} \text{ min}^{-1} \text{ mg}^{-1}$) is about 7 times higher than that by pristine g-C₃N₄ nanosheets ($0.5 \times 10^{-3} \text{ min}^{-1} \text{ mg}^{-1}$). The same trend was observed in the MO degradation under $\lambda > 420 \text{ nm}$ light illumination (Figure 4.3b). In terms of k values, the optimal loading level of PCZ QDs was also found to be 2 wt% with a high k value of $2.1 \times 10^{-3} \text{ min}^{-1} \text{ mg}^{-1}$ (Figure S4.11). The similar trend can be attributed to a similar mechanism (to be discussed later on) underlying these two cases, wherein both g-C₃N₄ and PCZ QDs can be simultaneously excited. It is difficult to distinctly differentiate the exact contribution from each of these two components to the enhanced photocatalytic properties.

To elucidate the important impact of the PCZ QDs, the reaction system was exposed to $\lambda > 495 \text{ nm}$ light, where only the QDs can be excited, and in this case 7 wt% PCZ QDs loaded sample shows the best photocatalytic activity with the k value of $8.4 \times 10^{-4} \text{ min}^{-1} \text{ mg}^{-1}$ (Figure 4.3c and Figure S4.12). With the further increase of PCZ QDs loading, a great decrease of k value was observed for 11 wt% QDs/g-C₃N₄ sample ($4.1 \times 10^{-4} \text{ min}^{-1} \text{ mg}^{-1}$).

In addition to the enhanced UV and visible photocatalytic activity, as expected, the as-prepared PCZ QDs/g-C₃N₄ photocatalysts show superior activity under NIR light irradiation (Figure 4.3d and 3e). This is also one of the reasons that the NIR-responsive PCZ QDs were selected and used in this work. Because only the PCZ QDs can be excited under NIR illumination, the underlying mechanism of NIR photocatalysis is similar to that of $\lambda > 495 \text{ nm}$ light photocatalysis. The optimized k value ($9.9 \times 10^{-3} \text{ h}^{-1} \text{ mg}^{-1}$) was also obtained by the 7 wt% QDs/g-C₃N₄ sample in the NIR photocatalysis. According to our extensive literature search (Table S4.1), for NIR photocatalysis, the herein obtained k value is higher than the largest value ($6.18 \times 10^{-3} \text{ h}^{-1} \text{ mg}^{-1}$) ever reported for g-C₃N₄ based photocatalysts.²⁶⁰ Among the similar reaction systems, *i.e.*, with the comparable catalyst concentration and power of light sources, the k value obtained by the 7 wt% QDs/g-C₃N₄ is higher than that of upconversion involved photocatalysts. Although our NIR activity value is still lower than that under UV and visible lights, the beneficial effect of the combination of NIR-responsive PCZ QDs with the g-C₃N₄ nanosheets for NIR photocatalysis is

clearly demonstrated, which opens the door for making more effective NIR photocatalysts by exploring stable, core/shell structured NIR QDs.

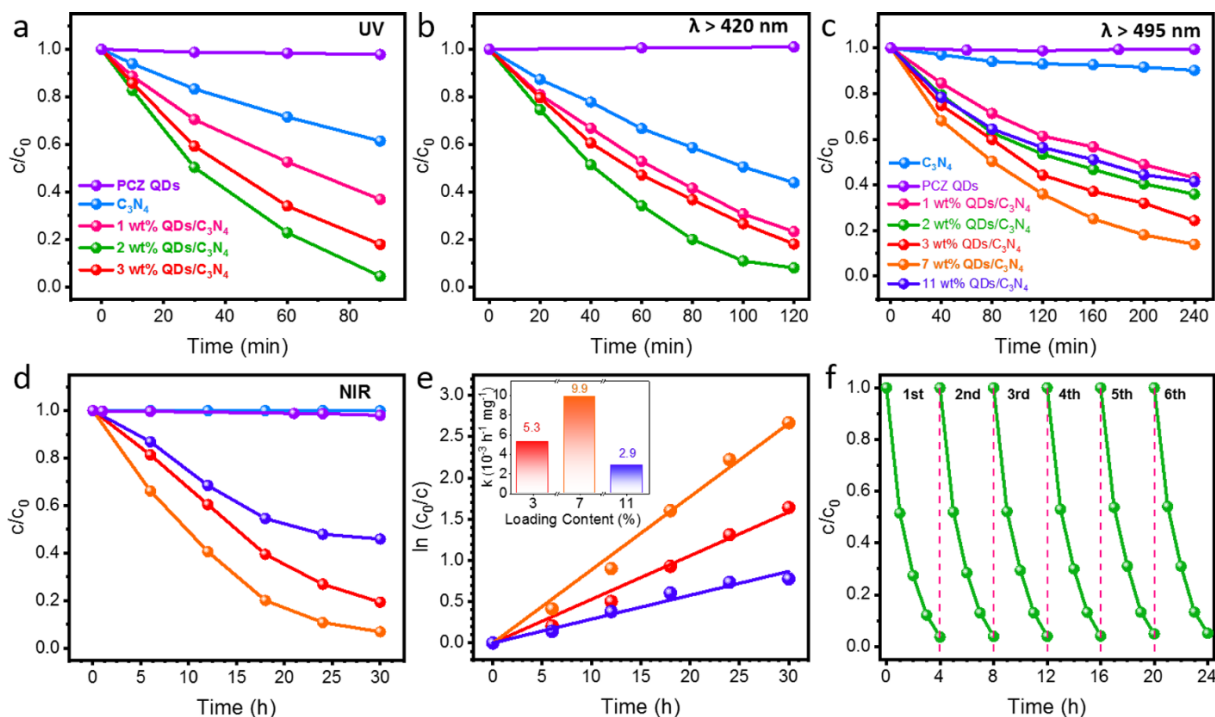


Figure 4.3 Photocatalytic degradation of MO over bare PCZ QDs and 0-11 wt% QDs/g-C₃N₄ samples under (a) UV, (b) $\lambda > 420$ nm, (c) $\lambda > 495$ nm, and (d) NIR light irradiation (980 nm). (e) The plot of $\ln(c_0/c)$ vs reaction time of (d). (f) Photocatalytic stability of 2 wt % QDs/g-C₃N₄ photocatalyst in six successive cycling reactions under simulated solar light irradiation.

Considering practical applications, the photocatalytic activity and stability of 2 wt % QDs/g-C₃N₄ photocatalyst were studied in the degradation of MO under simulated solar light illumination (AM 1.5). As displayed in Fig. S13, negligible degradation of MO was observed in the presence of bare PCZ QDs after 4 h of solar light irradiation. The 2 wt % QDs/g-C₃N₄ sample shows enhanced photocatalytic activity with a k value of $7.6 \times 10^{-2} \text{ h}^{-1} \text{ mg}^{-1}$, which is about 2.6 times higher than that of pristine g-C₃N₄ ($2.9 \times 10^{-2} \text{ h}^{-1} \text{ mg}^{-1}$). This experiment was repeated for 6 runs with the total time of 24 h and the 2 wt % QDs/g-C₃N₄ photocatalyst keeps a high activity in MO removal, indicating the as-prepared composite photocatalysts possess good stability for photocatalysis. It is noteworthy that no metal release was detected by ICP-OES in the solution after photocatalysis (Table S4.2), while increasing concentrations of Pb and Cd elements were detected for the solution of PbS@CdS QDs with increasing solar light irradiation time (Table S4.3). This is a strong evidence for the structural robustness of the thin ZnS shell and its complete coverage around the PbS@CdS core@shell QDs, further supporting the strong coupling between PCZ QDs and g-

C₃N₄. This result reveals that the use of PCZ QDs/g-C₃N₄ as a photocatalyst will not introduce secondary pollution by releasing heavy metals during water treatment.

4.3.3 Charge transfer dynamics and PEC measurements

To gain deep insights into the charge transfer pathways for the enhanced photocatalytic activities, various spectroscopic and PEC tests were carried out (Figure 4.4a-4.4f). Figure 4.4a shows the steady-state PL spectra of g-C₃N₄ and 2 wt% QDs/g-C₃N₄ samples. Under the excitation of 375 nm, they both show a peak at ~460 nm in their PL spectra, corresponding to the recombination of the photo-induced electrons and holes in g-C₃N₄.⁴²¹ The considerable PL quenching of 2 wt% QDs/g-C₃N₄ indicates that radiative recombination has vanished,^{336,428,429} which can be attributed to the efficient interfacial charge transfer of electrons from g-C₃N₄ to PCZ QDs. The charge carrier dynamics was investigated by a TRPL spectroscopy (Figure 4.4b). A bi-exponential fitting equation was found most suitable and thus applied to analyze the TRPL decay curves. The derived lifetime components and calculated average PL lifetimes are summarized in Table S4.4. 2 wt% QDs/g-C₃N₄ shows a shorter average PL lifetime (420 ± 25 ns) than g-C₃N₄ (522 ± 16 ns). The notable decrease of PL lifetime of g-C₃N₄ in the PCZ QDs/g-C₃N₄ reveals the introduction of additional non-radiative charge carrier decay or transfer pathway(s), suggesting that the addition of PCZ QDs can effectively facilitate the separation of photo-generated charge carriers in g-C₃N₄.^{404,430} The TRPL results are consistent with those of the steady-state PL spectra.

Solid-state ESR was also used to study the transfer and separation of charge carriers at room temperature (Figure 4.4c). A signal centered at the g value of 2.003 is shown in the ESR spectra of both g-C₃N₄ and PCZ QDs/g-C₃N₄, corresponding to the unpaired electrons of C atoms in the CN aromatic rings within the π-bonded nanosized clusters.^{431,432} The evidently enhanced ESR signals, when the visible light irradiation is turned on, provide evidence for the promoted photo-generation of radical pairs in the samples.^{431,432} The ESR signal of PCZ QDs/g-C₃N₄ is stronger than that of g-C₃N₄, confirming the charge transfer from g-C₃N₄ to PCZ QDs and the prohibited charge carrier recombination,^{383,433,434} which is consistent with the lower PL peak intensity of g-C₃N₄ in PCZ QDs/g-C₃N₄ sample.

In addition, to investigate the charge transfer pathways of the NIR light reaction system, the steady-state PL spectra of PCZ QDs and 7 wt% QDs/g-C₃N₄ (the optimal sample in terms of photocatalytic activity under NIR light) were measured upon the excitation of 780 nm (Figure 4.4d). Under the NIR light irradiation, only the charge carriers in PCZ QDs can be excited, and their radiative recombination generates the PL emission. In comparison to bare PCZ QDs, the

quenched PL peak intensity of the QDs in 7 wt% QDs/g-C₃N₄ manifests the hindered radiative recombination after the introduction of g-C₃N₄.

To further ascertain the transfer and separation efficiency of the photoinduced charges, PEC experiments were performed (Figure 4.4e-4.4f). Figure 4.4e displays the transient photocurrent responses of g-C₃N₄ and PCZ QDs/g-C₃N₄ samples during the on-and-off cycles under simulated solar light. The photocurrent density of PCZ QDs/g-C₃N₄ (11.3 $\mu\text{A cm}^{-2}$) is ~ 7.5 times higher than that of g-C₃N₄ (1.5 $\mu\text{A cm}^{-2}$), which reveals that the introduction of PCZ QDs can greatly promote the separation of the photoinduced charge carriers. This argument is also confirmed by the electrochemical impedance spectroscopy (EIS) measurements (Figure 4.4f). The smaller arc radius in the EIS Nyquist plots of the PCZ QDs/g-C₃N₄ sample is indicative of a lower charge transfer resistance than g-C₃N₄ both in the dark and under irradiation. All these positively contribute to the enhanced photocatalytic activity in MO removal of PCZ QDs/g-C₃N₄. Moreover, the reversible and almost unchanged photocurrent density during more than 800 s of repeated light on/off cycles is another proof of the excellent stability of the as-prepared g-C₃N₄ and PCZ QDs/g-C₃N₄ photocatalysts.

4.3.4 Detection of active species

For better understanding the underlying mechanism of photocatalytic degradation of MO, the involved active species were detected by trapping experiments using three different scavengers (Figure 4.4g). Specifically, Na₂EDTA, BQ, and t-BuOH act as the scavengers for capturing h⁺, •O₂⁻ and •OH radicals, respectively. After 4 h of solar light irradiation, in the presence of 2 wt% QDs/g-C₃N₄, the photocatalytic removal ratio of MO in BQ-added system was reduced by 90% compared to the scavenger-free system. However, the addition of Na₂EDTA and t-BuOH has almost no impact on the photocatalytic activity. The results suggest that •O₂⁻ radical plays the most important role in the photocatalytic degradation of MO by the PCZ QDs/g-C₃N₄ sample. In addition, a standard DMPO spin-trapping ESR method was used to verify the participation of •O₂⁻ (Figure 4.4h) and •OH (Figure 4.4i) radicals in the ethanol dispersion and aqueous dispersion, respectively. After visible light irradiation, both g-C₃N₄ and PCZ QDs/g-C₃N₄ samples show clear DMPO-•O₂⁻ signals. Compared with g-C₃N₄, the signal intensity in the case of PCZ QDs/g-C₃N₄ is much stronger, implying the higher concentration of •O₂⁻ radicals.^{434,435} As •O₂⁻ is generated from the reaction of excited electrons with dissolved O₂, the higher •O₂⁻ concentration can be attributed to the prominent charge separation in PCZ QDs/g-C₃N₄, which makes it more

photocatalytically efficient in MO degradation. No DMPO-•OH signals were detected in both ethanol and aqueous dispersions, which is in agreement with the trapping experiment results.

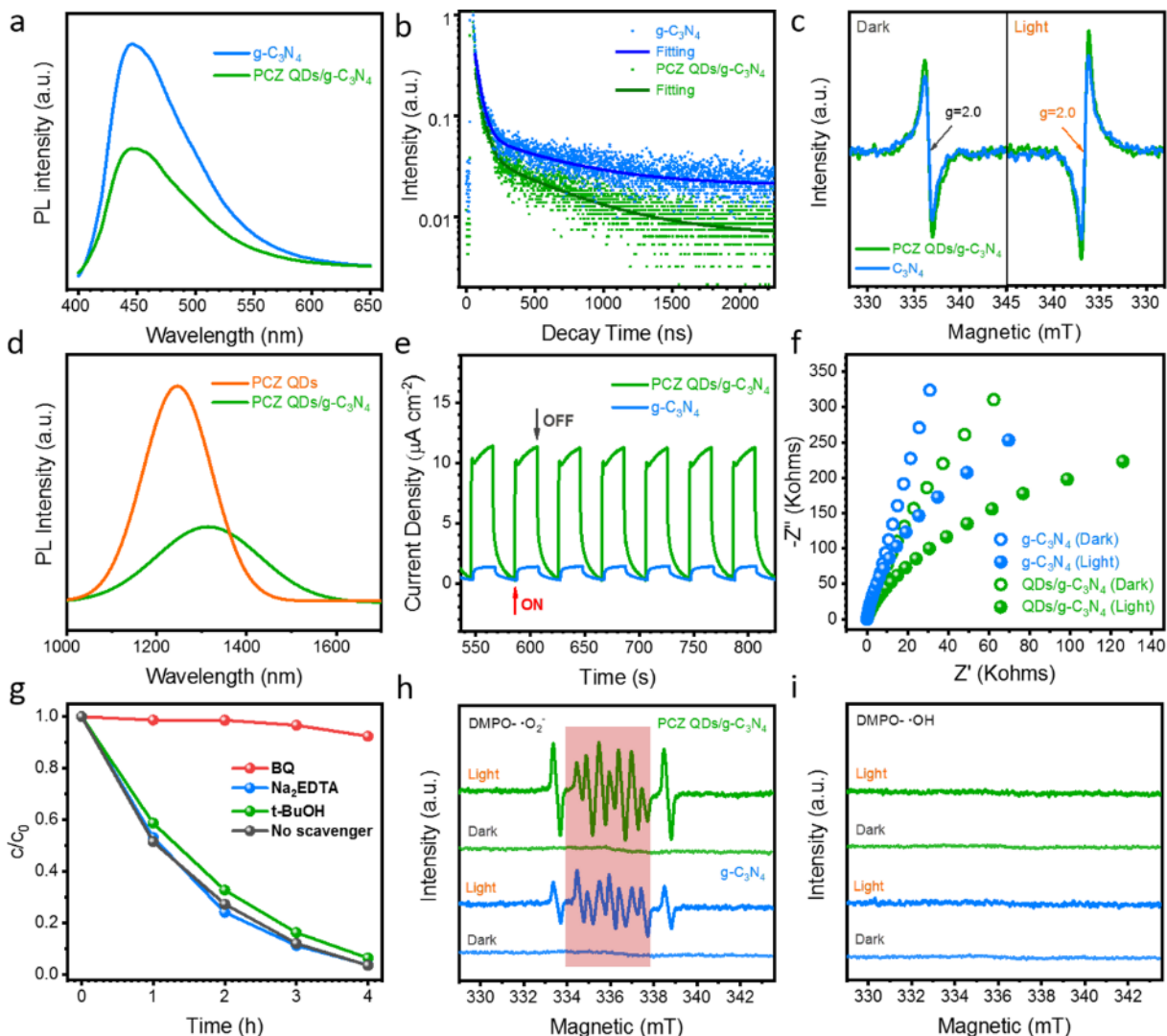


Figure 4.4 (a) PL spectra with the excitation at 375 nm, (b) TRPL decay curves with emission at 460 nm, and (c) solid-state ESR spectra in the dark and after visible light irradiation of g-C₃N₄ and 2 wt% QDs/g-C₃N₄. (d) PL spectra with the excitation at 780 nm of PCZ QDs and 7 wt% QDs/g-C₃N₄. (e) Photocurrent response and (f) EIS Nyquist plots in the dark and under simulated solar light irradiation of g-C₃N₄ and PCZ QDs/g-C₃N₄ samples. (g) Photocatalytic degradation of MO over 2 wt% QDs/g-C₃N₄ in the presence of three different scavengers under simulated solar light irradiation. DMPO spin-trapping ESR spectra of (h) •O₂⁻ and (i) •OH radicals for g-C₃N₄ and PCZ QDs/g-C₃N₄ in the dark and under visible light ($\lambda > 420$ nm) irradiation.

4.3.5 Proposed possible mechanism

Based on all the above results, the possible mechanisms of the photocatalytic degradation of MO under different light irradiations were proposed. The approximate VB and CB positions (vs vacuum level) of PCZ QDs and g-C₃N₄ were obtained from previous reports,^{381,390,412,436,437} and the corresponding energy diagram was constructed (Figure 4.5). Under UV or $\lambda > 420$ nm light

illumination, the excitations of both g-C₃N₄ and PCZ QDs take place. The charge recombination can be greatly mitigated via the charge transfer between g-C₃N₄ and PCZ QDs (Figure 4.5a). As the major absorbing and catalytic component is g-C₃N₄ in the composite, its band excitation is reasonably expected to dominate the photocatalysis process, and PCZ QDs mainly act as the acceptor of excited electrons from g-C₃N₄ to suppress the charge recombination in g-C₃N₄ and thus enhance overall photocatalytic activity. The transfer of electrons from g-C₃N₄ to PCZ QDs and the suppressed charge carrier recombination have been confirmed by steady-state PL, TRPL and solid-state ESR spectra, as well as PEC measurements. The electrons in the valence band (VB) of g-C₃N₄ are excited to the conduction band (CB) and further transferred to PCZ QDs. The electrons then react with the dissolved O₂ to produce •O₂⁻ radicals for photocatalysis, which has been verified by the trapping experiment and DMPO spin-trapping ESR method. The loading of excessive PCZ QDs can decrease the number of photons reaching the g-C₃N₄ surface due to the QDs surface coverage. Although electrons and holes can be generated due to the excitation of PCZ QDs, the competition between the absorption of PCZ QDs and g-C₃N₄ makes 2 wt% the optimal loading content of PCZ QDs under UV and λ > 420 nm light irradiation.

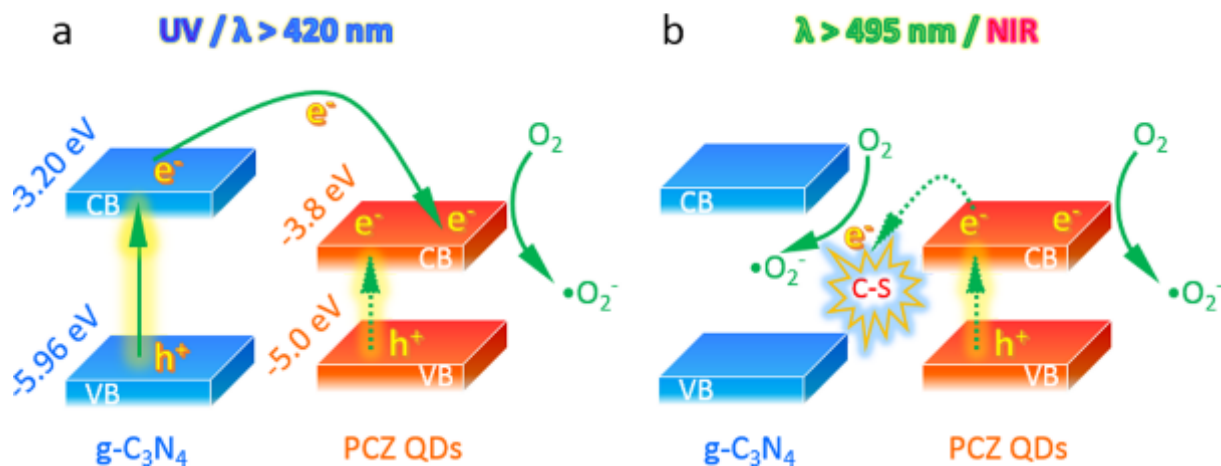


Figure 4.5 Proposed possible mechanism for the photocatalysis over PCZ QDs/g-C₃N₄ samples under a) UV or λ > 420 nm and b) λ > 495 nm or NIR light irradiation. Band energies (in eV referenced to the vacuum level) are taken from literatures.

When the system is irradiated by λ > 495 nm or NIR light (980 nm), according to the absorption spectra, the excitation of g-C₃N₄ can be excluded (Figure 4.5b). The photocatalytic absorption is solely determined by the loaded PCZ QDs. Thanks to the formed C-S bonds, which quite likely act as interfacial charge trapping sites between PCZ QDs and g-C₃N₄, the excited electrons in the PCZ QDs can be transferred to the C-S energy level and participate in the photocatalysis. The charge transfer has also been confirmed by the quenched and red-shifted steady-state PL spectra

upon excitation of 780 nm. Excessive PCZ QDs loaded on the surface of g-C₃N₄ nanosheets, although can increase light absorption, tend to aggregate and thus reduce the effectively active sites accessible to reactants (Fig. S14), resulting in the decreased photocatalytic activity. The interplay of these competing factors yields 7 wt% as the optimal loading level of PCZ QDs, leading to the best photocatalytic activity.

4.4 Conclusions

In summary, a 0D/2D photocatalyst composed of UV, visible and NIR-responsive and water-dispersible PCZ QDs/g-C₃N₄ was rationally designed and synthesized for the first time. Thanks to the broadband spectral response of uniformly distributed, ultra-small, high-quality PCZ QDs, efficient charge separation and transfer, as well as strong coupling between PCZ QDs/g-C₃N₄ by forming the C-S bond, the prepared PCZ QDs/g-C₃N₄ exhibits excellent photocatalytic activities in organic dye degradation under UV, visible and NIR light irradiations. Especially for NIR-driven photocatalysis, the composite with optimized PCZ QDs loading outperforms the best-reported photocatalysts. Remarkably, the PCZ QDs/g-C₃N₄ also possesses excellent recycling performance and no metal release was detected in the solution after photocatalysis. Through investigating the charge transfer dynamics and detecting involved active species, the underlying mechanisms for photocatalysis under different light irradiations were clearly elucidated. This work paves a way to synthesize broad-solar-spectrum 0D/2D photocatalyst that is of great potential in water treatment and extensive (photo)electronic applications.

Acknowledgements

Financial support from the Natural Sciences and Engineering Research Council of Canada (NSERC) in the context of a NSERC-Discovery Grant and NSERC-Strategic Grant (with the support of Canadian Solar Inc.) and le Fonds de recherche du Quebec-Nature et technologies (FRQNT) is greatly appreciated. M.C. is also grateful to the Canada Research Chairs Program. Q.Z. acknowledges scholarships from the China Scholarship Council (CSC, No. 201506220152) and FRQNT (258513).

4.5 Supporting Information

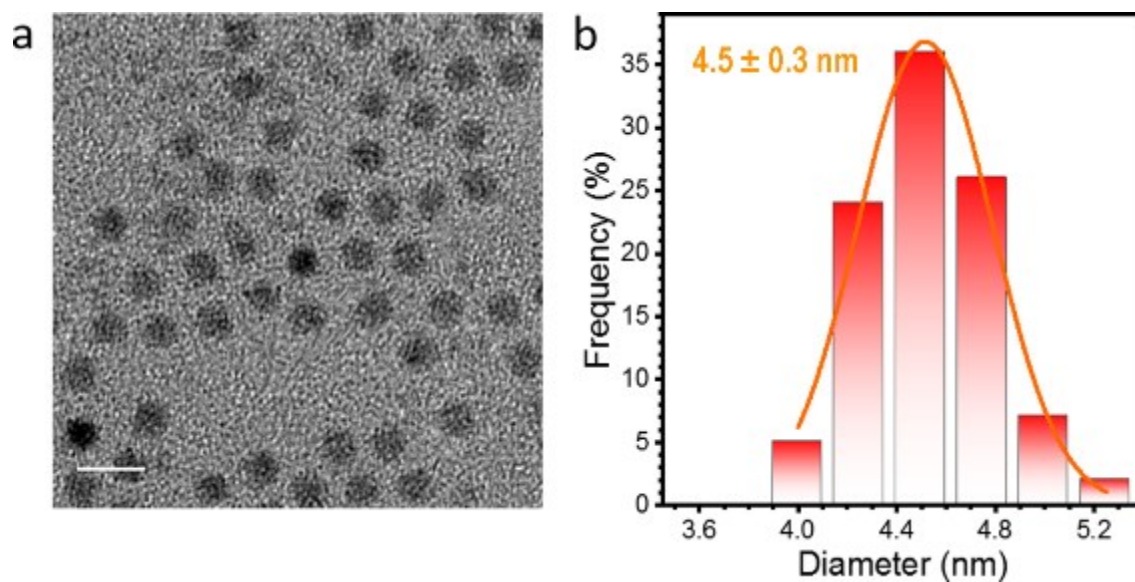


Figure S4.1 TEM image of prepared PbS QDs and (b) size distribution. Scale bar: 10 nm.

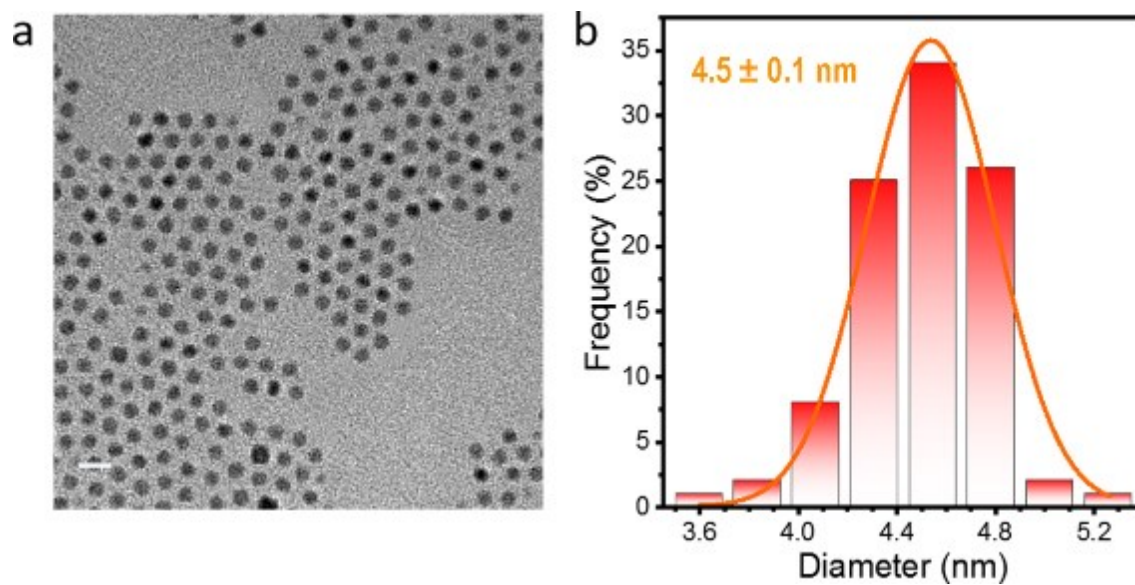


Figure S4.2 TEM image of prepared PbS@CdS core@shell QDs and (b) size distribution. Scale bar: 10 nm.

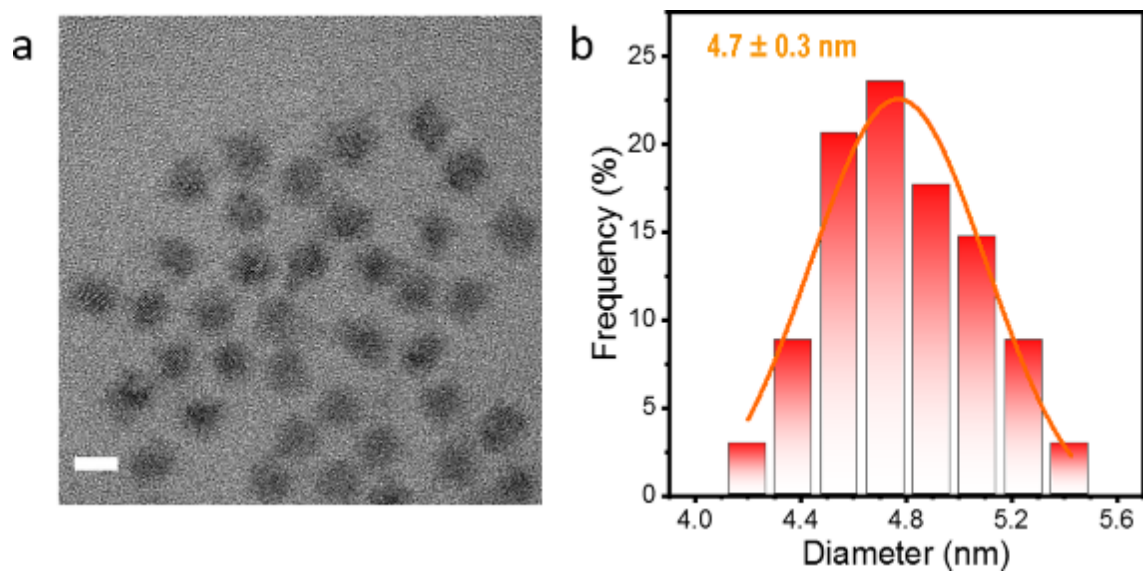


Figure S4.3 (a) TEM image of prepared PCZ core@shell@shell QDs and (b) size distribution. Scale bar: 5 nm.

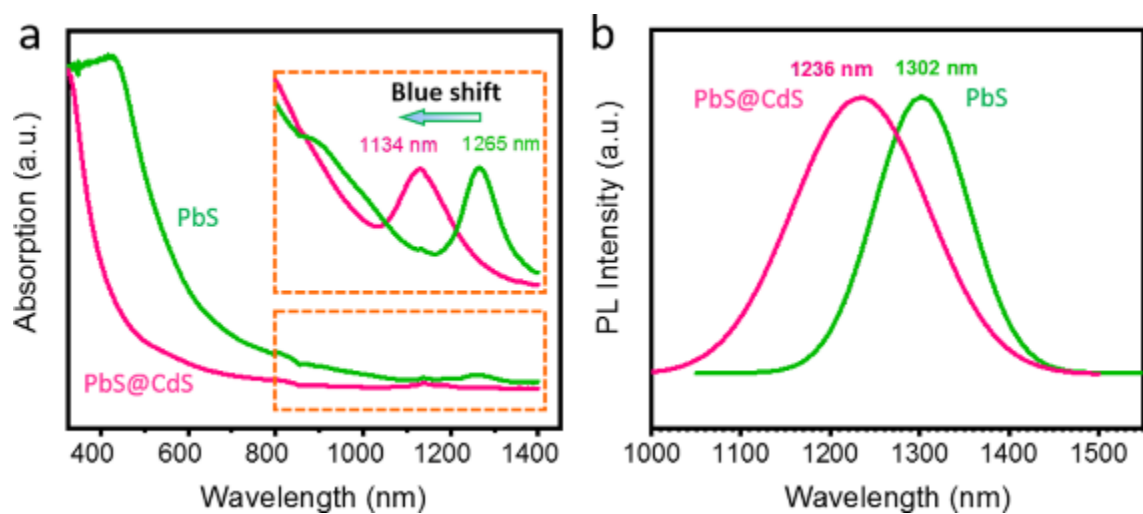


Figure S4.4 (a) Absorption and (b) steady-state photoluminescence (PL) spectra of PbS, and PbS@CdS core@shell QDs.

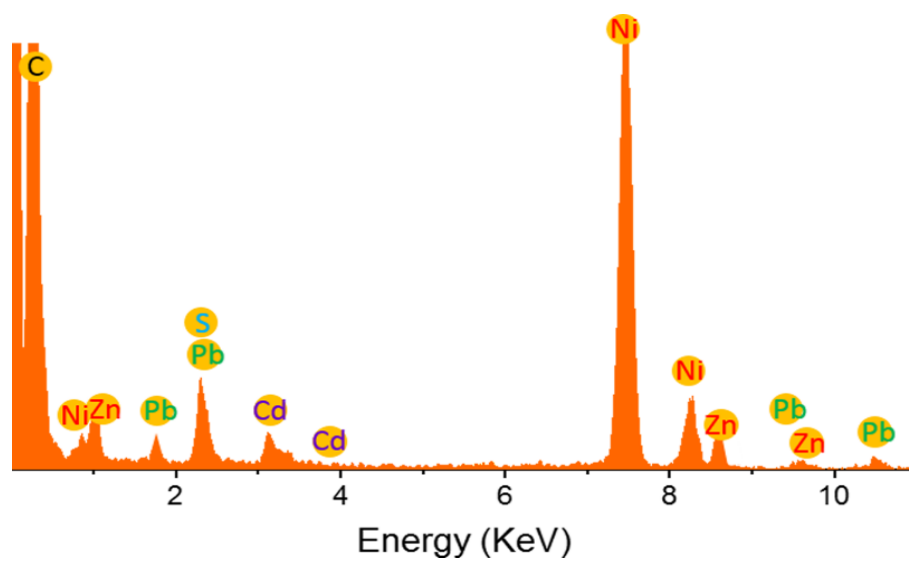


Figure S4.5 Energy dispersive X-ray spectroscopy (EDX) spectrum of PCZ QDs sample.

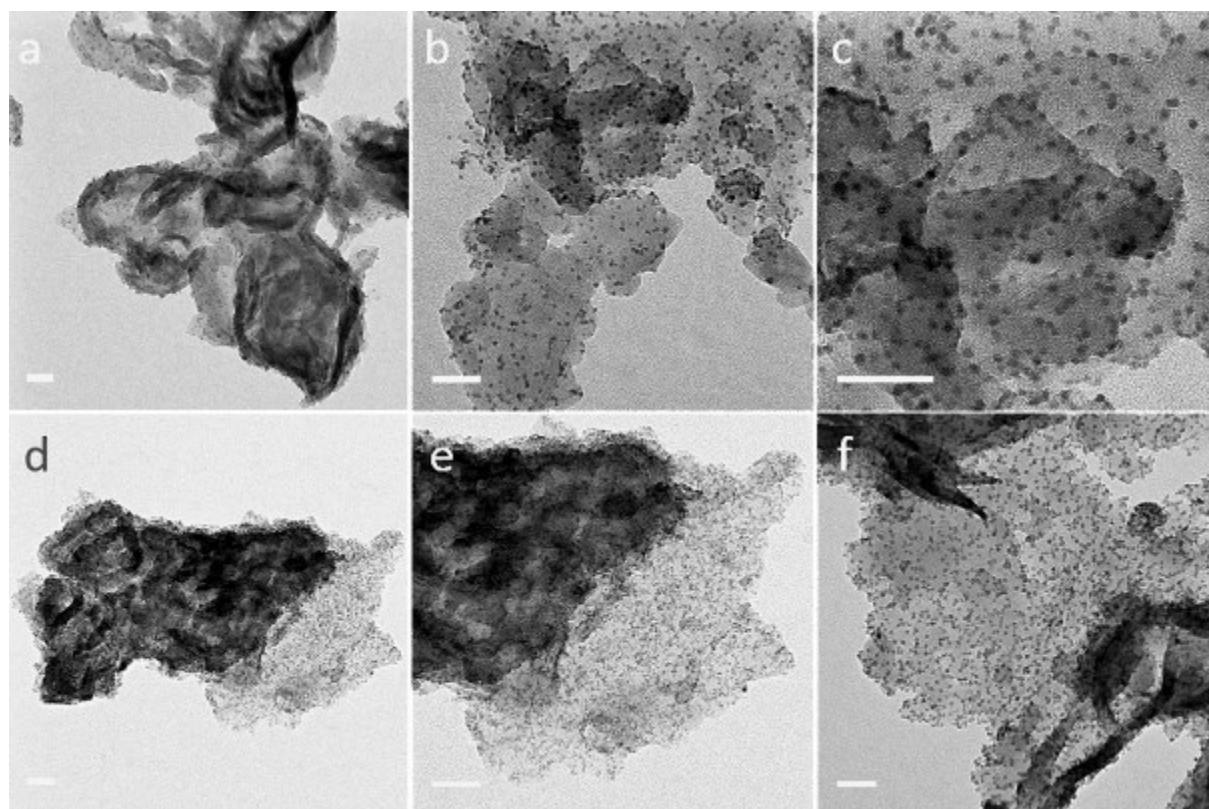


Figure S4.6 (a) TEM images of (a-c) 1 wt% QDs/g-C₃N₄ and (d-f) 7 wt% QDs/g-C₃N₄. Scale bars: 50 nm.

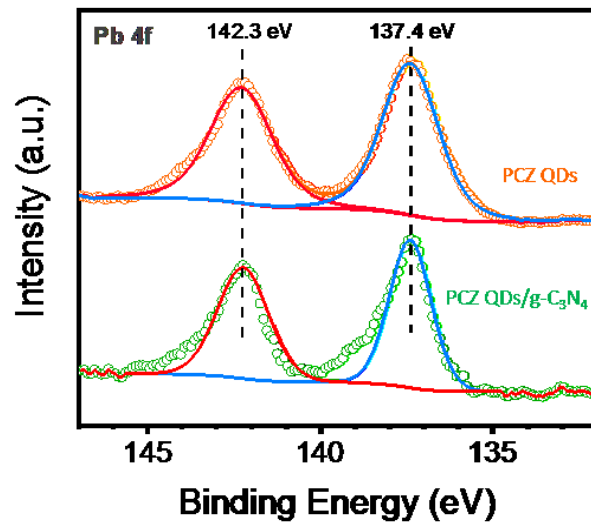


Figure S4.7 High-resolution Pb 4f XPS spectra of PCZ QDs and PCZ QDs/g-C₃N₄.

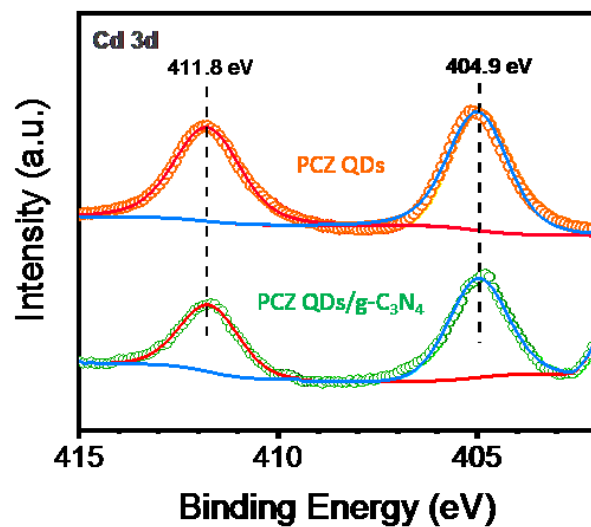


Figure S4.8 High-resolution Cd 3d XPS spectra of PCZ QDs and PCZ QDs/g-C₃N₄.

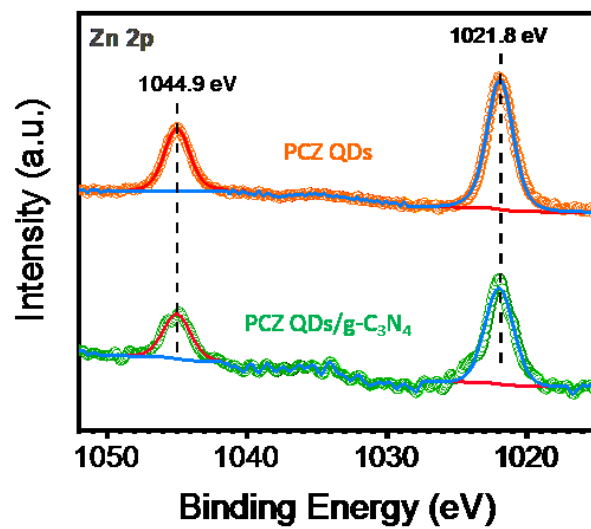


Figure S4.9 High-resolution Zn 2p XPS spectra of PCZ QDs and PCZ QDs/g-C₃N₄.

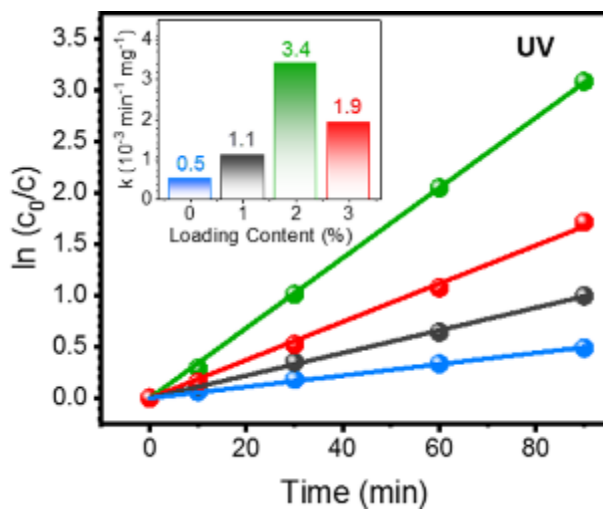


Figure S4.10 Plot of $\ln(c_0/c)$ vs time of photocatalytic degradation of MO under UV light irradiation.

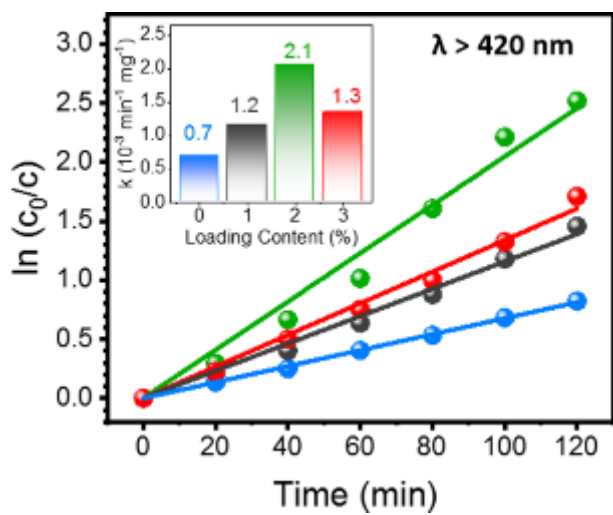


Figure S4.11 Plot of $\ln(c_0/c)$ vs time of photocatalytic degradation of MO under $\lambda > 420 \text{ nm}$ light irradiation.

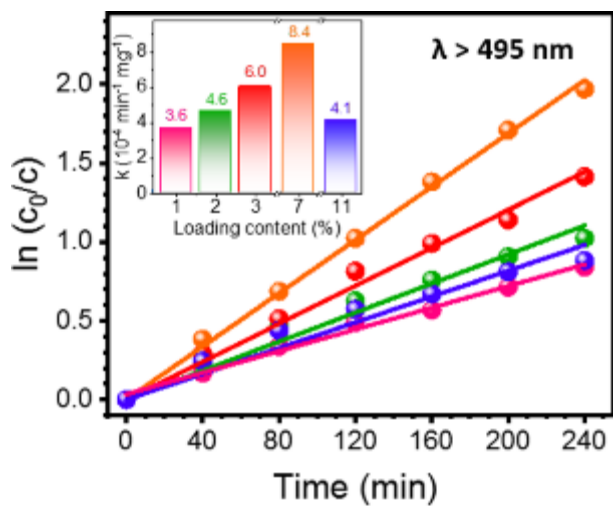


Figure S4.12 Plot of $\ln(c_0/c)$ vs time of photocatalytic degradation of MO under $\lambda > 495 \text{ nm}$ light irradiation.

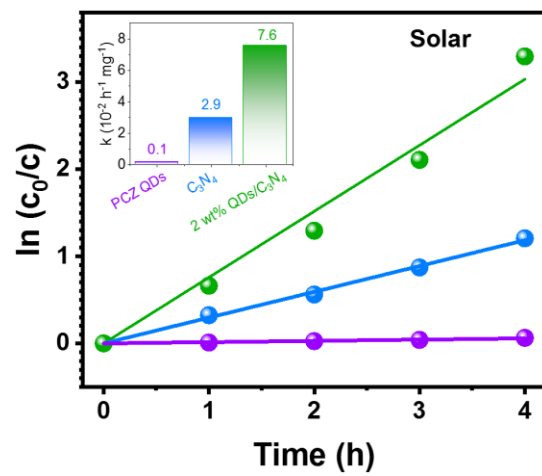


Figure S4.13 Plot of $\ln(c_0/c)$ vs time of photocatalytic degradation of MO under simulated solar light irradiation.

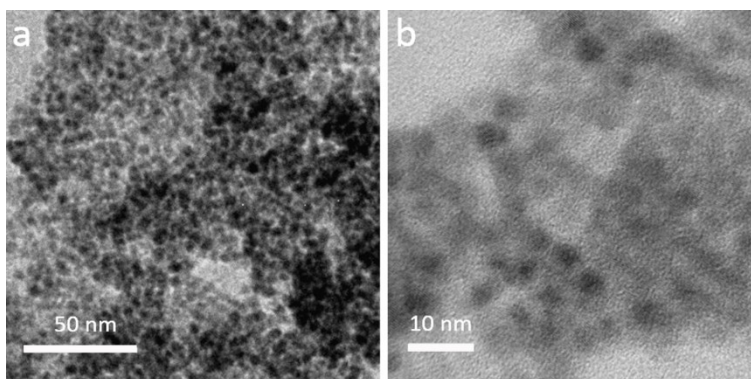


Figure S4.14 TEM images of 11 wt% QDs/g- C_3N_4 sample at different magnifications. Serious agglomerations of PCZ QDs occur in this sample.

Table S4.1 Reaction rates for photocatalytic degradation of organics under NIR light irradiation in recent published literatures.

References	Photocatalyst	Organics ^e	Catalyst concentration (mg L ⁻¹)	Light source	K value (10 ⁻³ h ⁻¹ mg ⁻¹)
188	Au-NYF/g-C ₃ N ₄ ^a	MO	400	980 nm 2 W laser	3.5
145	NYF@TiO ₂ -Au ^a	MO	1000	980 nm 2W laser	7.0
373	BiVO ₄ /CF ^b	MO	1000	980 nm 2W laser	0.56
195	NYF/Cu ₂ ZnSnSe ₄ ^c	RhB	300	>760 nm 150 W Xe lamp	9.5
184	NYF@TiO ₂ /RGO ^d	MB	1000	980 nm 2W laser	2.8
		MO	1000	980 nm 2W laser	2.0
260	Sb ₂ S ₃ /g-C ₃ N ₄	MO	1000	>760 nm 300 W Xe lamp	6.18
This work	PCZ QDs/g-C ₃ N ₄	MO	400	980 nm 2W laser	9.9

^a NYF (NaYF₄:Yb³⁺,Er³⁺,Tm³⁺); ^b CF (CaF₂:Er³⁺,Tm³⁺,Yb³⁺); ^c NYF (NaYF₄:Yb³⁺,Tm³⁺); ^d NYF@TiO₂/RGO (NaYF₄:Yb³⁺,Tm³⁺@TiO₂/ reduced graphene oxide); ^e RhB (rhodamine B), MB (methyl blue), MO (methyl orange) dyes

Table S4.2 ICP-OES detection of metals released into the reaction solution after 24 h of photocatalysis under simulated solar light irradiation in the presence of PCZ QDs/g-C₃N₄.

Elements	Wavelength (nm)	Concentration (ppm) ^a	Detecting Limit (ppm)
Pb	217.000	-	0.10
	220.353	-	0.14
Cd	214.439	-	0.020
	228.802	-	0.015
Zn	213.857	-	0.009
	206.200	-	0.025

^a - The concentration is below detecting limit.

Table S4.3 ICP-OES detection of metals released into the reaction solution for PbS@CdS QDs under simulated solar light irradiation.

Time (h)	Elements	Wavelength (nm)	Concentration (ppm) ^a	Detecting Limit (ppm)
0	Pb	217.000	-	0.10
		220.353	-	0.14
	Cd	214.439	-	0.020
		228.802	-	0.015
0.5	Pb	217.000	0.97	0.10
		220.353	0.73	0.14
	Cd	214.439	0.05	0.020
		228.802	0.05	0.015
1	Pb	217.000	1.31	0.10
		220.353	1.29	0.14
	Cd	214.439	0.09	0.020
		228.802	0.08	0.015
12	Pb	217.000	4.30	0.10
		220.353	4.25	0.14
	Cd	214.439	0.26	0.020
		228.802	0.25	0.015

^a - The concentration is below detecting limit.

Table S4.4 PL Lifetime of g-C₃N₄ and PCZ QDs/g-C₃N₄ samples obtained from TRPL measurements with excitation and emission at 408 nm and 460 nm, respectively.

Sample	τ_1 (a ₁)	τ_2 (a ₂)	τ
g-C ₃ N ₄	48 ns (64%)	591 ns (36%)	522 ± 16 ns
PCZ QDs/g-C ₃ N ₄	45 ns (67%)	490 ns (33%)	420 ± 25 ns

5 METAL-FREE BLACK PHOSPHORUS/CARBON NITRIDE

Ice-Assisted Synthesis of Black Phosphorus Nanosheets as a Metal-Free Photocatalyst: 2D/2D Heterostructure for Broadband H₂ Evolution

Synthèse Assistée Par La Glace De Nanofeuilles De Phosphore Noir En Photocatalyseur Sans Métal: Hétérostructure 2D/2D Pour L'évolution Large Bande Du H₂

Authors:

Qingzhe Zhang[†], Shengyun Huang[†], Jiujun Deng[‡], Deepak Thrithamarassery Gangadharan[†], Fan Yang[†], Zhenhe Xu[§], Giacomo Giorgi^{||}, Maurizia Palummo[⊥], Mohamed Chaker[†], Dongling Ma^{**†}

[†] Institut National de la Recherche Scientifique (INRS), Centre Énergie Matériaux et Télécommunications, Université du Québec, 1650 Boulevard Lionel-Boulet, Varennes, Québec J3X 1S2, Canada

[‡] Institute for Energy Research Jiangsu University, Zhenjiang, Jiangsu 212013, China

[§] The Key Laboratory of Inorganic Molecule-Based Chemistry of Liaoning Province, College of Applied Chemistry, Shenyang University of Chemical Technology, Shenyang 110142, China

^{||} Dipartimento di Ingegneria Civile e Ambientale (DICA), Università degli Studi di Perugia, Via G. Duranti, Perugia 06125 and CNR-ISTM, Perugia 06123, Italy

[⊥] Dipartimento di Fisica, Università degli Studi di Roma "Tor Vergata", Via della Ricerca Scientifica 1, Roma 00133, Italy

Title of the journal:

Advanced Functional Materials

Publication Date: May 9, 2019

Volume 29, Issue 28, Pages 1902486 (1 to 10)

DOI: 10.1002/adfm.201902486

Contribution of authors:

Qingzhe Zhang and Prof. Dongling Ma conceived and designed the research. Qingzhe Zhang prepared all the samples and conducted most of the characterizations, such as XRD, XPS, UV-

Visible-NIR absorption spectra, and photoelectrochemical measurements and all the photocatalytic H₂ evolution reactions. Qingzhe Zhang measured the Zeta potential of samples with the assistance of Galyna Shul from Université du Québec à Montréal (UQAM). Gwenaël Chamoulaud from UQAM and Deepak Thrithamarassery Gangadharan carried out the AFM measurement. Fan Yang assisted me in the measurement of PL spectra. The TEM measurements were performed by Jean-Philippe Masse at Polytechnique Montréal. Theoretical calculations and the related analysis were provided by Prof. Giacomo Giorgi and Prof. Maurizia Palummo from Università degli Studi di Perugia (Italy) and Università degli Studi di Perugia (Italy), respectively. Prof. Mohamed Chaker and Prof. Dongling Ma supervised the experimental work. Qingzhe Zhang wrote the manuscript, which was carefully modified by Prof. Dongling Ma. Prof. Mohamed Chaker also gave good comments on revising the manuscript. All authors discussed the results and commented on the manuscript.

Link between articles:

To more efficiently utilize solar photons from UV to NIR regions, an effective heterojunction composed of 0D NIR-responsive PCZ QDs and 2D g-C₃N₄ nanosheets was rationally constructed and demonstrated in Chapter 4. The broadband optical absorption of high-quality PCZ QDs highly dispersed on the surface of the g-C₃N₄ nanosheets and their strong interaction yield efficient charge transfer between them and endow PCZ QDs/g-C₃N₄ with effective photocatalytic activity from UV to NIR regions. Although PCZ QDs/g-C₃N₄ showed good recycling performance and no metal release was detected in the solution after photocatalysis, the use of heavy-metal based QDs always constitutes a big concern in the application of environmental purification.

To address this concern, to utilize solar energy more environmentally-friendly, without introducing heavy-metal containing materials, and more cost-effectively, a completely metal-free 2D/2D heterojunction of BP/g-C₃N₄ was designed and synthesized. The introduction of narrow-bandgap BP is expected to endow g-C₃N₄ with broadband activity in photocatalytic H₂ evolution. Furthermore, the 2D/2D heterojunction is supposed to promote charge separation, make BP stable and make BP/g-C₃N₄ possess high activity and long-term stability in H₂ evolution.

5.1 Introduction

Solar H₂ evolution has shown great potential as a green technology in solving energy crisis.^{44,438-440} Taking economic and environmental factors into consideration, the development of efficient, low-cost, stable and nontoxic photocatalyst is highly desired and crucial for the widespread implementation of solar fuel technology. For acquiring the above listed beneficial features, visible-light-responsive graphitic carbon nitride (g-C₃N₄), a two-dimensional (2D) metal-free photocatalyst, has been extensively explored in photocatalysis. Though g-C₃N₄ was discovered to be feasible for photocatalytic water splitting, obtaining a relatively high efficiency of H₂ production still largely relies on the loading of noble metal co-catalysts because of the high recombination rate of the charge carriers in g-C₃N₄.^{102,341,384,441,442} Furthermore, the relatively wide bandgap (2.7 eV) confines its light response mainly into the ultraviolet (UV) range and only slightly into a narrow region of the visible light range ($\lambda < 460$ nm).^{115,188} To solve these problems, numerous strategies have been developed, mainly including morphology tuning, doping with metal/non-metal ions, and heterojunction creation.^{93,94,328,368,443} However, quite limited progresses have been achieved thus far. Aiming to enhance the harvesting of solar light efficiently and economically, the development of novel g-C₃N₄-based metal-free photocatalysts with a broader photo-response range is of great significance.

Black phosphorus (BP), a layered material that consists of corrugated atomic planes with strong intra-layer chemical bonding and weak interlayer Van der Waals interactions, has attracted tremendous interest of material scientists. Since the successful preparation of 2D BP with atom-thick layer in early 2014, it has provoked a surge of research with its enticing electrical and optical properties.^{279,282,291,444-449} Differentiating from previously reported 2D nanomaterial, such as graphene, BP possesses a tunable thickness-dependent bandgap that spans from ~0.3 eV (bulk) to ~2.0 eV (monolayer) in addition to sufficiently high carrier mobility and photo-electronic response.^{279,291,445,447-449} These favorable properties render BP, particularly few-layer BP nanosheets (≤ 10 nm in thickness), a fascinating candidate for diverse applications in transistors, photodetectors, solar cells, bio-imaging and phototherapy.^{280,449-455} Notably, BP has demonstrated its great potential as a broadband photocatalyst for the harvesting of solar energy due to its narrow and direct bandgap.^{58,319,456-459} However, certain inherent problems existing in the exfoliated BP nanosheets bring practical challenges for their actual application. For example, BP is very reactive to moisture and ambient oxygen, and can be easily oxidized due to the exposed lone pairs at its surface.^{289,293-295,447,453,458,460} The roughening caused by the exfoliation can further accelerate the

surface oxidation, which may proceed exponentially during the first hour after exfoliation.²⁹⁴ As a consequence, the semiconducting properties of BP deteriorate rapidly, reflected from significantly increased contact resistance and reduced carrier mobility.^{289,293,294} It is thus of paramount importance to develop effective strategies to retard or, even better, completely eliminate the degradation of BP. Recently, several approaches were developed to protect BP from oxidation with various levels of success.^{449,461-464} Among them, the non-covalent surface coverage of BP with other inert 2D materials, such as poly (methyl methacrylate), graphene or hexagonal boron nitride, was proposed as an effective way.^{289,462} Hence, it is rationally anticipated that the combination of BP with g-C₃N₄ nanosheets can highly likely yield both enhanced stability and broadband solar harvesting capability in photocatalytic H₂ production.

For the preparation of few-layer BP nanosheets, the mechanical and liquid exfoliation from bulk BP has been extensively used.^{293,460,465-467} As BP possesses stronger interlayer interactions compared with graphene and other 2D materials, the exfoliation by ultrasonication would be difficult and would require long processing time (>15 h) or a sonicator with high power.^{293,460,465-467} However, the yield of few-layer BP nanosheets is still very low.^{293,467} As the P-P bond is remarkably weaker than the C-C bond, such long duration or high power of sonication are known to generate nanosheets with reduced lateral size and anomalous structural defects.^{293,468} In addition to the instability, such structural features can also accelerate charge carrier recombination and restrict the practical applications of BP in electronics and optoelectronics.

Herein, we present a novel, time-effective ice-assisted exfoliation method to prepare few-layer BP nanosheets for the first time. It led to the greatly improved yield of few-layer BP nanosheets, while required much shorter time and largely reduced power for liquid exfoliation from bulk BP. To gain long-term stability under ambient atmosphere, the few-layer BP and g-C₃N₄ nanosheets were integrated into a single, 2D-on-2D architecture (BP/g-C₃N₄). As a result, the oxidative degradation of BP was greatly inhibited. The as-synthesized metal-free BP/g-C₃N₄ photocatalysts exhibit high photocatalytic H₂ evolution efficiency from water and excellent stability under broadband light irradiation. This work opens a new facile path for the fast preparation of high-quality BP nanosheets with high yield and renders a great promise for BP-based photocatalysts for efficient solar H₂ evolution.

5.2 Results and Discussions

5.2.1 Preparation of BP nanosheets and BP/g-C₃N₄ photocatalysts

To prepare BP nanosheets, bulk BP crystals were exfoliated in N-Methyl-2-pyrrolidone (NMP) using a NMP-ice-assisted ultrasonication method, which is detailed in the Experimental Section and schematically illustrated in Figure 5.1a. When the bulk BP powder is dispersed into NMP, the space between BP layers is filled with this solvent. As the melting point of NMP is -24 °C, after being placed into direct contact with liquid nitrogen bath, the dispersion starts to freeze. The gradually grown NMP ice crystals intercalate into BP layers to enlarge the interlayer spacing of BP, which largely reduces the interlayer Van der Waals interactions and is favourable for the next-step easy exfoliation to generate BP nanosheets. Subsequently, the frozen dispersion undergoes ultrasonication, and the BP nanosheets are successfully exfoliated from the bulk BP. The ultrasonic vibration of NMP ice between the layers facilitates the exfoliation process. The required total time and the output power of the sonicator were less than 2 h and 70 W, respectively. Compared with the conventional liquid phase exfoliation,^{293,460,465-467} both the processing time and sonication power are greatly reduced in our developed method. As a result, high-quality BP nanosheets with larger lateral size and less anomalous structural defects were obtained.^{293,468} Furthermore, a high yield of few-layer BP nanosheets was achieved with this unique approach. According to the inductively coupled plasma optical emission spectroscopy (ICP-OES) analysis, 18.75 mg of few-layer BP nanosheets were obtained from 25 mg of bulk BP with a yield of 75%, which is much higher than previously reported values (Table S5.1 in the Supporting Information). The obtained BP nanosheet-in-isopropanol (IPA) dispersion is brown and very stable, and there is no aggregation and color change over four weeks during storage (Figure S5.1a-5.1b). To form the 2D-on-2D assembly, g-C₃N₄ powder was introduced into various volumes of BP dispersion (Figure S5.1c). Much precipitation was observed at the bottom of the solution, meanwhile the supernatant turned to colorless and transparent after incubation at room temperature for 30 min (Figure S5.1d), suggesting the successful integration and high coupling efficiency of BP with g-C₃N₄ nanosheets. Figure S5.1e presents the Zeta potentials of BP and g-C₃N₄ in IPA, which are positive and negative, respectively, at pH around 7 that is the pH value of the coupling solution. It is clear that the strong electrostatic interaction between BP and g-C₃N₄ contributes to their efficient integration. In the current investigation, three BP/g-C₃N₄ composites containing 3, 10 and 15% (in mass) of BP were prepared.

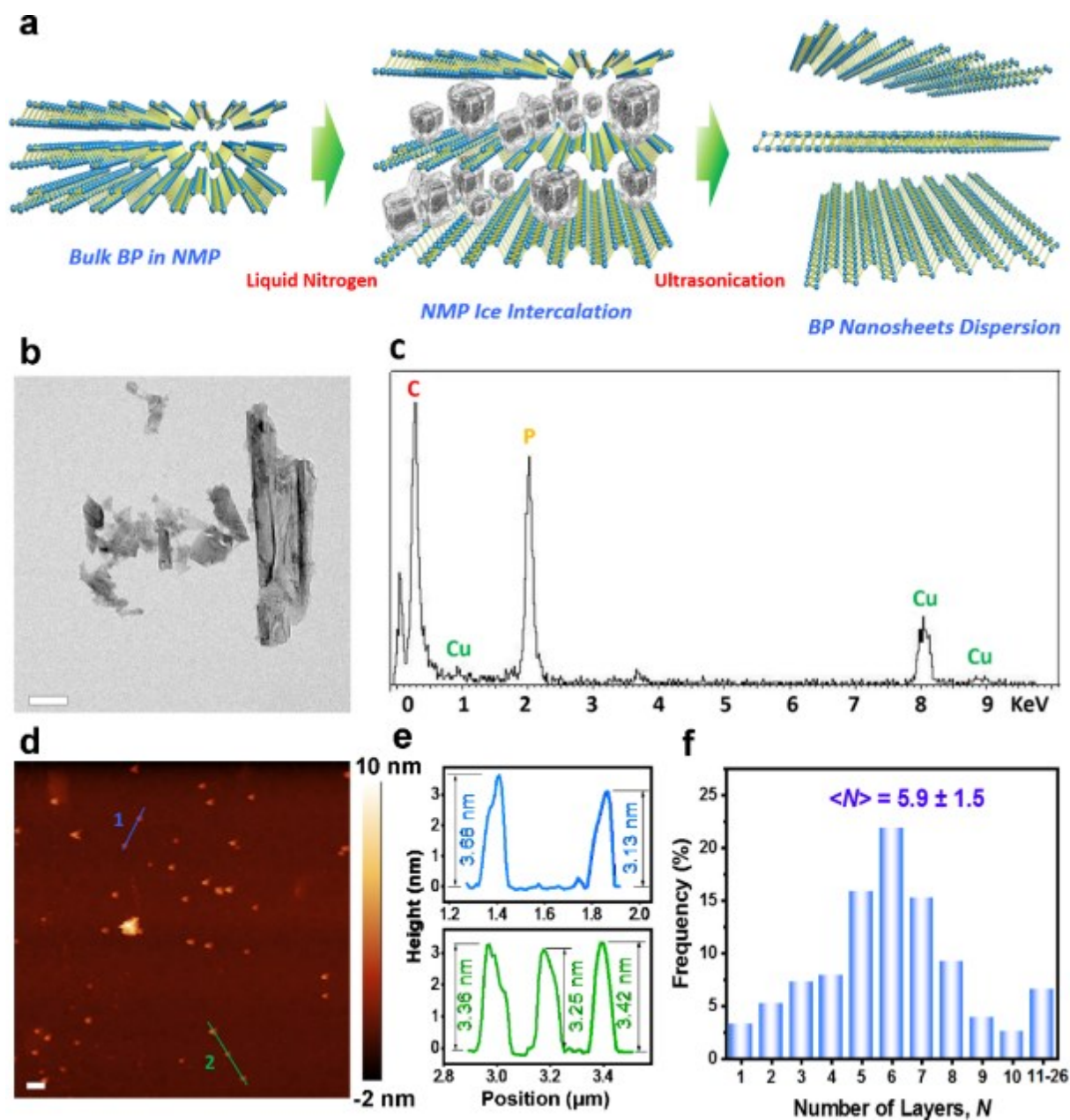


Figure 5.1 (a) Schematic illustration of the preparation of BP nanosheets with NMP-ice-assisted exfoliation method. (b) TEM image of BP nanosheets and (c) EDX spectrum of (b). (d) Tapping mode AFM topographical image of few-layer BP nanosheets. Scale bars in (b) and (d) are 500 nm. (e) The height profiles of BP nanosheets along the blue Line 1 and green Line 2 in (d). (f) Distribution of BP layers calculated from the height profiles of 150 BP nanosheets in AFM images.

5.2.2 Morphological and structural characterization

The morphology of the as-prepared BP nanosheets was characterized by a transmission electron microscope (TEM). Typical TEM images of BP nanosheets show a lamellar morphology with a lateral size of 50 nm to 3 μm (Figure 5.1b and Figure S5.2a-5.2d). Only the peaks of C, Cu and P elements were observed in the the energy-dispersive X-ray (EDX) spectrum (Figure 5.1c),

indicating that pure BP without any detectable oxidation was obtained *via* the NMP-ice-assisted exfoliation method. The thickness distribution of BP nanosheets was investigated using atomic force microscopy (AFM) height measurements (Figure 5.1d-5.1f). Lines 1 and 2 in Figure 5.1d are randomly selected and their corresponding height profiles are displayed in Figure 5.1e. Assuming the thickness of a monolayer BP is 0.53 nm,^{280,295,450} the number of layers of the generated BP nanosheets could be estimated from the AFM height measurements. Figure 5.1f shows the statistical histogram of the number of BP layers, which was obtained from the height profiles of 150 randomly selected individual BP nanosheets in AFM images. The mean number of layers was determined to be $\langle N \rangle = 5.9 \pm 1.5$, and about 93% of the observed BP nanosheets have a thickness of less than 10 nm. The large pieces observed in AFM images are due to single thicker BP or stacking of several BP sheets during sample preparation. A higher magnification AFM image better shows the sheet morphology (Figure S5.2d).

The g-C₃N₄ shows a free-standing graphene-like wrinkled nanosheet structure (Figure 5.2a). As displayed in Figure 5.2b-5.2d, the initial morphologies of BP and g-C₃N₄ nanosheets were remained after their integration (here we use 3 wt% BP/g-C₃N₄ as an example). The nanosheets marked with arrows in Figure 5.2d are supposed to be BP considering their relatively “regular” edges, which are further corroborated by the high-angle annular dark field (HAADF) scanning TEM (STEM) image (Figure 5.2e) and corresponding STEM-EDX elemental mappings (Figure 5.2f-5.2i). The STEM-EDX mapping of C, N and P clearly confirms the co-existence of g-C₃N₄ and BP, and shows the stacking and the close interaction of these two components. The high-resolution TEM (HRTEM) image reveals lattice fringes of 0.34 nm and 0.26 nm, attributed to the (021) and (040) planes of the BP crystals (Figure 5.2j), respectively.⁴⁵³ The presence of C, N and P peaks indicates the successful preparation of BP/g-C₃N₄ hybrid nanosheets with high purity and without detectable oxidative degradation (Figure 5.2k), which is consistent with the STEM-EDX mapping results and is further verified by the following X-ray photoelectron spectroscopy (XPS) analysis.

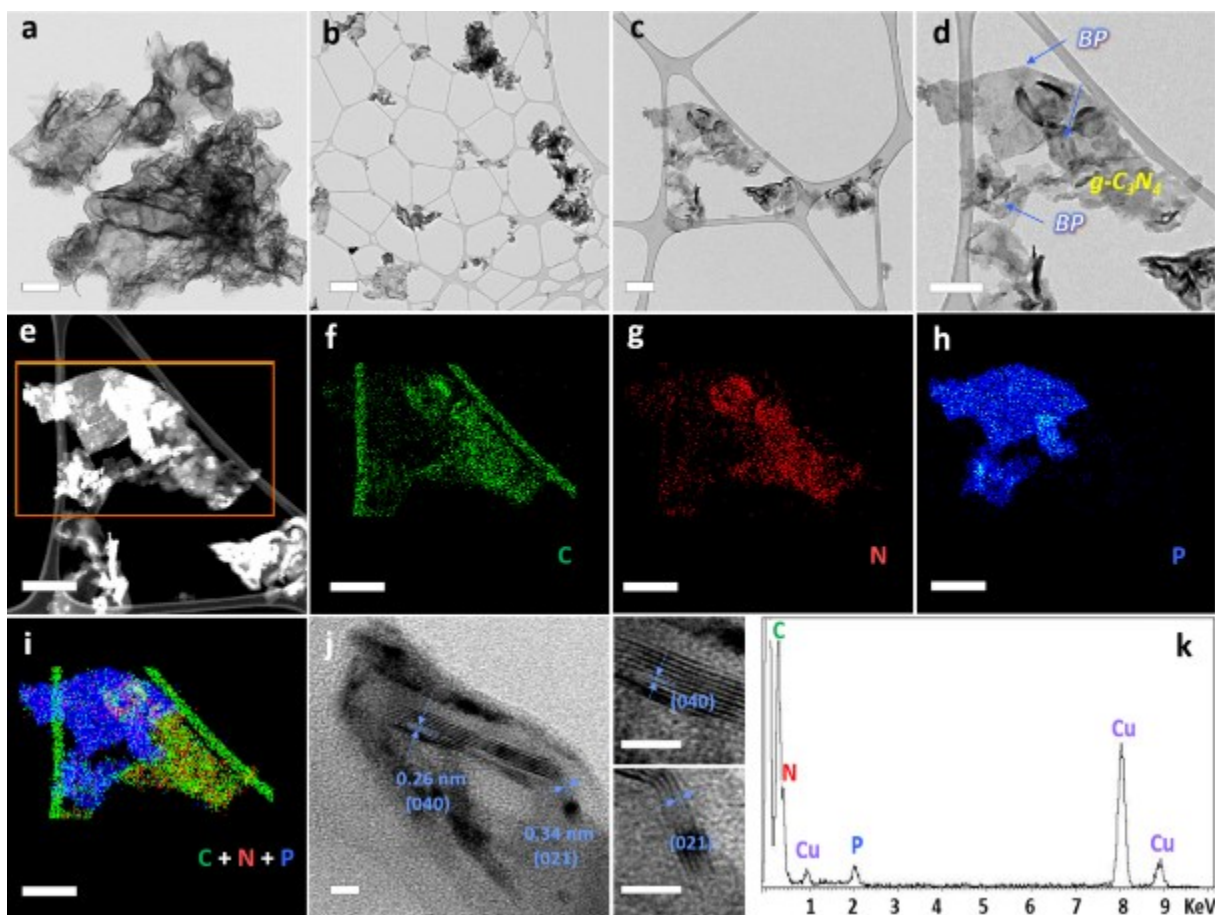


Figure 5.2 Typical TEM images of (a) g-C₃N₄ and (b-d) BP/g-C₃N₄ with different magnifications. (e) HAADF STEM image of (d), (f-i) STEM-EDX mapping of C, N, P, and the overlay of all the elements of the selected area in (e). (j) HRTEM image of BP/g-C₃N₄, and (k) EDX spectrum of (j). Scale bars: (a) and (c-i), 250 nm; (b), 1 μ m; (j), 5 nm. The TEM grids used in (a), (j) and (k) are carbon film coated copper grids, and those used in the other figures are lacey carbon film coated nickel grids.

The composition and the chemical states of the as-prepared samples are assessed using XPS (Figure 5.3 and Figure S5.3). In the XPS survey spectra of 3 wt% BP/g-C₃N₄ (Figure S5.3), only the peaks assigned to C, N, O and P elements were observed, signifying the high purity of the prepared samples and the successful integration of BP and g-C₃N₄ nanosheets. As previously reported, O1s peak was observed in the XPS spectrum of g-C₃N₄, which results from the O₂ or H₂O adsorbed on the sample surface.^{469,470} The similar atomic O percentages of g-C₃N₄ (3.61%) and BP/g-C₃N₄ (3.59%) strongly support that no further oxidation occurred during the preparation of BP/g-C₃N₄ hybrid sample (Table S5.2). All these results suggest the remarkable coupling efficiency between BP and g-C₃N₄ nanosheets. To specify which bonds form in the prepared BP/g-C₃N₄ sample, peak deconvolution was performed for the C1s, N1s and P2p XPS spectra (Figure 5.3a-5.3c).

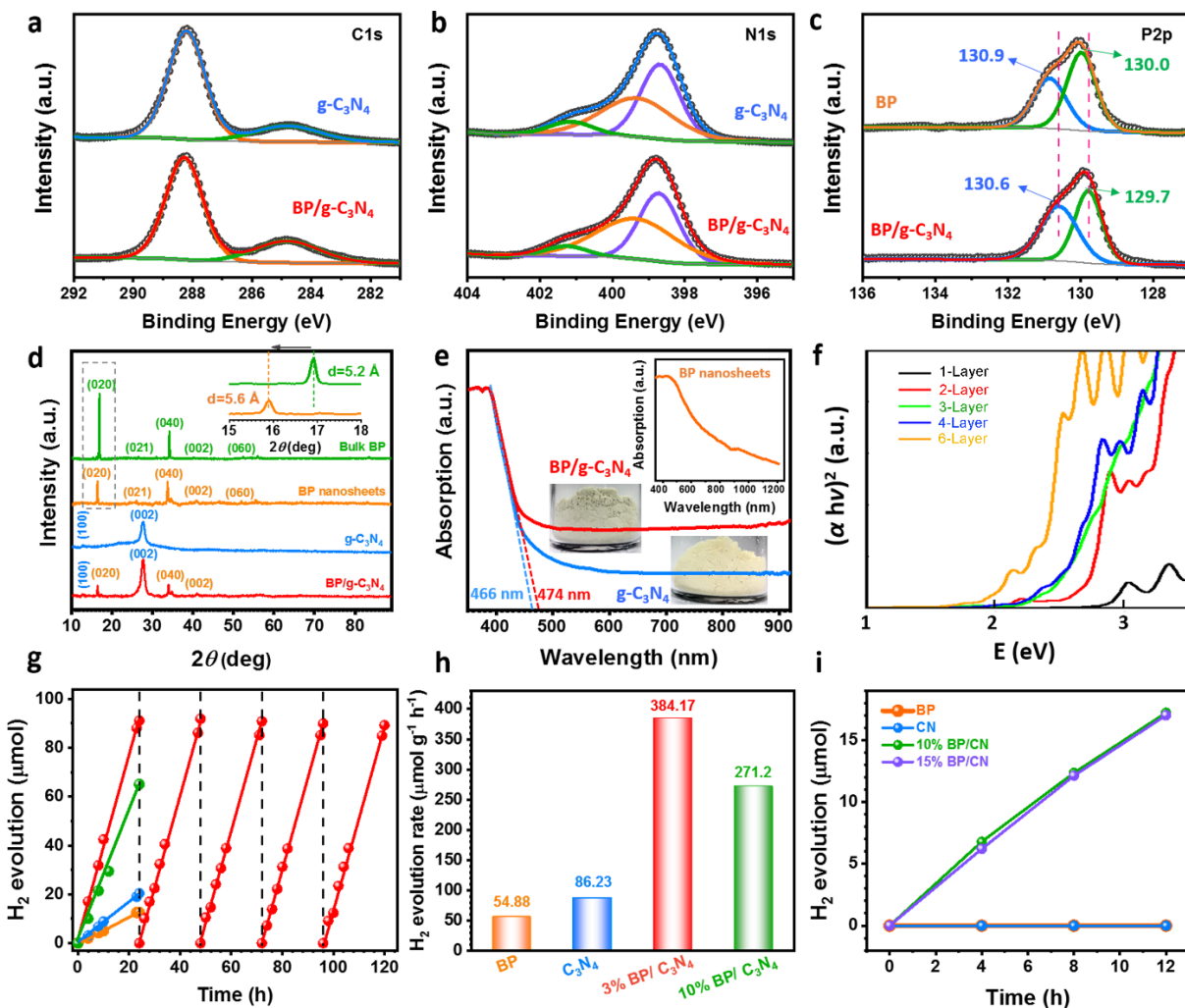


Figure 5.3 High-resolution (a) C1s and (b) N1s XPS spectra of g-C₃N₄ and BP/g-C₃N₄, and (c) P2p XPS spectra of BP and BP/g-C₃N₄ samples. (d) XRD patterns of bulk BP, BP nanosheets, g-C₃N₄ and BP/g-C₃N₄ samples. The inset is the amplification of XRD patterns of bulk BP and BP nanosheets in the lower-angle range, which is marked by the dashed rectangle in (d). (e) UV-vis-NIR absorption spectra of g-C₃N₄ and BP/g-C₃N₄ powder samples. Insets in (e) are the absorption spectrum of BP nanosheets in dispersion (top), photos of BP/g-C₃N₄ (middle) and g-C₃N₄ (bottom) powders. (f) Theoretical Tauc-plot curves of BP with different layer numbers (1-4 and 6 layers). (g, i) Photocatalytic H₂ evolution and (h) H₂ evolution rate achieved in the presence of BP (orange), g-C₃N₄ (blue), 3 wt% BP/g-C₃N₄ (red), 10 wt% BP/g-C₃N₄ (green) and 15 wt% BP/g-C₃N₄ (purple) photocatalysts under (g-h) $\lambda > 420$ nm and (i) $\lambda > 475$ nm light irradiations.

The high-resolution C1s XPS spectrum presents two distinct peaks at 284.8 and 288.3 eV (Figure 5.3a), which can be assigned to the graphitic sp² C=C bonds in the surface adventitious carbon contaminations and in the C-N aromatic heterocycles, respectively.^{52,328,345} The main N1s peak was deconvoluted into three peaks (Figure 5.3b), located at 398.6, 399.4 and 401.1 eV, which are assigned to the sp² hybridized N in triazine rings (C=N-C), tertiary N (N-(C)₃) and amino group (C-N-H), respectively.^{336,418,471,472} As shown in Figure 5.3c, the fitting result of P2p spectrum shows two peaks at binding energies of 129.8 and 130.6 eV, corresponding to P2p_{3/2} and P2p_{1/2},

respectively. In the case of BP/g-C₃N₄, the P2p peaks shift to lower binding energy as compared to BP alone. This means that the electron density of P atoms increases, highly likely due to partial electron transfer from N atoms. Similar observation has been reported by others and it supports the strong interfacial interaction between BP and g-C₃N₄, which is supposed to introduce shallow charge trapping sites and suppress charge carrier recombination and thus be beneficial for photocatalysis.^{319,427} This is quite different from the case of deep trapping sites, which can facilitate charge recombination and are detrimental to photocatalysis.⁴⁷³ It is noteworthy that the peak in the range of 133.5~134.0 eV, ascribed to oxidized P (P_xO_y),^{319,457,474} was not observed in the P2p XPS spectra of either BP or BP/g-C₃N₄, indicating that P was not considerably oxidized during both the exfoliation process of bulk BP to BP nanosheets and the preparation process of BP/g-C₃N₄ hybrid sample. The developed, time-efficient NMP-ice-assisted exfoliation method played a vital role in protecting BP from oxidation by shortening the ultrasonication time and reducing the possibility of exposure to O₂.

Figure 5.3d shows the X-ray diffraction system (XRD) patterns of bulk BP, exfoliated BP nanosheets, g-C₃N₄ and 3 wt% BP/g-C₃N₄ samples. The diffraction peaks shown in the patterns of bulk BP and BP nanosheets can be well indexed to the orthorhombic BP with space group Cmca (64) according to the standard pattern of BP (JCPDS No. 73-1358).^{452,454} Furthermore, the lower-angle peak originated from the periodic stacking of layers exhibits a downshift from 16.95° of the BP bulk counterpart to 15.89° of the exfoliated BP nanosheets, corresponding to the inter-plane distance increasing from 5.2 Å to 5.6 Å, respectively (inset of Figure 5.3d). This result confirms that the intercalation of NMP ice crystals can enlarge the inter-planar spacing of BP, and further facilitates its easy exfoliation by reducing the interlayer Van der Waals interactions. In the XRD pattern of g-C₃N₄, the two peaks present at 13.0° and 27.4° are ascribed to the in-planar arrangement of the tri-s-triazine unit and the inter-planar stacking of the conjugated aromatic system, respectively.^{102,140,188,328,415,472} For the diffractogram of BP/g-C₃N₄ sample, both the characteristic diffraction peaks of BP and g-C₃N₄ were observed, once again confirming their successful integration. No additional diffraction peaks were observed, implying no new crystalline phases or compounds are formed during the coupling reaction.

5.2.3 Optical properties

The optical properties of BP nanosheets in IPA, g-C₃N₄ and 3 wt% BP/g-C₃N₄ nanosheets were investigated as displayed in the UV-visible-near infrared (UV-vis-NIR) absorption spectra (Figure 5.3e). The BP nanosheets show a quite broad absorption band from UV to NIR regions, whilst g-

C₃N₄ exhibits a typical semiconductor-like absorption spectrum in the UV and blue regions with the absorption edge of around 466 nm. Through Tauc plots (Figure S5.4), the bandgap energy (E_g) of as-prepared BP and g-C₃N₄ nanosheets were estimated to be ~1.39 eV and ~2.66 eV, respectively.

Figure 5.3f shows the theoretical Tauc-plot curves obtained from the ab-initio absorbance spectra calculated for BP of different layer thickness (1-4 and 6 layers). They were calculated by performing state-of-the-art Many-Body Perturbation theory calculations (namely GW method and Bethe-Salpeter equation)³²⁴ on top of density functional theory (DFT) simulations,³²⁵ as detailed in Supporting Information. Although a direct comparison with the experimental curve shown in Figure S5.4a is quite difficult, due to the presence at experimental level of several thicknesses and to the assumption, at theoretical level of perfect isolated layers in a vacuum dielectric screening, the broad feature from visible to NIR is in line with what experimentally observed and supports the experimental estimation of an average thickness of about 6 layers. It is worth to underline that the calculated optical gaps can be better extracted from the position of the first optical peak in the absorption curves (Figure S5.5) and are due to bound excitons. The binding energies decrease with the increasing BP layer numbers, as due to smaller quantum confinement effect and larger dielectric screening. Indeed the calculated GW electronic (transport) gaps (Figure S5.6) are systematically larger than the energetic position of the first optical peaks.^{126,293,475}

For the BP/g-C₃N₄ 2D-on-2D assembled nanosheet photocatalyst, in addition to the absorption of g-C₃N₄, a largely enhanced tail absorption in the visible and NIR regions was clearly observed due to the introduction of BP nanosheets. This can greatly benefit to the visible light-driven photocatalytic H₂ production. Furthermore, a slight red-shift of the absorption edge was observed in the spectrum of BP/g-C₃N₄ (474 nm) compared to that of g-C₃N₄ (466 nm), confirming the strong N-P interactions between BP and g-C₃N₄.

5.2.4 Photocatalytic H₂ evolution

The photocatalytic H₂ production in the presence of BP, g-C₃N₄, 3 wt% BP/g-C₃N₄ and 10 wt% BP/g-C₃N₄ photocatalysts under $\lambda > 420$ nm light irradiation and the stability measurement of BP/g-C₃N₄ are shown in Figure 5.3g-5.3h. All the samples show H₂ evolution from water containing triethanolamine, which acts as the sacrificial electron donor to quench the photoinduced holes. The as-prepared BP/g-C₃N₄ photocatalyst exhibits much larger H₂ evolution amount (93.14 μ mol), compared to BP (13.18 μ mol) and g-C₃N₄ samples (20.43 μ mol) after 24 h

of light irradiation. As displayed in Figure 5.3h, the highest H₂ evolution rate was achieved by BP/g-C₃N₄ (384.17 μmol g⁻¹ h⁻¹), which is about 7 times and 4.5 times higher than that of pure BP (54.88 μmol g⁻¹ h⁻¹) and g-C₃N₄ (86.23 μmol g⁻¹ h⁻¹), respectively. The fast recombination of photo-generated charge carriers in BP and g-C₃N₄ should be responsible for their poor photocatalytic activities. In the BP/g-C₃N₄ composite, the excited electrons in the conduction band (CB) of g-C₃N₄ are possibly transferred to BP nanosheets and suppress the recombination of charge carriers in g-C₃N₄, resulting in further enhanced photocatalytic activity, as confirmed by the following constructed energy diagrams. Under λ > 420 nm light irradiation, the excitation of g-C₃N₄ plays a major role in producing H₂. When the BP content increases to 10 wt%, the g-C₃N₄ content is accordingly reduced, leading to a decreased H₂ evolution rate (271.2 μmol g⁻¹ h⁻¹). The H₂ production rate achieved by 3 wt% BP/g-C₃N₄ is comparable to or even higher than that of the reported photocatalyst with loading of the Pt precious metal as a co-catalyst (Table S5.3). Furthermore, a decrease of only about 2% was observed in the H₂ evolution by the as-synthesized BP/g-C₃N₄ photocatalyst after 120 h (the longest time period under the current investigation) of visible light irradiation, which suggests that it possesses excellent stability in water under light illumination. The P2p XPS spectra of BP and BP/g-C₃N₄ after photocatalytic experiment were measured (Figure S5.7). An additional peak at ~134 eV, assigned to the oxidized P, appeared after photocatalysis, which accounts for 21.6 at% and 7.5 at% of P in BP and BP/g-C₃N₄, respectively (Table S5.4). This indicates that the introduction of g-C₃N₄ greatly retards the oxidation of BP by ~3 times. Though a small portion of P in BP/g-C₃N₄ was oxidized, the photocatalytic activity was not noticeably affected. Furthermore, no obvious change was observed in the XRD pattern (Figure S5.8) and TEM images (Figure S5.9a-5.9b) of the BP/g-C₃N₄ after photocatalysis. The EDX spectrum (Figure S5.99c) shows a small peak of O, which is attributed to the oxidation of BP and is consistent with the XPS analysis (Figure S5.7).

Figure 5.3i shows the photocatalytic H₂ production by the prepared samples under λ > 475 nm light irradiation. No H₂ was detected in the presence of bare BP, g-C₃N₄ or 3 wt% BP/g-C₃N₄ photocatalysts, while 10 wt% BP/g-C₃N₄ sample exhibits a H₂ generation rate of 143.47 μmol g⁻¹ h⁻¹ (Figure S5.10). When BP loading content increases to 15 wt%, no obvious further enhancement was observed in H₂ evolution. In this scenario (λ > 475 nm irradiation), g-C₃N₄ cannot be excited and only BP excitation contributes to H₂ evolution, but the fast charge carrier recombination in BP greatly decreases the use of excited electrons and holes in photocatalysis. As a result, both g-C₃N₄-only and BP-only samples show inferior activity. The combination of BP and g-C₃N₄ may introduce shallow interfacial charge trap sites, which can promote the charge separation in BP.⁴⁷³ This well explains the clearly observed photoactivity with BP loading of 10%

and 15% with respect to plain g-C₃N₄ and BP samples. However, higher loading (15% vs 10%) does not necessarily lead to higher activity due to the limited trap sites. These results suggest that the as-prepared BP/g-C₃N₄ is an economic, efficient and stable, completely metal-free photocatalyst, exempt of introducing any metal as co-catalyst, allowing H₂ production under broadband light irradiation.

5.2.5 PEC measurements and charge transfer dynamics

The photoelectrochemical (PEC) properties of the as-prepared g-C₃N₄ and 3 wt% BP/g-C₃N₄ samples were evaluated by electrochemical impedance spectroscopy (EIS) and transient photocurrent responses (Figure 5.4a-5.4b). Some useful information for the charge transfer resistance can be extracted from the high frequency region of the Nyquist plots. The significantly decreased arc radii are exhibited in the EIS Nyquist plots of 3 wt% BP/g-C₃N₄ compared with that of g-C₃N₄ both in the dark and under simulated solar light irradiation (Figure 5.4a), suggesting that the introduction of BP leads to the increase of the interfacial charge transfer rate in the BP/g-C₃N₄ sample.^{188,341,376,472} To further verify the improved PEC performance, the transient photocurrent responses for more than ten light on-off cycles were measured under simulated solar light irradiation (Figure 5.4b). The photocurrent density rapidly increases to a saturation value and remains constant once the light is switched on, while it immediately returns to nearly zero when the light is turned off. The saturated photocurrent density of BP/g-C₃N₄ (~5.28 μA cm⁻²) is about 4.8 times higher than that of plain g-C₃N₄ photocatalysts (~1.11 μA cm⁻²). The increased photocurrent density strongly verifies that the introduction of BP nanosheets can facilitate charge separation/transport,^{341,476} and/or enhance the visible light absorption due to their narrower bandgap. Altogether they contribute to the improved photocatalytic H₂ evolution rate under visible light irradiation. It is worth noting that the measurement of photocurrent density of the electrodes was also done under constant light irradiation for longer time (5400 s) and repeated for 3 runs (Figure S5.11). Only slight fluctuations were observed for the recorded photocurrent data among the 3 runs, which are in the range of measurement error. For each run, almost no decrease was observed, which supports that the as-synthesized BP/g-C₃N₄ samples possess good stability under light irradiation.

Figure 5.4c shows the steady-state photoluminescence (PL) spectra of g-C₃N₄ and 3 wt% BP/g-C₃N₄ samples. Under the excitation of 380 nm, they both show a peak at ~457 nm in their PL spectra, corresponding to the recombination of the photo-induced electrons and holes in g-C₃N₄.⁴²¹ The PL quenching in BP/g-C₃N₄ indicates greatly suppressed recombination,^{336,428,429}

which can be attributed to the efficient interfacial charge transfer from g-C₃N₄ to BP. The charge carrier dynamics was investigated by time-resolved PL (TRPL) spectroscopy (Figure 5.4d). A bi-exponential fitting equation was applied to analyze the TRPL decay curves due to their complexity. The decay kinetics of BP/g-C₃N₄ shows a shorter average PL lifetime (486 ± 5 ns) than that of g-C₃N₄ (534 ± 8 ns). The decreased PL lifetime in the BP/g-C₃N₄ heterojunction supports that the introduction of BP can effectively facilitate the separation of photo-generated charge carriers.^{404,430}

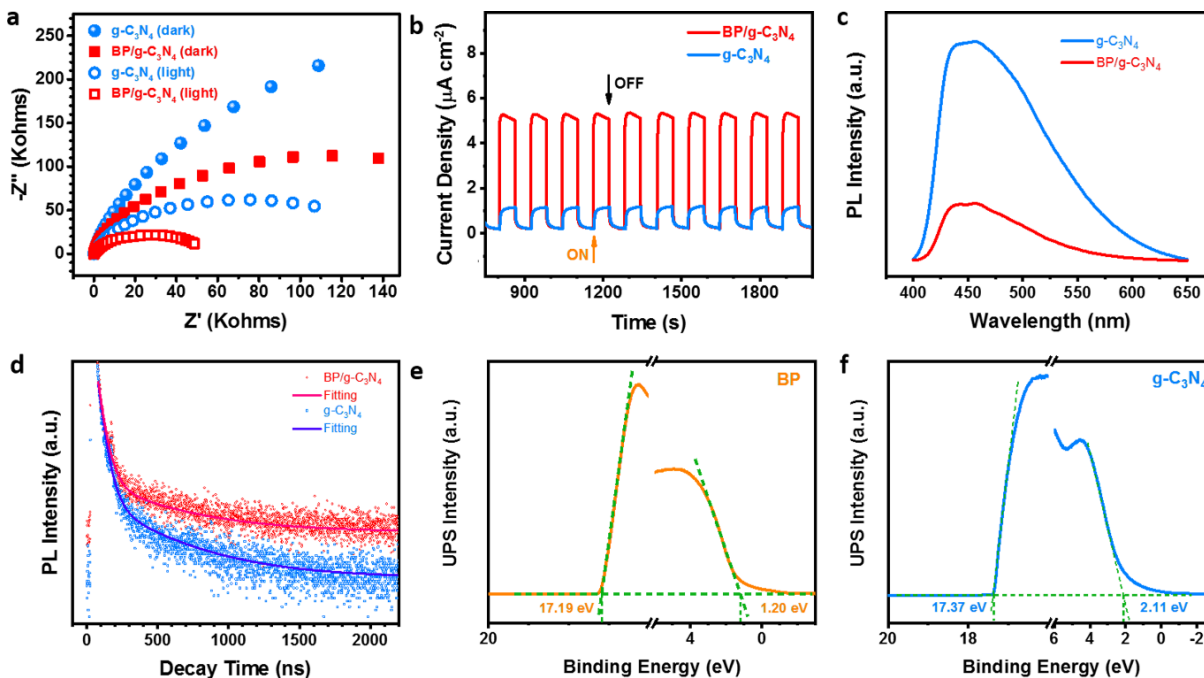


Figure 5.4 (a) EIS Nyquist plots of g-C₃N₄ and BP/g-C₃N₄ with and without illumination. (b) Transient photocurrent density response of g-C₃N₄ and BP/g-C₃N₄ during light on/off cycles under a 0.2 V bias versus Ag/AgCl electrode. (c) Steady-state PL spectra with the excitation at 380 nm, and (d) TRPL decay curves measured at 457 nm of g-C₃N₄ and BP/g-C₃N₄ samples. Valence band UPS cut-off spectra of (e) BP and (f) g-C₃N₄ samples.

5.2.6 UPS measurement

To better understand the nature of BP/g-C₃N₄ as an efficient photocatalyst for H₂ evolution, ultraviolet photoelectron spectroscopy (UPS) measurements were performed to determine the energy levels of BP and g-C₃N₄ nanosheets (Figure 5.4e-5.4f). The intersections of the extrapolated linear portion at high and low binding energies with the baseline give the edges of the UPS spectra, from which the UPS widths of BP and g-C₃N₄ are determined to be 15.99 eV and 14.95 eV, respectively.⁵² Then the VB energy (E_{VB}) values of BP and g-C₃N₄ were estimated to be 5.23 eV and 5.96 eV, respectively, by subtracting the width of the UPS spectra from the excitation energy (21.22 eV). Combining with the measured E_g from the absorption spectra, the

CB energy values (E_{CB}) of BP (4.18 eV) and g-C₃N₄ (3.3 eV) were estimated from $E_{CB} = E_{VB} - E_g$.^{52,319} These values in eV are all converted to electrochemical energy potentials in V according to the reference standard for which -4.44 eV vs. vacuum level equals 0 V vs. reversible hydrogen electrode (RHE).⁵²

5.2.7 Mechanism of photocatalytic H₂ evolution under different light irradiations

Based on the UPS measurement results, the possible mechanism for the largely enhanced photocatalytic activity in H₂ evolution of BP/g-C₃N₄ photocatalysts is proposed. As schematically illustrated in Figure 5.5, the CB energy level of BP is more positive (-0.60 V) than that of g-C₃N₄ (-1.18 V), and both of them are more negative than the reduction potential of H⁺/H₂ (~ 0 V). In addition, the VB energy level of BP is higher than that of g-C₃N₄. These properly positioned bands are suitable for the transfer of charge carriers for water splitting, corroborating the capability of BP/g-C₃N₄ as a metal-free photocatalyst for H₂ evolution. Under $\lambda > 420$ nm light irradiation, mainly the electrons in the VB of g-C₃N₄ are excited to its CB, leaving behind the positively-charged holes in the VB (Figure 5.5a). Afterwards, the excited electrons can be further transferred into the CB of adjacent BP, largely suppressing the recombination of charge carriers and promoting the reduction of H₂O to produce H₂. In addition to benefiting from the suitable energy levels of BP and g-C₃N₄, the charge transfer process is also efficiently promoted by the presence of certain trap sites. At the same time, the holes in the VB of g-C₃N₄ can be immediately captured by the hole-sacrificial agent triethanolamine (TEOA) to generate its oxide. In this process, BP mainly plays a role as the charge acceptor to inhibit the charge carrier recombination and leads to efficient H₂ evolution. Another possible pathway of hole transfer is from the VB of g-C₃N₄ to that of BP, where the holes were consumed by reacting with TEOA.⁴⁷⁷ In this case, BP absorption and the presence of interfacial trap states also contribute to the enhanced photocatalytic activity, but are not dominating owing to their much smaller ratio than g-C₃N₄. Under $\lambda > 475$ nm light irradiation, the excitation of g-C₃N₄ can be excluded. BP cannot by itself act as the effective photocatalyst either, for photocatalytic H₂ production, due to the fast charge carrier recombination in it. While in the BP/g-C₃N₄ composite, the excited electrons in the CB of BP are captured by the interfacial trap sites and participate in the H₂ evolution (Figure 5.5b). Simultaneously, the holes left behind in the VB of BP are scavenged by TEOA to generate CO₂ and water.

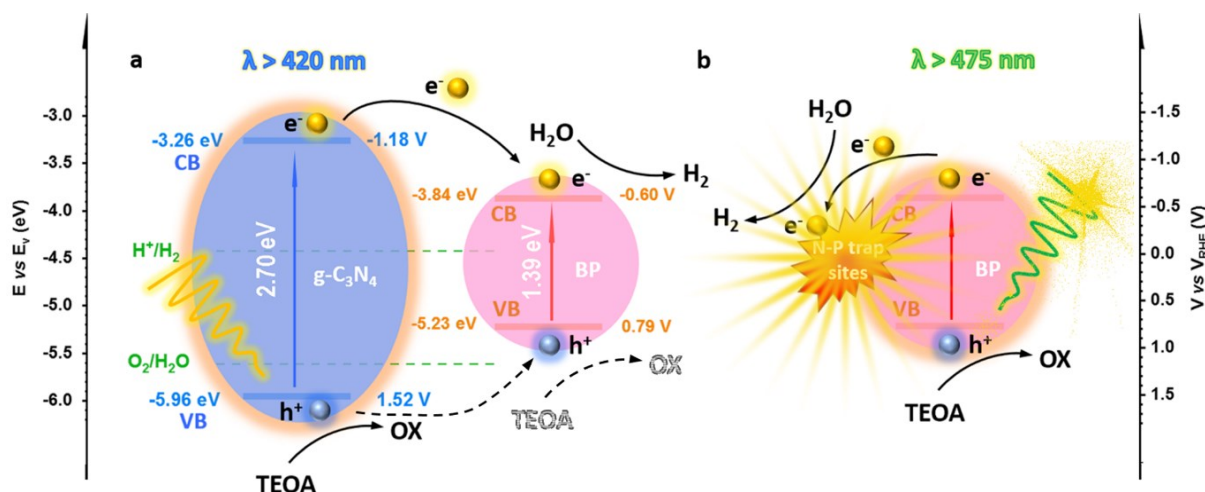


Figure 5.5 Schematic energy diagram of BP/g-C₃N₄ photocatalyst and proposed possible mechanism for the photocatalytic H₂ evolution under (a) $\lambda > 420$ nm and (b) $\lambda > 475$ nm light irradiation.

5.3 Conclusions

In conclusion, a novel metal-free efficient BP/g-C₃N₄ visible light photocatalyst was developed. The NMP-ice-assisted exfoliation method was presented for the first time to prepare few-layer BP nanosheets from bulk BP, which leads to high yield of few-layer BP nanosheets with large lateral size and largely reduced duration and power for liquid exfoliation. The combination of BP with g-C₃N₄ leads to largely enhanced photocatalytic activity in H₂ production under both $\lambda > 420$ nm and $\lambda > 475$ nm light irradiation. The intensive interaction at the interface of BP and g-C₃N₄ greatly promotes charge transfer from excited g-C₃N₄ to BP, which can also introduce interfacial trap sites to capture the electrons from excited BP for photocatalysis. Furthermore, the introduction of g-C₃N₄ protects BP from oxidation and the as-prepared BP/g-C₃N₄ photocatalyst shows excellent long-term stability in photocatalytic H₂ production. This work provides a facile preparation approach of high-quality BP nanosheets and renders a successful paradigm for the design of metal-free photocatalyst to improve the charge-carrier dynamics for efficient and broadband water splitting.

Acknowledgements

Financial support from the Natural Sciences and Engineering Research Council of Canada (NSERC) in the context of NSERC-Discovery Grant and NSERC-Strategic Grant (with the support of Canadian Solar Inc.), le Fonds de recherche du Quebec-Nature et technologies (FRQNT), National Natural Science Foundation of China (NSFC 51402198; NSFC 21808090) and Natural Science Foundation of Liaoning Province (201602592) is greatly appreciated. M.C. is also grateful

to the Canada Research Chairs Program. In addition, Q.Z. acknowledges the support under State Scholarship Fund from the China Scholarship Council (CSC, No. 201506220152). M.P. thanks INFN for financial support through the National project Nemesys. M.P. and G.G. acknowledge PRACE and ISCRA-B and C initiatives for awarding access to computing resources on Marconi at CINECA, Italy.

5.4 Supporting Information

5.4.1 Experimental section

5.4.1.1 Materials

BP crystals of high-purity (~99.998%) were purchased from Smart Elements, N-Methyl-2-pyrrolidone (NMP, 99.5%, anhydrous), isopropanol (IPA, 99.5%, anhydrous), urea (NH₂CONH₂), nitric acid (HNO₃), N,N-Dimethylformamide (DMF) and triethanolamine (≥99.0%) were purchased from Sigma-Aldrich and used as received without further purification. The ultrapure water (18.2 MΩ cm, 25 °C), obtained from a Millipore Ultrapure water system, was used throughout the current study.

5.4.1.2 NMP-Ice-assisted preparation of BP nanosheets

BP nanosheets were synthesized by developing a NMP-ice-assisted exfoliation method. Specifically, 25 mg of bulk BP was ground into ultrafine powder and dispersed into 25 mL of NMP solvent. The dispersion was completely frozen with a liquid nitrogen bath for 5-10 min, and then sonicated in a bath sonicator (BRANSONIC, 70 W, 40 kHz) for ~10 min to make the “NMP ice” melt. The procedure of freezing and melting was repeated 3 times. To protect the BP from oxygen and water, the dispersion was sealed in a vial, and all the experimental manipulations were performed in a glovebox or with nitrogen bubbling. Afterwards, the dispersion was centrifuged at 4000 rpm for 15 min to remove the residual un-exfoliated BP. The light yellow supernatant was decanted gently, which was the dispersion of BP nanosheets in NMP. The obtained BP nanosheets were washed with IPA by centrifugation at 12000 rpm for 2 times. The collected precipitate was re-dispersed into 25 mL of IPA. The concentration of BP in this dispersion was determined to be 0.75 mg mL⁻¹ by Inductively Coupled Plasma Optical Emission Spectroscopy (ICP-OES).

5.4.1.3 Preparation of g-C₃N₄ nanosheets

The g-C₃N₄ nanosheets were synthesized by our previously reported thermal polymerization method.^{188,384} Generally, urea (30 g) was placed into a covered alumina crucible and then heated in a quartz tube furnace with a heating rate of 2 °C min⁻¹ to 250, 350, and 550 °C, and maintained at these three target temperatures for 1, 2, and 2 h, respectively. After being naturally cooled down to room temperature, the yellow powder was collected and washed for three times with HNO₃ (0.1 mol L⁻¹) and water to remove potential alkaline residue (e.g., ammonia). After centrifugation, the precipitate was dried in the vacuum at 80 °C overnight.

5.4.1.4 Preparation of BP/g-C₃N₄ photocatalysts

BP/g-C₃N₄ nanosheets were prepared by dispersing 10 mg of g-C₃N₄ powder into 0.4 mL of BP nanosheet dispersion in IPA. The mixture was stirred for 2 h to couple BP nanosheets with g-C₃N₄ nanosheets under the protection of N₂. Subsequently, the sample was collected by centrifugation at 6000 rpm for 5 min, and then washed completely with IPA. The final product was obtained by drying the washed sample in an oven under vacuum at 60 °C overnight. The obtained BP/g-C₃N₄ nanosheets contain about 3 wt% of BP. The composites with 10 wt% and 15 wt% of BP were prepared with adding 1.3 mL and 2 mL of BP dispersion, respectively.

5.4.1.5 Characterization

A transmission electron microscope (TEM, JEOL 2100F), equipped with an energy-dispersive X-ray (EDX) spectrometer, was employed and operated at an accelerating voltage of 200 kV to study the microstructure and composition of the prepared samples. The topography image of the BP nanosheets on a pre-cleaned glass was observed by an atomic force microscopy (AFM, Bruker, MultiMode 8) in a tapping mode. Zeta potential of the as-prepared BP and g-C₃N₄ nanosheets in IPA was recorded with a Brookhaven ZetaPlus system in a standard 10 mm all-side-transparent polymethyl methacrylate cuvette. The crystalline structure was analyzed by an X-ray diffraction system (XRD, PANalytical X'Pert MRD, operated at 45 kV and 40 mA) with a Cu K α radiation source ($\lambda = 0.15406$ nm). X-ray photoelectron spectroscopy (XPS) was performed with a VG Escalab 220i-XL spectrometer equipped with a twin anode Al K α radiation X-ray source. All the XPS spectra were calibrated using the C1s peak at 284.8 eV as reference. Ultraviolet photoelectron spectroscopy (UPS) measurements were carried out with an unfiltered Helium gas discharge lamp emitting predominantly at 21.22 eV to determine the valence band (VB) position

of as-prepared BP and g-C₃N₄ samples. The UV-visible-near infrared (UV-vis-NIR) absorption spectra of g-C₃N₄, BP nanosheets and BP/g-C₃N₄ powder were obtained using a scan spectrometer (Varian Cary 5000) equipped with an integrating sphere. The bandgap energy (E_g) of the prepared g-C₃N₄ and BP nanosheets were determined from Tauc plots, *i.e.* $(\alpha hv)^2$ as a function of hv . The concentration of BP nanosheets in IPA dispersion and the content of BP in the composites were determined by an IRIS Intrepid II XSP ICP-AES (Thermal Scientific, USA). Steady-state photoluminescence (PL) and time-resolved PL (TRPL) spectra were obtained by a Horiba Jobin Yvon Fluorolog-3 fluorescence spectrometer. The PL lifetimes were calculated by fitting the TRPL decay curves with a bi-exponential fitting equation.

5.4.1.6 Photoelectrochemical measurements

Photoelectrochemical (PEC) properties were measured with a standard three electrode system in an electrochemical workstation (CHI 660E, CH Instruments). The working electrode was prepared by coating the as-synthesized sample on fluorine-doped tin oxide (FTO) glass with its boundaries being protected by Scotch tape. Specifically, 2 mg of powder sample was dispersed into 2 mL of DMF under sonication for 30 min to obtain evenly dispersed slurry, which was drop-casted onto the FTO glass. After drying under ambient condition, the epoxy resin glue was used to isolate the uncoated part of the FTO glass. A Pt wire and a Ag/AgCl electrode were used as the counter and reference electrode, respectively. The 0.2 M of Na₂SO₄ (pH = 6.8) aqueous solution pre-purged with nitrogen for 30 min was used as an electrolyte. A solar simulator equipped with an AM1.5G filter (LCS-100, Newport) was utilized as the light source. Nyquist plots were recorded over the frequency range of 100 mHz to 100 kHz at a bias of 0.2 V.

5.4.1.7 Photocatalytic H₂ evolution

Photocatalytic H₂ evolution experiment was performed in a 500 mL Pyrex top-irradiation reactor with a quartz cover. A 300 W Xenon lamp equipped with cut-off filters (420 nm and 475 nm) was used to provide the irradiation source in the visible wavelength range. Typically, 10 mg of photocatalysts were dispersed in 100 mL of aqueous solution containing 10% of triethanolamine (TEOA) as sacrificial reagents. The mixture was deaerated by N₂ gas for 20 min and sonicated for 5 min. The system was sealed and vacuumed prior to photocatalysis. During the irradiation, the suspension was stirred continuously and kept at a constant temperature by circulating cooling water. The evolved H₂ was analyzed by a gas chromatography (GC, 7890B, Agilent Technologies) equipped with a thermal conductivity detector. For stability measurements, the photocatalysts

were collected from the final reaction slurry by centrifugation, and then washed with ethanol and water thoroughly. Subsequently, the recycled sample underwent the photocatalytic H₂ evolution experiment under identical conditions and repeated for 5 cycles with a total irradiation time of 120 h.

5.4.2 Theoretical calculations

Calculated absorption spectra (Figure 5.3f) were obtained by performing Many-Body Perturbation theory calculations (namely GW method and Bethe-Salpeter equation)³²⁴ on top of density functional theory (DFT) simulations.³²⁵ In the G₀W₀ simulations we used a cutoff of 40 Ry to expand the wavefunctions, 160 Ry to evaluate the difference between the exchange self-energy and exchange-correlation matrix elements $\langle \Sigma_x - V_{xc} \rangle$. For the screening term W and the correlation self-energy matrix elements $\langle \Sigma_c \rangle$ we performed careful convergence tests for the monolayer finding that 12 Ry and 400 bands provide well converged gaps within 0.05 eV. We further checked that using lower convergence parameters, namely 6 Ry and 100 bands in G the gap correction reduces of about 0.1 eV. For the same system we verified that performing partial self-consistency in the Green Function as GW₀ scheme the gap increases of about 0.1 eV. In order to speed up the calculations we performed, for all the other systems, calculations using a cutoff of 6 Ry and N_b= (N)*100 (N number of layers) bands and avoiding self-consistency. We then added the estimated difference of 0.2 eV, after verifying that this value really occurs for the case of the bilayer. The convergence on k-points has been carefully checked both at GW and BSE level and a grid of 24×21×1 is enough to converge both quantities within 0.1 eV. A box-like cutoff in the Coulomb potential, as implemented in the yambo code, has been used to avoid spurious interactions between the images and speed up the convergence with the vacuum size. The geometries of the layered structures have been obtained using norm conserving pseudopotentials³²⁶ and Perdew-Burke-Ernzerhof (PBE) exchange-correlation functional with Van der Waals correction,³²⁷ able to reproduce with very good accuracy the structural lattice parameters of bulk BP. The vacuum in the aperiodic direction has been selected to be larger than 15 Å for monolayer and bilayer and for all the other cases larger than the thickness of the few-layer phosphorene atomic structure.

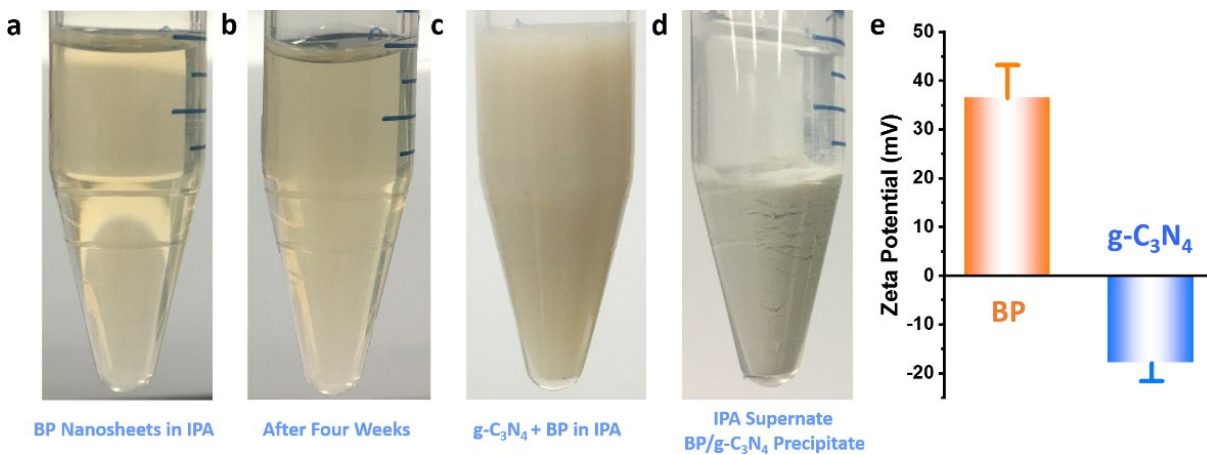


Figure S5.1 Photographs of BP nanosheets in IPA a) at the first day, b) after four weeks, c) after adding $g-C_3N_4$, and d) after the incubation at room temperature for 30 min. e) The zeta potentials of BP and $g-C_3N_4$ nanosheets in IPA at pH around 7.

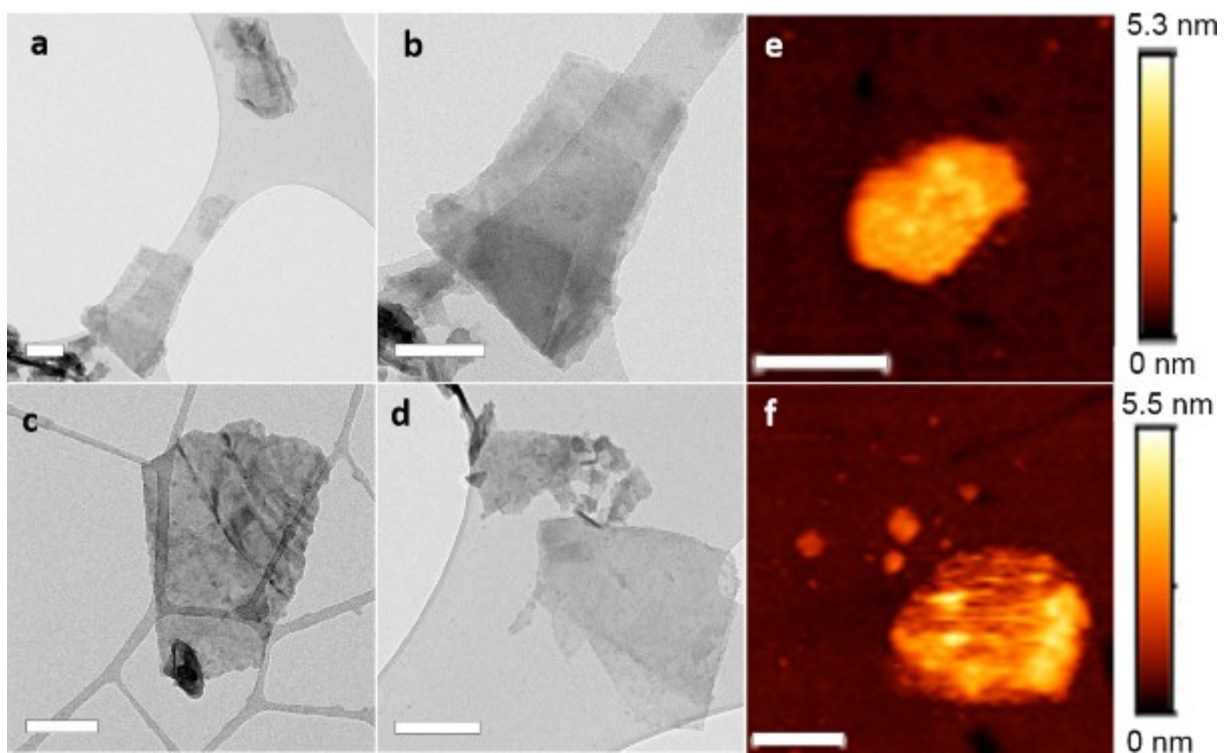


Figure S5.2 (a-d) TEM and (e-f) AFM images of BP nanosheets with different magnifications (Scale bar: 500 nm).

Table S5.1 Comparison of the yield of few-layer BP nanosheets from different exfoliation methods.

Reference	Sonication Bath		Tip Sonicator		Few-layer BP yield
	Power/W	Time/h	Power/W	Time/h	
ACS Nano, 2015, 9, 8869 ²⁹³	70	13			26%
Adv. Mater. 2016, 28, 510 ⁴⁶⁷	380	20			30%
ACS Catal. 2016, 6, 8009 ⁴⁵⁶	-	8			15%
J. Am. Chem. Soc. 2017, 139, 13234 ³¹⁹			10	4	20%
Angew. Chem., Int. Ed. 2018, 57, 1 ⁴⁷⁴			10	4	20%
This work	70	2			75%

Table S5.2 Atomic composition of g-C₃N₄ and BP/g-C₃N₄ photocatalysts.

Sample	C atom %	N atom %	O atom %	P atom%
g-C ₃ N ₄	46.71	49.68	3.61	0
BP/g-C ₃ N ₄	46.70	47.41	3.59	3.30

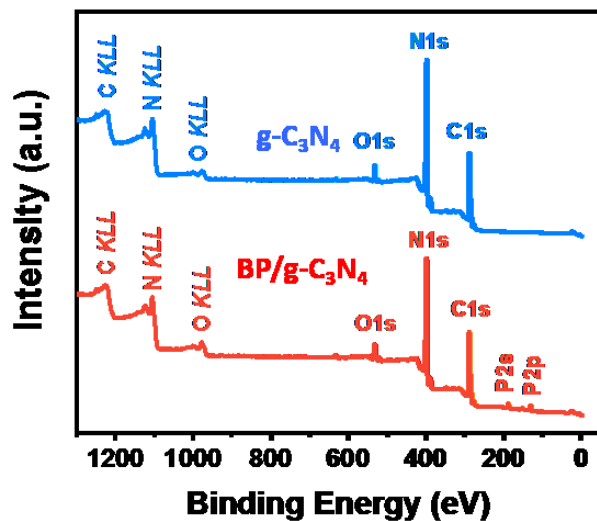


Figure S5.3 XPS survey spectra of g-C₃N₄ and BP/g-C₃N₄ nanosheets.

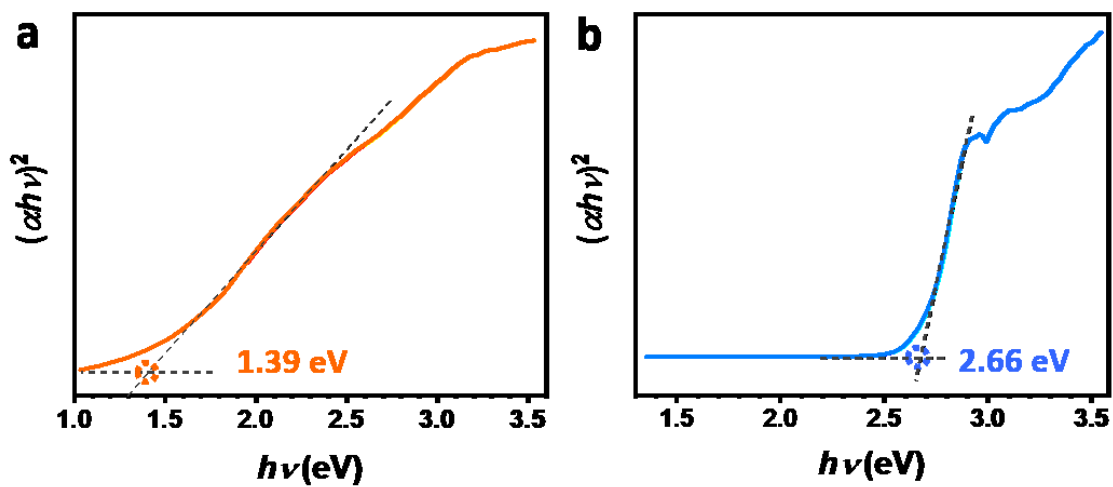


Figure S5.4 Representative direct Tauc plots of (a) BP nanosheets and (b) g-C₃N₄ samples used to determine their bandgap energy.

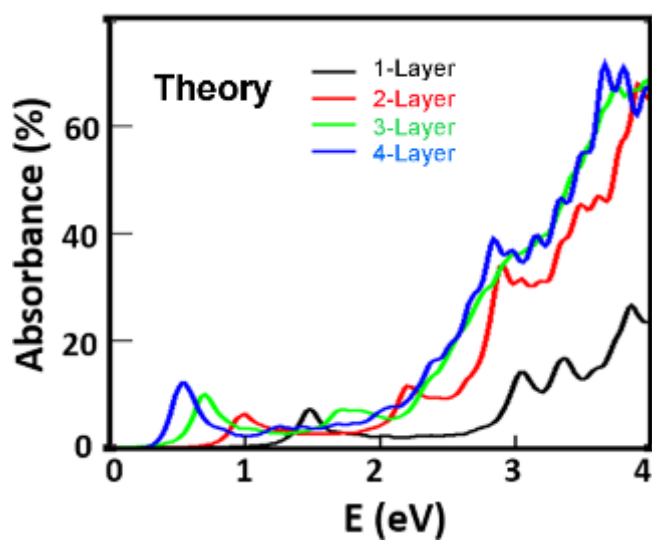


Figure S5.5 Theoretical calculations of the absorption spectra of BP with different numbers of layers (1-4 layers).

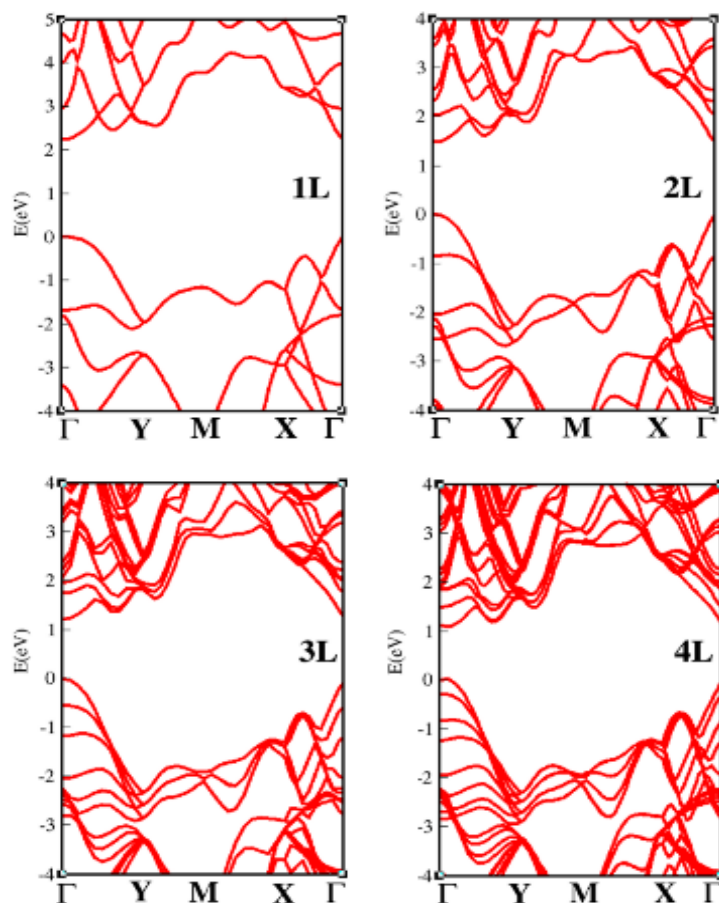


Figure S5.6 Calculated electronic GW band structures of BP with different numbers of layers (1-4 layers).

Table S5.3 Photocatalytic H₂ production rate under visible light ($\lambda > 420$ nm) irradiation.

References	Metal	Catalysts	H ₂ evolution rate ($\mu\text{mol g}^{-1} \text{h}^{-1}$)
<i>Nat. Mater.</i> 2009 , 8, 76 ⁴⁷⁸	3 wt% Pt	C ₃ N ₄	106.94
<i>Chem. Mater.</i> 2015 , 27, 4930 ³³⁷	1 wt% Pt	H ₂ treated g-C ₃ N ₄	29.63
<i>J. Catal.</i> 2016 , 342, 55 ⁴⁷⁹	1 wt% Pt	g-C ₃ N ₄ /TiO ₂	29.97
<i>Appl. Catal., B</i> 2016 , 192, 116 ⁴⁸⁰	3 wt% Pt	Br-modified g-C ₃ N ₄	960
<i>Adv. Mater.</i> 2017 , 29, 1700008 ⁴⁸¹	3 wt% Pt	crystalline CN nanosheets	1060
<i>Appl. Catal., B</i> 2018 , 224, 1 ¹²⁶	3 wt% Pt	O-doped C ₃ N ₄ nanorods	732
<i>Science</i> 2015 , 347, 970 ⁵²	free	CDots-C ₃ N ₄	105
<i>Angew. Chem., Int. Ed.</i> 2018 , 57, 2160 ⁴⁸²	free	BP/BiVO ₄	160
This work	free	BP/g-C₃N₄	384.17

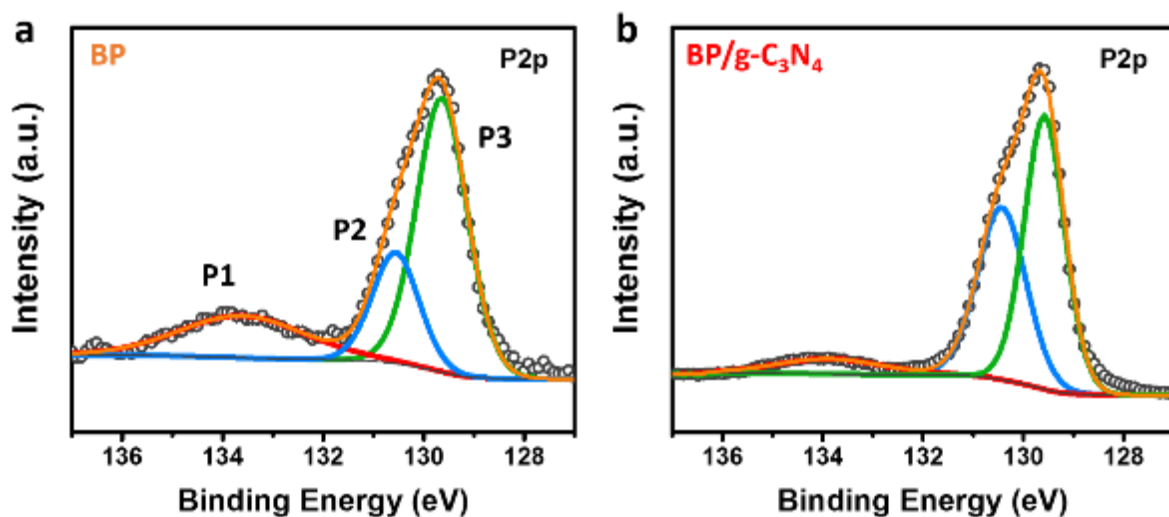


Figure S5.7 P2p XPS spectra of BP and BP/g-C₃N₄ samples after photocatalysis under visible light ($\lambda > 420$ nm) irradiation for 24 h.

Table S5.4 The atomic percentage of P1, P2, and P3 in BP and BP/g-C₃N₄ photocatalysts estimated from Figure S5.3.

Sample	P1 %	P2 %	P3 %
BP	21.6	21.2	57.2
BP/g-C₃N₄	7.5	39.9	52.6

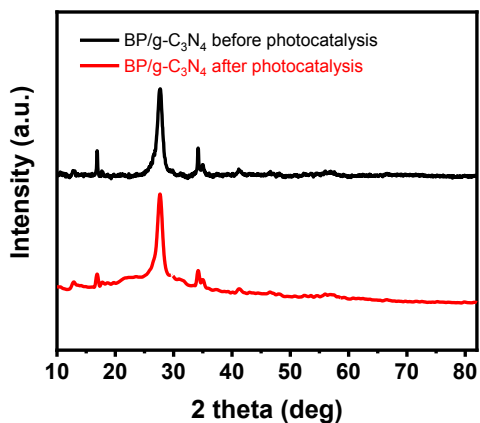


Figure S5.8 XRD pattern of BP/g-C₃N₄ sample before and after photocatalytic reaction.

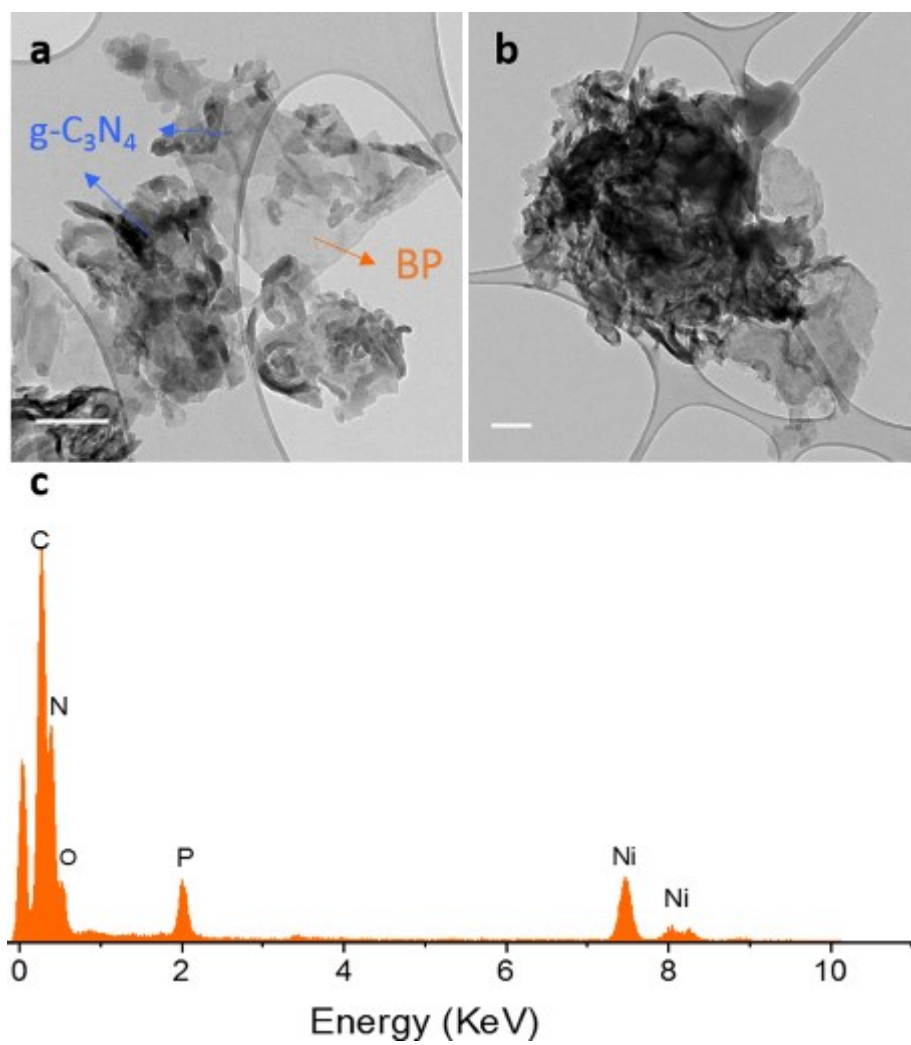


Figure S5.9 TEM images and EDX spectrum of BP/ $g\text{-C}_3\text{N}_4$ after photocatalysis. Scale bars: 200 nm.

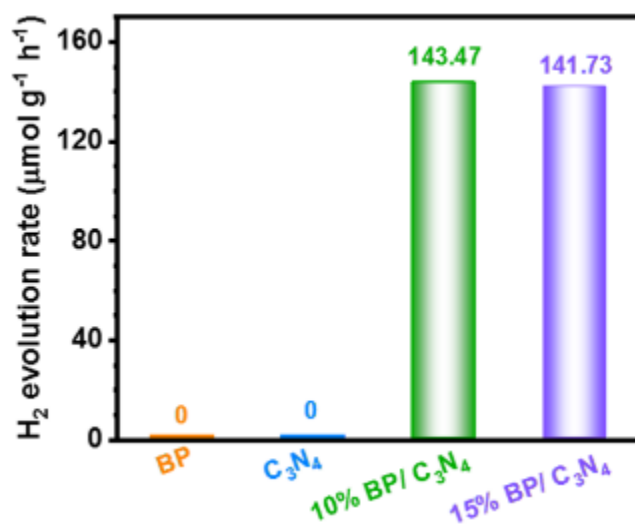


Figure S5.10 H₂ evolution rate achieved in the presence of BP (orange), g-C₃N₄ (blue), 10% BP/g-C₃N₄ (green) and 15% BP/g-C₃N₄ (purple) photocatalysts under ($\lambda > 475$ nm light irradiation).

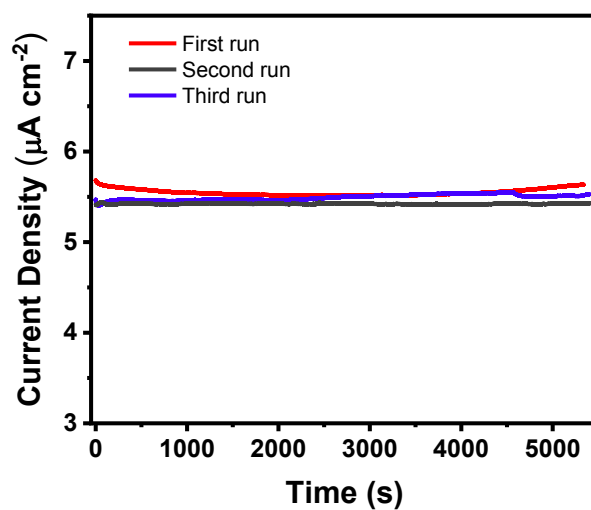


Figure S5.11 Photocurrent density of BP/g-C₃N₄ sample under constant simulated solar light irradiation under a 0.2 V bias versus Ag/AgCl electrode recorded for 5400 s (1.5 h) for 3 runs.

6 CONCLUSIONS AND PERSPECTIVES

6.1 Conclusions

Among the various categories of semiconductor photocatalysts, g-C₃N₄ has attracted tremendous interest of material scientists by virtue of its fascinating merits, such as nontoxicity, facile preparation, moderate bandgap, strong redox capability, “earth-abundant” nature, and good physicochemical stability. However, g-C₃N₄ still suffers from poor photocatalytic activity and low quantum efficiency due to the high recombination rate of photogenerated charge carriers. Moreover, the optical bandgap (2.7 eV) of g-C₃N₄ largely restrains the range of its visible light absorption to wavelengths shorter than 460 nm. Accordingly, the large portion of visible light, which accounts for ~43% of incoming solar energy, remains underutilized. Thus, the development of efficient and broadband responsive (from UV, visible to NIR regions) g-C₃N₄ based photocatalysts is a task of great significance and urgency, though challenging. To this end, in this thesis, three kinds of broadband g-C₃N₄ based photocatalysts were designed and synthesized, which were used for photocatalytic degradation of organic dyes and H₂ production. The specific conclusions are as follows.

In Chapter 3, both plasmonic and UC effects were introduced into photocatalysis to gain largely broadened light response range and enhanced photocatalytic activity. The Au-NYF/g-C₃N₄ composite photocatalysts with different Au contents were successfully designed and prepared for the first time by subtly integrating Au NPs, NYF microspheres and g-C₃N₄ nanosheets into a single nanoarchitecture. The as-synthesized Au-NYF/g-C₃N₄ photocatalysts successfully use solar light from UV–visible to NIR regions, and show exceptional activity in the photocatalytic degradation of MO compared with plain g-C₃N₄, as well as excellent stability. On the basis of optical properties and photodegradation experiments under different light irradiations, the underlying mechanisms were elucidated. The photocatalysis pathways were also unveiled by performing trapping experiments of active species. The present study offered a feasible strategy to design and simultaneously prepare plasmon- and UC-enhanced high-performance photocatalysts for effectively harvesting solar energy over a wide spectral range.

In chapter 4, a 0D/2D photocatalyst composed of UV, visible and NIR-responsive and water-dispersible PCZ QDs/g-C₃N₄ was rationally designed and synthesized for the first time. Thanks to the broadband spectral response of uniformly distributed, ultra-small, high-quality PCZ QDs, efficient charge separation and transfer, as well as strong coupling between PCZ QDs/g-C₃N₄ by forming the C-S bond, the prepared PCZ QDs/g-C₃N₄ exhibits excellent photocatalytic activities

in organic dye degradation under UV, visible and NIR light irradiations. Especially for NIR-driven photocatalysis, the composite with optimized PCZ QDs loading outperforms the best-reported photocatalysts. Remarkably, the PCZ QDs/g-C₃N₄ also possesses excellent recycling performance and no metal release was detected in the solution after photocatalysis. Through investigating the charge transfer dynamics and detecting involved active species, the underlying mechanisms for photocatalysis under different light irradiations were clearly elucidated. This work paves a way to synthesize broad-solar-spectrum 0D/2D photocatalyst that is of great potential in water treatment and extensive (photo)electronic applications.

In chapter 5, a novel metal-free efficient BP/g-C₃N₄ visible light photocatalyst was developed. The NMP ice-assisted exfoliation method was presented for the first time to prepare few-layer BP nanosheets from bulk BP, which leads to high yield of few-layer BP nanosheets with large lateral size and largely reduced duration and power for liquid exfoliation. The combination of BP with g-C₃N₄ leads to largely enhanced photocatalytic activity in H₂ production under both $\lambda > 420$ nm and $\lambda > 475$ nm light irradiation. The intensive interaction at the interface of BP and g-C₃N₄ greatly promotes charge transfer from excited g-C₃N₄ to BP, which can also introduce interfacial trap sites to capture the electrons from excited BP for photocatalysis. Furthermore, the introduction of g-C₃N₄ protects BP from oxidation and the as-prepared BP/g-C₃N₄ photocatalyst shows excellent long-term stability in photocatalytic H₂ production. This work provides a facile preparation approach of high-quality BP nanosheets and renders a successful paradigm for the design of metal-free photocatalyst to improve the charge-carrier dynamics for efficient and broadband water splitting.

6.2 Perspectives

We have tried different strategies to develop efficient and broadband (from UV to NIR regions) photocatalysts for energy conversion and environmental pollution control. Even though certain progress have been made, the research on the development and applications of full-solar-spectrum photocatalysts with high photocatalytic efficiency is still far from satisfaction. Therefore, significant efforts are still required to further move the research area forward, and the following challenges and research directions are worth being paid special attention.

(1) The textural and surface properties of g-C₃N₄ are still required to be improved. The specific surface area of currently-reported g-C₃N₄ nanosheets is about an order of magnitude lower than the theoretical value of ideal monolayer g-C₃N₄ (2500 m² g⁻¹). Synthesis methods can be optimized to form a close contact between g-C₃N₄ and the coupled material, which is important

for efficient interfacial charge transfer. The surface chemistry of g-C₃N₄ is desired to be tuned for the easy-loading of other materials to form heterostructure and favorable for the adsorption of reactants.

(2) Although the loading of UC materials has shown great potential in broadening the optical response of g-C₃N₄ photocatalysts from the UV and visible to NIR regimes, there are still a number of constraints in the practical application of UC particles for photocatalytic reactions, such as low absorption capacity, low quantum yield, preference for lasers with specific, limited wavelengths as excitation sources. To overcome these challenges, it is attractive and feasible to explore and/or use a mixture of diverse UC particles sensitized by different types of sensitizer and activator dopants. Constructing core@shell UC structures to suppress the non-radiative decay of UC PL emissions represents another promising approach. Developing UC materials which can be excited by broadband irradiations through introducing some materials (e.g. synthetic dyes, transition metals and quantum dots) with large absorption cross sections appears very feasible. The introduction of the SPR effect can concentrate the excitation light source and thus effectively enhance light absorption also. In addition, coupling with plasmonic metals and sensitization with dyes can also increase the energy transfer rate and efficiency, and thus results in an enhanced quantum yield. To make full utilization of UC emissions, the rational structure design of UC particle-g-C₃N₄ photocatalysts is of great significance. For example, the upconverting-core@g-C₃N₄-shell structure allows UC photons in all directions to have a chance of being absorbed, and the close contact between the UC materials and g-C₃N₄ greatly facilitates the energy transfer between them. The selection of suitable dopants, enabling as large a spectral overlap as possible between the UC emissions and g-C₃N₄ absorption, is very important in harvesting the emissions from UC particles.

(3) Low-cost broadband g-C₃N₄ based photocatalysts are expected to be developed. Plasmonic noble metallic NPs, such as Au NRs, have been loaded onto g-C₃N₄ nanosheets to make the composite possess broadband and enhanced photocatalytic performance. However, their practical application is severely limited by the high cost and rarity of noble metals. Some other plasmonic materials, such as Cu, CuS, TiN, and W₁₈O₄₉, can be promising candidates. Thanks to the well-studied synthetic methods of plasmonic materials the tunable SPR effect has great potential in the development of broadband g-C₃N₄ based photocatalysts. In addition, non-metal materials substitutes for metal-containing ones are also strongly encouraged.

(4) Constructing narrow-bandgap semiconductor/g-C₃N₄ photocatalytic systems with suitable band structures is pivotal for efficient solar energy conversion. The band positions can influence

the redox capability of the photocatalysts, while narrow-bandgap semiconductors normally have weak reduction or weak oxidization potential. Both the broadband absorption of narrow-bandgap semiconductor and the strong redox capability of g-C₃N₄ are desired. The construction of a Z-scheme photocatalytic system can achieve both at the same time. Exploring suitable semiconductors to form Z-scheme heterojunction with g-C₃N₄ is of significance and challenges.

(5) A fundamental understanding of the mechanism behind the charge transfer in metallic NPs/g-C₃N₄ or narrow-bandgap/g-C₃N₄ heterojunctions is critical. For example, the SPR-induced hot electron transfer pathway and kinetics (including the rate of back transfer), which play an important role in improving the photocatalytic activity, are still difficult to be determined. More explorations have to be conducted in this research direction. Unified predictive models are highly desired to give guidance in the effective design of broadband g-C₃N₄ based composite photocatalysts. In addition, state-of-art characterization techniques are in urgent demand. In particular, the in situ ultrafast characterizations of the behavior and fate of charge carriers at the surface and interface during photocatalysis will be able to provide valuable information and largely help with better understanding of the processes.

BIBLIOGRAPHY

1. Hall C, Tharakan P, Hallock J, Cleveland C, Jefferson M (2003) Hydrocarbons and the evolution of human culture. *Nature* 426(6964):318-322.
2. Poizot P, Dolhem F (2011) Clean energy new deal for a sustainable world: from non-CO₂ generating energy sources to greener electrochemical storage devices. *Energy Environ. Sci.* 4(6):2003-2019.
3. Wu HL, Li XB, Tung CH, Wu LZ (2019) Semiconductor Quantum Dots: An Emerging Candidate for CO₂ Photoreduction. *Adv. Mater.* 31(36):1900709.
4. Dalle KE, Warnan J, Leung JJ, Reuillard B, Karmel IS, Reisner E (2019) Electro- and Solar-Driven Fuel Synthesis with First Row Transition Metal Complexes. *Chem. Rev.* 119(4):2752-2875.
5. Morton O (2006) Solar energy: A new day dawning?: Silicon Valley sunrise. *Nature* 443(7107):19-22.
6. Lewis NS, Nocera DG (2006) Powering the planet: Chemical challenges in solar energy utilization. *Proc. Natl. Acad. Sci.* 103(43):15729-15735.
7. Wang Z, Li C, Domen K (2019) Recent developments in heterogeneous photocatalysts for solar-driven overall water splitting. *Chem. Soc. Rev.* 48(7):2109-2125.
8. Lewis NS (2007) Toward cost-effective solar energy use. *Science* 315(5813):798-801.
9. Di J, Xiong J, Li HM, Liu Z (2018) Ultrathin 2D Photocatalysts: Electronic-Structure Tailoring, Hybridization, and Applications. *Adv. Mater.* 30(1):1704548.
10. Low JX, Yu JG, Jaroniec M, Wageh S, Al-Ghamdi AA (2017) Heterojunction Photocatalysts. *Adv. Mater.* 29(20):1601694.
11. Schneider J, Matsuoka M, Takeuchi M, Zhang JL, Horiuchi Y, Anpo M, Bahnemann DW (2014) Understanding TiO₂ Photocatalysis: Mechanisms and Materials. *Chem. Rev.* 114(19):9919-9986.
12. Fujishima A, Honda K (1972) Electrochemical Photolysis of Water at a Semiconductor Electrode. *Nature* 238(5358):37-38.
13. Frank SN, Bard AJ (1977) Heterogeneous photocatalytic oxidation of cyanide ion in aqueous solutions at titanium dioxide powder. *J. Am. Chem. Soc.* 99(1):303-304.
14. Hoffmann MR, Martin ST, Choi WY, Bahnemann DW (1995) Environmental Applications of Semiconductor Photocatalysis. *Chem. Rev.* 95(1):69-96.
15. Zhang Y, He S, Guo W, Hu Y, Huang J, Mulcahy JR, Wei WD (2018) Surface-Plasmon-Driven Hot Electron Photochemistry. *Chem. Rev.* 118(6):2927-2954.
16. Wang SC, Liu G, Wang LZ (2019) Crystal Facet Engineering of Photoelectrodes for Photoelectrochemical Water Splitting. *Chem. Rev.* 119(8):5192-5247.
17. Zhang JL, Wu YM, Xing MY, Leghari SAK, Sajjad S (2010) Development of modified N doped TiO₂ photocatalyst with metals, nonmetals and metal oxides. *Energy Environ. Sci.* 3(6):715-726.
18. Kubacka A, Fernandez-Garcia M, Colon G (2012) Advanced Nanoarchitectures for Solar Photocatalytic Applications. *Chem. Rev.* 112(3):1555-1614.

19. Jing LQ, Zhou W, Tian GH, Fu HG (2013) Surface tuning for oxide-based nanomaterials as efficient photocatalysts. *Chem. Soc. Rev.* 42(24):9509-9549.
20. Wang W, Tade MO, Shao ZP (2015) Research progress of perovskite materials in photocatalysis- and photovoltaics-related energy conversion and environmental treatment. *Chem. Soc. Rev.* 44(15):5371-5408.
21. Pelaez M, Nolan NT, Pillai SC, Seery MK, Falaras P, Kontos AG, Dunlop PSM, Hamilton JWJ, Byrne JA, O'Shea K, Entezari MH, Dionysiou DD (2012) A review on the visible light active titanium dioxide photocatalysts for environmental applications. *Appl. Catal., B* 125:331-349.
22. Li J, Li H, Zhan GM, Zhang LZ (2017) Solar Water Splitting and Nitrogen Fixation with Layered Bismuth Oxyhalides. *Acc. Chem. Res.* 50(1):112-121.
23. Chen XZ, Li N, Kong ZZ, Ong WJ, Zhao XJ (2018) Photocatalytic fixation of nitrogen to ammonia: state-of-the-art advancements and future prospects. *Mater. Horiz.* 5(1):9-27.
24. Zhang GP, Chen DY, Li NJ, Xu QF, Li H, He JH, Lu JM (2018) Preparation of ZnIn₂S₄ nanosheet-coated CdS nanorod heterostructures for efficient photocatalytic reduction of Cr(VI). *Appl. Catal., B* 232:164-174.
25. Crespo-Quesada M, Reisner E (2017) Emerging approaches to stabilise photocorroding electrodes and catalysts for solar fuel applications. *Energy Environ. Sci.* 10(5):1116-1127.
26. Kampouri S, Stylianou KC (2019) Dual-Functional Photocatalysis for Simultaneous Hydrogen Production and Oxidation of Organic Substances. *ACS Catal.* 9(5):4247-4270.
27. Edwards PP, Kuznetsov VL, David WIF, Brandon NP (2008) Hydrogen and fuel cells: Towards a sustainable energy future. *Energy Policy* 36(12):4356-4362.
28. Gaya UI, Abdullah AH (2008) Heterogeneous photocatalytic degradation of organic contaminants over titanium dioxide: A review of fundamentals, progress and problems. *J. Photochem. Photobiol., C* 9(1):1-12.
29. Yang MQ, Gao MM, Hong MH, Ho GW (2018) Visible-to-NIR Photon Harvesting: Progressive Engineering of Catalysts for Solar-Powered Environmental Purification and Fuel Production. *Adv. Mater.* 30(47):1802894.
30. Huang DL, Chen S, Zeng GM, Gong XM, Zhou CY, Cheng M, Xue WJ, Yan XL, Li J (2019) Artificial Z-scheme photocatalytic system: What have been done and where to go? *Coordin. Chem. Rev.* 385:44-80.
31. Jin XL, Ye LQ, Xie HQ, Chen G (2017) Bismuth-rich bismuth oxyhalides for environmental and energy photocatalysis. *Coordin. Chem. Rev.* 349:84-101.
32. Peng YK, Tsang SCE (2018) Facet-dependent photocatalysis of nanosize semiconductive metal oxides and progress of their characterization. *Nano Today* 18:15-34.
33. Fox MA, Dulay MT (1993) Heterogeneous photocatalysis. *Chem. Rev.* 93(1):341-357.
34. Xiao FX, Miao JW, Tao HB, Hung SF, Wang HY, Yang HB, Chen JZ, Chen R, Liu B (2015) One-Dimensional Hybrid Nanostructures for Heterogeneous Photocatalysis and Photoelectrocatalysis. *Small* 11(18):2115-2131.
35. Li A, Zhu WJ, Li CC, Wang T, Gong JL (2019) Rational design of yolk-shell nanostructures for photocatalysis. *Chem. Soc. Rev.* 48(7):1874-1907.
36. Bahnemann DW, Hilgendorff M, Memming R (1997) Charge carrier dynamics at TiO₂ particles: Reactivity of free and trapped holes. *J. Phys. Chem. B* 101(21):4265-4275.

37. Tang JW, Durrant JR, Klug DR (2008) Mechanism of photocatalytic water splitting in TiO₂. Reaction of water with photoholes, importance of charge carrier dynamics, and evidence for four-hole chemistry. *J. Am. Chem. Soc.* 130(42):13885-13891.
38. Colombo DP, Bowman RM (1996) Does interfacial charge transfer compete with charge carrier recombination? A femtosecond diffuse reflectance investigation of TiO₂ nanoparticles. *J. Phys. Chem.* 100(47):18445-18449.
39. Wang HL, Zhang LS, Chen ZG, Hu JQ, Li SJ, Wang ZH, Liu JS, Wang XC (2014) Semiconductor heterojunction photocatalysts: design, construction, and photocatalytic performances. *Chem. Soc. Rev.* 43(15):5234-5244.
40. Zhou HL, Qu YQ, Zeid T, Duan XF (2012) Towards highly efficient photocatalysts using semiconductor nanoarchitectures. *Energy Environ. Sci.* 5(5):6732-6743.
41. Ohtani B (2014) Revisiting the fundamental physical chemistry in heterogeneous photocatalysis: its thermodynamics and kinetics. *Phys. Chem. Chem. Phys.* 16(5):1788-1797.
42. Tan HL, Amal R, Ng YH (2017) Alternative strategies in improving the photocatalytic and photoelectrochemical activities of visible light-driven BiVO₄: a review. *J. Mater. Chem. A* 5(32):16498-16521.
43. Zhang P, Wang T, Gong JL (2015) Mechanistic Understanding of the Plasmonic Enhancement for Solar Water Splitting. *Adv. Mater.* 27(36):5328-5342.
44. Zhang Q, Thrithamarassery Gangadharan D, Liu Y, Xu Z, Chaker M, Ma D (2017) Recent Advancements in Plasmon-Enhanced Visible Light-Driven Water Splitting. *J. Materiomics* 3(1):33-50.
45. Bard AJ, Fox MA (1995) Artificial Photosynthesis-Solar Splitting of Water to Hydrogen and Oxygen. *Acc. Chem. Res.* 28(3):141-145.
46. Mascaretti L, Dutta A, Kment S, Shalaev VM, Boltasseva A, Zboril R, Naldoni A (2019) Plasmon-Enhanced Photoelectrochemical Water Splitting for Efficient Renewable Energy Storage. *Adv. Mater.* 31(31):1805513.
47. Kim JH, Lee JS (2019) Elaborately Modified BiVO₄ Photoanodes for Solar Water Splitting. *Adv. Mater.* 31(20):1806938.
48. Roger I, Shipman MA, Symes MD (2017) Earth-abundant catalysts for electrochemical and photoelectrochemical water splitting. *Nat. Rev. Chem.* 1(1):0003.
49. Seh ZW, Kibsgaard J, Dickens CF, Chorkendorff IB, Norskov JK, Jaramillo TF (2017) Combining theory and experiment in electrocatalysis: Insights into materials design. *Science* 355(6321):eaad4998.
50. Serpone N, Lawless D, Khairutdinov R, Pelizzetti E (1995) Subnanosecond Relaxation Dynamics in TiO₂ Colloidal Sols (Particle Sizes R_p = 1.0-13.4 nm) - Relevance to Heterogeneous Photocatalysis. *J. Phys. Chem.* 99(45):16655-16661.
51. Li Q, Li X, Wageh S, Al-Ghamdi AA, Yu JG (2015) CdS/Graphene Nanocomposite Photocatalysts. *Adv. Energy Mater.* 5(14):1500010.
52. Liu J, Liu Y, Liu NY, Han YZ, Zhang X, Huang H, Lifshitz Y, Lee ST, Zhong J, Kang ZH (2015) Metal-Free Efficient Photocatalyst for Stable Visible Water Splitting via a Two-Electron Pathway. *Science* 347(6225):970-974.
53. Liu XY, Chen H, Wang RL, Shang YQ, Zhang Q, Li W, Zhang GZ, Su J, Dinh CT, de Arquer FPG, Li J, Jiang J, Mi QX, Si R, Li XP, Sun YH, Long YT, Tian H, Sargent EH, Ning ZJ (2017)

- 0D-2D Quantum Dot: Metal Dichalcogenide Nanocomposite Photocatalyst Achieves Efficient Hydrogen Generation. *Adv. Mater.* 29(22):1605646.
54. Cheng FR, Jiang X, Zhang ZP, Ma RZ, Sasaki T, Pan F, Jing XP (2019) Preparation of 1D ultrathin niobate nanobelts by liquid exfoliation as photocatalysts for hydrogen generation. *Chem. Commun.* 55(17):2417-2420.
 55. Yang T, Wang H, Ou XM, Lee CS, Zhang XH (2012) Iodine-Doped-Poly(3,4-Ethylenedioxythiophene)-Modified Si Nanowire 1D Core-Shell Arrays as an Efficient Photocatalyst for Solar Hydrogen Generation. *Adv. Mater.* 24(46):6199-6203.
 56. Wu M, Zhang J, He BB, Wang HW, Wang R, Gong YS (2019) In-situ construction of coral-like porous P-doped g-C₃N₄ tubes with hybrid 1D/2D architecture and high efficient photocatalytic hydrogen evolution. *Appl. Catal., B* 241:159-166.
 57. Qiao M, Liu J, Wang Y, Li YF, Chen ZF (2018) PdSeO₃ Monolayer: Promising Inorganic 2D Photocatalyst for Direct Overall Water Splitting Without Using Sacrificial Reagents and Cocatalysts. *J. Am. Chem. Soc.* 140(38):12256-12262.
 58. Rahman MZ, Kwong CW, Davey K, Qiao SZ (2016) 2D Phosphorene as a Water Splitting Photocatalyst: Fundamentals to Applications. *Energy Environ. Sci.* 9(3):709-728.
 59. Ganguly P, Harb M, Cao Z, Cavallo L, Breen A, Dervin S, Dionysiou DD, Pillai SC (2019) 2D Nanomaterials for Photocatalytic Hydrogen Production. *ACS Energy Lett.* 4(7):1687-1709.
 60. Ran JR, Gao GP, Li FT, Ma TY, Du AJ, Qiao SZ (2017) Ti₃C₂ MXene co-catalyst on metal sulfide photo-absorbers for enhanced visible-light photocatalytic hydrogen production. *Nat. Commun.* 8:13907.
 61. Li A, Chang XX, Huang ZQ, Li CC, Wei YJ, Zhang L, Wang T, Gong JL (2016) Thin Heterojunctions and Spatially Separated Cocatalysts To Simultaneously Reduce Bulk and Surface Recombination in Photocatalysts. *Angew. Chem., Int. Ed.* 55(44):13734-13738.
 62. Zhu W, Chen Z, Pan Y, Dai R, Wu Y, Zhuang Z, Wang D, Peng Q, Chen C, Li Y (2018) Functionalization of Hollow Nanomaterials for Catalytic Applications: Nanoreactor Construction. *Adv. Mater.* 31(38):1800426.
 63. Xiao M, Wang Z, Lyu M, Luo B, Wang S, Liu G, Cheng HM, Wang L (2019) Hollow Nanostructures for Photocatalysis: Advantages and Challenges. *Adv. Mater.* 31(38):1801369.
 64. Zhou L, Zhuang Z, Zhao H, Lin M, Zhao D, Mai L (2017) Intricate Hollow Structures: Controlled Synthesis and Applications in Energy Storage and Conversion. *Adv. Mater.* 29(20):1602914.
 65. Zhang Q, Jin X, Xu Z, Zhang J, Rendon UF, Razzari L, Chaker M, Ma D (2018) Plasmonic Au Loaded Hierarchical Hollow Porous TiO₂ Spheres: Synergistic Catalysts for Nitroaromatic Reduction. *J. Phys. Chem. Lett.* 9(18):5317-5326.
 66. Bian ZF, Zhu J, Li HX (2016) Solvothermal alcoholysis synthesis of hierarchical TiO₂ with enhanced activity in environmental and energy photocatalysis. *J. Photochem. Photobiol., C* 28:72-86.
 67. Wang W-K, Chen J-J, Lou Z-Z, Kim S, Fujitsuka M, Yu H-Q, Majima T (2019) Single-molecule and-particle probing crystal edge/corner as highly efficient photocatalytic sites on a single TiO₂ particle. *Proc. Natl. Acad. Sci.* 116(38):18827-18833.
 68. Guo Q, Ma Z, Zhou C, Ren Z, Yang X (2019) Single Molecule Photocatalysis on TiO₂ Surfaces. *Chem. Rev.* 119(20):11020-11041.

69. Qian RF, Zong HX, Schneider J, Zhou GD, Zhao T, Li YL, Yang J, Bahnemann DW, Pan JH (2019) Charge carrier trapping, recombination and transfer during TiO₂ photocatalysis: An overview. *Catal. Today* 335:78-90.
70. Akhavan O (2010) Graphene Nanomesh by ZnO Nanorod Photocatalysts. *ACS Nano* 4(7):4174-4180.
71. Lee KM, Lai CW, Ngai KS, Juan JC (2016) Recent developments of zinc oxide based photocatalyst in water treatment technology: A review. *Water Res.* 88:428-448.
72. Ong CB, Ng LY, Mohammad AW (2018) A review of ZnO nanoparticles as solar photocatalysts: Synthesis, mechanisms and applications. *Renewable Sustainable Energy Rev.* 81:536-551.
73. Kambur A, Pozan GS, Boz I (2012) Preparation, characterization and photocatalytic activity of TiO₂-ZrO₂ binary oxide nanoparticles. *Appl. Catal., B* 115:149-158.
74. Bansal P, Chaudhary GR, Mehta SK (2015) Comparative study of catalytic activity of ZrO₂ nanoparticles for sonocatalytic and photocatalytic degradation of cationic and anionic dyes. *Chem. Eng. J.* 280:475-485.
75. Tian JY, Shao Q, Zhao JK, Pan D, Dong MY, Jia CXZ, Ding T, Wu TT, Guo ZH (2019) Microwave solvothermal carboxymethyl chitosan templated synthesis of TiO₂/ZrO₂ composites toward enhanced photocatalytic degradation of Rhodamine B. *J. Colloid Interface Sci.* 541:18-29.
76. Zhou XM, Xu QL, Lei WY, Zhang TT, Qi XY, Liu G, Deng K, Yu JG (2014) Origin of Tunable Photocatalytic Selectivity of Well-Defined alpha-Fe₂O₃ Nanocrystals. *Small* 10(4):674-679.
77. Mishra M, Chun DM (2015) alpha-Fe₂O₃ as a photocatalytic material: A review. *Appl. Catal., A* 498:126-141.
78. Jiang ZF, Wan WM, Li HM, Yuan SQ, Zhao HJ, Wong PK (2018) A Hierarchical Z-Scheme alpha-Fe₂O₃/g-C₃N₄ Hybrid for Enhanced Photocatalytic CO₂ Reduction. *Adv. Mater.* 30(10):1706108.
79. Wang GM, Ling YC, Wang HY, Yang XY, Wang CC, Zhang JZ, Li Y (2012) Hydrogen-treated WO₃ nanoflakes show enhanced photostability. *Energy Environ. Sci.* 5(3):6180-6187.
80. Kim J, Lee CW, Choi W (2010) Platinized WO₃ as an Environmental Photocatalyst that Generates OH Radicals under Visible Light. *Environ. Sci. Technol.* 44(17):6849-6854.
81. Ma M, Zhang K, Li P, Jung MS, Jeong MJ, Park JH (2016) Dual Oxygen and Tungsten Vacancies on a WO₃ Photoanode for Enhanced Water Oxidation. *Angew. Chem., Int. Ed.* 55(39):11819-11823.
82. Tan HL, Wen XM, Amal R, Ng YH (2016) BiVO₄ {010} and {110} Relative Exposure Extent: Governing Factor of Surface Charge Population and Photocatalytic Activity. *J. Phys. Chem. Lett.* 7(7):1400-1405.
83. Li P, Chen XY, He HC, Zhou X, Zhou Y, Zou ZG (2018) Polyhedral 30-Faceted BiVO₄ Microcrystals Predominantly Enclosed by High-Index Planes Promoting Photocatalytic Water-Splitting Activity. *Adv. Mater.* 30(1):1703119.
84. Li GQ, Shen QY, Yang ZZ, Kou SW, Zhang F, Zhang WF, Guo HZ, Du YG (2019) Photocatalytic behaviors of epitaxial BiVO₄ (010) thin films. *Appl. Catal., B* 248:115-119.
85. Yi H, Yan M, Huang DL, Zeng GM, Lai C, Li MF, Huo XQ, Qin L, Liu SY, Liu XG, Li BS, Wang H, Shen MC, Fu YK, Guo XY (2019) Synergistic effect of artificial enzyme and 2D nano-

- structured Bi_2WO_6 for eco-friendly and efficient biomimetic photocatalysis. *Appl. Catal., B* 250:52-62.
86. Zargazi M, Entezari MH (2019) Anodic electrophoretic deposition of Bi_2WO_6 thin film: high photocatalytic activity for degradation of a binary mixture. *Appl. Catal., B* 242:507-517.
 87. Tian J, Sang Y, Yu G, Jiang H, Mu X, Liu H (2013) A Bi_2WO_6 -Based Hybrid Photocatalyst with Broad Spectrum Photocatalytic Properties under UV, Visible, and Near-Infrared Irradiation. *Adv. Mater.* 25(36):5075-5080.
 88. Chai ZG, Zeng TT, Li Q, Lu LQ, Xiao WJ, Xu DS (2016) Efficient Visible Light-Driven Splitting of Alcohols into Hydrogen and Corresponding Carbonyl Compounds over a Ni-Modified CdS Photocatalyst. *J. Am. Chem. Soc.* 138(32):10128-10131.
 89. Cheng L, Xiang QJ, Liao YL, Zhang HW (2018) CdS-Based photocatalysts. *Energy Environ. Sci.* 11(6):1362-1391.
 90. Sun QM, Wang N, Yu JH, Yu JC (2018) A Hollow Porous CdS Photocatalyst. *Adv. Mater.* 30(45):1804368.
 91. Yu WW, Guo XW, Song CS, Zhao ZK (2019) Visible-light-initiated one-pot clean synthesis of nitrene from nitrobenzene and benzyl alcohol over CdS photocatalyst. *J. Catal.* 370:97-106.
 92. Wang XC, Blechert S, Antonietti M (2012) Polymeric Graphitic Carbon Nitride for Heterogeneous Photocatalysis. *ACS Catal.* 2(8):1596-1606.
 93. Ong WJ, Tan LL, Ng YH, Yong ST, Chai SP (2016) Graphitic Carbon Nitride ($\text{g-C}_3\text{N}_4$)-Based Photocatalysts for Artificial Photosynthesis and Environmental Remediation: Are We a Step Closer To Achieving Sustainability? *Chem. Rev.* 116(12):7159-7329.
 94. Fu J, Yu J, Jiang C, Cheng B (2018) $\text{g-C}_3\text{N}_4$ -Based Heterostructured Photocatalysts. *Adv. Energy Mater.* 8(3):1701503.
 95. Wang H, Zhang X, Xie Y (2019) Photoresponsive Polymeric Carbon Nitride-Based Materials: Design and Application. *Mater. Today* 23:72-86.
 96. Zheng Y, Liu J, Liang J, Jaroniec M, Qiao SZ (2012) Graphitic carbon nitride materials: controllable synthesis and applications in fuel cells and photocatalysis. *Energy Environ. Sci.* 5(5):6717-6731.
 97. Zheng Y, Lin LH, Wang B, Wang XC (2015) Graphitic Carbon Nitride Polymers toward Sustainable Photoredox Catalysis. *Angew. Chem., Int. Ed.* 54(44):12868-12884.
 98. Cao S, Low J, Yu J, Jaroniec M (2015) Polymeric Photocatalysts Based on Graphitic Carbon Nitride. *Adv. Mater.* 27(13):2150-2176.
 99. Dong GP, Zhang YH, Pan QW, Qiu JR (2014) A fantastic graphitic carbon nitride ($\text{g-C}_3\text{N}_4$) material: Electronic structure, photocatalytic and photoelectronic properties. *J. Photochem. Photobiol., C* 20:33-50.
 100. Sano T, Tsutsui S, Koike K, Hirakawa T, Teramoto Y, Negishi N, Takeuchi K (2013) Activation of graphitic carbon nitride ($\text{g-C}_3\text{N}_4$) by alkaline hydrothermal treatment for photocatalytic NO oxidation in gas phase. *J. Mater. Chem. A* 1(21):6489-6496.
 101. Maeda K, Wang XC, Nishihara Y, Lu DL, Antonietti M, Domen K (2009) Photocatalytic Activities of Graphitic Carbon Nitride Powder for Water Reduction and Oxidation under Visible Light. *J. Phys. Chem. C* 113(12):4940-4947.

102. Wang X, Maeda K, Thomas A, Takahabe K, Xin G, Carlsson JM, Domen K, Antonietti M (2009) A Metal-Free Polymeric Photocatalyst for Hydrogen Production from Water under Visible Light. *Nat. Mater.* 8(1):76-80.
103. Yan SC, Li ZS, Zou ZG (2009) Photodegradation Performance of g-C₃N₄ Fabricated by Directly Heating Melamine. *Langmuir* 25(17):10397-10401.
104. Xiao YT, Tian GH, Li W, Xie Y, Jiang BJ, Tian CG, Zhao DY, Fu HG (2019) Molecule Self-Assembly Synthesis of Porous Few-Layer Carbon Nitride for Highly Efficient Photoredox Catalysis. *J. Am. Chem. Soc.* 141(6):2508-2515.
105. Liang J, Zheng Y, Chen J, Liu J, Hulicova-Jurcakova D, Jaroniec M, Qiao SZ (2012) Facile Oxygen Reduction on a Three-Dimensionally Ordered Macroporous Graphitic C₃N₄/Carbon Composite Electrocatalyst. *Angew. Chem., Int. Ed.* 51(16):3892-3896.
106. Ji HH, Chang F, Hu XF, Qin W, Shen JW (2013) Photocatalytic degradation of 2,4,6-trichlorophenol over g-C₃N₄ under visible light irradiation. *Chem. Eng. J.* 218:183-190.
107. Han Q, Wang B, Zhao Y, Hu CG, Qu LT (2015) A Graphitic-C₃N₄ "Seaweed" Architecture for Enhanced Hydrogen Evolution. *Angew. Chem., Int. Ed.* 54(39):11433-11437.
108. Dong F, Wang ZY, Sun YJ, Ho WK, Zhang HD (2013) Engineering the nanoarchitecture and texture of polymeric carbon nitride semiconductor for enhanced visible light photocatalytic activity. *J. Colloid Interface Sci.* 401:70-79.
109. Zou YD, Yang BB, Liu Y, Ren Y, Ma JH, Zhou XR, Cheng XW, Deng YH (2018) Controllable Interface -Induced Co-Assembly toward Highly Ordered Mesoporous Pt@TiO₂/g-C₃N₄ Heterojunctions with Enhanced Photocatalytic Performance. *Adv. Funct. Mater.* 28(50):1806214.
110. Zhang GG, Zhang JS, Zhang MW, Wang XC (2012) Polycondensation of thiourea into carbon nitride semiconductors as visible light photocatalysts. *J. Mater. Chem.* 22(16):8083-8091.
111. Niu P, Zhang LL, Liu G, Cheng HM (2012) Graphene-Like Carbon Nitride Nanosheets for Improved Photocatalytic Activities. *Adv. Funct. Mater.* 22(22):4763-4770.
112. Jorge AB, Martin DJ, Dhanoa MTS, Rahman AS, Makwana N, Tang JW, Sella A, Cora F, Firth S, Darr JA, McMillan PF (2013) H₂ and O₂ Evolution from Water Half-Splitting Reactions by Graphitic Carbon Nitride Materials. *J. Phys. Chem. C* 117(14):7178-7185.
113. Zhu BC, Xia PF, Ho WK, Yu JG (2015) Isoelectric point and adsorption activity of porous g-C₃N₄. *Appl. Surf. Sci.* 344:188-195.
114. Wang K, Li Q, Liu BS, Cheng B, Ho WK, Yu JG (2015) Sulfur-doped g-C₃N₄ with enhanced photocatalytic CO₂-reduction performance. *Appl. Catal., B* 176:44-52.
115. Zhang JS, Chen XF, Takahabe K, Maeda K, Domen K, Epping JD, Fu XZ, Antonietti M, Wang XC (2010) Synthesis of a Carbon Nitride Structure for Visible-Light Catalysis by Copolymerization. *Angew. Chem., Int. Ed.* 49(2):441-444.
116. Shi XW, Fujitsuka M, Kim S, Majima T (2018) Faster Electron Injection and More Active Sites for Efficient Photocatalytic H₂ Evolution in g-C₃N₄/MoS₂ Hybrid. *Small* 14(11):1703277.
117. Ruan D, Kim S, Fujitsuka M, Majima T (2018) Defects Rich g-C₃N₄ with Mesoporous Structure for Efficient Photocatalytic H₂ Production under Visible Light Irradiation. *Appl. Catal., B* 238:638-646.
118. Yu FT, Wang ZQ, Zhang SC, Ye HN, Kong KY, Gong XQ, Hua JL, Tian H (2018) Molecular Engineering of Donor-Acceptor Conjugated Polymer/g-C₃N₄ Heterostructures for

- Significantly Enhanced Hydrogen Evolution Under Visible-Light Irradiation. *Adv. Funct. Mater.* 28(47):1804512.
119. Yan L, Gu ZJ, Zheng XP, Zhang CY, Li X, Zhao LN, Zhao YL (2017) Elemental Bismuth-Graphene Heterostructures for Photocatalysis from Ultraviolet to Infrared Light. *ACS Catal.* 7(10):7043-7050.
 120. Wang G, Huang BB, Ma XC, Wang ZY, Qin XY, Zhang XY, Dai Y, Whangbo MH (2013) $\text{Cu}_2(\text{OH})\text{PO}_4$, a Near-Infrared-Activated Photocatalyst. *Angew. Chem., Int. Ed.* 52(18):4810-4813.
 121. Wang L, Xu X, Cheng Q, Dou SX, Du Y (2019) Near-Infrared-Driven Photocatalysts: Design, Construction, and Applications. *Small* DOI: 10.1002/smll.201904107.
 122. Meng NN, Ren J, Liu Y, Huang Y, Petit T, Zhang B (2018) Engineering oxygen-containing and amino groups into two-dimensional atomically-thin porous polymeric carbon nitrogen for enhanced photocatalytic hydrogen production. *Energy Environ. Sci.* 11(3):566-571.
 123. Wang Y, Zhang JS, Wang XC, Antonietti M, Li HR (2010) Boron- and Fluorine-Containing Mesoporous Carbon Nitride Polymers: Metal-Free Catalysts for Cyclohexane Oxidation. *Angew. Chem., Int. Ed.* 49(19):3356-3359.
 124. Zhao D, Dong CL, Wang B, Chen C, Huang YC, Diao Z, Li S, Guo L, Shen S (2019) Synergy of Dopants and Defects in Graphitic Carbon Nitride with Exceptionally Modulated Band Structures for Efficient Photocatalytic Oxygen Evolution. *Adv. Mater.* 31(43):1903545.
 125. Zhang YJ, Mori T, Ye JH, Antonietti M (2010) Phosphorus-Doped Carbon Nitride Solid: Enhanced Electrical Conductivity and Photocurrent Generation. *J. Am. Chem. Soc.* 132(18):6294-6295.
 126. Zeng Y, Liu X, Liu C, Wang L, Xia Y, Zhang S, Luo S, Pei Y (2018) Scalable One-Step Production of Porous Oxygen-Doped g- C_3N_4 Nanorods with Effective Electron Separation for Excellent Visible-Light Photocatalytic Activity. *Appl. Catal., B* 224:1-9.
 127. Xia P, Antonietti M, Zhu B, Heil T, Yu J, Cao S (2019) Designing Defective Crystalline Carbon Nitride to Enable Selective CO_2 Photoreduction in the Gas Phase. *Adv. Funct. Mater.* 29(15):1900093.
 128. Zhang N, Li XY, Ye HC, Chen SM, Ju HX, Liu DB, Lin Y, Ye W, Wang CM, Xu Q, Zhu JF, Song L, Jiang J, Xiong YJ (2016) Oxide Defect Engineering Enables to Couple Solar Energy into Oxygen Activation. *J. Am. Chem. Soc.* 138(28):8928-8935.
 129. Zhou G, Shan Y, Hu YY, Xu XY, Long LY, Zhang JL, Dai J, Guo JH, Shen JC, Li S, Liu LZ, Wu XL (2018) Half-metallic carbon nitride nanosheets with micro grid mode resonance structure for efficient photocatalytic hydrogen evolution. *Nat. Commun.* 9:3366.
 130. Tong ZW, Yang D, Li Z, Nan YH, Ding F, Shen YC, Jiang ZY (2017) Thylakoid-Inspired Multishell g- C_3N_4 Nanocapsules with Enhanced Visible-Light Harvesting and Electron Transfer Properties for High-Efficiency Photocatalysis. *ACS Nano* 11(1):1103-1112.
 131. Tahir M, Cao CB, Butt FK, Idrees F, Mahmood N, Ali Z, Aslam I, Tanveer M, Rizwan M, Mahmood T (2013) Tubular graphitic- C_3N_4 : a prospective material for energy storage and green photocatalysis. *J. Mater. Chem. A* 1(44):13949-13955.
 132. Sun JH, Zhang JS, Zhang MW, Antonietti M, Fu XZ, Wang XC (2012) Bioinspired hollow semiconductor nanospheres as photosynthetic nanoparticles. *Nat. Commun.* 3:1139.

133. Tian N, Huang HW, Du X, Dong F, Zhang YH (2019) Rational nanostructure design of graphitic carbon nitride for photocatalytic applications. *J. Mater. Chem. A* 7(19):11584-11612.
134. Zhang XH, Yu LJ, Zhuang CS, Peng TY, Li RJ, Li XG (2014) Highly Asymmetric Phthalocyanine as a Sensitizer of Graphitic Carbon Nitride for Extremely Efficient Photocatalytic H₂ Production under Near-Infrared Light. *ACS Catal.* 4(1):162-170.
135. Li Z, Wu YQ, Lu GX (2016) Highly efficient hydrogen evolution over Co(OH)₂ nanoparticles modified g-C₃N₄ co-sensitized by Eosin Y and Rose Bengal under Visible Light Irradiation. *Appl. Catal., B* 188:56-64.
136. Zhang HY, Li S, Lu R, Yu AC (2015) Time-Resolved Study on Xanthene Dye-Sensitized Carbon Nitride Photocatalytic Systems. *ACS Appl. Mater. Interfaces* 7(39):21868-21874.
137. Takanebe K, Kamata K, Wang XC, Antonietti M, Kubota J, Domen K (2010) Photocatalytic hydrogen evolution on dye-sensitized mesoporous carbon nitride photocatalyst with magnesium phthalocyanine. *Phys. Chem. Chem. Phys.* 12(40):13020-13025.
138. Ma TY, Ran JR, Dai S, Jaroniec M, Qiao SZ (2015) Phosphorus-Doped Graphitic Carbon Nitrides Grown In Situ on Carbon-Fiber Paper: Flexible and Reversible Oxygen Electrodes. *Angew. Chem., Int. Ed.* 54(15):4646-4650.
139. Tan CL, Cao XH, Wu XJ, He QY, Yang J, Zhang X, Chen JZ, Zhao W, Han SK, Nam GH, Sindoro M, Zhang H (2017) Recent Advances in Ultrathin Two-Dimensional Nanomaterials. *Chem. Rev.* 117(9):6225-6331.
140. Han Q, Wang B, Gao J, Cheng Z, Zhao Y, Zhang Z, Qu L (2016) Atomically Thin Mesoporous Nanomesh of Graphitic C₃N₄ for High-Efficiency Photocatalytic Hydrogen Evolution. *ACS Nano* 10(2):2745-2751.
141. Li YX, Ouyang SX, Xu H, Hou WS, Zhao M, Chen HY, Ye JH (2019) Targeted Exfoliation and Reassembly of Polymeric Carbon Nitride for Efficient Photocatalysis. *Adv. Funct. Mater.* 29(27):1901024.
142. Yang S, Gong Y, Zhang J, Zhan L, Ma L, Fang Z, Vajtai R, Wang X, Ajayan PM (2013) Exfoliated Graphitic Carbon Nitride Nanosheets as Efficient Catalysts for Hydrogen Evolution Under Visible Light. *Adv. Mater.* 25(17):2452-2456.
143. Wang YB, Hong JD, Zhang W, Xu R (2013) Carbon nitride nanosheets for photocatalytic hydrogen evolution: remarkably enhanced activity by dye sensitization. *Catal. Sci. Technol.* 3(7):1703-1711.
144. Liu LQ, Ouyang SX, Ye JH (2013) Gold-Nanorod-Photosensitized Titanium Dioxide with Wide-Range Visible-Light Harvesting Based on Localized Surface Plasmon Resonance. *Angew. Chem., Int. Ed.* 52(26):6689-6693.
145. Xu ZH, Quintanilla M, Vetrone F, Govorov AO, Chaker M, Ma DL (2015) Harvesting Lost Photons: Plasmon and Upconversion Enhanced Broadband Photocatalytic Activity in Core@Shell Microspheres Based on Lanthanide-Doped NaYF₄, TiO₂, and Au. *Adv. Funct. Mater.* 25(20):2950-2960.
146. Teixeira IF, Barbosa ECM, Tsang SCE, Camargo PHC (2018) Carbon nitrides and metal nanoparticles: from controlled synthesis to design principles for improved photocatalysis. *Chem. Soc. Rev.* 47(20):7783-7817.
147. Nasir MS, Yang GR, Ayub I, Wang S, Wang L, Wang XJ, Yan W, Peng SJ, Ramakarishna S (2019) Recent development in graphitic carbon nitride based photocatalysis for hydrogen generation. *Appl. Catal., B* 257:117855.

148. Auzel F (2004) Upconversion and anti-stokes processes with f and d ions in solids. *Chem. Rev.* 104(1):139-173.
149. Zhou B, Shi BY, Jin DY, Liu XG (2015) Controlling Upconversion Nanocrystals for Emerging Applications. *Nat. Nanotechnol.* 10(11):924-936.
150. Liu XG, Yan CH, Capobianco JA (2015) Photon upconversion nanomaterials. *Chem. Soc. Rev.* 44(6):1299-1301.
151. Liu YJ, Lu YQ, Yang XS, Zheng XL, Wen SH, Wang F, Vidal X, Zhao JB, Liu DM, Zhou ZG, Ma CS, Zhou JJ, Piper JA, Xi P, Jin DY (2017) Amplified stimulated emission in upconversion nanoparticles for super-resolution nanoscopy. *Nature* 543(7644):229-233.
152. Zhang Q, Yang F, Xu Z, Chaker M, Ma D (2019) Are Lanthanide-Doped Upconversion Materials Good Candidates for Photocatalysis? *Nanoscale Horiz.* 4(3):579-591.
153. Wang F, Banerjee D, Liu YS, Chen XY, Liu XG (2010) Upconversion nanoparticles in biological labeling, imaging, and therapy. *Analyst* 135(8):1839-1854.
154. Wang F, Liu XG (2008) Upconversion multicolor fine-tuning: Visible to near-infrared emission from lanthanide-doped NaYF₄ nanoparticles. *J. Am. Chem. Soc.* 130(17):5642-5643.
155. Qin X, Liu XW, Huang W, Bettinelli M, Liu XG (2017) Lanthanide-Activated Phosphors Based on 4f-5d Optical Transitions: Theoretical and Experimental Aspects. *Chem. Rev.* 117(5):4488-4527.
156. Li Y, Gecevicius M, Qiu JR (2016) Long persistent phosphors-from fundamentals to applications. *Chem. Soc. Rev.* 45(8):2090-2136.
157. Chen X, Jin LM, Kong W, Sun TY, Zhang WF, Liu XH, Fan J, Yu SF, Wang F (2016) Confining energy migration in upconversion nanoparticles towards deep ultraviolet lasing. *Nat. Commun.* 7:10304.
158. Mandl GA, Rojas-Gutierrez PA, Capobianco JA (2018) A NIR-responsive azobenzene-based supramolecular hydrogel using upconverting nanoparticles. *Chem. Commun.* 54:5847-5850.
159. Li Y, Tang JL, Pan DX, Sun LD, Chen CY, Liu Y, Wang YF, Shi S, Yan CH (2016) A Versatile Imaging and Therapeutic Platform Based on Dual-Band Luminescent Lanthanide Nanoparticles toward Tumor Metastasis Inhibition. *ACS Nano* 10(2):2766-2773.
160. Zhang XH, Blasiak B, Marengo AJ, Trudel S, Tomanek B, van Veggel FCJM (2016) Design and Regulation of NaHoF₄ and NaDyF₄ Nanoparticles for High-Field Magnetic Resonance Imaging. *Chem. Mater.* 28(9):3060-3072.
161. Feng L, He F, Liu B, Yang G, Gai S, Yang P, Li C, Dai Y, Lv R, Lin J (2016) g-C₃N₄ Coated Upconversion Nanoparticles for 808 nm Near-Infrared Light Triggered Phototherapy and Multiple Imaging. *Chem. Mater.* 28(21):7935-7946.
162. Zhuo Z, Liu YS, Liu DJ, Huang P, Jiang FL, Chen XY, Hong MC (2017) Manipulating energy transfer in lanthanide-doped single nanoparticles for highly enhanced upconverting luminescence. *Chem. Sci.* 8(7):5050-5056.
163. Dong H, Sun LD, Li LD, Si R, Liu R, Yan CH (2017) Selective Cation Exchange Enabled Growth of Lanthanide Core/Shell Nanoparticles with Dissimilar Structure. *J. Am. Chem. Soc.* 139(51):18492-18495.
164. Xu JT, Han W, Cheng ZY, Yang PP, Bi HT, Yang D, Niu N, He F, Gai SL, Lin J (2018) Bioresponsive and near infrared photon co-enhanced cancer theranostic based on upconversion nanocapsules. *Chem. Sci.* 9(12):3233-3247.

165. Han SY, Qin X, An ZF, Zhu YH, Liang LL, Han Y, Huang W, Liu XG (2016) Multicolour synthesis in lanthanide-doped nanocrystals through cation exchange in water. *Nat. Commun.* 7:13059.
166. Liu DM, Xu XX, Du Y, Qin X, Zhang YH, Ma CS, Wen SH, Ren W, Goldys EM, Piper JA, Dou SX, Liu XG, Jin DY (2016) Three-dimensional controlled growth of monodisperse sub-50 nm heterogeneous nanocrystals. *Nat. Commun.* 7:10254.
167. Han S, Samanta A, Xie XJ, Huang L, Peng JJ, Park SJ, Teh DBL, Choi Y, Chang YT, All AH, Yang YM, Xing BG, Liu XG (2017) Gold and Hairpin DNA Functionalization of Upconversion Nanocrystals for Imaging and In Vivo Drug Delivery. *Adv. Mater.* 29(18):1700244.
168. Chen QS, Xie XJ, Huang BL, Liang LL, Han SY, Yi ZG, Wang Y, Li Y, Fan DY, Huang L, Liu XG (2017) Confining Excitation Energy in Er³⁺-Sensitized Upconversion Nanocrystals through Tm³⁺-Mediated Transient Energy Trapping. *Angew. Chem., Int. Ed.* 56(26):7605-7609.
169. Chen S, Weitemier AZ, Zeng X, He LM, Wang XY, Tao YQ, Huang AJY, Hashimoto-dani Y, Kano M, Iwasaki H, Parajuli LK, Okabe S, Teh DBL, All AH, Tsutsui-Kimura I, Tanaka KF, Liu XG, McHugh TJ (2018) Near-infrared deep brain stimulation via upconversion nanoparticle-mediated optogenetics. *Science* 359(6376):679-683.
170. Shi S, Sun LD, Xue YX, Dong H, Wu K, Guo SC, Wu BT, Yan CH (2018) Scalable Direct Writing of Lanthanide-Doped KMnF₃ Perovskite Nanowires into Aligned Arrays with Polarized Up-Conversion Emission. *Nano Lett.* 18(5):2964-2969.
171. Rodriguez-Sevilla P, Zhang YH, de Sousa N, Marques MI, Sanz-Rodriguez F, Jaque D, Liu XG, Haro-Gonzalez P (2016) Optical Torques on Upconverting Particles for Intracellular Microrheometry. *Nano Lett.* 16(12):8005-8014.
172. Zhang YH, Huang L, Liu XG (2016) Unraveling Epitaxial Habits in the NaLnF₄ System for Color Multiplexing at the Single-Particle Level. *Angew. Chem., Int. Ed.* 55(19):5718-5722.
173. Zhu XJ, Feng W, Chang J, Tan YW, Li JC, Chen M, Sun Y, Li FY (2016) Temperature-feedback upconversion nanocomposite for accurate photothermal therapy at facile temperature. *Nat. Commun.* 7:10437.
174. Liu XW, Wang Y, Li XY, Yi ZG, Deng RR, Liang LL, Xie XJ, Loong DTB, Song SY, Fan DY, All AH, Zhang HJ, Huang L, Liu XG (2017) Binary temporal upconversion codes of Mn²⁺-activated nanoparticles for multilevel anti-counterfeiting. *Nat. Commun.* 8:899.
175. Liu XW, Li XY, Qin X, Xie XJ, Huang L, Liu XG (2017) Hedgehog-Like Upconversion Crystals: Controlled Growth and Molecular Sensing at Single-Particle Level. *Adv. Mater.* 29(37):1702315.
176. Wang L, Gao C, Liu KY, Liu YX, Ma LY, Liu LD, Du XX, Zhou J (2016) Cypate-Conjugated Porous Upconversion Nanocomposites for Programmed Delivery of Heat Shock Protein 70 Small Interfering RNA for Gene Silencing and Photothermal Ablation. *Adv. Funct. Mater.* 26(20):3480-3489.
177. Savchuk OA, Carvajal JJ, Brites CDS, Carlos LD, Aguilo M, Diaz F (2018) Upconversion thermometry: a new tool to measure the thermal resistance of nanoparticles. *Nanoscale* 10(14):6602-6610.
178. Quintanilla M, Ren FQ, Ma DL, Vetrone F (2014) Light Management in Upconverting Nanoparticles: Ultrasmall Core/Shell Architectures to Tune the Emission Color. *ACS Photonics* 1(8):662-669.

179. Som S, Das S, Yang CY, Lu CH (2016) Enhanced upconversion of NaYF₄:Er³⁺/Yb³⁺ phosphors prepared via the rapid microwave-assisted hydrothermal route at low temperature: phase and morphology control. *Opt. Lett.* 41(3):464-467.
180. Tang YN, Di WH, Zhai XS, Yang RY, Qin WP (2013) NIR-Responsive Photocatalytic Activity and Mechanism of NaYF₄:Yb,Tm@TiO₂ Core-Shell Nanoparticles. *ACS Catal.* 3(3):405-412.
181. Xu DX, Lian ZW, Fu ML, Yuan BL, Shi JW, Cui HJ (2013) Advanced near-infrared-driven photocatalyst: Fabrication, characterization, and photocatalytic performance of beta-NaYF₄:Yb³⁺,Tm³⁺@TiO₂ core@shell microcrystals. *Appl. Catal., B* 142:377-386.
182. Wang W, Ding MY, Lu CH, Ni YR, Xu ZZ (2014) A study on upconversion UV-vis-NIR responsive photocatalytic activity and mechanisms of hexagonal phase NaYF₄:Yb³⁺,Tm³⁺@TiO₂ core-shell structured photocatalyst. *Appl. Catal., B* 144:379-385.
183. Wang W, Huang WJ, Ni YR, Lu CH, Xu ZZ (2014) Different Upconversion Properties of beta-NaYF₄:Yb³⁺,Tm³⁺/Er³⁺ in Affecting the Near-Infrared-Driven Photocatalytic Activity of High-Reactive TiO₂. *ACS Appl. Mater. Interfaces* 6(1):340-348.
184. Wang WJ, Li YC, Kang ZW, Wang F, Yu JC (2016) A NIR-driven photocatalyst based on alpha-NaYF₄:Yb,Tm@TiO₂ core-shell structure supported on reduced graphene oxide. *Appl. Catal., B* 182:184-192.
185. Pickering JW, Bhethanabotla VR, Kuhn JN (2017) Assessment of mechanisms for enhanced performance of TiO₂/YAG:Yb³⁺,Er³⁺ composite photocatalysts for organic degradation. *Appl. Catal., B* 202:147-155.
186. Qiu ZL, Shu J, Tang DP (2018) Near-Infrared-to-Ultraviolet Light-Mediated Photoelectrochemical Aptasensing Platform for Cancer Biomarker Based on Core Shell NaYF₄:Yb,Tm@TiO₂ Upconversion Microrods. *Anal. Chem.* 90(1):1021-1028.
187. Xu JS, Brenner TJK, Chen ZP, Neher D, Antonietti M, Shalom M (2014) Upconversion-Agent Induced Improvement of g-C₃N₄ Photocatalyst under Visible Light. *ACS Appl. Mater. Interfaces* 6(19):16481-16486.
188. Zhang Q, Deng J, Xu Z, Chaker M, Ma D (2017) High-Efficiency Broadband C₃N₄ Photocatalysts: Synergistic Effects from Upconversion and Plasmons. *ACS Catal.* 7(9):6225-6234.
189. Li XF, Ren H, Zou ZJ, Sun JJ, Wang JY, Liu ZH (2016) Energy gap engineering of polymeric carbon nitride nanosheets for matching with NaYF₄:Yb,Tm: enhanced visible-near infrared photocatalytic activity. *Chem. Commun.* 52(3):453-456.
190. Huang MZ, Yuan BL, Dai LY, Fu ML (2015) Toward NIR driven photocatalyst: Fabrication, characterization, and photocatalytic activity of beta-NaYF₄:Yb³⁺,Tm³⁺/g-C₃N₄ nanocomposite. *J. Colloid Interface Sci.* 460:264-272.
191. Tou MJ, Mei YY, Bai S, Luo ZG, Zhang Y, Li ZQ (2016) Depositing CdS nanoclusters on carbon-modified NaYF₄:Yb,Tm upconversion nanocrystals for NIR-light enhanced photocatalysis. *Nanoscale* 8(1):553-562.
192. Feng WH, Zhang LL, Zhang Y, Yang Y, Fang ZB, Wang B, Zhang SY, Liu P (2017) Near-infrared-activated NaYF₄:Yb³⁺, Er³⁺/Au/CdS for H₂ production via photoreforming of bio-ethanol: plasmonic Au as light nanoantenna, energy relay, electron sink and co-catalyst. *J. Mater. Chem. A* 5(21):10311-10320.
193. Liu XH, Di WH, Qin WP (2017) Cooperative luminescence mediated near infrared photocatalysis of CaF₂:Yb@BiVO₄ composites. *Appl. Catal., B* 205:158-164.

194. Ullah S, Ferreira-Neto EP, Hazra C, Parveen R, Rojas-Mantilla HD, Calegaro ML, Serge-Correales YE, Rodrigues UP, Ribeiro SJL (2019) Broad spectrum photocatalytic system based on BiVO₄ and NaYbF₄:Tm³⁺ upconversion particles for environmental remediation under UV-vis-NIR illumination. *Appl. Catal., B* 243:121-135.
195. Yang YW, Que WX, Zhang XY, Yin XT, Xing YL, Que MD, Zhao HY, Du YP (2017) High-quality Cu₂ZnSnS₄ and Cu₂ZnSnSe₄ nanocrystals hybrid with ZnO and NaYF₄: Yb, Tm as efficient photocatalytic sensitizers. *Appl. Catal., B* 200:402-411.
196. Guo XY, Song WY, Chen CF, Di WH, Qin WP (2013) Near-infrared photocatalysis of beta-NaYF₄:Yb³⁺,Tm³⁺@ZnO composites. *Phys. Chem. Chem. Phys.* 15(35):14681-14688.
197. Tian QY, Yao WJ, Wu ZH, Liu J, Liu L, Wu W, Jiang CZ (2017) Full-spectrum-activated Z-scheme photocatalysts based on NaYF₄:Yb³⁺/Er³⁺, TiO₂ and Ag₆Si₂O₇. *J. Mater. Chem. A* 5(45):23566-23576.
198. Zhang F, Zhang CL, Wang WN, Cong HP, Qian HS (2016) Titanium Dioxide/Upconversion Nanoparticles/Cadmium Sulfide Nanofibers Enable Enhanced Full-Spectrum Absorption for Superior Solar Light Driven Photocatalysis. *ChemSusChem* 9(12):1449-1454.
199. Linic S, Christopher P, Ingram DB (2011) Plasmonic-Metal Nanostructures for Efficient Conversion of Solar to Chemical Energy. *Nat. Mater.* 10(12):911-921.
200. Kelly KL, Coronado E, Zhao LL, Schatz GC (2003) The optical properties of metal nanoparticles: The influence of size, shape, and dielectric environment. *J. Phys. Chem. B* 107(3):668-677.
201. Warren SC, Thimsen E (2012) Plasmonic solar water splitting. *Energy Environ. Sci.* 5(1):5133-5146.
202. El-Sayed MA (2001) Some interesting properties of metals confined in time and nanometer space of different shapes. *Acc. Chem. Res.* 34(4):257-264.
203. Burda C, Chen XB, Narayanan R, El-Sayed MA (2005) Chemistry and properties of nanocrystals of different shapes. *Chem. Rev.* 105(4):1025-1102.
204. Rycenga M, Cobley CM, Zeng J, Li WY, Moran CH, Zhang Q, Qin D, Xia YN (2011) Controlling the Synthesis and Assembly of Silver Nanostructures for Plasmonic Applications. *Chem. Rev.* 111(6):3669-3712.
205. Xia YN, Xiong YJ, Lim B, Skrabalak SE (2009) Shape-Controlled Synthesis of Metal Nanocrystals: Simple Chemistry Meets Complex Physics? *Angew. Chem., Int. Ed.* 48(1):60-103.
206. Zhan C, Chen X-J, Yi J, Li J-F, Wu D-Y, Tian Z-Q (2018) From plasmon-enhanced molecular spectroscopy to plasmon-mediated chemical reactions. *Nat. Rev. Chem.* 2(9):216-230.
207. Cushing SK, Chen CJ, Dong CL, Kong XT, Govorov AO, Liu RS, Wu N (2018) Tunable Nonthermal Distribution of Hot Electrons in a Semiconductor Injected from a Plasmonic Gold Nanostructure. *ACS Nano* 12(7):7117-7126.
208. Jain PK, Lee KS, El-Sayed IH, El-Sayed MA (2006) Calculated absorption and scattering properties of gold nanoparticles of different size, shape, and composition: Applications in biological imaging and biomedicine. *J. Phys. Chem. B* 110(14):7238-7248.
209. Kowalska E, Abe R, Ohtani B (2009) Visible light-induced photocatalytic reaction of gold-modified titanium(IV) oxide particles: action spectrum analysis. *Chem. Commun.* 2:241-243.
210. Brongersma ML, Halas NJ, Nordlander P (2015) Plasmon-induced hot carrier science and technology. *Nat. Nanotechnol.* 10(1):25-34.

211. Zhang XM, Chen YL, Liu RS, Tsai DP (2013) Plasmonic photocatalysis. *Rep. Prog. Phys.* 76(4):046401.
212. Valenti M, Jonsson MP, Biskos G, Schmidt-Ott A, Smith WA (2016) Plasmonic nanoparticle-semiconductor composites for efficient solar water splitting. *J. Mater. Chem. A* 4(46):17891-17912.
213. Sa J, Tagliabue G, Friedli P, Szlachetko J, Rittmann-Frank MH, Santomauro FG, Milne CJ, Sigg H (2013) Direct observation of charge separation on Au localized surface plasmons. *Energy Environ. Sci.* 6(12):3584-3588.
214. Wu K, Chen J, McBride JR, Lian T (2015) Efficient hot-electron transfer by a plasmon-induced interfacial charge-transfer transition. *Science* 349(6248):632-635.
215. Govorov AO, Zhang H, Demir HV, Gun'ko YK (2014) Photogeneration of hot plasmonic electrons with metal nanocrystals: Quantum description and potential applications. *Nano Today* 9(1):85-101.
216. Govorov AO, Zhang H, Gun'ko YK (2013) Theory of Photoinjection of Hot Plasmonic Carriers from Metal Nanostructures into Semiconductors and Surface Molecules. *J. Phys. Chem. C* 117(32):16616-16631.
217. Zhang H, Govorov AO (2014) Optical Generation of Hot Plasmonic Carriers in Metal Nanocrystals: The Effects of Shape and Field Enhancement. *J. Phys. Chem. C* 118(14):7606-7614.
218. Torimoto T, Horibe H, Kameyama T, Okazaki K, Ikeda S, Matsumura M, Ishikawa A, Ishihara H (2011) Plasmon-Enhanced Photocatalytic Activity of Cadmium Sulfide Nanoparticle Immobilized on Silica-Coated Gold Particles. *J. Phys. Chem. Lett.* 2(16):2057-2062.
219. Awazu K, Fujimaki M, Rockstuhl C, Tominaga J, Murakami H, Ohki Y, Yoshida N, Watanabe T (2008) A plasmonic photocatalyst consisting of silver nanoparticles embedded in titanium dioxide. *J. Am. Chem. Soc.* 130(5):1676-1680.
220. Kumar MK, Krishnamoorthy S, Tan LK, Chiam SY, Tripathy S, Gao H (2011) Field Effects in Plasmonic Photocatalyst by Precise SiO₂ Thickness Control Using Atomic Layer Deposition. *ACS Catal.* 1(4):300-308.
221. Anger P, Bharadwaj P, Novotny L (2006) Enhancement and quenching of single-molecule fluorescence. *Phys. Rev. Lett.* 96(11):113002.
222. Lee J, Javed T, Skeini T, Govorov AO, Bryant GW, Kotov NA (2006) Bioconjugated Ag nanoparticles and CdTe nanowires: Metamaterials with field-enhanced light absorption. *Angew. Chem., Int. Ed.* 45(29):4819-4823.
223. Liu ZW, Hou WB, Pavaskar P, Aykol M, Cronin SB (2011) Plasmon Resonant Enhancement of Photocatalytic Water Splitting Under Visible Illumination. *Nano Lett.* 11(3):1111-1116.
224. Cushing SK, Li J, Meng F, Senty TR, Suri S, Zhi M, Li M, Bristow AD, Wu N (2012) Photocatalytic activity enhanced by plasmonic resonant energy transfer from metal to semiconductor. *J. Am. Chem. Soc.* 134(36):15033-15041.
225. Li JT, Cushing SK, Zheng P, Meng FK, Chu D, Wu NQ (2013) Plasmon-Induced Photonic and Energy-Transfer Enhancement of Solar Water Splitting by a Hematite Nanorod Array. *Nat. Commun.* 4:2651.
226. Bohren CF, Huffman DR (2008) *Absorption and scattering of light by small particles*. John Wiley & Sons.

227. Maier SA (2007) *Plasmonics: fundamentals and applications*. Springer Science & Business Media.
228. Hodak JH, Henglein A, Hartland GV (2000) Photophysics of nanometer sized metal particles: Electron-phonon coupling and coherent excitation of breathing vibrational modes. *J. Phys. Chem. B* 104(43):9954-9965.
229. Christopher P, Ingram DB, Linic S (2010) Enhancing Photochemical Activity of Semiconductor Nanoparticles with Optically Active Ag Nanostructures: Photochemistry Mediated by Ag Surface Plasmons. *J. Phys. Chem. C* 114(19):9173-9177.
230. Cheng NY, Tian JQ, Liu Q, Ge CJ, Qusti AH, Asiri AM, Al-Youbi AO, Sun XP (2013) Au-Nanoparticle-Loaded Graphitic Carbon Nitride Nanosheets: Green Photocatalytic Synthesis and Application toward the Degradation of Organic Pollutants. *ACS Appl. Mater. Interfaces* 5(15):6815-6819.
231. Pawar RC, Pyo Y, Ahn SH, Lee CS (2015) Photoelectrochemical properties and photodegradation of organic pollutants using hematite hybrids modified by gold nanoparticles and graphitic carbon nitride. *Appl. Catal., B* 176:654-666.
232. Liu J, Yang YM, Liu NY, Liu Y, Huang H, Kang ZH (2014) Total photocatalysis conversion from cyclohexane to cyclohexanone by C₃N₄/Au nanocomposites. *Green Chem.* 16(10):4559-4565.
233. Bai XJ, Zong RL, Li CX, Liu D, Liu YF, Zhu YF (2014) Enhancement of visible photocatalytic activity via Ag@C₃N₄ core-shell plasmonic composite. *Appl. Catal., B* 147:82-91.
234. Fu YS, Huang T, Zhang LL, Zhu JW, Wang X (2015) Ag/g-C₃N₄ catalyst with superior catalytic performance for the degradation of dyes: a borohydride-generated superoxide radical approach. *Nanoscale* 7(32):13723-13733.
235. Yang YX, Guo YN, Liu FY, Yuan X, Guo YH, Zhang SQ, Guo W, Huo MX (2013) Preparation and enhanced visible-light photocatalytic activity of silver deposited graphitic carbon nitride plasmonic photocatalyst. *Appl. Catal., B* 142:828-837.
236. Zada A, Humayun M, Raziq F, Zhang X, Qu Y, Bai L, Qin C, Jing L, Fu H (2016) Exceptional Visible-Light-Driven Cocatalyst-Free Photocatalytic Activity of g-C₃N₄ by Well Designed Nanocomposites with Plasmonic Au and SnO₂. *Adv. Energy Mater.* 6(21):1601190.
237. Ye XC, Gao YZ, Chen J, Reifsnnyder DC, Zheng C, Murray CB (2013) Seeded Growth of Monodisperse Gold Nanorods Using Bromide-Free Surfactant Mixtures. *Nano Lett.* 13(5):2163-2171.
238. Ye XC, Zheng C, Chen J, Gao YZ, Murray CB (2013) Using Binary Surfactant Mixtures To Simultaneously Improve the Dimensional Tunability and Monodispersity in the Seeded Growth of Gold Nanorods. *Nano Lett.* 13(2):765-771.
239. Li D, Yu SH, Jiang HL (2018) From UV to Near-Infrared Light-Responsive Metal-Organic Framework Composites: Plasmon and Upconversion Enhanced Photocatalysis. *Adv. Mater.* 30:1707377.
240. Tian QY, Yao WJ, Wu W, Liu J, Wu ZH, Liu L, Dai ZG, Jiang CZ (2017) Efficient UV-Vis-NIR Responsive Upconversion and Plasmonic-Enhanced Photocatalyst Based on Lanthanide-Doped NaYF₄/SnO₂/Ag. *ACS Sustain. Chem. Eng.* 5(11):10889-10899.
241. Wei N, Cui HZ, Song Q, Zhang LQ, Song XJ, Wang K, Zhang YF, Li J, Wen J, Tian J (2016) Ag₂O nanoparticle/TiO₂ nanobelt heterostructures with remarkable photo-response and photocatalytic properties under UV, visible and near-infrared irradiation. *Appl. Catal., B* 198:83-90.

242. Xu M, Han L, Dong SJ (2013) Facile Fabrication of Highly Efficient g-C₃N₄/Ag₂O Heterostructured Photocatalysts with Enhanced Visible-Light Photocatalytic Activity. *ACS Appl. Mater. Interfaces* 5(23):12533-12540.
243. Tian J, Yan TJ, Qiao Z, Wang LL, Li WJ, You JM, Huang BB (2017) Anion-exchange synthesis of Ag₂S/Ag₃PO₄ core/shell composites with enhanced visible and NIR light photocatalytic performance and the photocatalytic mechanisms. *Appl. Catal., B* 209:566-578.
244. Li X, Shen D, Liu C, Li JZ, Zhou YJ, Song XH, Huo PW, Wang HQ, Yan YS (2019) Fabricated rGO-modified Ag₂S nanoparticles/g-C₃N₄ nanosheets photocatalyst for enhancing photocatalytic activity. *J. Colloid Interface Sci.* 554:468-478.
245. Li Y, Liu X, Tan L, Cui Z, Jing D, Yang X, Liang Y, Li Z, Zhu S, Zheng Y (2019) Eradicating Multidrug-Resistant Bacteria Rapidly Using a Multi Functional g-C₃N₄@Bi₂S₃ Nanorod Heterojunction with or without Antibiotics. *Adv. Funct. Mater.* 29(20):1900946.
246. Clark RM, Kotsakidis JC, Weber B, Berean KJ, Carey BJ, Field MR, Khan H, Ou JZ, Ahmed T, Harrison CJ, Cole IS, Latham K, Kalantar-zadeh K, Daeneke T (2016) Exfoliation of Quasi-Stratified Bi₂S₃ Crystals into Micron-Scale Ultrathin Corrugated Nanosheets. *Chem. Mater.* 28(24):8942-8950.
247. Wu ZZ, Yuan XZ, Wang H, Wu ZB, Jiang LB, Wang H, Zhang L, Xiao ZH, Chen XH, Zeng GM (2017) Facile synthesis of a novel full-spectrum-responsive CO₂.₆₇S₄ nanoparticles for UV-, vis- and NIR-driven photocatalysis. *Appl. Catal., B* 202:104-111.
248. Tomic S, Bernasconi L, Searle BG, Harrison NM (2014) Electronic and Optical Structure of Wurtzite CuInS₂. *J. Phys. Chem. C* 118(26):14478-14484.
249. Qi YX, Liu QC, Tang KB, Liang ZH, Ren ZB, Liu XM (2009) Synthesis and Characterization of Nanostructured Wurtzite CuInS₂: A New Cation Disordered Polymorph of CuInS₂. *J. Phys. Chem. C* 113(10):3939-3944.
250. Huang WC, Tseng CH, Chang SH, Tuan HY, Chiang CC, Lyu LM, Huang MH (2012) Solvothermal Synthesis of Zincblende and Wurtzite CuInS₂ Nanocrystals and Their Photovoltaic Application. *Langmuir* 28(22):8496-8501.
251. Chang K, Hai X, Ye JH (2016) Transition Metal Disulfides as Noble-Metal-Alternative Co-Catalysts for Solar Hydrogen Production. *Adv. Energy Mater.* 6(10):1502555.
252. Mak KF, Lee C, Hone J, Shan J, Heinz TF (2010) Atomically Thin MoS₂: A New Direct-Gap Semiconductor. *Phys. Rev. Lett.* 105(13):136805.
253. Eda G, Yamaguchi H, Voiry D, Fujita T, Chen MW, Chhowalla M (2011) Photoluminescence from Chemically Exfoliated MoS₂. *Nano Lett.* 11(12):5111-5116.
254. Chia XY, Eng AYS, Ambrosi A, Tan SM, Pumera M (2015) Electrochemistry of Nanostructured Layered Transition-Metal Dichalcogenides. *Chem. Rev.* 115(21):11941-11966.
255. Pang YP, Uddin MN, Chen W, Javaid S, Barker E, Li YG, Suvorova A, Saunders M, Yin ZY, Jia GH (2019) Colloidal Single-Layer Photocatalysts for Methanol-Storable Solar H₂ Fuel. *Adv. Mater.* 31(49):1905540.
256. Miller EM, Kroupa DM, Zhang JB, Schulz P, Marshall AR, Kahn A, Lany S, Luther JM, Beard MC, Perkins CL, van de Lagemaat J (2016) Revisiting the Valence and Conduction Band Size Dependence of PbS Quantum Dot Thin Films. *ACS Nano* 10(3):3302-3311.

257. Hou B, Cho Y, Kim BS, Hong J, Park JB, Ahn SJ, Sohn JI, Cha S, Kim JM (2016) Highly Monodispersed PbS Quantum Dots for Outstanding Cascaded-Junction Solar Cells. *ACS Energy Lett.* 1(4):834-839.
258. Wise FW (2000) Lead Salt Quantum Dots: The Limit of Strong Quantum Confinement. *Acc. Chem. Res.* 33(11):773-780.
259. McDonald SA, Konstantatos G, Zhang SG, Cyr PW, Klem EJD, Levina L, Sargent EH (2005) Solution-Processed PbS Quantum Dot Infrared Photodetectors and Photovoltaics. *Nat. Mater.* 4(2):138-142.
260. Wang H, Yuan XZ, Wang H, Chen XH, Wu ZB, Jiang LB, Xiong WP, Zeng GM (2016) Facile synthesis of Sb₂S₃/ultrathin g-C₃N₄ sheets heterostructures embedded with g-C₃N₄ quantum dots with enhanced NIR-light photocatalytic performance. *Appl. Catal., B* 193:36-46.
261. Huo Y, Zhang JF, Dai K, Li Q, Lv JL, Zhu GP, Liang CH (2019) All-solid-state artificial Z-scheme porous g-C₃N₄/Sn₂S₃-DETA heterostructure photocatalyst with enhanced performance in photocatalytic CO₂ reduction. *Appl. Catal., B* 241:528-538.
262. Whittles TJ, Burton LA, Skelton JM, Walsh A, Veal TD, Dhanak VR (2016) Band Alignments, Valence Bands, and Core Levels in the Tin Sulfides SnS, SnS₂, and Sn₂S₃: Experiment and Theory. *Chem. Mater.* 28(11):3718-3726.
263. Wang YR, Liu ZT, Wang CX, Yi X, Chen RP, Ma LB, Hu Y, Zhu GY, Chen T, Tie ZX, Ma J, Liu J, Jin Z (2018) Highly Branched VS₄ Nanodendrites with 1D Atomic-Chain Structure as a Promising Cathode Material for Long-Cycling Magnesium Batteries. *Adv. Mater.* 30(32):1802563.
264. Rout CS, Kim BH, Xu X, Yang J, Jeong HY, Odkhuu D, Park N, Cho J, Shin HS (2013) Synthesis and Characterization of Patronite Form of Vanadium Sulfide on Graphitic Layer. *J. Am. Chem. Soc.* 135(23):8720-8725.
265. Braga D, Lezama IG, Berger H, Morpurgo AF (2012) Quantitative Determination of the Band Gap of WS₂ with Ambipolar Ionic Liquid-Gated Transistors. *Nano Lett.* 12(10):5218-5223.
266. Jo S, Ubrig N, Berger H, Kuzmenko AB, Morpurgo AF (2014) Mono- and Bilayer WS₂ Light-Emitting Transistors. *Nano Lett.* 14(4):2019-2025.
267. Voiry D, Yamaguchi H, Li JW, Silva R, Alves DCB, Fujita T, Chen MW, Asefa T, Shenoy VB, Eda G, Chhowalla M (2013) Enhanced catalytic activity in strained chemically exfoliated WS₂ nanosheets for hydrogen evolution. *Nat. Mater.* 12(9):850-855.
268. Sang YH, Zhao ZH, Zhao MW, Hao P, Leng YH, Liu H (2015) From UV to Near-Infrared, WS₂ Nanosheet: A Novel Photocatalyst for Full Solar Light Spectrum Photodegradation. *Adv. Mater.* 27(2):363-369.
269. Ma YN, Li J, Liu EZ, Wan J, Hu XY, Fan J (2017) High efficiency for H₂ evolution and NO removal over the Ag nanoparticles bridged g-C₃N₄ and WS₂ heterojunction photocatalysts. *Appl. Catal., B* 219:467-478.
270. Wang XW, Miao ZH, Ma Y, Chen HJ, Qian HS, Zha ZB (2017) One-pot solution synthesis of shape-controlled copper selenide nanostructures and their potential applications in photocatalysis and photothermal therapy. *Nanoscale* 9(38):14512-14519.
271. Malik MA, O'Brien P, Revaprasadu N (1999) A novel route for the preparation of CuSe and CuInSe₂ nanoparticles. *Adv. Mater.* 11(17):1441-1444.
272. Brotons-Gisbert M, Andres-Peuares D, Suh J, Hidalgo F, Abargues R, Rodriguez-Canto PJ, Segura A, Cros A, Tobias G, Canadell E, Ordejon P, Wu JQ, Martinez-Pastor JP, Sanchez-

- Royo JF (2016) Nanotexturing To Enhance Photoluminescent Response of Atomically Thin Indium Selenide with Highly Tunable Band Gap. *Nano Lett.* 16(5):3221-3229.
273. He C, Zhang JH, Zhang WX, Li TT (2019) Type-II InSe/g-C₃N₄ Heterostructure as a High-Efficiency Oxygen Evolution Reaction Catalyst for Photoelectrochemical Water Splitting. *J. Phys. Chem. Lett.* 10(11):3122-3128.
274. Mudd GW, Svatek SA, Ren T, Patane A, Makarovskiy O, Eaves L, Beton PH, Kovalyuk ZD, Lashkarev GV, Kudrynskiy ZR, Dmitriev AI (2013) Tuning the Bandgap of Exfoliated InSe Nanosheets by Quantum Confinement. *Adv. Mater.* 25(40):5714-5718.
275. Tian Y, Li G, Zhang Y, Luo D, Wang X, Zhao Y, Liu H, Ji P, Du X, Li J, Chen Z (2019) Low-Bandgap Se-Deficient Antimony Selenide as a Multifunctional Polysulfide Barrier toward High-Performance Lithium-Sulfur Batteries. *Adv. Mater.* 32(4):1904876.
276. Wu W, Li Y, Liang LM, Hao QY, Zhang J, Liu H, Liu CC (2019) Enhanced Broadband Responsivity of Ni-Doped Sb₂Se₃ Nanorod Photodetector. *J. Phys. Chem. C* 123(23):14781-14789.
277. Wang ZX, Safdar M, Jiang C, He J (2012) High-Performance UV-Visible-NIR Broad Spectral Photodetectors Based on One-Dimensional In₂Te₃ Nanostructures. *Nano Lett.* 12(9):4715-4721.
278. Li ZJ, Dai Y, Ma XC, Zhu YT, Huang BBA (2014) Tuning photocatalytic performance of the near-infrared-driven photocatalyst Cu₂(OH)PO₄ based on effective mass and dipole moment. *Phys. Chem. Chem. Phys.* 16(7):3267-3273.
279. Li L, Yu Y, Ye GJ, Ge Q, Ou X, Wu H, Feng D, Chen XH, Zhang Y (2014) Black Phosphorus Field-Effect Transistors. *Nat. Nanotechnol.* 9(5):372-377.
280. Buscema M, Groenendijk DJ, Blanter SI, Steele GA, van der Zant HSJ, Castellanos-Gomez A (2014) Fast and Broadband Photoresponse of Few-Layer Black Phosphorus Field-Effect Transistors. *Nano Lett.* 14(6):3347-3352.
281. Yang B, Wan B, Zhou Q, Wang Y, Hu W, Lv W, Chen Q, Zeng Z, Wen F, Xiang J, Yuan S, Wang J, Zhang B, Wang W, Zhang J, Xu B, Zhao Z, Tian Y, Liu Z (2016) Te-Doped Black Phosphorus Field-Effect Transistors. *Adv. Mater.* 28(42):9408-9415.
282. Liu H, Du YC, Deng YX, Ye PD (2015) Semiconducting Black Phosphorus: Synthesis, Transport Properties and Electronic Applications. *Chem. Soc. Rev.* 44(9):2732-2743.
283. Kim ES, Nishimura N, Magesh G, Kim JY, Jang JW, Jun H, Kubota J, Domen K, Lee JS (2013) Fabrication of CaFe₂O₄/TaON Heterojunction Photoanode for Photoelectrochemical Water Oxidation. *J. Am. Chem. Soc.* 135(14):5375-5383.
284. Cao SY, Yan XQ, Kang Z, Liang QJ, Liao XQ, Zhang Y (2016) Band alignment engineering for improved performance and stability of ZnFe₂O₄ modified CdS/ZnO nanostructured photoanode for PEC water splitting. *Nano Energy* 24:25-31.
285. Sheikh A, Yengantiwar A, Deo M, Kelkar S, Ogale S (2013) Near-Field Plasmonic Functionalization of Light Harvesting Oxide-Oxide Heterojunctions for Efficient Solar Photoelectrochemical Water Splitting: The AuNP/ZnFe₂O₄/ZnO System. *Small* 9(12):2091-2096.
286. Hou Y, Li XY, Zhao QD, Quan X, Chen GH (2010) Electrochemical Method for Synthesis of a ZnFe₂O₄/TiO₂ Composite Nanotube Array Modified Electrode with Enhanced Photoelectrochemical Activity. *Adv. Funct. Mater.* 20(13):2165-2174.

287. Wang H, Zhang X, Xie Y (2018) Photocatalysis in Two-Dimensional Black Phosphorus: The Roles of Many-Body Effects. *ACS Nano* 12(10):9648-9653.
288. Feng RJ, Lei WY, Liu G, Liu MH (2018) Visible- and NIR-Light Responsive Black-Phosphorus-Based Nanostructures in Solar Fuel Production and Environmental Remediation. *Adv. Mater.* 30(49):1804770.
289. Hirsch A, Hauke F (2017) Post Graphene 2D Chemistry: The Emerging Field of Molybdenum Disulfide and Black Phosphorus Functionalization. *Angew. Chem., Int. Ed.* 57(16):4338-4354.
290. Qiu M, Ren WX, Jeong T, Won M, Park GY, Sang DK, Liu LP, Zhang H, Kim JS (2018) Omnipotent phosphorene: a next-generation, two-dimensional nanoplatform for multidisciplinary biomedical applications. *Chem. Soc. Rev.* 47(15):5588-5601.
291. Reich ES (2014) Phosphorene Excites Materials Scientists. *Nature* 506:19.
292. Zhu MS, Osakada Y, Kim S, Fujitsuka M, Majima T (2017) Black phosphorus: A promising two dimensional visible and near-infrared-activated photocatalyst for hydrogen evolution. *Appl. Catal., B* 217:285-292.
293. Woomer AH, Farnsworth TW, Hu J, Wells RA, Donley CL, Warren SC (2015) Phosphorene: Synthesis, Scale-Up, and Quantitative Optical Spectroscopy. *ACS Nano* 9(9):8869-8884.
294. Ziletti A, Carvalho A, Campbell DK, Coker DF, Neto AHC (2015) Oxygen Defects in Phosphorene. *Phys. Rev. Lett.* 114(4):046801.
295. Favron A, Gaufres E, Fossard F, Phaneuf-L'Heureux AL, Tang NYW, Levesque PL, Loiseau A, Leonelli R, Francoeur S, Martel R (2015) Photooxidation and Quantum Confinement Effects in Exfoliated Black Phosphorus. *Nat. Mater.* 14(8):826-832.
296. Talapin DV, Lee JS, Kovalenko MV, Shevchenko EV (2010) Prospects of Colloidal Nanocrystals for Electronic and Optoelectronic Applications. *Chem. Rev.* 110(1):389-458.
297. Alivisatos AP (1996) Perspectives on the physical chemistry of semiconductor nanocrystals. *J. Phys. Chem.* 100(31):13226-13239.
298. Norris DJ, Bawendi MG (1996) Measurement and assignment of the size-dependent optical spectrum in CdSe quantum dots. *Phys. Rev. B* 53(24):16338-16346.
299. Efros AL, Efros AL (1982) Interband absorption of light in a semiconductor sphere. *Soviet Physics Semiconductors-Ussr* 16(7):772-775.
300. Panfil YE, Oded M, Banin U (2018) Colloidal Quantum Nanostructures: Emerging Materials for Display Applications. *Angew. Chem., Int. Ed.* 57(16):4274-4295.
301. Ratanatawanate C, Xiong CR, Balkus KJ (2008) Fabrication of PbS quantum dot doped TiO₂ nanotubes. *ACS Nano* 2(8):1682-1688.
302. Wang DF, Zhao HG, Wu NQ, El Khakani MA, Ma DL (2010) Tuning the Charge-Transfer Property of PbS-Quantum Dot/TiO₂-Nanobelt Nanohybrids via Quantum Confinement. *J. Phys. Chem. Lett.* 1(7):1030-1035.
303. Donega CD (2011) Synthesis and properties of colloidal heteronanocrystals. *Chem. Soc. Rev.* 40(3):1512-1546.
304. Smith AM, Nie SM (2010) Semiconductor Nanocrystals: Structure, Properties, and Band Gap Engineering. *Acc. Chem. Res.* 43(2):190-200.
305. Wheeler DA, Zhang JZ (2013) Exciton Dynamics in Semiconductor Nanocrystals. *Adv. Mater.* 25(21):2878-2896.

306. Moreels I, Justo Y, De Geyter B, Haustraete K, Martins JC, Hens Z (2011) Size-Tunable, Bright, and Stable PbS Quantum Dots: A Surface Chemistry Study. *ACS Nano* 5(3):2004-2012.
307. Kershaw SV, Jing LH, Huang XD, Gao MY, Rogach AL (2017) Materials aspects of semiconductor nanocrystals for optoelectronic applications. *Mater. Horiz.* 4(2):155-205.
308. Murray CB, Norris DJ, Bawendi MG (1993) Synthesis and Characterization of Nearly Monodisperse Cde (E = S, Se, Te) Semiconductor Nanocrystallites. *J. Am. Chem. Soc.* 115(19):8706-8715.
309. Carey GH, Abdelhady AL, Ning ZJ, Thon SM, Bakr OM, Sargent EH (2015) Colloidal Quantum Dot Solar Cells. *Chem. Rev.* 115(23):12732-12763.
310. Koole R, Schapotschnikow P, Donega CD, Vlugt TJH, Meijerink A (2008) Time-dependent photoluminescence spectroscopy as a tool to measure the ligand exchange kinetics on a quantum dot surface. *ACS Nano* 2(8):1703-1714.
311. Wang W, Zhao LJ, Wang Y, Xue WN, He FF, Xie YL, Li Y (2019) Facile Secondary Deposition for Improving Quantum Dot Loading in Fabricating Quantum Dot Solar Cells. *J. Am. Chem. Soc.* 141(10):4300-4307.
312. Du J, Du ZL, Hu JS, Pan ZX, Shen Q, Sung JK, Long DH, Dong H, Sun LT, Zhong XH, Wan LJ (2016) Zn-Cu-In-Se Quantum Dot Solar Cells with a Certified Power Conversion Efficiency of 11.6%. *J. Am. Chem. Soc.* 138(12):4201-4209.
313. Wang W, Feng WL, Du J, Xue WN, Zhang LL, Zhao LL, Li Y, Zhong XH (2018) Cosensitized Quantum Dot Solar Cells with Conversion Efficiency over 12%. *Adv. Mater.* 30(11):1705746.
314. Yang ZY, Fan JZ, Proppe AH, de Arquer FPG, Rossouw D, Voznyy O, Lan XZ, Liu M, Walters G, Quintero-Bermudez R, Sun B, Hoogland S, Botton GA, Kelley SO, Sargent EH (2017) Mixed-quantum-dot solar cells. *Nat. Commun.* 8:1325.
315. Shi GZ, Kaewprajak A, Ling XF, Hayakawa A, Zhou SJ, Song B, Kang Y, Hayashi T, Altun ME, Nakaya M, Liu ZK, Wang HB, Sagawa T, Ma WL (2019) Finely Interpenetrating Bulk Heterojunction Structure for Lead Sulfide Colloidal Quantum Dot Solar Cells by Convective Assembly. *ACS Energy Lett.* 4(4):960-967.
316. Tan L, Li PD, Sun BQ, Chaker M, Ma DL (2017) Stabilities Related to Near-Infrared Quantum Dot-Based Solar Cells: The Role of Surface Engineering. *ACS Energy Lett.* 2(7):1573-1585.
317. Li XX, Xie KY, Song L, Zhao MJ, Zhang ZP (2017) Enhanced Photocarrier Separation in Hierarchical Graphitic-C₃N₄-Supported CuInS₂ for Noble-Metal-Free Z-Scheme Photocatalytic Water Splitting. *ACS Appl. Mater. Interfaces* 9(29):24577-24583.
318. Liang SH, Zhang DF, Pu XP, Yao XT, Han RT, Yin J, Ren XZ (2019) A novel Ag₂O/g-C₃N₄ p-n heterojunction photocatalysts with enhanced visible and near-infrared light activity. *Sep. Purif. Technol.* 210:786-797.
319. Zhu M, Kim S, Mao L, Fujitsuka M, Zhang J, Wang X, Majima T (2017) Metal-Free Photocatalyst for H₂ Evolution in Visible to Near-Infrared Region: Black Phosphorus/Graphitic Carbon Nitride. *J. Am. Chem. Soc.* 139(37):13234-13242.
320. Lu LL, Xu XX, An KL, Wang Y, Shi FN (2018) Coordination Polymer Derived NiS@g-C₃N₄ Composite Photocatalyst for Sulfur Vacancy and Photothermal Effect Synergistic Enhanced H₂ Production. *ACS Sustain. Chem. Eng.* 6(9):11869-11876.

321. Wang XW, Han Z, Yu LH, Liu CT, Liu YF, Wu G (2018) Synthesis of Full-Spectrum-Response $\text{Cu}_2(\text{OH})\text{PO}_4/\text{g-C}_3\text{N}_4$ Photocatalyst with Outstanding Photocatalytic H_2O_2 Production Performance via a "Two Channel Route". *ACS Sustain. Chem. Eng.* 6(11):14542-14553.
322. Benayas A, Ren FQ, Carrasco E, Marzal V, del Rosal B, Gonfa BA, Juarranz A, Sanz-Rodriguez F, Jaque D, Garcia-Sole J, Ma DL, Vetrone F (2015) PbS/CdS/ZnS Quantum Dots: A Multifunctional Platform for In Vivo Near-Infrared Low-Dose Fluorescence Imaging. *Adv. Funct. Mater.* 25(42):6650-6659.
323. Ren FQ, Zhao HG, Vetrone F, Ma DL (2013) Microwave-Assisted Cation Exchange toward Synthesis of Near-Infrared Emitting PbS/CdS Core/Shell Quantum Dots with Significantly Improved Quantum Yields through a Uniform Growth Path. *Nanoscale* 5(17):7800-7804.
324. Giannozzi P, Baroni S, Bonini N, Calandra M, Car R, Cavazzoni C, Ceresoli D, Chiarotti GL, Cococcioni M, Dabo I, Dal Corso A, de Gironcoli S, Fabris S, Fratesi G, Gebauer R, Gerstmann U, Gougoussis C, Kokalj A, Lazzeri M, Martin-Samos L, Marzari N, Mauri F, Mazzarello R, Paolini S, Pasquarello A, Paulatto L, Sbraccia C, Scandolo S, Sclauzero G, Seitsonen AP, Smogunov A, Umari P, Wentzcovitch RM (2009) QUANTUM ESPRESSO: a Modular and Open-Source Software Project for Quantum Simulations of Materials. *J. Phys.-Condens. Matter* 21(39):395502.
325. Marini A, Hogan C, Gruning M, Varsano D (2009) yambo: An ab initio Tool for Excited State Calculations. *Comput. Phys. Commun.* 180(8):1392-1403.
326. Schlipf M, Gygi F (2015) Optimization Algorithm for the Generation of ONCV Pseudopotentials. *Comput. Phys. Commun.* 196:36-44.
327. Grimme S (2006) Semiempirical GGA-Type Density Functional Constructed with a Long-Range Dispersion Correction. *J. Comput. Chem.* 27(15):1787-1799.
328. Lau VW-h, Moudrakovski I, Botari T, Weinberger S, Mesch MB, Duppe V, Senker J, Blum V, Lotsch BV (2016) Rational design of carbon nitride photocatalysts by identification of cyanamide defects as catalytically relevant sites. *Nat. Commun.* 7:12165.
329. Fujishima A, Honda K (1972) Electrochemical photolysis of water at a semiconductor electrode. *Nature* 238:37-38.
330. Wang H, Zhang L, Chen Z, Hu J, Li S, Wang Z, Liu J, Wang X (2014) Semiconductor heterojunction photocatalysts: design, construction, and photocatalytic performances. *Chem. Soc. Rev.* 43(15):5234-5244.
331. Asahi R, Morikawa T, Irie H, Ohwaki T (2014) Nitrogen-doped titanium dioxide as visible-light-sensitive photocatalyst: designs, developments, and prospects. *Chem. Rev.* 114(19):9824-9852.
332. Dhakshinamoorthy A, Asiri AM, García H (2016) Metal–Organic Framework (MOF) Compounds: Photocatalysts for Redox Reactions and Solar Fuel Production. *Angew. Chem., Int. Ed.* 55(18):5414-5445.
333. Zhang Q, Bao N, Wang X, Hu X, Miao X, Chaker M, Ma D (2016) Advanced Fabrication of Chemically Bonded Graphene/ TiO_2 Continuous Fibers with Enhanced Broadband Photocatalytic Properties and Involved Mechanisms Exploration. *Sci. Rep.* 6:38066.
334. Ong W-J, Tan L-L, Chai S-P, Yong S-T, Mohamed AR (2015) Surface charge modification via protonation of graphitic carbon nitride ($\text{g-C}_3\text{N}_4$) for electrostatic self-assembly construction of 2D/2D reduced graphene oxide (rGO)/ $\text{g-C}_3\text{N}_4$ nanostructures toward enhanced photocatalytic reduction of carbon dioxide to methane. *Nano Energy* 13:757-770.

335. Pan C, Xu J, Wang Y, Li D, Zhu Y (2012) Dramatic Activity of $C_3N_4/BiPO_4$ Photocatalyst with Core/Shell Structure Formed by Self-Assembly. *Adv. Funct. Mater.* 22(7):1518-1524.
336. Ye C, Li J-X, Li Z-J, Li X-B, Fan X-B, Zhang L-P, Chen B, Tung C-H, Wu L-Z (2015) Enhanced Driving Force and Charge Separation Efficiency of Protonated g- C_3N_4 for Photocatalytic O_2 Evolution. *ACS Catal.* 5(11):6973-6979.
337. Tay Q, Kanhere P, Ng CF, Chen S, Chakraborty S, Huan ACH, Sum TC, Ahuja R, Chen Z (2015) Defect Engineered g- C_3N_4 for Efficient Visible Light Photocatalytic Hydrogen Production. *Chem. Mater.* 27(14):4930-4933.
338. Xu H, Yan J, Xu Y, Song Y, Li H, Xia J, Huang C, Wan H (2013) Novel visible-light-driven AgX/graphite-like C_3N_4 (X=Br, I) hybrid materials with synergistic photocatalytic activity. *Appl. Catal., B* 129:182-193.
339. Zou ZG, Ye JH, Sayama K, Arakawa H (2001) Direct splitting of water under visible light irradiation with an oxide semiconductor photocatalyst. *Nature* 414(6864):625-627.
340. Woznica M, Chaoui N, Taabache S, Blechert S (2014) THF: An Efficient Electron Donor in Continuous Flow Radical Cyclization Photocatalyzed by Graphitic Carbon Nitride. *Chem.-Eur. J.* 20(45):14624-14628.
341. Zheng D, Cao XN, Wang X (2016) Precise Formation of a Hollow Carbon Nitride Structure with a Janus Surface To Promote Water Splitting by Photoredox Catalysis. *Angew. Chem., Int. Ed.* 55(38):11512-11516.
342. Zhang G, Lan Z-A, Lin L, Lin S, Wang X (2016) Overall water splitting by Pt/g- C_3N_4 photocatalysts without using sacrificial agents. *Chem. Sci.* 7(5):3062-3066.
343. Huang ZF, Song JJ, Pan L, Wang ZM, Zhang XQ, Zou JJ, Mi WB, Zhang XW, Wang L (2015) Carbon nitride with simultaneous porous network and O-doping for efficient solar-energy-driven hydrogen evolution. *Nano Energy* 12:646-656.
344. Tan X, Tahini HA, Smith SC (2016) p-Doped Graphene/Graphitic Carbon Nitride Hybrid Electrocatalysts: Unraveling Charge Transfer Mechanisms for Enhanced Hydrogen Evolution Reaction Performance. *ACS Catal.* 6(10):7071-7077.
345. Kong HJ, Won DH, Kim J, Woo SI (2016) Sulfur-Doped g- $C_3N_4/BiVO_4$ Composite Photocatalyst for Water Oxidation under Visible Light. *Chem. Mater.* 28(5):1318-1324.
346. Zhang X, Meng Z, Rao D, Wang Y, Shi Q, Liu Y, Wu H, Deng K, Liu H, Lu R (2016) Efficient band structure tuning, charge separation, and visible-light response in ZrS_2 -based van der Waals heterostructures. *Energy Environ. Sci.* 9(3):841-849.
347. Hou Y, Zuo F, Dagg AP, Liu JK, Feng PY (2014) Branched WO_3 Nanosheet Array with Layered C_3N_4 Heterojunctions and CoO_x Nanoparticles as a Flexible Photoanode for Efficient Photoelectrochemical Water Oxidation. *Adv. Mater.* 26(29):5043-5049.
348. Christoforidis KC, Montini T, Bontempi E, Zafeiratos S, Jaen JJD, Fornasiero P (2016) Synthesis and photocatalytic application of visible-light active $\beta-Fe_2O_3/g-C_3N_4$ hybrid nanocomposites. *Appl. Catal., B* 187:171-180.
349. Shalom M, Guttentag M, Fettkenhauer C, Inal S, Neher D, Llobet A, Antonietti M (2014) In Situ Formation of Heterojunctions in Modified Graphitic Carbon Nitride: Synthesis and Noble Metal Free Photocatalysis. *Chem. Mater.* 26(19):5812-5818.
350. Marimuthu A, Zhang JW, Linic S (2013) Tuning Selectivity in Propylene Epoxidation by Plasmon Mediated Photo-Switching of Cu Oxidation State. *Science* 339(6127):1590-1593.

351. Christopher P, Xin HL, Linic S (2011) Visible-light-enhanced catalytic oxidation reactions on plasmonic silver nanostructures. *Nat. Chem.* 3(6):467-472.
352. Clavero C (2014) Plasmon-induced hot-electron generation at nanoparticle/metal-oxide interfaces for photovoltaic and photocatalytic devices. *Nat. Photonics* 8(2):95-103.
353. Tan TH, Scott J, Ng YH, Taylor RA, Aguey-Zinsou KF, Amal R (2016) Understanding Plasmon and Band Gap Photoexcitation Effects on the Thermal-Catalytic Oxidation of Ethanol by TiO₂-Supported Gold. *ACS Catal.* 6(3):1870-1879.
354. Wang FL, Jiang YJ, Lawes DJ, Ball GE, Zhou CF, Liu ZW, Amal R (2015) Analysis of the Promoted Activity and Molecular Mechanism of Hydrogen Production over Fine Au-Pt Alloyed TiO₂ Photocatalysts. *ACS Catal.* 5(7):3924-3931.
355. Xue JJ, Ma SS, Zhou YM, Zhang ZW, He M (2015) Facile Photochemical Synthesis of Au/Pt/g-C₃N₄ with Plasmon-Enhanced Photocatalytic Activity for Antibiotic Degradation. *ACS Appl. Mater. Interfaces* 7(18):9630-9637.
356. Han CC, Wu LN, Ge L, Li YJ, Zhao Z (2015) AuPd bimetallic nanoparticles decorated graphitic carbon nitride for highly efficient reduction of water to H₂ under visible light irradiation. *Carbon* 92:31-40.
357. Zhang JM, Chen GZ, Chaker M, Rosei F, Ma DL (2013) Gold nanoparticle decorated ceria nanotubes with significantly high catalytic activity for the reduction of nitrophenol and mechanism study. *Appl. Catal., B* 132:107-115.
358. Xu ZH, Liu YL, Ren FQ, Yang F, Ma DL (2016) Development of Functional Nanostructures and their Applications in Catalysis and Solar Cells. *Coord. Chem. Rev.* 320:153-180.
359. Zhang JM, Chaker M, Ma DL (2017) Pulsed laser ablation based synthesis of colloidal metal nanoparticles for catalytic applications. *J. Colloid Interface Sci.* 489:138-149.
360. Zhang DS, Goekce B, Barcikowski S (2017) Laser Synthesis and Processing of Colloids: Fundamentals and Applications. *Chem. Rev.* 117(5):3990-4103.
361. Qin WP, Zhang DS, Zhao D, Wang LL, Zheng KZ (2010) Near-infrared photocatalysis based on YF₃: Yb³⁺, Tm³⁺/TiO₂ core/shell nanoparticles. *Chem. Commun.* 46(13):2304-2306.
362. Meng FL, Luo Y, Zhou YL, Zhang JW, Zheng YZ, Cao GZ, Tao X (2016) Integrated plasmonic and upconversion starlike Y₂O₃:Er/Au@TiO₂ composite for enhanced photon harvesting in dye-sensitized solar cells. *J. Power Sources* 316:207-214.
363. Wang D, Zhu L, Chen JF, Dai LM (2016) Liquid Marbles Based on Magnetic Upconversion Nanoparticles as Magnetically and Optically Responsive Miniature Reactors for Photocatalysis and Photodynamic Therapy. *Angew. Chem., Int. Ed.* 55(36):10795-10799.
364. Lopez-Orozco S, Inayat A, Schwab A, Selvam T, Schwieger W (2011) Zeolitic Materials with Hierarchical Porous Structures. *Adv. Mater.* 23(22-23):2602-2615.
365. Martha S, Nashim A, Parida KM (2013) Facile synthesis of highly active g-C₃N₄ for efficient hydrogen production under visible light. *J. Mater. Chem. A* 1(26):7816-7824.
366. Dong F, Wu LW, Sun YJ, Fu M, Wu ZB, Lee SC (2011) Efficient synthesis of polymeric g-C₃N₄ layered materials as novel efficient visible light driven photocatalysts. *J. Mater. Chem. A* 21(39):15171-15174.
367. Heer S, Kompe K, Gudel HU, Haase M (2004) Highly efficient multicolour upconversion emission in transparent colloids of lanthanide-doped NaYF₄ nanocrystals. *Adv. Mater.* 16(23-24):2102-2105.

368. Sun L, Yang MJ, Huang JF, Yu DS, Hong W, Chen XD (2016) Freestanding Graphitic Carbon Nitride Photonic Crystals for Enhanced Photocatalysis. *Adv. Funct. Mater.* 26(27):4943-4950.
369. Zhang Q, Lima DQ, Lee I, Zaera F, Chi MF, Yin YD (2011) A Highly Active Titanium Dioxide Based Visible-Light Photocatalyst with Nonmetal Doping and Plasmonic Metal Decoration. *Angew. Chem., Int. Ed.* 50(31):7088-7092.
370. Liu YS, Tu DT, Zhu HM, Li RF, Luo WQ, Chen XY (2010) A Strategy to Achieve Efficient Dual-Mode Luminescence of Eu^{3+} in Lanthanides Doped Multifunctional NaGdF_4 Nanocrystals. *Adv. Mater.* 22(30):3266-3271.
371. Wu YM, Liti HB, Zhang JL, Chen F (2009) Enhanced Photocatalytic Activity of Nitrogen-Doped Titania by Deposited with Gold. *J. Phys. Chem. C* 113(33):14689-14695.
372. Huang SQ, Gu L, Miao C, Lou ZY, Zhu NW, Yuan HP, Shan AD (2013) Near-infrared photocatalyst of $\text{Er}^{3+}/\text{Yb}^{3+}$ codoped ($\text{CaF}_2@ \text{TiO}_2$) nanoparticles with active-core/active-shell structure. *J. Mater. Chem. A* 1(27):7874-7879.
373. Huang SQ, Zhu NW, Lou ZY, Gu L, Miao C, Yuan HP, Shan AD (2014) Near-infrared photocatalysts of $\text{BiVO}_4/\text{CaF}_2:\text{Er}^{3+}$, Tm^{3+} , Yb^{3+} with enhanced upconversion properties. *Nanoscale* 6(3):1362-1368.
374. Kumar S, Surendar T, Baruah A, Shanker V (2013) Synthesis of a novel and stable g- C_3N_4 - Ag_3PO_4 hybrid nanocomposite photocatalyst and study of the photocatalytic activity under visible light irradiation. *J. Mater. Chem. A* 1(17):5333-5340.
375. Pan CS, Zhu YF (2010) New Type of BiPO_4 Oxy-Acid Salt Photocatalyst with High Photocatalytic Activity on Degradation of Dye. *Environ. Sci. Technol.* 44(14):5570-5574.
376. Li MX, Luo WJ, Cao DP, Zhao X, Li ZS, Yu T, Zou ZG (2013) A Co-catalyst-Loaded Ta_3N_5 Photoanode with a High Solar Photocurrent for Water Splitting upon Facile Removal of the Surface Layer. *Angew. Chem., Int. Ed.* 52(42):11016-11020.
377. Mubeen S, Lee J, Singh N, Kramer S, Stucky GD, Moskovits M (2013) An Autonomous Photosynthetic Device in Which All Charge Carriers Derive from Surface Plasmons. *Nat. Nanotechnol.* 8(4):247-251.
378. Zhang F, Shi YF, Sun XH, Zhao DY, Stucky GD (2009) Formation of Hollow Upconversion Rare-Earth Fluoride Nanospheres: Nanoscale Kirkendall Effect During Ion Exchange. *Chem. Mater.* 21(21):5237-5243.
379. Dong B, Cao BS, He YY, Liu Z, Li ZP, Feng ZQ (2012) Temperature Sensing and In Vivo Imaging by Molybdenum Sensitized Visible Upconversion Luminescence of Rare-Earth Oxides. *Adv. Mater.* 24(15):1987-1993.
380. Ehrmaier J, Domcke W, Opalka D (2018) Mechanism of Photocatalytic Water Oxidation by Graphitic Carbon Nitride. *J. Phys. Chem. Lett.* 9(16):4695-4699.
381. Zhang Q, Huang S, Deng J, Gangadharan DT, Yang F, Xu Z, Giorgi G, Palummo M, Chaker M, Ma D (2019) Ice-Assisted Synthesis of Black Phosphorus Nanosheets as a Metal-Free Photocatalyst: 2D/2D Heterostructure for Broadband H_2 Evolution. *Adv. Funct. Mater.* 29(28):1902486.
382. Zhang Q, Yang F, Zhou S, Bao N, Xu Z, Chaker M, Ma D (2020) Broadband photocatalysts enabled by 0D/2D heterojunctions of near-infrared quantum dots/graphitic carbon nitride nanosheets. *Appl. Catal., B* 270:118879.

383. Li J, Zhang Z, Cui W, Wang H, Cen W, Johnson G, Jiang G, Zhang S, Dong F (2018) The Spatially Oriented Charge Flow and Photocatalysis Mechanism on Internal van der Waals Heterostructures Enhanced g-C₃N₄. *ACS Catal.* 8(9):8376-8385.
384. Xu ZH, Kibria MG, AlOtaibi B, Duchesne PN, Besteiro LV, Gao Y, Zhang QZ, Mi ZT, Zhang P, Govorov AO, Mai LQ, Chaker M, Ma DL (2018) Towards enhancing photocatalytic hydrogen generation: Which is more important, alloy synergistic effect or plasmonic effect? *Appl. Catal., B* 221:77-85.
385. Pietryga JM, Werder DJ, Williams DJ, Casson JL, Schaller RD, Klimov VI, Hollingsworth JA (2008) Utilizing the Lability of Lead Selenide to Produce Heterostructured Nanocrystals with Bright, Stable Infrared Emission. *J. Am. Chem. Soc.* 130(14):4879-4885.
386. Grenland JJ, Maddux CJA, Kelley DF, Kelley AM (2017) Charge Trapping versus Exciton Delocalization in CdSe Quantum Dots. *J. Phys. Chem. Lett.* 8(20):5113-5118.
387. Chistyakov AA, Zvaigzne MA, Nikitenko VR, Tameev AR, Martynov IL, Prezhdo OV (2017) Optoelectronic Properties of Semiconductor Quantum Dot Solids for Photovoltaic Applications. *J. Phys. Chem. Lett.* 8(17):4129-4139.
388. Li X-B, Tung C-H, Wu L-Z (2018) Semiconducting Quantum Dots for Artificial Photosynthesis. *Nat. Rev. Chem.* 2:160-173.
389. Chuang CHM, Brown PR, Bulovic V, Bawendi MG (2014) Improved Performance and Stability in Quantum Dot Solar Cells through Band Alignment Engineering. *Nat. Mater.* 13(8):796-801.
390. He C, Weinberg DJ, Nepomnyashchii AB, Lian SC, Weiss EA (2016) Control of the Redox Activity of PbS Quantum Dots by Tuning Electrostatic Interactions at the Quantum Dot/Solvent Interface. *J. Am. Chem. Soc.* 138(28):8847-8854.
391. Nasilowski M, Nienhaus L, Bertram SN, Bawendi MG (2017) Colloidal Atomic Layer Deposition Growth of PbS/CdS Core/Shell Quantum Dots. *Chem. Commun.* 53(5):869-872.
392. Chaudhuri RG, Paria S (2012) Core/Shell Nanoparticles: Classes, Properties, Synthesis Mechanisms, Characterization, and Applications. *Chem. Rev.* 112(4):2373-2433.
393. Moroz P, Kholmicheva N, Mellott B, Liyanage G, Rijal U, Bastola E, Huband K, Khon E, McBride K, Zamkov M (2013) Suppressed Carrier Scattering in CdS-Encapsulated PbS Nanocrystal Films. *ACS Nano* 7(8):6964-6977.
394. Zhao HG, Liang HY, Gonfa BA, Chaker M, Ozaki T, Tijssen P, Vidal F, Ma DL (2014) Investigating Photoinduced Charge Transfer in Double- and Single-Emission PbS@CdS Core@Shell Quantum Dots. *Nanoscale* 6(1):215-225.
395. Gonfa BA, Zhao HG, Li JT, Qiu JX, Saidani M, Zhang SQ, Izquierdo R, Wu NQ, El Khakani MA, Ma DL (2014) Air-Processed Depleted Bulk Heterojunction Solar Cells Based on PbS/CdS Core-Shell Quantum Dots and TiO₂ Nanorod Arrays. *Sol. Energy Mater. Sol. Cells* 124:67-74.
396. Zhao HG, Chaker M, Ma DL (2011) Effect of CdS shell thickness on the optical properties of water-soluble, amphiphilic polymer-encapsulated PbS/CdS core/shell quantum dots. *J. Mater. Chem.* 21(43):17483-17491.
397. Zhao HG, Wang DF, Zhang T, Chaker M, Ma DL (2010) Two-step synthesis of high-quality water-soluble near-infrared emitting quantum dots via amphiphilic polymers. *Chem. Commun.* 46(29):5301-5303.

398. Ren FQ, del Rosal B, An SY, Yang F, Carrasco E, Benayas A, Oh JK, Jaque D, de la Fuente AJ, Vetrone F, Ma DL (2017) Development and Investigation of Ultrastable PbS/CdS/ZnS Quantum Dots for Near-Infrared Tumor Imaging. *Part. Part. Syst. Charact.* 34(2):1600242.
399. Derfus AM, Chan WCW, Bhatia SN (2004) Probing the Cytotoxicity Of Semiconductor Quantum Dots. *Nano Lett.* 4(1):11-18.
400. Kirchner C, Liedl T, Kudera S, Pellegrino T, Javier AM, Gaub HE, Stolzle S, Fertig N, Parak WJ (2005) Cytotoxicity of Colloidal CdSe and CdSe/ZnS Nanoparticles. *Nano Lett.* 5(2):331-338.
401. Ye L, Yong KT, Liu LW, Roy I, Hu R, Zhu J, Cai HX, Law WC, Liu JW, Wang K, Liu J, Liu YQ, Hu YZ, Zhang XH, Swihart MT, Prasad PN (2012) A Pilot Study in Non-Human Primates Shows No Adverse Response to Intravenous Injection of Quantum Dots. *Nat. Nanotechnol.* 7(7):453-458.
402. Yamashita SI, Hamada M, Nakanishi S, Saito H, Nosaka Y, Wakida SI, Biju V (2015) Auger Ionization Beats Photo-Oxidation of Semiconductor Quantum Dots: Extended Stability of Single-Molecule Photoluminescence. *Angew. Chem., Int. Ed.* 54(13):3892-3896.
403. Nikitskiy I, Goossens S, Kufer D, Lasanta T, Navickaite G, Koppens FHL, Konstantatos G (2016) Integrating an Electrically Active Colloidal Quantum Dot Photodiode with a Graphene Phototransistor. *Nat. Commun.* 7:11954.
404. Ye MY, Zhao ZH, Hu ZF, Liu LQ, Ji HM, Shen ZR, Ma TY (2017) 0D/2D Heterojunctions of Vanadate Quantum Dots/Graphitic Carbon Nitride Nanosheets for Enhanced Visible-Light-Driven Photocatalysis. *Angew. Chem., Int. Ed.* 56(29):8407-8411.
405. Ran JR, Ma TY, Gao GP, Du XW, Qiao SZ (2015) Porous P-Doped Graphitic Carbon Nitride Nanosheets for Synergistically Enhanced Visible-Light Photocatalytic H₂ Production. *Energy Environ. Sci.* 8(12):3708-3717.
406. Wei YZ, Ren ZW, Zhang AD, Mao P, Li H, Zhong XH, Li WW, Yang SY, Wang JZ (2018) Hybrid Organic/PbS Quantum Dot Bilayer Photodetector with Low Dark Current and High Detectivity. *Adv. Funct. Mater.* 28(11):1706690.
407. Han JH, Luo SP, Yin XW, Zhou Y, Nan H, Li JB, Li X, Oron D, Shen HP, Lin H (2018) Hybrid PbS Quantum-Dot-in-Perovskite for High-Efficiency Perovskite Solar Cell. *Small* 14(31):1801016.
408. Moreels I, Lambert K, Smeets D, De Muynck D, Nollet T, Martins JC, Vanhaecke F, Vantomme A, Delerue C, Allan G, Hens Z (2009) Size-Dependent Optical Properties of Colloidal PbS Quantum Dots. *ACS Nano* 3(10):3023-3030.
409. Ceron EN, Ortgies DH, del Rosal B, Ren F, Benayas A, Vetrone F, Ma D, Sanz-Rodriguez F, Sole JG, Jaque D, Rodriguez EM (2015) Hybrid Nanostructures for High-Sensitivity Luminescence Nanothermometry in the Second Biological Window. *Adv. Mater.* 27(32):4781-4787.
410. del Rosal B, Carrasco E, Ren FQ, Benayas A, Vetrone F, Sanz-Rodriguez F, Ma DL, Juarranz A, Jaque D (2016) Infrared-Emitting QDs for Thermal Therapy with Real-Time Subcutaneous Temperature Feedback. *Adv. Funct. Mater.* 26(33):6060-6068.
411. Jeong S, Song I, Lee W, Ryu YM, Jung Y, Kim SY, Kim K, Hong SC, Myung SJ, Kim S (2017) Cancer-Microenvironment-Sensitive Activatable Quantum Dot Probe in the Second Near-Infrared Window. *Nano Lett.* 17(3):1378-1386.

412. Supran GJ, Song KW, Hwang GW, Correa RE, Scherer J, Dauler EA, Shirasaki Y, Bawendi MG, Bulovic V (2015) High-Performance Shortwave-Infrared Light-Emitting Devices Using Core-Shell (PbS-CdS) Colloidal Quantum Dots. *Adv. Mater.* 27(8):1437-1442.
413. Kovalenko MV, Schaller RD, Jarzab D, Loi MA, Talapin DV (2012) Inorganically Functionalized PbS-CdS Colloidal Nanocrystals: Integration into Amorphous Chalcogenide Glass and Luminescent Properties. *J. Am. Chem. Soc.* 134(5):2457-2460.
414. Neo DCJ, Cheng C, Stranks SD, Fairclough SM, Kim JS, Kirkland AI, Smith JM, Snaith HJ, Assender HE, Watt AAR (2014) Influence of Shell Thickness and Surface Passivation on PbS/CdS Core/Shell Colloidal Quantum Dot Solar Cells. *Chem. Mater.* 26(13):4004-4013.
415. Martin DJ, Reardon PJT, Moniz SJA, Tang JW (2014) Visible Light-Driven Pure Water Splitting by a Nature-Inspired Organic Semiconductor-Based System. *J. Am. Chem. Soc.* 136(36):12568-12571.
416. Liang QH, Li Z, Huang ZH, Kang FY, Yang QH (2015) Holey Graphitic Carbon Nitride Nanosheets with Carbon Vacancies for Highly Improved Photocatalytic Hydrogen Production. *Adv. Funct. Mater.* 25(44):6885-6892.
417. Zhang JS, Zhang MW, Yang C, Wang XC (2014) Nanospherical Carbon Nitride Frameworks with Sharp Edges Accelerating Charge Collection and Separation at a Soft Photocatalytic Interface. *Adv. Mater.* 26(24):4121-4126.
418. Yu HJ, Shi R, Zhao YX, Bian T, Zhao YF, Zhou C, Waterhouse GIN, Wu LZ, Tung CH, Zhang TR (2017) Alkali-Assisted Synthesis of Nitrogen Deficient Graphitic Carbon Nitride with Tunable Band Structures for Efficient Visible-Light-Driven Hydrogen Evolution. *Adv. Mater.* 29(16):1605148.
419. Jun YS, Lee EZ, Wang XC, Hong WH, Stucky GD, Thomas A (2013) From Melamine-Cyanuric Acid Supramolecular Aggregates to Carbon Nitride Hollow Spheres. *Adv. Funct. Mater.* 23(29):3661-3667.
420. Lee EZ, Jun YS, Hong WH, Thomas A, Jin MM (2010) Cubic Mesoporous Graphitic Carbon (IV) Nitride: An All-in-One Chemosensor for Selective Optical Sensing of Metal Ions. *Angew. Chem., Int. Ed.* 49(50):9706-9710.
421. Kang YY, Yang YQ, Yin LC, Kang XD, Wang LZ, Liu G, Cheng HM (2016) Selective Breaking of Hydrogen Bonds of Layered Carbon Nitride for Visible Light Photocatalysis. *Adv. Mater.* 28(30):6471-6477.
422. Liu Y, Yan K, Zhang JD (2016) Graphitic Carbon Nitride Sensitized with CdS Quantum Dots for Visible-Light-Driven Photoelectrochemical Aptasensing of Tetracycline. *ACS Appl. Mater. Interfaces* 8(42):28255-28264.
423. Virieux H, Le Troedec M, Cros-Gagneux A, Ojo WS, Delpech F, Nayral C, Martinez H, Chaudret B (2012) InP/ZnS Nanocrystals: Coupling NMR and XPS for Fine Surface and Interface Description. *J. Am. Chem. Soc.* 134(48):19701-19708.
424. Zhang ZY, Huang JD, Zhang MY, Yuan L, Dong B (2015) Ultrathin Hexagonal SnS₂ Nanosheets Coupled with g-C₃N₄ Nanosheets as 2D/2D Heterojunction Photocatalysts toward High Photocatalytic Activity. *Appl. Catal., B* 163:298-305.
425. Ye LJ, Wang D, Chen SJ (2016) Fabrication and Enhanced Photoelectrochemical Performance of MoS₂/S-Doped g-C₃N₄ Heterojunction Film. *ACS Appl. Mater. Interfaces* 8(8):5280-5289.

426. Liu G, Niu P, Sun CH, Smith SC, Chen ZG, Lu GQ, Cheng HM (2010) Unique Electronic Structure Induced High Photoreactivity of Sulfur-Doped Graphitic C₃N₄. *J. Am. Chem. Soc.* 132(33):11642-11648.
427. Li XG, Bi WT, Zhang L, Tao S, Chu WS, Zhang Q, Luo Y, Wu CZ, Xie Y (2016) Single-Atom Pt as Co-Catalyst for Enhanced Photocatalytic H₂ Evolution. *Adv. Mater.* 28(12):2427-2431.
428. Wang S, Guan BY, Wang X, Lou XWD (2018) Formation of Hierarchical Co₉S₈@ZnIn₂S₄ Heterostructured Cages as an Efficient Photocatalyst for Hydrogen Evolution. *J. Am. Chem. Soc.* 140(45):15145-15148.
429. Kong L, Ji Y, Dang Z, Yan J, Li P, Li Y, Liu SF (2018) g-C₃N₄ Loading Black Phosphorus Quantum Dot for Efficient and Stable Photocatalytic H₂ Generation under Visible Light. *Adv. Funct. Mater.* 28(22):1800668.
430. Cao S, Li H, Tong T, Chen H-C, Yu A, Yu J, Chen HM (2018) Single-Atom Engineering of Directional Charge Transfer Channels and Active Sites for Photocatalytic Hydrogen Evolution. *Adv. Funct. Mater.* 28(32):1802169.
431. Shi L, Wang T, Zhang HB, Chang K, Ye JH (2015) Electrostatic Self-Assembly of Nanosized Carbon Nitride Nanosheet onto a Zirconium Metal-Organic Framework for Enhanced Photocatalytic CO₂ Reduction. *Adv. Funct. Mater.* 25(33):5360-5367.
432. Zheng Y, Lin LH, Ye XJ, Guo FS, Wang XC (2014) Helical Graphitic Carbon Nitrides with Photocatalytic and Optical Activities. *Angew. Chem., Int. Ed.* 53(44):11926-11930.
433. Fan XQ, Zhang LX, Cheng RL, Wang M, Li ML, Zhou YJ, Shi JL (2015) Construction of Graphitic C₃N₄-Based Intramolecular Donor-Acceptor Conjugated Copolymers for Photocatalytic Hydrogen Evolution. *ACS Catal.* 5(9):5008-5015.
434. Shi AY, Li HH, Yin S, Liu B, Zhang JC, Wang YH (2017) Effect of Conjugation Degree and Delocalized π -System on the Photocatalytic Activity of Single Layer g-C₃N₄. *Appl. Catal., B* 218:137-146.
435. Sun CY, Xu QH, Xie Y, Ling Y, Hou Y (2018) Designed Synthesis of Anatase-TiO₂ (B) Biphase Nanowire/ZnO Nanoparticle Heterojunction for Enhanced Photocatalysis. *J. Mater. Chem. A* 6(18):8289-8298.
436. Lee H, Leventis HC, Moon SJ, Chen P, Ito S, Haque SA, Torres T, Nuesch F, Geiger T, Zakeeruddin SM, Gratzel M, Nazeeruddin MK (2009) PbS and CdS Quantum Dot-Sensitized Solid-State Solar Cells: "Old Concepts, New Results". *Adv. Funct. Mater.* 19(17):2735-2742.
437. Jasieniak J, Califano M, Watkins SE (2011) Size-Dependent Valence and Conduction Band-Edge Energies of Semiconductor Nanocrystals. *ACS Nano* 5(7):5888-5902.
438. Fujishima A, Honda K (1972) Photolysis-Decomposition of Water at the Surface of an Irradiated Semiconductor. *Nature* 238(5385):37-38.
439. Maeda K, Teramura K, Lu DL, Takata T, Saito N, Inoue Y, Domen K (2006) Photocatalyst Releasing Hydrogen from Water - Enhancing Catalytic Performance Holds Promise for Hydrogen Production by Water Splitting in Sunlight. *Nature* 440(7082):295-295.
440. Kudo A, Miseki Y (2009) Heterogeneous Photocatalyst Materials for Water Splitting. *Chem. Soc. Rev.* 38(1):253-278.
441. Zhang GG, Lan ZA, Wang XC (2016) Conjugated Polymers: Catalysts for Photocatalytic Hydrogen Evolution. *Angew. Chem., Int. Ed.* 55(51):15712-15727.
442. Ou HH, Yang PJ, Lin LH, Anpo M, Wang XC (2017) Carbon Nitride Aerogels for the Photoredox Conversion of Water. *Angew. Chem., Int. Ed.* 56(36):10905-10910.

443. Chen XF, Zhang JS, Fu XZ, Antonietti M, Wang XC (2009) Fe-g-C₃N₄-Catalyzed Oxidation of Benzene to Phenol Using Hydrogen Peroxide and Visible Light. *J. Am. Chem. Soc.* 131(33):11658-11659.
444. Deng YX, Luo Z, Conrad NJ, Liu H, Gong YJ, Najmaei S, Ajayan PM, Lou J, Xu XF, Ye PD (2014) Black Phosphorus-Monolayer MoS₂ van der Waals Heterojunction p-n Diode. *ACS Nano* 8(8):8292-8299.
445. Liu H, Neal AT, Zhu Z, Luo Z, Xu XF, Tomanek D, Ye PD (2014) Phosphorene: An Unexplored 2D Semiconductor with a High Hole Mobility. *ACS Nano* 8(4):4033-4041.
446. Xia FN, Wang H, Xiao D, Dubey M, Ramasubramaniam A (2014) Two-Dimensional Material Nanophotonics. *Nat. Photonics* 8(12):899-907.
447. Ling X, Wang H, Huang SX, Xia FN, Dresselhaus MS (2015) The Renaissance of Black Phosphorus. *Proc. Natl. Acad. Sci.* 112(15):4523-4530.
448. Kou LZ, Chen CF, Smith SC (2015) Phosphorene: Fabrication, Properties, and Applications. *J. Phys. Chem. Lett.* 6(14):2794-2805.
449. Ryder CR, Wood JD, Wells SA, Yang Y, Jariwala D, Marks TJ, Schatz GC, Hersam MC (2016) Covalent Functionalization and Passivation of Exfoliated Black Phosphorus via Aryl Diazonium Chemistry. *Nat. Chem.* 8(6):598-603.
450. Xia FN, Wang H, Jia YC (2014) Rediscovering Black Phosphorus as an Anisotropic Layered Material for Optoelectronics and Electronics. *Nat. Commun.* 5:4458.
451. Sun J, Zheng GY, Lee HW, Liu N, Wang HT, Yao HB, Yang WS, Cui Y (2014) Formation of Stable Phosphorus-Carbon Bond for Enhanced Performance in Black Phosphorus Nanoparticle-Graphite Composite Battery Anodes. *Nano Lett.* 14(8):4573-4580.
452. Wang H, Yang XZ, Shao W, Chen SC, Xie JF, Zhang XD, Wang J, Xie Y (2015) Ultrathin Black Phosphorus Nanosheets for Efficient Singlet Oxygen Generation. *J. Am. Chem. Soc.* 137(35):11376-11382.
453. Sun Z, Xie H, Tang S, Yu XF, Guo Z, Shao J, Zhang H, Huang H, Wang H, Chu PK (2015) Ultrasmall Black Phosphorus Quantum Dots: Synthesis and Use as Photothermal Agents. *Angew. Chem., Int. Ed.* 54(39):11526-11530.
454. Zhang X, Xie H, Liu Z, Tan C, Luo Z, Li H, Lin J, Sun L, Chen W, Xu Z, Xie L, Huang W, Zhang H (2015) Black Phosphorus Quantum Dots. *Angew. Chem., Int. Ed.* 54(12):3653-3657.
455. Yang Y, Gao J, Zhang Z, Xiao S, Xie HH, Sun ZB, Wang JH, Zhou CH, Wang YW, Guo XY, Chu PK, Yu XF (2016) Black Phosphorus Based Photocathodes in Wideband Bifacial Dye-Sensitized Solar Cells. *Adv. Mater.* 28(40):8937-8944.
456. Lei WY, Zhang TT, Liu P, Rodriguez JA, Liu G, Liu MH (2016) Bandgap- and Local Field-Dependent Photoactivity of Ag/Black Phosphorus Nanohybrids. *ACS Catal.* 6(12):8009-8020.
457. Zhu MS, Cai XY, Fujitsuka M, Zhang JY, Majima T (2017) Au/La₂Ti₂O₇ Nanostructures Sensitized with Black Phosphorus for Plasmon-Enhanced Photocatalytic Hydrogen Production in Visible and Near-Infrared Light. *Angew. Chem., Int. Ed.* 56(8):2064-2068.
458. Zhu XJ, Zhang TM, Sun ZJ, Chen HL, Guan J, Chen X, Ji HX, Du PW, Yang SF (2017) Black Phosphorus Revisited: A Missing Metal-Free Elemental Photocatalyst for Visible Light Hydrogen Evolution. *Adv. Mater.* 29(17):1605776.

459. Hu W, Lin L, Zhang R, Yang C, Yang J (2017) Highly Efficient Photocatalytic Water Splitting over Edge-Modified Phosphorene Nanoribbons. *J. Am. Chem. Soc.* 139(43):15429-15436.
460. Kang J, Wood JD, Wells SA, Lee JH, Liu XL, Chen KS, Hersam MC (2015) Solvent Exfoliation of Electronic-Grade, Two-Dimensional Black Phosphorus. *ACS Nano* 9(4):3596-3604.
461. Wood JD, Wells SA, Jariwala D, Chen KS, Cho E, Sangwan VK, Liu XL, Lauhon LJ, Marks TJ, Hersam MC (2014) Effective Passivation of Exfoliated Black Phosphorus Transistors against Ambient Degradation. *Nano Lett.* 14(12):6964-6970.
462. Doganov RA, O'Farrell ECT, Koenig SP, Yeo YT, Ziletti A, Carvalho A, Campbell DK, Coker DF, Watanabe K, Taniguchi T, Neto AHC, Ozyilmaz B (2015) Transport Properties of Pristine Few-Layer Black Phosphorus by van der Waals Passivation in an Inert Atmosphere. *Nat. Commun.* 6:6647.
463. Zhu WN, Yogeesh MN, Yang SX, Aldave SH, Kim JS, Sonde S, Tao L, Lu NS, Akinwande D (2015) Flexible Black Phosphorus Ambipolar Transistors, Circuits and AM Demodulator. *Nano Lett.* 15(3):1883-1890.
464. Zhao YT, Wang HY, Huang H, Xiao QL, Xu YH, Guo ZN, Xie HH, Shao JD, Sun ZB, Han WJ, Yu XF, Li PH, Chu PK (2016) Surface Coordination of Black Phosphorus for Robust Air and Water Stability. *Angew. Chem., Int. Ed.* 55(16):5003-5007.
465. Brent JR, Savjani N, Lewis EA, Haigh SJ, Lewis DJ, O'Brien P (2014) Production of Few-Layer Phosphorene by Liquid Exfoliation of Black Phosphorus. *Chem. Commun.* 50(87):13338-13341.
466. Yasaei P, Kumar B, Foroozan T, Wang CH, Asadi M, Tuschel D, Indacochea JE, Klie RF, Salehi-Khojin A (2015) High-Quality Black Phosphorus Atomic Layers by Liquid-Phase Exfoliation. *Adv. Mater.* 27(11):1887-1892.
467. Chen L, Zhou GM, Liu ZB, Ma XM, Chen J, Zhang ZY, Ma XL, Li F, Cheng HM, Ren WC (2016) Scalable Clean Exfoliation of High-Quality Few-Layer Black Phosphorus for a Flexible Lithium Ion Battery. *Adv. Mater.* 28(3):510-517.
468. Batmunkh M, Shearer CJ, Biggs MJ, Shapter JG (2016) Solution Processed Graphene Structures for Perovskite Solar Cells. *J. Mater. Chem. A* 4(7):2605-2616.
469. Dong F, Zhao ZW, Xiong T, Ni ZL, Zhang WD, Sun YJ, Ho WK (2013) In Situ Construction of g-C₃N₄/g-C₃N₄ Metal-Free Heterojunction for Enhanced Visible-Light Photocatalysis. *ACS Appl. Mater. Interfaces* 5(21):11392-11401.
470. Cao YQ, Zhang ZZ, Long JL, Liang J, Lin H, Lin HX, Wang XX (2014) Vacuum Heat-Treatment of Carbon Nitride for Enhancing Photocatalytic Hydrogen Evolution. *J. Mater. Chem. A* 2(42):17797-17807.
471. Zhang JQ, An XH, Lin N, Wu WT, Wang LZ, Li ZT, Wang RQ, Wang Y, Liu JX, Wu MB (2016) Engineering Monomer Structure of Carbon Nitride for the Effective and Mild Photooxidation Reaction. *Carbon* 100:450-455.
472. Peng G, Xing L, Barrio J, Volokh M, Shalom M (2017) A General Synthesis of Porous Carbon Nitride Films with Tunable Surface Area and Photophysical Properties. *Angew. Chem., Int. Ed.* 56(5):1-7.
473. Leijtens T, Eperon GE, Pathak S, Abate A, Lee MM, Snaith HJ (2013) Overcoming Ultraviolet Light Instability of Sensitized TiO₂ with Meso-Superstructured Organometal Tri-Halide Perovskite Solar Cells. *Nat. Commun.* 4:2885.

474. Zhu M, Sun Z, Fujitsuka M, Majima T (2018) Z-Scheme Photocatalytic Overall Pure-Water Splitting on 2D Heterostructure of Black Phosphorus/BiVO₄ under Visible Light. *Angew. Chem., Int. Ed.* 57(8):1-6.
475. Qiu DY, da Jornada FH, Louie SG (2017) Environmental Screening Effects in 2D Materials: Renormalization of the Bandgap, Electronic Structure, and Optical Spectra, of Few-Layer Black Phosphorus. *Nano Lett.* 17(8):4706-4712.
476. Shi D, Zheng R, Sun MJ, Cao X, Sun CX, Cui CJ, Liu CS, Zhao J, Du M (2017) Semiconductive Copper(I)-Organic Frameworks for Efficient Light-Driven Hydrogen Generation Without Additional Photosensitizers and Cocatalysts. *Angew. Chem., Int. Ed.* 56(46):14637-14641.
477. Ran JR, Guo WW, Wang HL, Zhu BC, Yu JG, Qiao SZ (2018) Metal-Free 2D/2D Phosphorene/g-C₃N₄ Van der Waals Heterojunction for Highly Enhanced Visible-Light Photocatalytic H₂ Production. *Adv. Mater.* 30(25):1800128.
478. Ritter KA, Lyding JW (2009) The influence of edge structure on the electronic properties of graphene quantum dots and nanoribbons. *Nat. Mater.* 8(3):235-242.
479. Tay QL, Wang XH, Zhao X, Hong JD, Zhang Q, Xu R, Chen Z (2016) Enhanced visible light hydrogen production via a multiple heterojunction structure with defect-engineered g-C₃N₄ and two-phase anatase/brookite TiO₂. *J. Catal.* 342:55-62.
480. Lan Z-A, Zhang G, Wang X (2016) A facile synthesis of Br-modified g-C₃N₄ semiconductors for photoredox water splitting. *Appl. Catal., B* 192:116-125.
481. Ou H, Lin L, Zheng Y, Yang P, Fang Y, Wang X (2017) Tri-s-triazine-Based Crystalline Carbon Nitride Nanosheets for an Improved Hydrogen Evolution. *Adv. Mater.* 29(22):1700008.
482. Zhu MS, Sun ZC, Fujitsuka M, Majima T (2018) Z-Scheme Photocatalytic Water Splitting on a 2D Heterostructure of Black Phosphorus/Bismuth Vanadate Using Visible Light. *Angew. Chem., Int. Ed.* 57(8):2160-2164.

SOMMAIRE RÉCAPITULATIF

L'introduction

Avec la croissance industrielle non réglementée et à l'augmentation constante de la population mondiale, la crise énergétique et la pollution de l'environnement provoquée par la forte consommation de combustibles fossiles ont été les deux principaux problèmes auxquels l'homme est confronté. L'énergie solaire est apparue comme une alternative prometteuse aux combustibles fossiles limités et son utilisation efficace est également attrayante mais aussi challenging. La photocatalyse à semi-conducteurs, qui peut directement capter et convertir l'énergie solaire à la production de combustible écologique et la purification de l'environnement à la température ambiante et à la pression atmosphérique normale, a été reconnue comme l'une des stratégies durables et idéales pour répondre aux préoccupations énergétiques et environnementales mondiales. Ensuite, certains principes fondamentales de la photocatalyse et les exigences et les défis actuels en matière de photocatalyseurs sont présentés.

Parmi les différentes catégories de photocatalyseurs à semi-conducteurs, le nitrure de carbone graphitique ($g-C_3N_4$) présente un grand intérêt pour le domaine des matériaux, pour ses mérites tels que la non-toxicité, la facilité de préparation, la bande interdite modérée, la forte capacité rédox, l'abondance sur terre et la bonne stabilité physico-chimique. Cependant, le $g-C_3N_4$ souffre toujours d'une activité photocatalytique médiocre et d'un rendement quantique faible en raison du taux de recombinaison élevé des porteurs de charge photogénérés. En plus, la bande interdite optique (2,7 eV) du $g-C_3N_4$ limite grandement la plage d'absorption de la lumière visible aux longueurs d'onde inférieures à 460 nm. Ainsi, le développement de photocatalyseurs basés sur du $g-C_3N_4$ répondant efficacement dans une large bande d'absorption couvrant l'ultraviolet (UV), le visible, et l'infrarouge (NIR), demeure une tâche de grande importance et de grande urgence, bien que difficile.

Les dernières années ont été marquées par un regain d'intérêt pour l'utilisation de matériaux de conversion ascendante (UC), l'introduction de la résonance plasmonique de surface (SPR) via le chargement de nanostructures métalliques plasmoniques et la construction d'une hétérojonction par couplage avec un semi-conducteur à bande d'interdit plus étroite, qui ont efficacement contourné les défauts inhérents au $g-C_3N_4$ pour améliorer de manière inhabituelle l'efficacité photocatalytique de $g-C_3N_4$. Le progrès est conclu dans les trois stratégies, qui vise à obtenir la récolte solaire à large bande par le $g-C_3N_4$ pour une photocatalyse efficace, comprenant la

purification de l'environnement et le dégagement de H₂ de l'eau splitté, sont résumées aux avancées les plus récentes.

Zhang Q, Liu Y, Xu Z, Zhao Y, Chaker M, Ma D (2018) Visible-Light-Driven Photocatalysts. *Nanomaterials for Energy Conversion and Storage*, Wang D & Cao G (Eds.) World Scientific, New Jersey. p. 109-173.

Zhang Q, Yang F, Xu Z, Chaker M, Ma D (2019) Are lanthanide-doped upconversion materials good candidates for photocatalysis? *Nanoscale Horizons*, 4(3):579-591.

Zhang Q, Thrithamarassery Gangadharan D, Liu Y, Xu Z, Chaker M, Ma D (2017) Recent Advancements in Plasmon-Enhanced Visible Light-Driven Water Splitting. *Journal of Materiomics*, 3(1):33-50.

Objectif de la thèse

Actuellement, les photocatalyseurs à large bande rapportés basés sur le g-C₃N₄ et qui montrent effectivement une activité photocatalytique UV à NIR sont encore assez limités. Par conséquent, les objectifs de cette thèse sont les suivants:

- (1) Introduction des effets UC et plasmoniques dans la photocatalyse afin de construire des photocatalyseurs efficaces et à large bande pour la dégradation photocatalytique du colorant organique en solution aqueuse.
- (2) Déposer des QD sensibles au NIR sur des nano-feuilles de g-C₃N₄ pour récolter de manière plus économique des photons solaires allant des régions UV, visibles aux NIR, pour la dégradation photocatalytique d'un colorant organique en solution aqueuse.
- (3) Coupler un semi-conducteur 2D à bande d'interdit plus étroite avec des nano-feuilles 2D g-C₃N₄ afin de construire une hétérojonction 2D/2D sans métal, qui utilise l'énergie solaire de manière plus efficace, économique et respectueuse de l'environnement, pour la production à large bande d'un combustible vert avec zéro émission, H₂.

Section expérimentale

Le chapitre 2 fournit les détails expérimentaux et théorique. Les méthodes de synthèse de tous les échantillons, les informations de caractérisation, la dégradation photocatalytique de la production de colorant organique et de H₂, ainsi que les modèles et paramètres adoptés pour les calculs théoriques sont tous présentés.

Résultats et discussions

Le chapitre 3 correspond au premier objectif. Un photocatalyseur à large bande amélioré par plasmon et UC, basé sur du Au-NP de plasmonique et des conversions ascendantes de $\text{NaYF}_4:\text{Yb}^{3+}, \text{Er}^{3+}, \text{Tm}^{3+}$ (NYF) co-déposées par des nano-feuilles $\text{g-C}_3\text{N}_4$ a été subtilement synthétisé et utilisé pour la dégradation photocatalytique à large bande de MO. La publication liée à ce chapitre est:

Zhang Q, Deng J, Xu Z, Chaker M, Ma D (2017) High-Efficiency Broadband C_3N_4 Photocatalysts: Synergistic Effects from Upconversion and Plasmons. *ACS Catalysis*, 7(9):6225-6234.

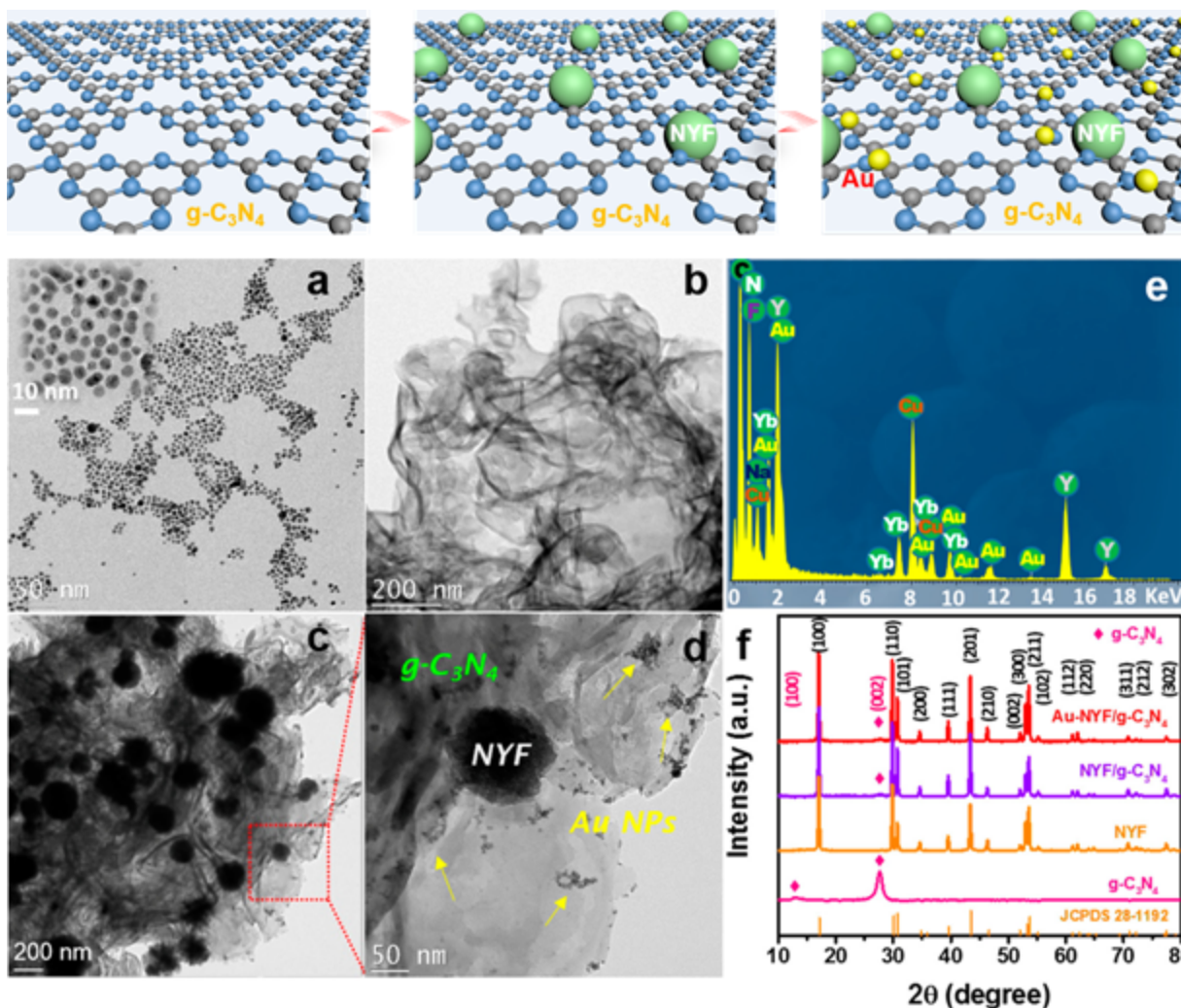


Figure R1 Les trois figures en haut présentent le processus de synthèse de Au-NYF/g-C₃N₄. Images TEM de (a) Au NPs, (b) nano-feuilles de g-C₃N₄, (c) photocatalyseurs 1 wt% Au-NYF/g-C₃N₄, (d) la vue agrandie et (e) le spectre EDX de la zone du rectangle dans (c) L'encart de (a) est l'image TEM en agrandissement de Au NP. (f) profils de diffraction des rayons X (XRD) d'échantillons de g-C₃N₄, NYF, NYF/g-C₃N₄ et 1 wt% Au-NYF/g-C₃N₄. Les données standards correspondantes à la phase $\beta\text{-NaYF}_4$ (JCPDS 28-1192) sont également indiquées en bas.

Nous avons synthétisé un photocatalyseur à large bande amélioré par plasmon et conversion ascendante (upconversion, UP), basé sur des nano-feuilles de g-C₃N₄ chargées de nanoparticules (NP) d'or et de microsphères de NaYF₄:Yb³⁺, Er³⁺, Tm³⁺ (NYF) (Au-NYF/g-C₃N₄). La synthèse en une simple étape de NYF en présence de g-C₃N₄, qui n'a pas été rapportée dans la littérature, conduit à la fois à un rendement élevé en NYF et à une efficacité de couplage élevée entre NYF et g-C₃N₄. La Figure R1 montre le processus de synthèse rapide d'Au-NYF/g-C₃N₄, d'images TEM, de spectres EDX et de diagrammes de XRD des échantillons préparés.

La structure Au-NYF/g-C₃N₄ présente une stabilité élevée, une large bande de photoréponse allant de l'UV aux régions visibles et NIR, ainsi qu'une activité photocatalytique nettement accrue au g-C₃N₄ lors de la dégradation du méthyl orange (MO). Comme montré par la Figure R2, avec l'optimisation de la charge en Au, la constante de vitesse normalisée avec la masse de catalyseur du catalyseur le plus performant, 1% en poids Au-NYF/g-C₃N₄ (0,032 h⁻¹ mg⁻¹) dépasse de loin celle de NYF/g-C₃N₄ et g-C₃N₄ (0,009 h⁻¹ mg⁻¹) x 3,6 fois sous λ > 420 nm irradiation lumineuse. Les hautes performances du nano-composite Au-NYF/g-C₃N₄ sous différentes irradiations lumineuses sont attribuées au fait que la séparation des charges est nettement favorisée et à la suppression de la recombinaison ainsi qu'au transfert efficace des porteurs de charge et de l'énergie entre ces composants. La séparation et le transfert de charge favorisés ont ensuite été confirmés par des mesures photoélectrochimiques. Le 1 wt% Au-NYF/g-C₃N₄ présente une densité de photocourant améliorée (environ 6,36 μA cm⁻²) par un facteur de 5,5 par rapport à celui de NYF/g-C₃N₄ (environ 1,15 μA cm⁻²).

Le fait que la séparation et le transfert de charge soient favorisés a ensuite été confirmé par des mesures photoélectrochimiques. Différents mécanismes de photo-dégradation réalisés séparément sous des éclairages UV, visible et NIR sont mis en évidence et discutés en détail. En simulant une illumination solaire, les espèces réactives impliquées ont été identifiées en effectuant des expériences de piégeage. Ces travaux mettent en évidence le grand potentiel de développement de photocatalyseurs à large bande basés sur le g-C₃N₄ hautement efficaces pour une utilisation complète du spectre solaire en intégrant des nanostructures plasmoniques et des matériaux à conversion ascendante.

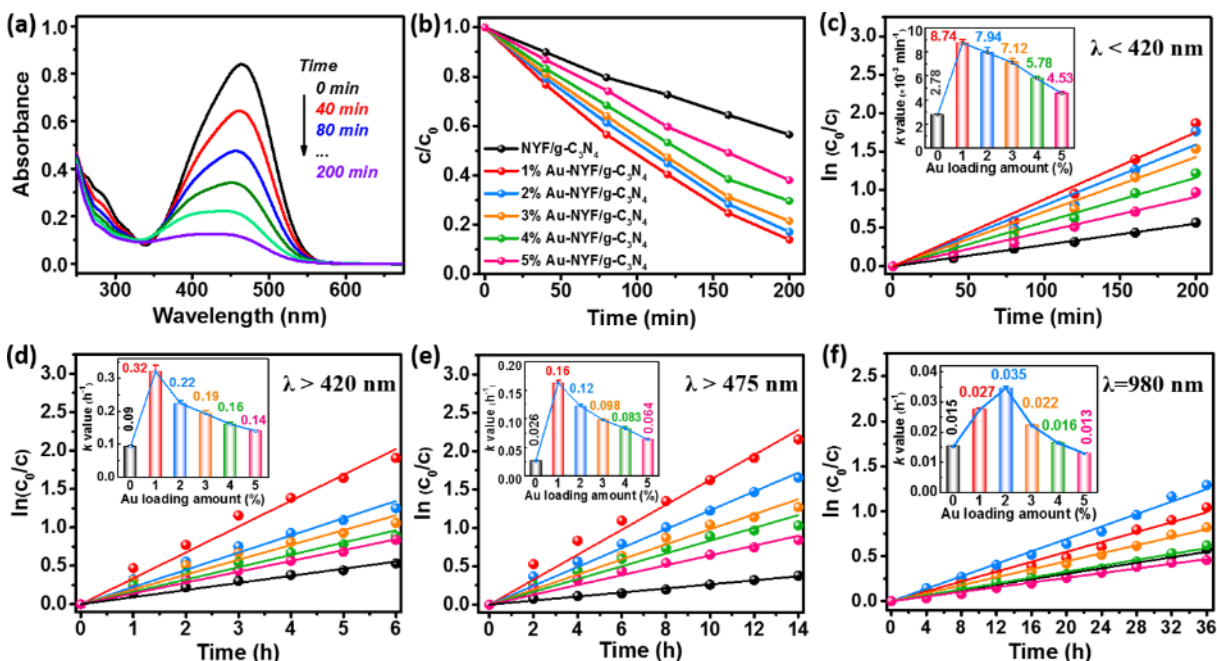


Figure R2 Spectre d'absorption UV-vis en fonction du temps pour la dégradation photocatalytique de MO sur 1 wt% Au-NYF/g-C₃N₄ (a) et la courbe de c/c_0 en fonction du temps de réaction (b) sous irradiation à la lumière UV. Le graphique de $\ln(c_0/c)$ en fonction du temps de réaction (c, d, e, f) pour la dégradation photocatalytique de MO sur x wt% Au-NYF/g-C₃N₄ (x = 0, 1, 2, 3, 4 et 5) les photocatalyseurs, sous lumière UV (c), $\lambda > 420$ nm (d), $\lambda > 475$ nm (e) et sous irradiation à la lumière NIR (f). Les encarts dedans (c, d, e, f) sont les constantes de vitesse apparentes (valeur k) en fonction de la charge en Au.

En raison de l'intermittence de l'énergie solaire et des divergences temporelles et géographiques entre la production et la demande, il faut rendre la récupération de l'énergie solaire plus efficace et plus rentable. Cependant, les métaux et les terres rares utilisées dans ce travail sont toujours chers. De plus, l'efficacité de conversion ascendante des matériaux de conversion ascendante dopés au lanthanide est assez faible. Pour utiliser l'énergie solaire de manière plus efficace et plus rentable, une hétérojonction 0D/2D basée sur des nano-feuilles de g-C₃N₄ chargées de points quantiques sensibles au NIR a été construite pour la dégradation de colorant organique dans les eaux usées.

Le chapitre 4 correspond au deuxième objectif. Des points quantiques (PCZ QDs) PbS@CdS@ZnS sensibles à l'infrarouge-proche(NIR) ont été chargés sur des nano-feuilles de g-C₃N₄ pour construire une hétérostructure 0D/2D, utilisée pour la récolte de photons solaires allant des UV, visibles aux régions NIR et permettant une dégradation photocatalytique efficace du MO. La publication liée à ce chapitre est:

Zhang Q, Yang F, Zhou S, Bao N, Xu Z, Chaker M, Ma D (2020) Broadband Photocatalysts Enabled by 0D/2D Heterojunctions of Near-Infrared Quantum Dots/Graphitic Carbon Nitride Nanosheets. *Applied Catalysis B: Environmental*, 270:118879.

Une hétérojonction, constituée de points quantiques PbS@CdS@ZnS core@shell@shell (PCZ QDs) et de g-C₃N₄ à deux dimensions (2D), et dénommée hétérojonction 0D/2D, a été synthétisée. En plus des avantages typiques des composites 0D/2D, tels qu'une courte distance de diffusion par charge et une mobilité élevée des charges, nos photocatalyseurs PCZ QDs/g-C₃N₄ offrent des fonctionnalités supplémentaires. L'absorption optique à large bande de PCZ QD de haute qualité dispersés sur toute la surface des nano-feuilles de g-C₃N₄ et leur forte interaction permettent un transfert de charge efficace entre eux. Ceci confère aux hétérojonctions PCZ QDs/g-C₃N₄ une activité photocatalytique élevée de l'UV à la région NIR (Figure R3).

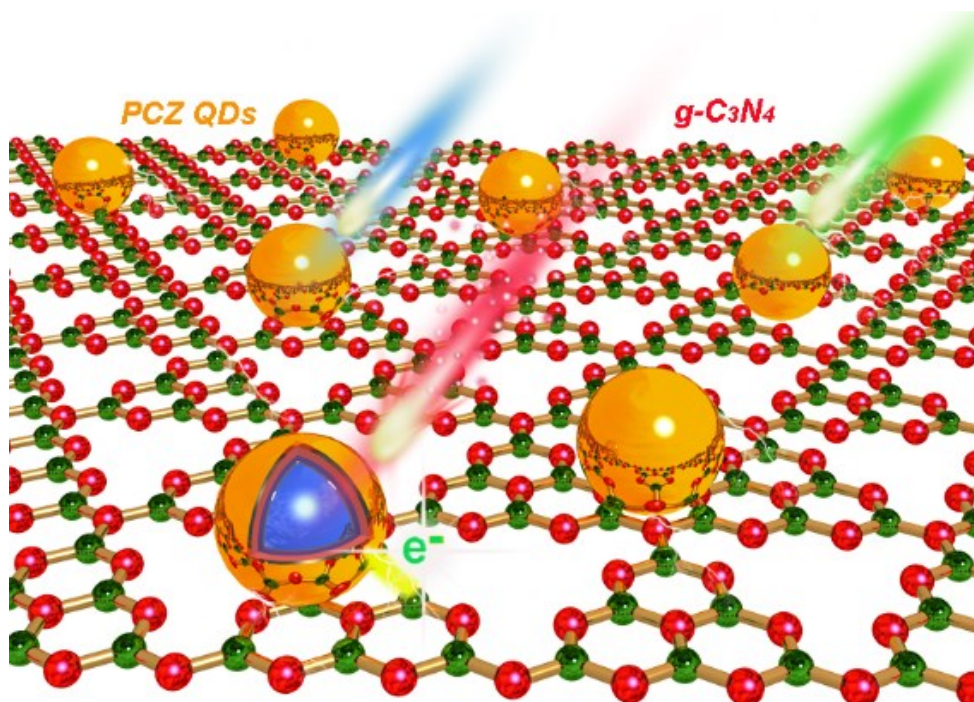


Figure R3 Hétérostructure 0D/2D de nano-feuilles PCZ QDs/g-C₃N₄ pour la collecte de photons solaires allant des régions UV, visibles aux régions NIR.

Une image TEM représentative de g-C₃N₄ montre la feuille nanométrique mince 2D (Figure R4a). Les figures R4b et R4c révèlent que les PCZ QDs dispersables dans l'eau, tels que préparés, sont bien définis, monodispersés et de taille assez uniforme avec un diamètre moyen de $4,7 \pm 0,3$ nm. Des franges de réseau claires sont représentées dans l'image HRTEM de PCZ QD et un espacement interplanaire de 0,30 nm a été observé (encadré de la figure R4c), ce qui correspond au plan de réseau (200) du nanocristal PbS cubique de sel gemme. La figure R4d-R4e montre les images TEM de 2 wt% QD/g-C₃N₄ à différents grossissements. Les QD ultra-petits sont uniformément répartis sur la surface des nano-feuilles de g-C₃N₄ sans aucune agglomération. Il est à noter qu'aucune QD libre n'a été observée, ce qui suggère l'efficacité élevée du couplage

entre les PCZ QDs et les nano-feuilles g-C₃N₄. Le spectre EDX (Figure R4g) et l'analyse XRD (Figure R4h) confirment l'intégration réussie des PCZ QDs et du g-C₃N₄.

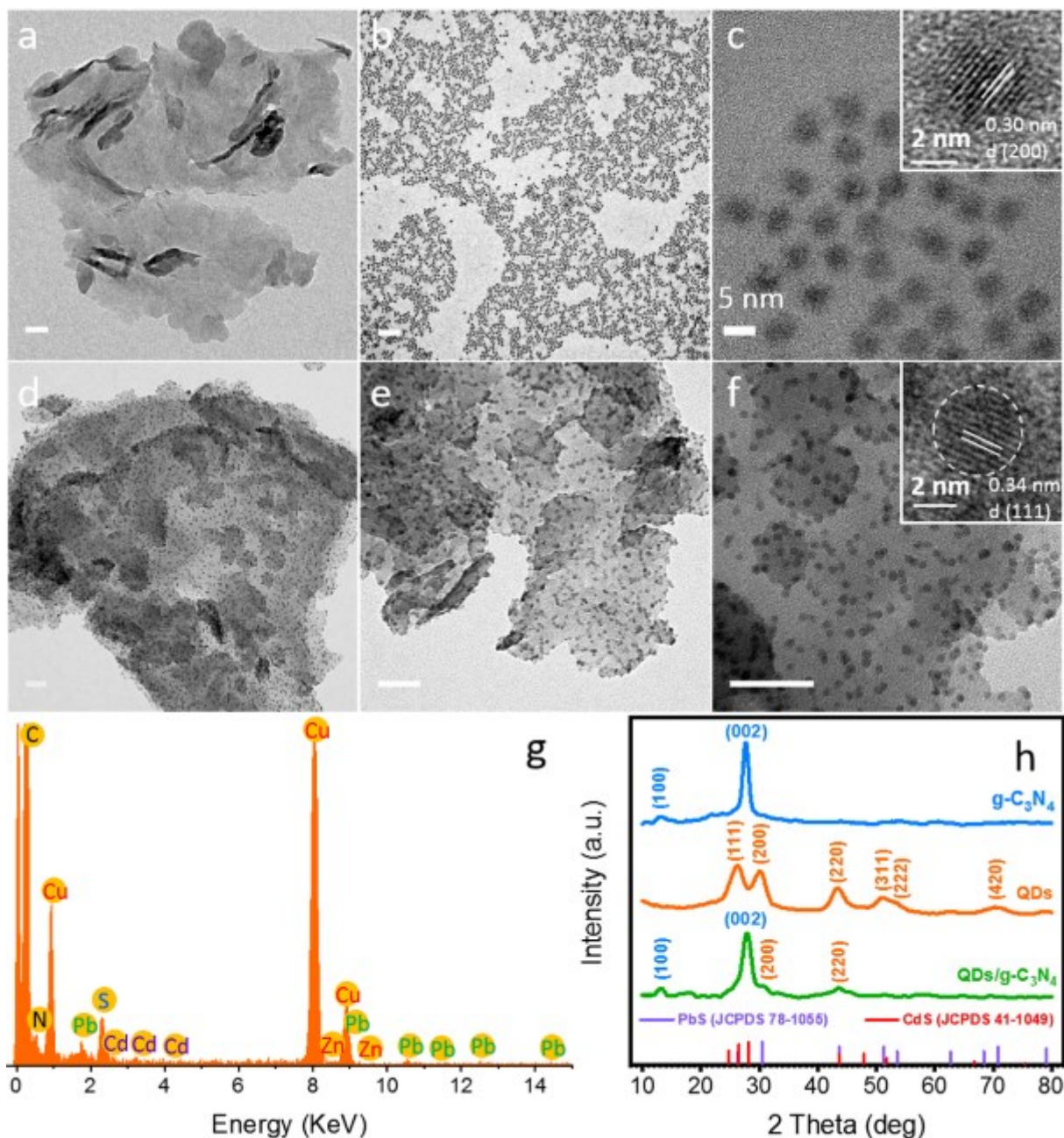


Figure R4 Images TEM de (a) nano-feuilles de g-C₃N₄, (b-c) QDs de PCZ, (d-f) 2 wt% QD/g-C₃N₄ avec des grossissements différents. Les encarts (c) et (f) sont les images HRTEM des PCZ QDs et des PCZ QDs/g-C₃N₄, respectivement. Les barres d'échelle en (a-b) et (d-f) sont à 50 nm. (g) spectre EDX de (f). (h) Modèles de diffraction des rayons X des échantillons de g-C₃N₄, de PCZ QDs et de PCZ QDs/g-C₃N₄.

En plus de l'activité photocatalytique UV et visible accrue, comme prévu, les photocatalyseurs PCZ QDs/g-C₃N₄ présentent une activité supérieure sous illumination de lumière NIR (Figure R5).

Avec l'optimisation des niveaux de charge des PCZ QD, l'efficacité photocatalytique normalisée est supérieure à la meilleure valeur rapportée dans la littérature pour la photocatalyse dans le NIR. Le transfert de charge a été étudié et analysé grâce à la spectroscopie à photoluminescence en régime continu et résolu dans le temps, par spectroscopie à spin électronique (ESR) ainsi que par des mesures photoélectrochimiques. Les radicaux superoxydes ont été identifiés comme l'espèce active la plus importante dans la photocatalyse par des expériences «scavenger» et des spectres d'ESR. Les PCZ QDs/g-C₃N₄ possèdent de bonnes performances de recyclage et aucun relâchement de métal n'a été détecté dans la solution après photocatalyse. Ce travail met en évidence le grand potentiel des photocatalyseurs QD/g-C₃N₄ 0D/2D dans la réalisation de la photocatalyse à large bande à haute efficacité et de dispositifs optoélectroniques fonctionnels pour une exploitation d'une spectre solaire complète.

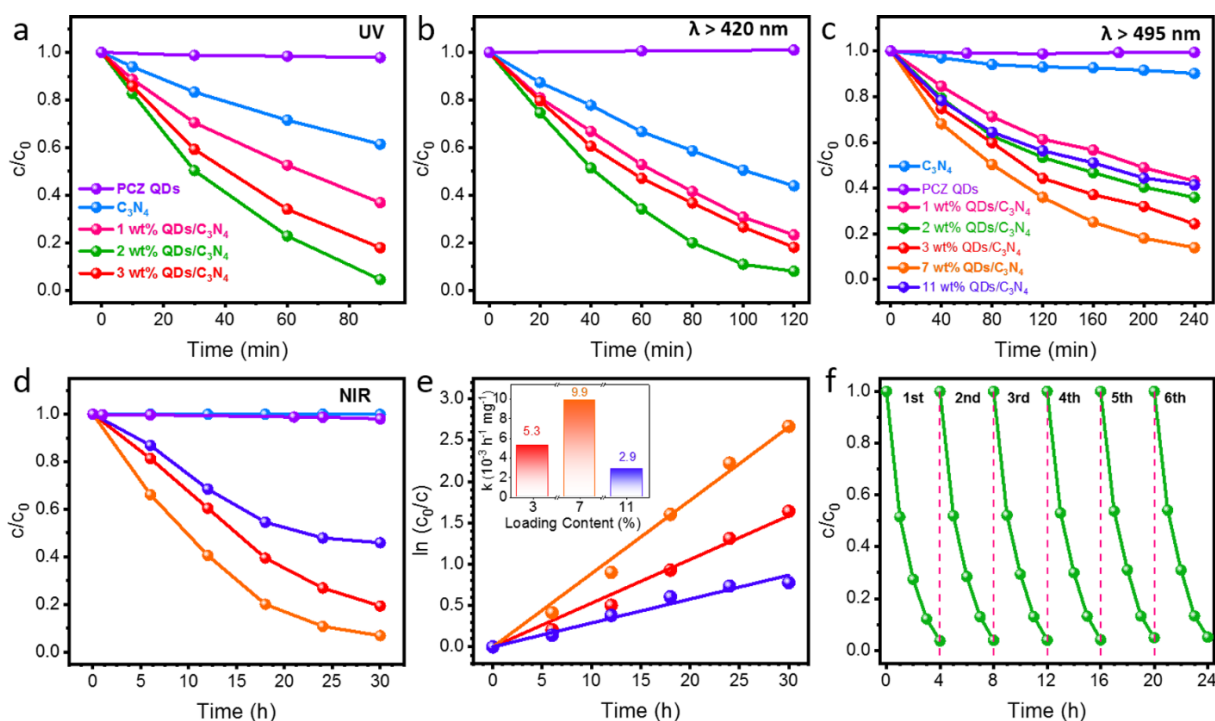


Figure R5 Dégradation photocatalytique de MO sur 0-11% en poids d'échantillons QD/g-C₃N₄ sous (a) UV, (b) $\lambda > 420$ nm, (c) $\lambda > 495$ nm et (d) irradiation par la lumière NIR (980 nm). e) Le graphique de $\ln(c_0/c)$ en fonction du temps de réaction de (d). f) Stabilité photocatalytique de 2% en poids QDs/photocatalyseur g-C₃N₄ dans six réactions de cyclage successives sous irradiation à la lumière solaire simulée.

Bien que les QD PCZ/g-C₃N₄ aient montré de bonnes performances de recyclage et qu'aucune libération de métal n'ait été détectée dans la solution après la photocatalyse, l'utilisation de QD à base de viande lourde constitue toujours un gros problème dans l'application de la purification environnementale. Afin de répondre à cette préoccupation, afin d'utiliser l'énergie solaire de manière plus respectueuse de l'environnement, sans introduire de matériaux contenant des

métaux lourds, et de manière plus rentable, une hétérojonction 2D/2D entièrement dépourvue de métal a été conçue et synthétisée. L'introduction de BP à bande d'interdit étroit devrait conférer au g-C₃N₄ une activité à large bande spectrale dans l'évolution photocatalytique de H₂. De plus, l'hétérojonction 2D/2D est censée favoriser la séparation des charges, rendre BP stable et rendre BP/g-C₃N₄ posséder une activité élevée et une stabilité à long terme dans évolution H₂.

Le chapitre 5 correspond au troisième objectif. Une hétérojonction 2D/2D de BP/g-C₃N₄ a été conçue et synthétisée pour le dégagement de H₂ photocatalytique à large bande. Les publications liées à ce chapitre sont:

Zhang Q, Huang S, Deng J, Gangadharan DT, Yang F, Xu Z, Giorgi G, Palumbo M, Chaker M, Ma D (2019) Ice-Assisted Synthesis of Black Phosphorus Nanosheets as a Metal-Free Photocatalyst: 2D/2D Heterostructure for Broadband H₂ Evolution. *Advanced Functional Materials*, 29(28):1902486.

Zhang Q, Ma D, Chaker M (2019) *Facile Method for Large-scale Producing Few-layer Black Phosphorus Nanosheets. International Patent*, PCT/CA2019/050813.

Une hétérojonction 2D/2D de phosphore noir (BP)/g-C₃N₄ a été conçue et synthétisée pour le dégagement photocatalytique de H₂. La méthode d'exfoliation assistée par de la glace développée ici pour la préparation de nano-feuilles de BP à partir de BP massif conduit à un rendement élevé en nano-feuilles de BP à plusieurs couches (6 couches en moyenne) avec une grande taille latérale et une exfoliation liquide de courte durée et de faible puissance. La distribution des épaisseurs de nanofeuilles de BP a été étudiée en utilisant des mesures de hauteur par microscopie à force atomique (AFM) (Figure R6).

Le g-C₃N₄ présente une structure de feuille nanométrique plissée semblable au graphène (**Figure R7a**). Comme montré par la Figure R7b–d, les morphologies initiales des nanofeuilles BP et g-C₃N₄ ont été conservées après leur intégration. Les nanofeuilles repérées par des flèches sur la figure R7d sont supposées être BP compte tenu de leurs bords relativement «normaux», ce que corroborent en outre l'image STEM de champ noir annulaire aux angles élevés (Figure R7e) et les cartographies élémentaires correspondantes (Figure R7f–i). La cartographie de C, N et P confirme clairement la coexistence de g-C₃N₄ et de BP, et montre l'empilement et l'interaction étroite entre ces deux composants. L'image TEM à haute résolution (HRTEM) révèle des franges de réseau de 0,34 et 0,26 nm, attribuées aux plans (021) et (040) des cristaux de BP (Figure R7j), respectivement. La présence de pics C, N et P indique que des nanofeuilles hybrides BP/g-C₃N₄ ont été préparées avec une pureté élevée et sans dégradation oxydative détectable (Figure R7k),

ce qui est cohérent avec les résultats de la cartographie STEM-EDX et est ensuite vérifié par analyse par XPS.

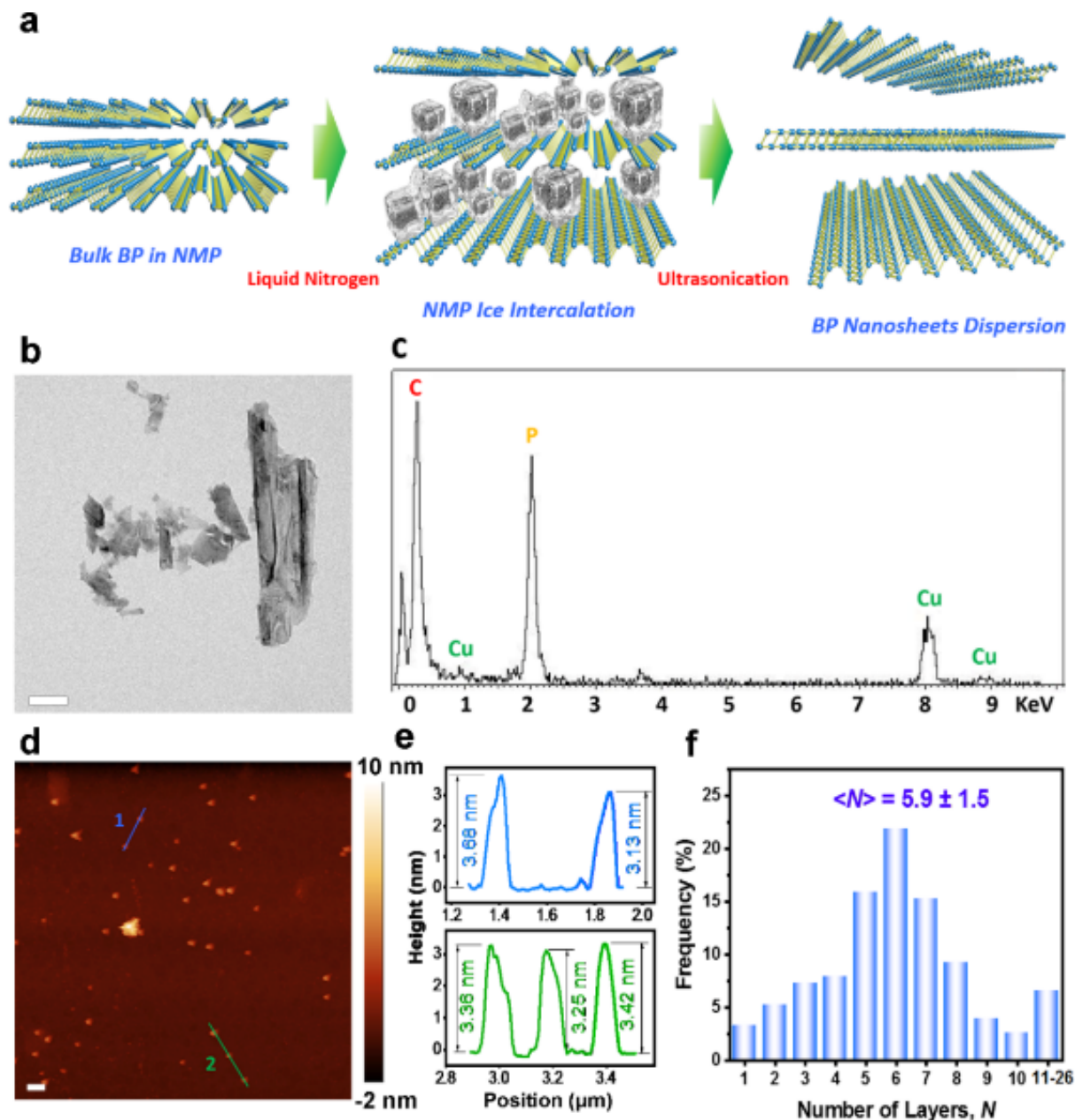


Figure R6 (a) Illustration schématique de la préparation de nano-feuilles de BP avec la méthode d'exfoliation assistée par NMP-glace. (b) image TEM de nano-feuilles de BP et (c) spectre EDX de (b). (d) Image topographique AFM en mode taroudage de nano-feuilles BP à plusieurs couches. Les barres d'échelle en b) et d) sont à 500 nm. (e) Les profils de hauteur des nano-feuilles de BP sur des lignes bleue 1 et verte 2 de (d). (f) Distribution des couches de BP calculée à partir des profils de hauteur de 150 nano-feuilles BP dans des images AFM.

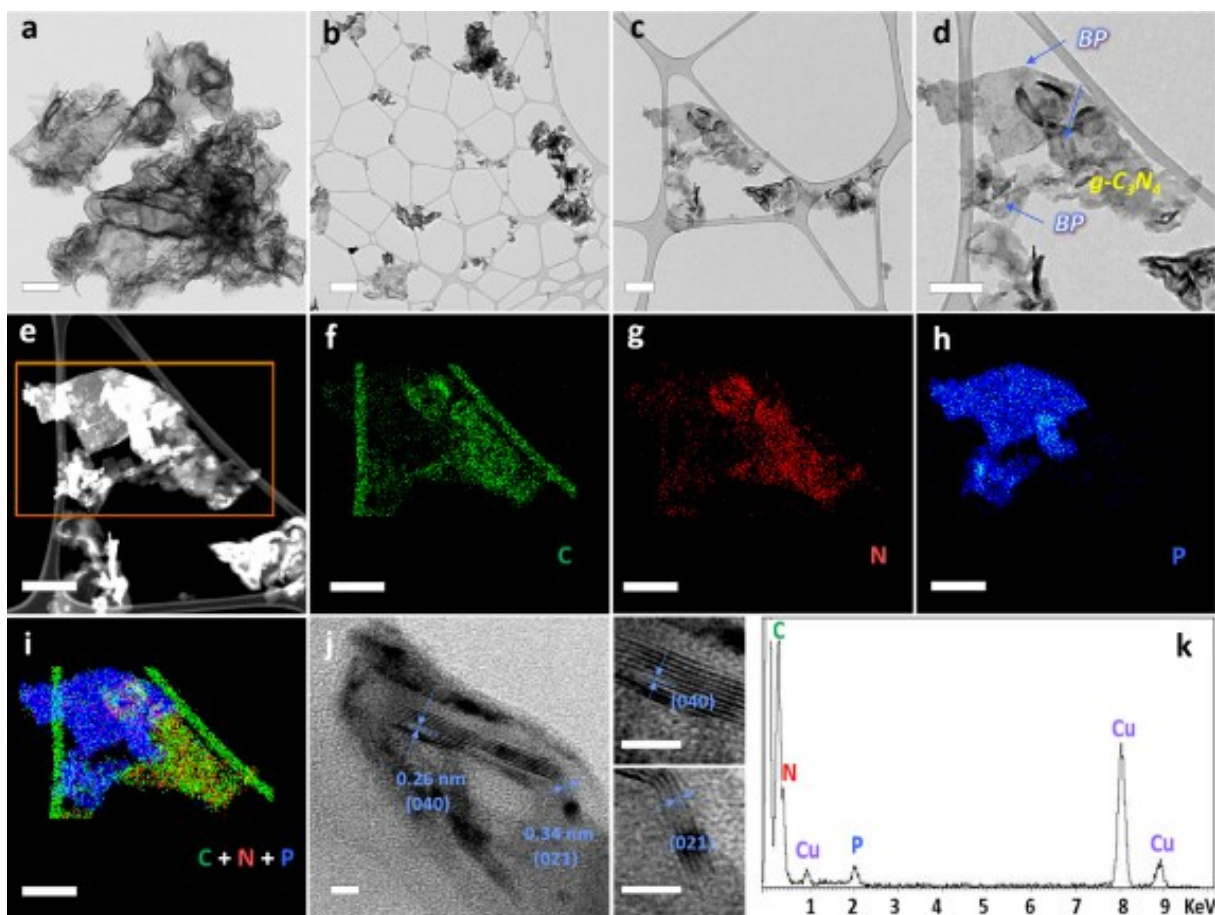


Figure R7 Images TEM typiques de (a) g-C₃N₄ et (b-d) BP/g-C₃N₄ avec des grossissements différents. (e) Image HAADF STEM de (d), (f-i) Cartographie STEM-EDX de C, N, P et superposition de tous les éléments de la zone sélectionnée dans (e). (j) image HRTEM de BP/g-C₃N₄ et (k) spectre EDX de (j). Barres d'échelle: (a) et (c-i), 250 nm; (b) 1 μ m; (j), 5 nm. Les grilles TEM utilisées en (a), (j) et (k) sont des grilles de cuivre recouvertes d'un film de carbone et celles utilisées dans les autres figures sont des grilles de nickel recouvertes d'un film de carbone.

La combinaison de BP avec le g-C₃N₄ protège le BP de l'oxydation et contribue à une activité accrue sous irradiation lumineuse $\lambda > 420$ nm et $\lambda > 475$ nm et à une grande stabilité à long terme. Le taux de production de H₂ à partir de BP/g-C₃N₄ (384,17 μ mol g⁻¹ h⁻¹) est comparable voire supérieur à ce qui a été rapporté dans la littérature, à savoir celui d'un photocatalyseur chargé de métaux précieux sous irradiation $\lambda > 420$ nm. Le transfert de charge efficace entre BP et g-C₃N₄ (probablement dû à la formation de liens N-P) et la large bande d'absorption (démontrés à la fois expérimentalement et théoriquement) contribuent à l'excellente performance photocatalytique. Les mécanismes possibles d'évolution de H₂ sous différents types d'irradiation lumineuse sont mis en évidence. Ce travail présente une nouvelle méthode plus simple pour préparer des nanomatériaux 2D et fournit un paradigme réussi pour la conception de photocatalyseurs sans métal avec une dynamique de porteur de charge améliorée pour la conversion d'énergie renouvelable.

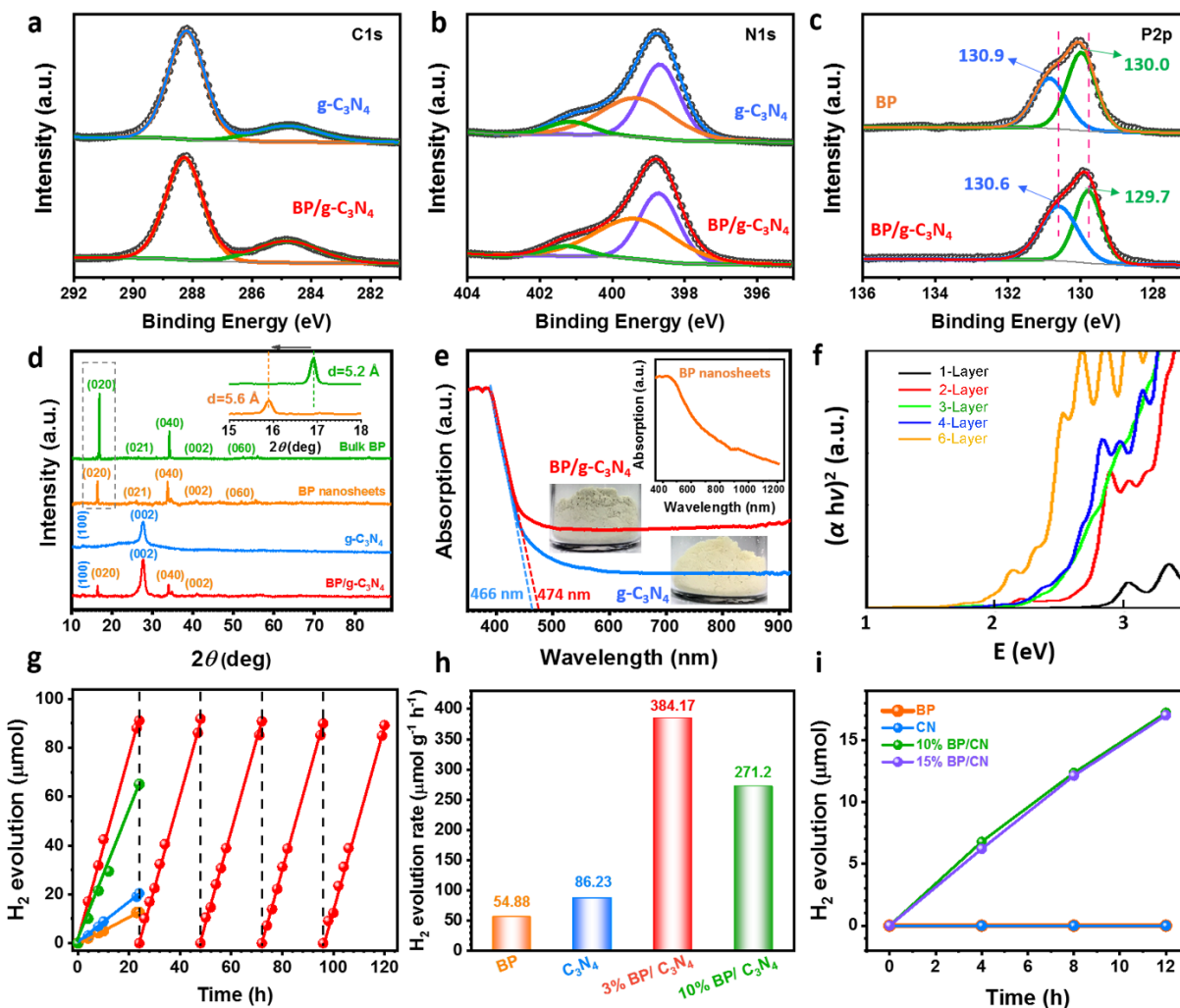


Figure R8 Spectres XPS haute résolution de (a) C1 et de (b) N1 de $g\text{-C}_3\text{N}_4$ et BP/ $g\text{-C}_3\text{N}_4$, et (c) de spectres P2p XPS de BP et de BP/ $g\text{-C}_3\text{N}_4$. (d) Modèles de diffraction des rayons x de feuilles de nanoparticules en vrac de BP, BP, $g\text{-C}_3\text{N}_4$ et BP/ $g\text{-C}_3\text{N}_4$. L'encart correspond à l'amplification des diagrammes de diffraction des rayons X de nano-feuilles BP et BP en masse dans la plage des angles inférieurs, indiquée par le rectangle en pointillé pointillé en (d). (e) spectres d'absorption UV-vis-NIR des échantillons de poudre de $g\text{-C}_3\text{N}_4$ et de BP/ $g\text{-C}_3\text{N}_4$. Les encarts dans (e) sont le spectre d'absorption de nano-feuilles de BP en dispersion (haut), des photos de poudres BP/ $g\text{-C}_3\text{N}_4$ (milieu) et $g\text{-C}_3\text{N}_4$ (bas). (f) Courbes théoriques de Tauc-plot de BP avec différents numéros de couche (1 à 4 et 6 couches). (g, i) évolution photocatalytique de H_2 et vitesse (h) de H_2 obtenue en présence de BP (orange), $g\text{-C}_3\text{N}_4$ (bleu), 3 wt% BP/ $g\text{-C}_3\text{N}_4$ (rouge), 10 wt% BP/ $g\text{-C}_3\text{N}_4$ (vert) et 15 wt% BP/ $g\text{-C}_3\text{N}_4$ (violet) sous (g-h) $\lambda > 420$ nm et (i) $\lambda > 475$ nm.

Conclusions

Le chapitre 6 résume brièvement les principales conclusions de ce travail et présente les défis et perspectives actuels de ce domaine dynamique.